Towards atomically controlled on-surface chemistry on insulating surfaces

DISSERTATION ZUR ERLANGUNG DES DOKTORGRADES DER NATURWISSENSCHAFTEN (DR. RER. NAT.) DER FAKULTÄT FÜR PHYSIK
DER UNIVERSITÄT REGENSBURG

vorgelegt von
Sophia Sokolov
aus München
im Jahr 2021

Das Promotionsgesuch wurde am 12. November 2021 eingereicht.
Die Arbeit wurde von Prof. Dr. Jascha Repp angeleitet.

Prüfungsausschuss:

Vorsitzende: Prof. Dr. I. Gierz-Pehla
1. Gutachter: Prof. Dr. J. Repp
2. Gutachter: Prof. Dr. F. Evers
Weiterer Prüfer: Prof. Dr. M. Scheer

Datum des Promotionskolloquiums: 16.02.2022.

Preface and Acknowledgment

The thesis and the therein presented work was prepared in a period of time spanning from February 2018 to December 2021 in the institute of experimental and applied physics in the faculty of physics of the university of Regensburg in in the working group of Mr. Prof. Dr. J. Repp.

I am very thankful to Mr. Prof. Dr. J. Repp for giving me the opportunity to work as a PhD student and write my thesis on intriguing topics. Observing how Mr. Prof. Dr. Jascha Repp interacts and communicates with each member of the group, made me especially thankful to be able to work in this group. It was very obvious that Mr. Prof. Dr. Jascha Repp spends a lot of time considering the individualities of each member of the group which reflected in the large amount of time he invested in every group member. I am very thankful for all the manifold opportunities to learn and expand my knowledge in the field of physics.

Special thanks to Mr. Dr. Jinbo Peng for the time we worked together, for the endless fruitful discussions during our project, the triplet and the triplet quenching experiments, but also during the project of the ether-bond fission. The time in the Laboratory passed by unbelievably fast because we were a good team and I am happy to have won a friend in the process.

I want to express my thank to Mr. Dr. Tobias Preis for the nice cooperation for the sensor built-up and for being a great conference buddy. I really enjoyed the calm and considerate presence of Mr. Dr. Tobias Preis.

I am very thankful for the fruitful collaboration of our group with the group of Mr. Prof. Dr. Harry Anderson from the University of Oxford, the group of Mr. Dr. Leo Gross from IBM Research - Zurich and the group of Mr. Prof. Dr. Ferdinand Evers from the University of Regensburg concerning the work on the ether-bond fission experiments. I really enjoyed the countless meetings with interesting discussions in a very open and easy-going atmosphere with helpful comments from all the collaborators. My thanks goes to Mr. Dr. Steffen Woltering who synthesized the required substances of highest purity in incredible short time. I am also very thankful for all the discussions and the calculations provided by Mr. Dr. Daniel Hernangómez-Pérez. I want to thank Mr. Dr. Laerte L. Patera for all

his contributions to the work and all the time spend together in the Laboratory in the beginning of the experiments to the ether-bond fission topic.

Moreover, I am thankful for being given the opportunity to participate in a fruitful collaboration for the triplet and the triplet quenching experiments of our group with Mr. Prof. Dr. John M. Lupton, Mr. Prof. Dr. Ferdinand Evers, Mr. Dr. Leo Gross and Mr. Dr. Daniel Hernangómez-Pérez. I could learn a lot through all the interesting discussions and ideas in the meetings.

Furthermore, I am thankful for the opportunity to participate in the fruitful collaboration in the Blatter radical experiments of our group with the group of Mrs. Prof. Dr. Latha Venkataraman and the group of Mr. Prof. Dr. Luis M. Campos. I really enjoyed the time in the laboratory together with Mr. Dr. Laerte L. Patera and Mrs. Prof. Dr. Latha Venkataraman. Especially in the field of physics fewer women are represented than men and subtle differences in the everyday working life arise compared to working in other research fields. From this perspective, I am even more thankful to get the opportunity to work with Mrs. Prof. Dr. Latha Venkataraman.

Finally, my thank goes to all the recent and past members of our group, with whom I was pleased to share my time in and outside the Laboratory. Everyone had an general attitude of offering to help regardless of the personal involvement on the respective topic.

Contents

Constants, Symbols and Acronyms

Constants

Elementary charge [1]	e	$= 1.6022 \cdot 10^{-19}\,\mathrm{C}$
Electron rest mass [1]	m_e	$= 9.1094 \cdot 10^{-31}\,\mathrm{kg}$
Planck's constant [1]	h	$= 4.1357 \cdot 10^{-15}\,\mathrm{eV\,s}$
Reduced Planck's constant	$\hbar$	$= \frac{h}{2\pi}$
Boltzmann constant [1]	k_B	$= 8.617386 \cdot 10^{-5}\,\mathrm{eV\,K^{-1}}$

Symbols

V_b	bias voltage	Φ	work function
E_F	Fermi energy	$\boldsymbol{r}_\mathrm{t}$	center of curvature of the tip apex
I	tunneling current	z	direction $\perp$ surface plane
Γ	transition rate	$\hat{\boldsymbol{V}}$	perturbation operator
Ψ	wave function	$T(E)$	transmission coefficient
ρ	density of states	$f(E)$	Fermi distribution function
s	tip-sample separation distance	M	matrix element of the perturbation operator
κ	decay constant	ω	angular frequency
Δf	frequency shift	m	mass
k	spring constant	A	oscillation amplitude
f	oscillation frequency	f_0	resonance frequency of the free cantilever
F_z	z-component of the force	V_z	potential contribution in the z-direction
V_cpd	contact potential difference voltage	C_z	z-component of the capacitance
V_g	gate voltage	V_dc	d.c. component of the voltage
V_ac	height of the voltage pulses (of a.c. polarity)	Δz	vertical offset from STM setpoint

T	temperature	T_K	Kondo temperature
c	concentration	J	exchange integral
U	Coulomb charging energy	Δ	broadening
$2\Gamma_K$	FWHM of the Kondo peak	q	form parameter
μ	electric dipole moment		

Acronyms

a.c.	alternating current
AC-STM	single electron alternate-charging STM
AFM	atomic force microscopy
FM-AFM	frequency-modulation AFM
nc-AFM	non-contact AFM
AO	atomic orbital
Au(111)	gold (111) single crystal surface
BLA	bond length alteration
CPD	contact potential difference
LCPD	local CPD
Cu(111)	copper (111) single crystal surface
d.c.	direct current
DFT	density functional theory
DOS	density of states
LDOS	local DOS
FWHM	full width at half maximum
GNR	graphene nanoribbon
AGNR	armchair edge GNR
HOMO	highest occupied molecular orbital
KPFM	Kelvin probe force microscopy
KPFS	Kelvin probe force spectroscopy
LT-UHV	low temperature ultra high vacuum

LUMO	lowest unoccupied molecular orbital
MEP	molecular electrostatic potential
Ml	monolayer
MO	molecular orbital
NaCl(2Ml)/Cu(111)	bilayer of sodium chloride on Cu(111)
NG	nanographene
SI	supplementary information
SOMO	singly occupied molecular orbital
SPM	scanning probe microscopy
STM	scanning tunneling microscopy
STS	scanning tunneling spectroscopy
SUMO	singly unoccupied molecular orbital

Introduction

Scanning probe microscopic (SPM) methods deeply rooted in the field of physics can be applied to problems existing in the field of chemistry. The atomic resolution in atomic force microscopy opens up the possibility to image and investigate the chemical structure of an individual molecule in real space [2]. Thereby, chemical reactions with one to a few individual molecules involved can be directly resolved [3–6]. Three exemplary publications that address long-standing questions of the field of chemistry deal with the real-space imaging of the anisotropic charge distribution of the σ-hole of carbon-halogen bonds [7], the direct investigation of an antiaromatic polycyclic hydrocarbon [8] and the hydration of ions on surfaces [9]. A variety of chemical substances were postulated but could not be synthesized so far. Some of these compounds could be generated and investigated in scanning tunneling microscopy (STM) and atomic force microscopy (AFM) experiments, such as higher acenes [10–12], cyclic acenes [13] or triangules [14–16]. Another essential question concerns the structure of carbyne [17, 18], a carbon allotrope in an infinite single strand form consisting of sp-hybridized carbon atoms. Two structures are proposed linking to two different bond orders [19, 20] and differences in their conductivity [21–24]. Model compounds for the two proposed forms of carbyne, possessing polyyne or cumulene moieties, could be directly studied by STM and AFM [25–32].

Physically motivated studies can benefit of chemical knowledge. For example, the generation of graphene nanoribbons or extended one-dimensional or two-dimensional π-conjugated carbon networks is often realized with synthetic bottom-up approaches, including specifically synthesized reactants employed for on-surface synthesis reactions [33–36]. Interesting electronic and magnetic properties of GNRs could be tailored by suitable synthesis and investigated by STM, scanning tunneling spectroscopy (STS) and AFM ranging from modified band structures with band gaps of different size [37, 38], over the presence of topological protected edge states [39, 40] to the nature of the magnetic coupling [41, 42].

In many research topics fundamental principles of physics and chemistry are deeply entangled. An example is the field of spintronics. Stable chemical compounds in an open-shell electronic configuration with distinct physical properties, e.g. slow spin-lattice and spin-spin relaxations times, need to be found. To synthesize a species stable in its open shell configuration with the desired physical properties, the type of the atoms and the chemical structure is decisive. For spintronic applications the chemical compound needs to

be in contact with a metal electrode and sustain its open-shell character under this condition [43]. STS experiments are suitable to investigate the magnetic properties of the species adsorbed onto metal surfaces via the Kondo resonance [42, 44–47]. Even spin chains could be synthesized by means of on-surface covalent coupling reactions and were investigated by STM/S [48].

Many chemical processes are carried out in solution, in gas-phase or at distinct interfaces, which often don't include a conductive surface. Adsorbates exhibit strong electronic coupling to metal surfaces. This strong coupling often impedes a direct comparison of processes investigated on metal surfaces to similar processes in different environments. For a better understanding of chemical processes it is therefore desired to directly investigate individual molecules on weakly interacting surfaces. On insulating surfaces usually the only source of interaction is of phononic nature and no electronic coupling needs to be considered [49]. Hence, the geometric and the electronic structure of individual molecules are usually less perturbed and can often, under caution, be compared to other systems [8, 30–32, 50, 51]. Thick insulating layers can be evaporated onto a metal substrate to electronically decouple an adsorbed chemical compound from the metal substrate completely.

Recent progress in the technique of STM and AFM has widened the field of applications. For example, spin relaxation times of individual adatoms could be investigated by including a pulse scheme with a pump-and-probe pulse to the STM [52]. Electronic states, including out-of-equilibrium states, could be probed on thick insulating layers [53, 54]. Additionally, the orbital densities of individual molecules could be mapped on thick insulating layers and out-of-equilibrium electronic states were addressed [55]. Very recently, the triplet lifetime of individual pentacene molecules could be determined by supplementing the AFM with an all-electronic pump-and-probe pulse scheme [56]. All these newly developed extensions of the AFM and STM technique widen the possibilities of employing these techniques for various physical and chemical processes.

The topics of this work are allocated to the cross-section of physics and chemistry. Two stable organic Blatter radical derivatives are investigated on a gold (111) single crystal surface. Their Kondo signature can be linked to different atomically resolved chemical functionalities of the individual molecules and the orbital density of the unpaired-electron orbital of one derivative can be mapped through the Kondo resonance [57]. Additionally, their assembling scheme at room temperature is investigated [57]. Several compounds with phenoxy functionalities are investigated on insulating bilayers. Reactive species are generated by tip-induced ether bond fission. Some of the reactive species serve as model compounds of carbyne. One reactive species is a representative of the quinoidal group. Quinoidal compounds often possess small singlet-triplet gaps [58]. A lot of compounds of this group are very reactive and their electronic structure and related properties are not fully understood [58]. Finally, a new method to detect lifetimes of electronic states on thick insulating layers is presented [56]. With this method the triplet decay time of individual pentacene molecules is determined and the quenching effect of molecular oxygen located

in close proximity is detected with atomic precision [56].

The thesis is subdivided into five chapters. In the first chapter the theoretical background to the presented topics is elucidated. The following chapter comprises a presentation of the apparatus and a summary of the experimental details. In the third chapter the results of the experiments with the two Blatter radical derivatives are discussed. In the fourth chapter the ether bond fission experiments are presented, including a discussion of the underlying cleaving mechanism and of the different interesting reactive species generated by the bond dissociation reaction. In the last chapter, the triplet lifetime and the quenching by molecular oxygen is investigated for single pentacene molecules.

Chapter 1

Theoretical background

This chapter introduces the reader to the theory of the concepts and methods applied in the experiments. The important considerations and equations are shown for the basics of scanning tunneling microscopy and spectroscopy (STM and STS), atomic force microscopy (AFM), kelvin probe force microscopy and spectroscopy (KPFM and KPFS) and single-electron alternate-charging scanning tunneling microscopy (AC-STM). Here, a brief introduction to these topics is provided, whereas the complete derivations are described in the cited literature. Additional theoretical background needed for the individual topics of this thesis is provided in the beginning of the corresponding chapters.

1.1 Scanning tunneling microscopy and spectroscopy

For the technique of scanning tunneling microscopy and spectroscopy the tunneling effect is applied. The measuring principle relies on two conducting (or semi-conducting) electrodes, a probing tip and a sample, with electrons tunneling from the tip into the sample or vice versa.

1.1.1 Scanning tunneling microscopy

This type of microscopy benefits especially of the strong dependence of the tunneling current on the distance. Following from Borns condition of square integrability, an area where classically no particle should be found, can no longer be treated with zero probability of stay for this particle. In quantum mechanics this particle needs to be described by an exponentially decaying wave function in the forbidden area. This implies that particles have a minor density probability in an area where they would classically not be allowed. The tunneling of electrons in a metal-vacuum-metal junction could be proven experimentally by Binnig and colleagues [59]. The phenomenon can be applied for atomically resolved microscopic measurements [60–62]. In the case of a simple one dimensional potential barrier the tunneling of one electron can be demonstrated analytically. The experimental setup of Binnig et al. [59] is more complex than the one dimensional potential barrier approach

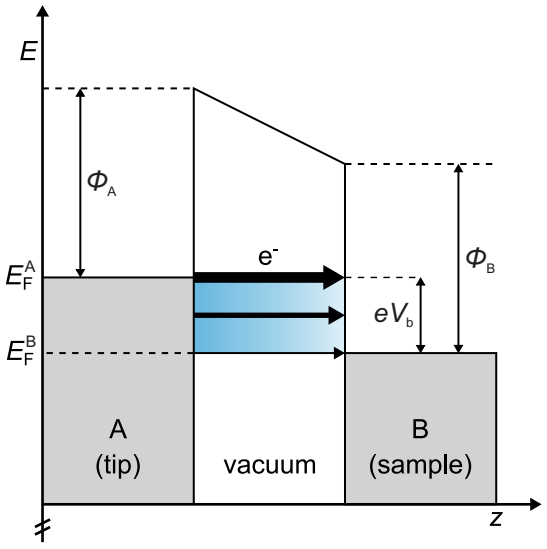

Fig. 1.1. Schematic energy potential perpendicular to the surface plane for an electron seeing two electrodes A and B with an applied bias voltage, V_b, separated by a vacuum gap at low temperatures. The grey area illustrates the Fermi-Dirac distribution at 0 K. Φ_A and Φ_B are the work functions of the two electrodes. For the experimental setup of an STM the electrodes can be assigned to tip and sample as indicated in the scheme. The scheme follows the common approach of applying a bias voltage to the sample with respect to the tip resulting in a lowering of the Fermi level of the sample by $|eV_b|$. The arrows illustrate the differences in tunneling probability depending on the different barrier height for electrons in different energetic level. Schematic is not drawn to scale.

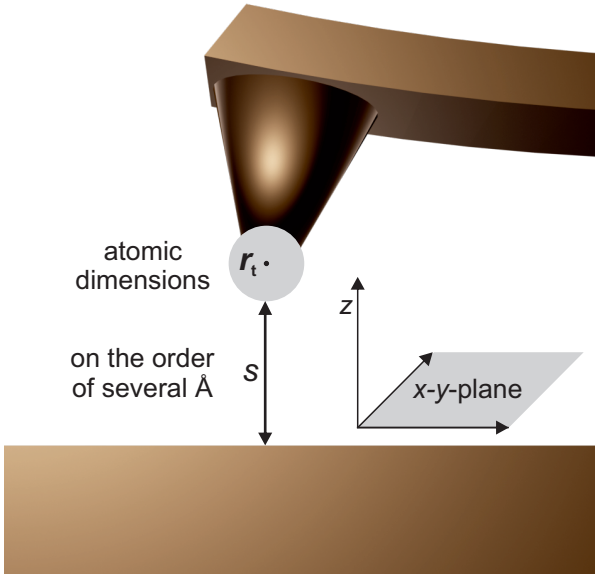

Fig. 1.2. Scheme of a conducting tip and sample in an STM set-up. The tip apex is modelled locally spherical and the wave function of the tip is constructed having s-character. Contributions with angular dependence ($l \neq 0$) are excluded. The center of curvature, $\boldsymbol{r}_t$, is marked at the locally spherical tip apex of atomic dimensions. The distance between tip and sample surface, s, is illustrated in the model. The distance, s, usually amounts to several Ångström.

and yet the exponential dependence of the tunneling current on the distance remains [59]. In figure 1.1 the energy potential for an electron seeing a metal-vacuum-metal junction is depicted schematically. By applying a bias voltage, V_b, to electrode B with respect to electrode A one assures a net current flow in the case of a tunneling event.
In this study the z-axis is assigned to the axis perpendicular to the surface plane of the metal in real space, indicated in figure 1.2. By applying a bias voltage, V_b, to the electrode B the Fermi level of this electrode shifts with respect to the Fermi level of electrode A, lowering it by $|eV_\mathrm{b}|$. Electrode A refers to the tip and electrode B to the sample, because in most common STM-apparati the bias voltage is applied to the sample.
In some of the experiments a carbon monoxide (CO) molecule is adsorbed on the tip apex or films of sodium chloride (NaCl) are grown on the surface of the metal sample. While the specific role of the CO-tip termination or of insulating layers is discussed later on in this thesis, here only metallic electrodes are considered disregarding semiconductors.

In theory the tunneling current can be described with a time dependent first order perturbation approach introduced by Bardeen [63]. However, this perturbation ansatz differs from common first-order perturbation approaches, as therein the wave functions of initial and final state are non-orthogonalized and can be attributed to different hamiltonians. For specific reasons in the construction of the two many-particle states the matrix element can in the end be symmetrized and can be expressed by the current operator.
The initial and the final state of the system are each described by one many-body particle state applying quasi-particle occupation numbers. The initial state is described as a separated unperturbed system. The final state differs from the initial state by one electron, which is transferred from an occupied state in electrode A to a formerly unoccupied state of electrode B. The time dependent solution can then be expressed by a linear combination of the initial state with a set of final states.
The transition probability can be implemented applying Fermis Golden Rule [64] with a transition to a continuous set of final states.

$$\Gamma_{\mu\nu} = \frac{2\pi}{\hbar}\,\delta(E_\nu - E_\mu)\left|\left\langle \Psi_\nu \,\middle|\, \hat{\boldsymbol{V}} \,\middle|\, \Psi_\mu \right\rangle\right|^2, \tag{1.1}$$

where $\Gamma_{\mu\nu}$ is the transition rate, meaning the transition probability per time unit, $\hbar$ is the reduced Planck constant, μ and ν denote initial and final state, E_μ and E_ν are energies of initial and final states and $M_{\mu\nu} = \left\langle \Psi_\nu \,\middle|\, \hat{\boldsymbol{V}} \,\middle|\, \Psi_\mu \right\rangle$ represents the transition matrix element of the perturbation $\hat{\boldsymbol{V}}$. The term $\delta(E_\nu - E_\mu)$ shows that the energy of the initial and the final state must be the same, meaning that this process accounts only for elastic tunneling events. Energy conservation needs to be fulfilled for the many-particle states but the specific values of the energies of the initial and final state do not enter the symmetrized tunneling matrix element derived by Bardeen [63], equation 1.3. Hence, in the following it is sufficient to choose the single particle wave functions involved in the tunneling process. The wave function Ψ_μ represents the initially occupied single particle state (referred to

as initial state) and Ψ_ν represents the initially unoccupied single particle state, where the electron tunnels into (referred to as final state).
As already mentioned previously, the transition will proceed to a continuum of final states. Hence, the transition rate needs to be summed up over all possible final states of the energy interval of interest, $\mathrm{d}E_\nu$. Provided that the matrix element does not vary for the different final states of the energy of interest, the number of final states of energy E_ν can be described by the density of the final states, $\rho(E_\nu)$. Substituting this into the summation over all possible final states contributing to the energy of interest yields,

$$\sum_\nu \Gamma_{\mu\nu} = \int \mathrm{d}E_\nu \, \rho(E_\nu)\Gamma_{\mu\nu} = \frac{2\pi}{\hbar}\rho(E_\mu)\left|\left\langle \Psi_\nu \,\middle|\, \hat{V} \,\middle|\, \Psi_\mu \right\rangle\right|^2. \tag{1.2}$$

Note that the index of the density of states changes from ν to μ in equation 1.2, indicating that only those final states of the same energy as the initial state may enter the sum, in equation 1.1 formerly expressed with the term $\delta(E_\nu - E_\mu)$.
In the case of the metal-vacuum-metal junction some additional considerations can be done to match the general expression to the specific conditions of the system. Following Bardeens approach [63] the symmetrized matrix element may be expressed by the current density operator of the z-coordinate in the barrier region. The problem can be reduced formally to one dimension and can be expressed mathematically by an integration over a separation surface at an arbitrary position in the gap region,

$$M_{\mu\nu} = -\frac{\hbar^2}{2m_\mathrm{e}} \int_\Sigma \mathrm{d}\boldsymbol{S} \, (\Psi_\mu^* \boldsymbol{\nabla} \Psi_\nu - \Psi_\nu \boldsymbol{\nabla} \Psi_\mu^*), \tag{1.3}$$

with Σ being the separation surface in the vacuum gap and m_e the mass of an electron. The quantity in the integrand of equation 1.3 has similarities to the current operator. Here, Bardeen [63] assumed that the tunneling matrix element is constant and independent of energy.
On the basis of Bardeens theory [63] Tersoff and Hamann [65, 66] developed a theory for STM. They limited it to low bias voltages about zero and low temperature. While the temperature is usually low in the here presented STM measurements, the bias voltage is not close to zero.
For this reason a generalized equation of the net tunneling current is presented [67], following a similar approach as Tersoff and Hamann [65, 66], but taking somewhat higher bias voltages into consideration. For simplicity the undistorted wave functions $\Psi_{\mu,\nu}$ of the unperturbed system are seen as valid approximations for the wave functions of the system with applied bias.
By applying a positive bias voltage to the electrode B (sample) the Fermi level of this electrode is lowered by $|eV_\mathrm{b}|$. The states of electrode A (tip) mainly contributing to a measurable net tunneling current are then in the energy range starting from the Fermi level

of electrode A (tip, E_F^A) to the energy lowered by $|eV_b|$. This energy range is marked as a blue region in figure 1.1 and is henceforth referred to as bias voltage window. Electrons of this energy interval can tunnel elastically from electrode A (tip) to unoccupied states in electrode B (sample). The arrows in figure 1.1 pointing from electrode A through the vacuum barrier to electrode B illustrate the elastic tunneling process of the states mainly contributing to the net tunneling current. The thickness of the arrows indicates the varying tunneling probability caused by the difference in barrier height present for initial states at different energies. For finite temperatures the Fermi Dirac distribution function, indicated in figure 1.1 by the grey area for 0 K, blurs out and states in vicinity to the described energy range are contributing as well.
To set up the equation for the net tunneling current, some additional considerations need to be done. To obtain a current the transition rate, equation 1.2, needs to be multiplied by the coulomb charge of an electron, e. To account for spin degeneracy a factor two is introduced.
In the expression of the net tunneling current two summations need to be considered, the sum over all possible final states for one transition of a certain energy and the sum over all possible energy levels, where a transition contributes to a net current. To account for the latter an integral over the energy interval of contributing states needs to be set up. The Fermi Dirac distribution function, $f_{A,B}$ and the density of states $\rho_{A,B}$ include the summation over all possible final states. Additionally the Fermi Dirac distribution function accounts for Pauli's exclusion principle and effects of finite temperatures. When dealing with finite temperatures, the integral over all possible states contributing to a net tunneling current must start from $-\infty$ and go to ∞.
To derive an expression of the measured net tunneling current two general tunneling processes need to be taken into account. The tunneling of the electron from electrode A to electrode B and the back-tunneling of the electrons who have arrived in electrode B. To this point the initial and the final states were denoted with μ and ν, so that the approach was still general and any state of any electrode could be chosen. For the next step the electrodes A and B are explicitly mentioned for the instance of applying a positive voltage to electrode B, but the equation can be rephrased for any precondition, e.g. applying a negative voltage to electrode B or applying a voltage to electrode A. Taking all points made above into consideration results in equation 1.4.
STM measurements are often carried out at low temperatures ($k_B T \ll eV_b$) so that equation 1.4 simplifies to equation 1.5, where the Fermi Dirac distribution function can be approximated by a step function and the borders of the integrals can be specified.

$$I = \frac{4\pi e}{\hbar} \int_{-\infty}^{\infty} \mathrm{d}\epsilon \, [f_A(E_\mathrm{F}^\mathrm{A} - eV_\mathrm{b} + \epsilon) - f_\mathrm{B}(E_\mathrm{F}^\mathrm{B} + \epsilon)] \times \rho_\mathrm{A}(E_\mathrm{F}^\mathrm{A} - eV_\mathrm{b} + \epsilon)\rho_\mathrm{B}(E_\mathrm{F}^\mathrm{B} + \epsilon)|M|^2 \tag{1.4}$$

$$I = \frac{4\pi e}{\hbar} \int_{0}^{eV_\mathrm{b}} \mathrm{d}\epsilon \;\; \rho_\mathrm{A}(E_\mathrm{F}^\mathrm{A} - eV_\mathrm{b} + \epsilon)\rho_\mathrm{B}(E_\mathrm{F}^\mathrm{B} + \epsilon)|M|^2 \tag{1.5}$$

The Integration is proceeded over all energy levels contributing to the net tunneling current, denoted with $\mathrm{d}\epsilon$, in contrast to the previous equation 1.2 which integrates over all possible final states of the same energetic level, $\mathrm{d}E_\nu$. By changing to an integration over all contributing energetic levels the formerly referred to matrix element $M_{\mu\nu}$ is condensed to the expression M.
The tunneling matrix element M is essential for determining the transition rate and hence the detectable net tunneling current. However, it is not straightforward to determine M, because the wave functions of all initial and final states need to be known. Tersoff and Hamann [65, 66] modelled the wave function of tip and sample of the STM at the limit of low bias and low temperatures. For the sample they applied a plane wave ansatz in the x, y-plane, the sample surface plane, visualized in figure 1.2. The wave function of the sample surface decays exponentially in the z-axis in direction towards the tip. The arrangement of the atoms at the tip apex is generally not known. As a first approach Tersoff and Hamann [65, 66] modelled the tip apex as locally spherical. More importantly, they assumed an s-like behaviour of the tip apex excluding contributions with angular dependence ($l \neq 0$). Inserting these modelled wave functions into the expression for the tunneling matrix element M, equation 1.3, results in a dependence of the tunneling current (I) on the charge density of electronic states (DOS) of the tip ($\rho_\mathrm{t}(E)$) and on the charge density of electronic states of the sample ($\rho_\mathrm{s}(\boldsymbol{r}_\mathrm{t}, E)$) evaluated at the center of curvature of the effective tip, $\boldsymbol{r}_\mathrm{t}$, referred to as local density of states (LDOS),

$$I \propto \int_{0}^{eV_\mathrm{b}} \mathrm{d}\epsilon \, \rho_\mathrm{t}(E_\mathrm{F}^\mathrm{t}) - eV_\mathrm{b} + \epsilon)\rho_\mathrm{s}(\boldsymbol{r}_\mathrm{t}; E_\mathrm{F}^\mathrm{s} + \epsilon). \tag{1.6}$$

In the expression above the indices s and t refer to tip and sample, respectively. From here on it is no longer possible to employ any shape for the electrodes, since the geometry of tip and sample are already specified. A small bias voltage compared to the work functions of the electrodes is a condition which needs to be fulfilled. For metal electrodes with work functions typically in the range of several eV, bias voltages in the range of $\pm$ 2 V are applicable [67].
Lang [68] showed on the basis of the Tersoff and Hamanns expression for the limits of low bias and low temperatures [65], equation 1.6, that an adequate guess of $|M|^2$ is provided

by a one-dimensional WKB-approximation,

$$\rho_{\mathrm{s}}(\boldsymbol{r}_{\mathrm{t}}; E_{\mathrm{F}}^{s} + \epsilon) \propto \rho_{\mathrm{s}}(E_{\mathrm{F}}^{s} + \epsilon) T(s, \epsilon, eV_{\mathrm{b}}, \Phi_{\mathrm{t,s}}),$$
$$\rho_{\mathrm{s}}(\boldsymbol{r}_{\mathrm{t}}; E_{\mathrm{F}}^{\mathrm{s}} + \epsilon) \propto \rho_{\mathrm{s}}(E_{\mathrm{F}}^{\mathrm{s}} + \epsilon) \exp\{-2s\kappa\}, \tag{1.7}$$
$$\text{with } \kappa = \sqrt{\frac{2m_{\mathrm{e}}}{\hbar^2}(\Phi_{\mathrm{eff}} - \epsilon)}, \tag{1.8}$$
$$\text{and with } \Phi_{\mathrm{eff}} = \frac{\Phi_{\mathrm{t}} + \Phi_{\mathrm{s}} + eV_{\mathrm{b}}}{2}.$$

In the expressions above T is the transmission coefficient, s denotes the distance between the tip and the sample, see figure 1.2 for an illustration, m_{e} is the mass of an electron and Φ_{eff} is the effective barrier height with respect to the Fermi level of the sample, $E_{\mathrm{F}}^{\mathrm{s}}$. The trapezoidal shape of the barrier is approximated by a square barrier with an averaged height, Φ_{eff}, with $\Phi_{\mathrm{t,s}}$ being the work functions of tip and sample, see figure 1.1. With this approximation the expression for the tunneling current reduces to,

$$I \approx \frac{4\pi e}{\hbar} \int_0^{eV_{\mathrm{b}}} \mathrm{d}\epsilon \;\; \rho_{\mathrm{t}}(E_{\mathrm{F}}^{\mathrm{t}} - eV_{\mathrm{b}} + \epsilon) \rho_{\mathrm{s}}(E_{\mathrm{F}}^{\mathrm{s}} + \epsilon) \exp\{-2s\kappa\}. \tag{1.9}$$

Furthermore, the expression for κ can be simplified by making the assumption that most of the electrons contributing to the tunneling probability are close to the Fermi level of the tip for positive bias voltages, so that $\epsilon \approx eV_{\mathrm{b}}$. If the bias voltage is significantly smaller than the work functions of the electrodes, it can be omitted. Thus, for metal electrodes having work functions of several eV the equation 1.8 can often be simplified to,

$$\kappa = \sqrt{\frac{2m_{\mathrm{e}}}{\hbar^2}(\frac{\Phi_{\mathrm{t}} + \Phi_{\mathrm{s}}}{2})}. \tag{1.10}$$

The term $\exp\{-2\kappa s\}$ entering expression 1.9 is highly dependent on the distance between tip and sample, s. Assuming work functions for metals of several eV a change in the distance s of one Ångström corresponds to a change of roughly one order of magnitude in the tunneling probability. Therefore the measured current, equation 1.9, is highly sensitive to distance changes in the z-axis, making atomic resolution by means of STM accessible. However, the resolution in the lateral directions ($x - y$-plane) is highly dependent on the shape of the tip apex and its sharpness. By scanning over the surface and holding the current constant topographic maps of the surface with atomic resolution can be detected but caution needs to be taken when interpreting these images taken at specific bias voltages as not only information of the topography but also information of the electronic states of the tip and the sample can influence the results of the measurements, as can be seen in equation 1.9.

1.1.2 Scanning tunneling spectroscopy

The evaluation of the topography of a sample surface by STM is impeded by the fact that the results of the measurements include information of the electronic states of the sample surface and the tip apex, compare equation 1.9. However, the information of the electronic states of the sample surface is useful in scanning tunneling spectroscopic (STS) measurements [69].
Depending on which of the three parameters current, I, bias voltage, V_b, or distance between tip and sample, s, should be varied with respect to one another, one of these three parameters always needs to be held constant. In this study it is important to gain information about the orbitals of single molecules decoupled from the metal surface. For this purpose one needs to vary the bias voltage with respect to the tunneling current and the distance needs to be held constant. When observing the tunneling current with respect to the varying bias voltage an additional channel in the tunneling current opens up at the position of the bias voltage corresponding to a broadened orbital resonance of the adsorbate. This results in a steeper slope of the $I - V_\mathrm{b}$-curve. The change in slope enters as a peak in the $\mathrm{d}I\,/\,\mathrm{d}V - V_\mathrm{b}$-curve. To understand the characteristics of the spectra the example of a positive applied bias voltage to the sample with respect to the tip is considered with electrons tunneling from the tip to the sample. Under the assumptions that, first, the main contribution of the tunneling current arises from the electrons at the Fermi level of the tip tunneling to unoccupied states in the sample of the same energy that, second, the DOS of the tip is constant in the energy interval of interest and that, third, the matrix element in the energy interval of interest is constant the following dependence for the derivation of the current can be found [70],

$$\left(\frac{\mathrm{d}I}{\mathrm{d}V}\right)_{V=V_\mathrm{b}} \propto \rho_\mathrm{s}(E_\mathrm{F}^\mathrm{s} + eV_\mathrm{b})\rho_\mathrm{t}(E_\mathrm{F}^\mathrm{t})T(s, eV_\mathrm{b}, eV_\mathrm{b}, \Phi_\mathrm{A,B}). \tag{1.11}$$

In the expression 1.11 the dependency of the derivate of the current, $\mathrm{d}I\,/\,\mathrm{d}V$, on the density of states of the sample and the tip at the respective level of energy for constant values of z, ρ_s and M becomes evident.
This means that the electronic structure of the surface can be probed by ramping the bias voltage, but caution needs to be taken in the evaluation process. Influences of the tip may arise as the density of states of the tip may not be constant in the energy interval of interest or the assumption of an s-like behaviour of the tip is no longer valid.
When probing single molecules on the surface a comparison spectrum of the bare surface can help assigning the peaks to states of the molecule. On bare metal surfaces the broadening of the orbitals of the molecule due to electronic coupling with the metal is usually pronounced. Drastic changes in the electronic structure of the molecule may arise upon adsorption on the bare metal surface due to bond formation with the metal atoms. In contrast, sublimation of few monolayers (Ml) of a substance with a large bandgap, such as sodium chloride, lowers the possibilities of interaction of the molecules with this substrate substantially, while at the same time a net current at an applied bias voltage remains

detectable. If molecules get adsorbed on such few insulating layers on a metal substrate, the broadening of their orbital resonances is on the order of 300 meV [49]. The only source of interaction between the single molecule and the insulating layer is usually due to a phononic coupling among them.
So far, only elastic tunneling processes are taken into account. However, there are also channels for inelastic processes in certain systems, so that additional care needs to be taken in the evaluation process. Within the scope of this work no inelastic features, which are important in the evaluation process, arise in the spectroscopic measurements and hence they will not be addressed in this chapter.
Taking into account all the considerations resulting in the expression 1.11, the density of states of the sample is directly related to the first derivative of the current with respect to the voltage. For a direct measure of the latter a Lock-In amplifier can be applied with the advantage of having a high signal to noise ratio, since it operates as a narrow band-pass filter. The Lock-In amplifier adds a small alternating voltage signal resulting in a modulation of the tunneling current. If the modulation of the current is small enough, a first order Taylor expansion about the bias voltage V_b is sufficient to describe this process. Terminating the Taylor expansion after the linear term and substituting the bias modulation with time, $V(t) = V_\mathrm{b} + V_\mathrm{mod} \cdot \cos(\omega t)$, yields [71],

$$I(V,t) = I_0 + \frac{\mathrm{d}I(V_\mathrm{b})}{\mathrm{d}V} \cdot V_\mathrm{mod} \cdot \cos(\omega t), \tag{1.12}$$

where I_0 is the tunneling current arising for a non-modulated bias voltage V_b, V_mod is the amplitude of the modulation and $\cos(\omega t)$ determines the modulation of the bias voltage with time, t, at a angular frequency, ω. The term of interest, $\mathrm{d}I(V_\mathrm{b}) \,/\, \mathrm{d}V$, links directly to the expression 1.11, making the quantity, which determines the electronic properties of the sample (and the tip), directly accessible.

1.2 Atomic force microscopy

Binnig et al. [72] proposed the atomic force microscope (AFM), similar to the STM but based on small interatomic forces between the atoms at the tip apex and the atoms on the probed surface. Implementing force detection, as opposed to the detection of the tunneling current, a great variety of samples are accessible, such as all types of insulating samples.
In the work of Binnig et al. [72], different modes of operation of the AFM, including oscillating the cantilever at its resonance frequency, were already proposed. By estimating the magnitude of the forces present in the setup they came to the conclusion that atomic resolution should be in principle possible. In their first published experiments [72] signatures with atomic corrugation could be found. Quasi-atomic resolution was demonstrated shortly after the introduction of the AFM [73–77]. However, the images lack atomic defects or step edges. This could be rationalized by envisioning a tip apex constructed out of many laterally displaced mini tips [78]. As a result the signal of the force measurements would be

a superposition of all the different signals of the mini tips. The dominant features present in the images are then those of the periodic structures. Non-periodic structures, such as defects, could not be displayed with this tip apex. In contact mode true atomic resolution could be realized [79, 80]. However, for a standardized procedure to obtain atomic resolution on insulating surfaces, also including reactive surfaces, frequency modulation AFM (FM-AFM) is the favoured technique.
Frequency modulated AFM, also called non-contact AFM (nc-AFM), was introduced by Albrecht and colleagues [81]. This technique is more sensitive to the small short-ranged atomic forces needed for the atomic resolution. Additionally, the stability of the gap between tip and surface can be guaranteed under certain conditions maintaining a pristine tip and surface.
In FM-AFM the cantilever is oscillated close to its resonance frequency at a constant amplitude. When approaching the surface with the tip held at a constant amplitude, the frequency will change. An approximation of the frequency shift for small amplitudes is presented later on.
With the FM-AFM method atomic resolution was finally achieved for more complicated surfaces. The real atomic resolution of the reactive Si(111)-(7x7) surface was realized by Giessibl [82]. Soon after this defect motion could be imaged at room temperature on InP(110) by Sugawara and colleagues [83].
There are several modes of operation for the AFM. This section is focussing on the FM-AFM technique operated in ultra-high vacuum (UHV) at low temperatures (LT) of liquid helium (lHe), since these are the conditions applied for the experimental results presented in this thesis.
To establish an AFM apparatus which can routinely provide experimental results with atomic resolution several adaptations need to be implemented. For a better understanding of the requirements of atomic resolved AFM a comparison of the measured quantities in STM, the net tunneling current, I, with the measured quantity in FM-AFM, i.e. the frequency shift, Δf, is helpful.
The behaviour of the tunneling current as a function of the z-axis is purely monotonic. Opposed to this, the behaviour of the frequency shift measurements in z-direction is depending on a variety of different interactions between the tip and the sample surface. Overall, there is a regime with a monotonic dependence and a regime, where this dependence changes the sign. Thus setting up and working with a feed-back loop system is not straightforward.
In FM-AFM the deflection of the cantilever with time needs to be measured. The method to detect this deflection involves more steps to translate the signal to an electrical processable signal than the measurements of the tunneling current. Hence, detection in the regime of interatomic interactions, nanonewton regime [84], is more complicated. Also additional sources of noise can be identified. The noise sources can be categorized into thermal noise (white noise), oscillator noise (white noise), frequency drift noise ($1/f$-noise) and deflection detector noise ($\propto f$). The experimental FM-AFM measurements presented in this thesis are at LT-UHV conditions and the resonance frequency of the cantilever is relatively high, so that most of the noise sources do not turn out to be a problem. The most dominant noise in the frequency regime of interest is the deflection detector noise [78, 85], which can

be minimized by choosing the right compounds during the built-up [85].
The frequency shift depends on different types of interactions between tip and sample. The predominant contribution is attractive in nature and is of long-ranged character. It can be mainly attributed to van der Waals interactions. Van der Waals interactions do only have attractive contributions. As a result, for extended surfaces consisting of a high number of atoms, there are no cancelling contributions to the overall van der Waals force. The short ranged contributions of the single atoms add up to an overall long ranged force. For the interaction between extended flat surfaces and a spherically shaped tip, a distance dependence of the force of $1/z^2$ can be found [78, 86], in contrast to the $1/r^6$ distance dependence for the interaction of two single atoms [87]. The short ranged chemical forces, which are useful to gain atomic resolution are small in magnitude.
When the tip approaches the surface, the predominant long range interaction forces affect the tip and a jump-to-contact [78, 88, 89] may occur. Choosing the right parameters in FM-AFM this jump-to-contact can be avoided, guaranteeing a stable oscillation of the tip in a defined distance to the surface.
The detection of the cantilever deflection by employing piezoelectric sensors turned out to be reliable and involves less steps to translate the signal to an electrical processable signal than other set-ups. The deflection of the prong induces strain, which leads to surface charges, due to the piezoelectric effect. These surface charges are collected by the electrodes and can be measured as a current. Another advantage is that electric dissipation in the chosen piezoelectric material is very low, making it employable at lHe temperatures [78].
Good properties, especially for the requirements of high resolution FM-AFM imaging, were found for the so-called qPlus sensor [85, 90–92], a specially cut quartz tuning fork. With a resonance frequency of about 30 kHz [91] significant noise sources can be avoided. The spring constant of about 1800 N/m [91] guarantees stable oscillations at small amplitudes. With small amplitudes and relatively small tip-sample separation distances the contribution of the short ranged chemical forces to the overall signal can be maximized, so that atomic resolution can be obtained with low noise contribution [78, 85, 92, 93].

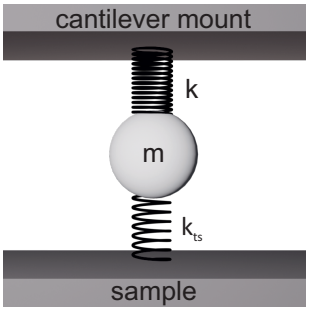

Fig. 1.3. Scheme illustrating the tip sample interactions. The cantilever can simply be expressed by a point mass of effective mass m attached to a spring with a spring constant k. The cantilever is mounted on a ceramic substrate (cantilever mount). Approaching with the tip towards the surface introduces an additional force contribution which can be expressed by a spring constant k_{ts}. This additional spring between tip and sample is related to the interaction forces between tip and sample in the approached position of the tip and is responsible for the frequency shift, Δf.

1.2.1 Frequency shift for small oscillation amplitudes of the cantilever

For small amplitudes, sufficiently stiff cantilevers and relatively small tip-sample separation distances the contribution of the short ranged chemical forces to the signal can be maximized [78, 85, 92, 93]. This is important for high resolution FM-AFM imaging, since the short ranged chemical forces are the basis for atomic resolution.
In FM-AFM the detected quantity is the frequency-shift, Δf. For small amplitudes in a weakly disturbed system the cantilever can be represented by a harmonic oscillator and the frequency shift can then be approximated by a Taylor expansion. First the resonance frequency, f_0, of the cantilever with retracted tip without any influence of the sample must be considered,

$$f_0 = \frac{1}{2\pi}\sqrt{\frac{k}{m}}. \tag{1.13}$$

In this equation m represents the mass of the cantilever.
With the tip in vicinity to the sample surface there is significant interaction among them. The influences of the sample on the resonance frequency of the cantilever can be expressed by an additional spring constant, k_{ts}, compare figure 1.3. The modified resonance frequency in the approached position, f, with k_{ts} accounting for the interactions between tip and sample, can be expressed by,

$$f = \frac{1}{2\pi}\sqrt{\frac{k + k_{\mathrm{ts}}}{m}}. \tag{1.14}$$

The additional spring constant, k_{ts}, can be associated with the force and potential contribution of the z-direction by

$$k_{\mathrm{ts}} = -\frac{\partial F_z}{\partial z} = \frac{\partial^2 V_z}{\partial z^2}. \tag{1.15}$$

Expanding a Taylor series of $f(k_{\mathrm{ts}})$ about zero yields,

$$f = f_0 + \frac{f_0}{2k}k_{\mathrm{ts}}. \tag{1.16}$$

Following this, one can deduce the frequency shift for the constraint of small amplitudes

to be,

$$\Delta f = f - f_0 = \frac{f_0}{2k} k_{\mathrm{ts}}. \tag{1.17}$$

Equation 1.17 suggests that for small amplitudes the frequency shift is directly connected to the force gradient of the z-direction. Additionally, the frequency shift is directly proportional to the derivative of the force component with respect to z, see equation 1.15. This means only changes in the force may be detected and the method has no direct access to static forces in the system.
In this approach, the equation of motion of an harmonic oscillator in one dimension and a Taylor expansion was applied. Alternatively, a more complicated approach describing a weakly perturbed harmonic oscillator with the Hamilton-Jacobi-formalism can be employed [86]. Notably, this approach leads to the same solution 1.17 under the condition of small amplitudes [86] rendering the here presented approach eligible.
For finite amplitudes the relation between frequency shift, Δf, and force gradient is not straightforward. The time average over one oscillation cycle needs to be considered. There are several methods to deconvolute the acting forces between tip and sample from the frequency shift data [94–101].
For a quantitative estimate of the force the different contributions often need to be modelled [86]. This can be achieved by adding attractive or repulsive short range contributions, e.g. Pauli repulsion or van der Waals attraction of the Lennard-Jones potential [78, 102] or the Morse potential [78, 103] and attractive long range contributions, e.g. the summed up van der Waals contribution for specials shapes and certain dimensions. These summed up van der Waals contributions were studied by Hamaker [104, 105] for different macroscopic shapes. For AFM experiments usually a cone or a spherically shaped tip and a flat extended surface are assumed [78, 86].

1.2.2 High resolution atomic force microscopy with functionalized tips

Gross et al. [2] succeeded to resolve the molecular structure of a single pentacene molecule by attaching a single CO molecule to the tip apex. The chemical structure was investigated on a copper (111) single crystal surface (Cu(111)) and on a bilayer (2Ml) of sodium chloride (NaCl) grown on top of the Cu(111) surface.
Following this finding, it was of great interest to form a detailed understanding of the enhanced resolution with CO-functionalized tips.
Moll et al. [106] analysed the contributions of the different forces to the signal of the frequency shift map by comparing experimental results with DFT calculations. Their model system of investigation was a single pentacene molecule adsorbed on a Cu(111) surface. They could attribute the resolution of the corrugations of atomic dimensions in the imaging process to the front CO molecule of the tip, while the rest of the tip could be omitted. It

was found by Bartels et al. [107], that the CO molecule always adsorbs with the carbon atom to the metal part of the tip with the oxygen being the frontmost atom on the tip apex. The precise adsorption geometry of the CO molecule on the tip apex may vary. For simplicity Moll et al. [106] used a CO molecule orientated perpendicular to the surface plane.
By comparing the experimental results of the Δf-maps with the calculations at different heights, which were set constant during the acquisition of one map, different features in the Δf-maps could be ascribed to different force contributions. They attributed a dark appearing halo surrounding the fine resolved structure to attractive van der Waals interactions exhibiting no atomic corrugation. The force contribution resulting in the highly resolved chemical structure of the pentacene molecule was found to be of repulsive nature. This helped to narrow down the force contributing to the atomic corrugation to the Pauli repulsion. The Pauli repulsion arises naturally from the Pauli exclusion principle. The wave functions of the CO molecule and the pentacene molecule will rearrange when brought together closer than a certain distance, preventing their overlap and resulting in an increase of the kinetic energy of the system. The calculated Pauli repulsion exhibited the atomic corrugation.
The two molecules need to be brought together closer than the distance of maximum attraction for atomic resolution due to Pauli repulsive interaction. Hence, it is very important that no bond formation occurs during the approaching process of the two molecules. It could be verified by calculations of Moll et al. [106] that this is indeed the case for a CO molecule. The inertness of the CO molecule is important for the highly resolved images of single molecules. If a bond formation would occur during the imaging process the image would no longer represent information of the pristine molecule on the surface, but would exhibit influences of the tip and structural changes would occur. Also the tip might pick up the molecule from the sample if chemical bonding occurs.
The CO is not rigid on the tip apex and it reacts to lateral potential changes of the surface by bending in different directions. As a result images look distorted and some features appear exaggerated compared to reality. There are several publications that deal with the the effects of the so-called CO-bending in the imaging process [108–113].
Adsorbing other species onto the tip apex may also increase the resolution, whereas the bending effects may vary. Especially xenon (Xe) and oxygen (O) terminated tips are known to produce less distortions in the images due to relaxation processes of the Xe on the tip apex [114, 115]. Examples for different tip functionalizations are xenon, bromine, oxygen atoms or methane molecules [109, 114–117].
Besides the mapping of anisotropic force contributions due to covalent bonding the possibility of imaging hydrogen bonds was postulated by Zhang and colleagues [118]. However, this assignment is controversial and different publications reveal systems with intermolecular contrast in AFM images, where no intermolecular bonding was present [119–121].
For highly resolved images of single molecules it is often desired to image the molecule in the pristine sate without any disturbance evoked by hybridization with the surface. Metal surfaces are reactive and hybridization with the molecule may lead to distortion and deviations from the pristine chemical structure. In contrast, inert insulating surfaces such as

sodium chloride do not or do not strongly hybridize with adsorbed molecules, rendering probing of the pristine structure possible in many cases. Therefore, it is often desired to achieve a sufficient decoupling of the surface and at the same time still being able to perform simultaneous STM and AFM measurements. For this purpose it is helpful to evaporate few layers of sodium chloride onto the metal sample surface. When working with a few monolayers of sodium chloride (two to three Ml usually) the molecules are already decoupled from the metal surface and do not show severe hybridization effects, while at the same time performing STM and STS measurements is possible without any restrictions [122]. There are many publications investigating thin sodium chloride layers on metal surfaces paving the way for routinely applying them in experiment [123–126].

1.2.3 Kelvin probe force microscopy and spectroscopy

The Kelvin probe principle, based on the concept of Kelvin [127], deals with metal plates located in close vicinity to each other, which are in electrical contact, compare figure 1.4**b**. As shown in the following, the difference of the work functions of the two metal plates brought in close vicinity can be detected by the electric field between the two metals.
Zisman [128] introduced a detection mechanism based on minimizing an alternating current component evoked by oscillating one of the metal plates brought in vicinity to the other one.
Smoluchowski [129] investigated work function differences for different surfaces of the same crystal. It was found that dipole moments on the surface double layer have an effect on the work functions. Hence, the work function varies according to the geometry of the respective surface. In general the probability distribution of particles may not end abruptly at the termination of a bulk substance (surface). The differences in mass of electrons and protons lead to different probability distributions in real space. The electron cloud protrudes further into the vacuum than the proton distribution at the surface. This leads to a surface dipole formation and in principal would lead to an increase of the work function for a simple flat surface. However, the volume protruding the surface is less confined than in the average available volume segment per particle in the bulk and the electron density protruding out of the surface plane smears out. This introduces an inhomogeneity of the electron density distribution on the surface as compared to the bulk. As a result the atomic cores are no longer screened sufficiently by the electron cloud at all positions of the surface and at certain positions of the surface the work function is decreased. The Smoluchowski effect [129] can be adapted to different surface geometries, including step edges [130], to explain the varying work functions. The local effects on the work function due to adsorbates [131, 132] can also be explained by introducing dipole moments and charged states. For negatively or partially negatively charged adsorbates an image charge in the bulk metal needs to be considered. The image charge and the charge on the surface form a dipole and alter the work function locally. In general positive charges or partially positive charges on the surface have a lowering effect on the work function, while negative charges or partially negative charges exhibit an elevating effect on the work function.
To detect local variations of the work functions on a surface, a detection method with a

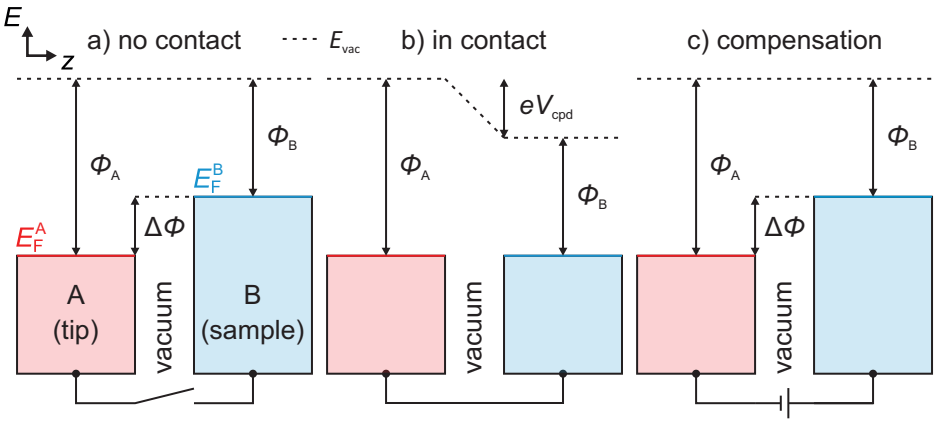

Fig. 1.4. Schematic of the working principle of Kelvin probe force microscopy (KPFM). **a)** Two electrodes are in close proximity with no electrical contact. The vacuum levels E_{vac} align. And the two work functions of the two electrodes differ by $\Delta\Phi = \Phi_{\mathrm{A}} - \Phi_{\mathrm{B}}$. **b)** Upon contacting the two electrodes their Fermi levels align. An electrical field builds up, due to charge flow and the presence of an attractive electrostatic force between the two electrodes. The voltage drop between the two electrodes due to the electrical field, the so-called contact potential difference voltage, V_{cpd}, corresponds to the difference in work functions, $e \cdot V_{\mathrm{cpd}} = \Delta\Phi$. **c)** Applying a voltage equal to V_{cpd} compensates the electrical field which can be applied as a detection mechanism.

high lateral resolution is required. For this reason the AFM was employed. The difference in work functions of the two electrodes, tip and sample, can be deduced from the electrostatic force contributions, on which the AFM is sensitive. Weaver and Abraham [133] and Nonnenmacher et al. [134] were the first to apply the Kelvin method to the AFM. This technique is called Kelvin probe force microscopy (KPFM) with the detected quantity being the force.
To understand the measuring principle, the geometry of the tip and the sample can be omitted and a general capacitor approach can be applied. The energy of the electrostatic contribution, E_{el}, can be expressed by,

$$E_{\mathrm{el}} = \frac{1}{2} C_z (V_{\mathrm{b}} - V_{\mathrm{cpd}})^2, \tag{1.18}$$

where C_z is the capacitance between the two electrodes exhibiting a z dependence and V_{cpd} is the contact potential difference voltage. The contact potential difference (CPD) can be expressed as the difference in the two work functions, $\Delta\Phi$, of the two involved electrodes,

$$e \cdot V_{\mathrm{cpd}} = \Delta\Phi = \Phi_{\mathrm{t}} - \Phi_{\mathrm{s}}. \tag{1.19}$$

Here, the indices t and s, as specified previously, refer to tip and sample, respectively. In

the results presented in this work the FM-AFM method is applied, with the cantilever oscillating at its resonance frequency. This method is sensitive to the force gradient, see equation 1.15. Note, that equation 1.15 is limited to the use of small amplitudes. From the relation 1.15 one can deduce that the frequency shift contribution of the electrostatic interaction, is proportional to the second derivative of the electrostatic energy contribution with respect to the z-component,

$$\Delta f \propto \frac{1}{2}\frac{\partial^2 C}{\partial z^2}(V_\mathrm{b} - V_\mathrm{cpd})^2. \tag{1.20}$$

Expression 1.20 shows only the electrostatic contribution to the frequency shift signal. However, important qualitative information can be deduced. Recording the frequency shift as a function of the bias voltage will result in a parabola, the so called Kelvin parabola [123], compare figure 1.6**a**. This parabola will have its vertex at the position of the bias voltage $V = V_\mathrm{cpd}$. The offset in the Δf-axis of a recorded Kelvin parabola cannot be deduced from expression 1.20, since it only shows the electrostatic contribution to the frequency shift. As already discussed above there are several contributions to the overall force and hence to the overall frequency shift, e.g. van der Waals interaction or Pauli repulsion. However, only the electrostatic force contributions do vary when sweeping the bias voltage and the others do not. Hence, they lead to a constant offset of the parabola in the Δf-axis.
The second derivative of the capacitance with respect to z in expression 1.20 leads to a high local resolution of the contact potential difference of a sample surface in KPFM measurements. The highly locally resolved contact potential difference is referred to as local contact potential difference (LCPD) [135]. The high resolution can be understood by considering the dimensions of the cantilever/tip-vacuum-sample junction and their corresponding contribution to the capacitance term of relation 1.20. In general, the width of the gap in the z-axis is in the Ångström regime and the contribution to the overall capacitance of the junction is small. However, according to the relation of 1.20 the frequency-shift is not proportional to the capacitance, but to $\frac{\partial^2 C}{\partial z^2}$. This means, changes in the capacitance with respect to the z-axis and the dimensions of the junction in z have a significant impact on the frequency shift. During KPFM measurements, the capacitance varies in the small, several Ångström wide, gap region, leading to a dominant contribution to the detected frequency-shift signal and resulting in a high lateral resolution of the LCPD. With the same argument it can be understood, that smaller tip-sample separation distances lead to a higher accuracy of the FM-KPFM results [136, 137]. Also in this context it can be understood that the tip apex has a higher contribution to the measurement results in this technique compared to areas of the tip, which have a larger distance to the sample surface.
The detection of the contact potential difference voltage can give information on the work functions of the two electrodes, see equation 1.19. For this purpose the force contribution of the electrostatic force needs to be minimized, the corresponding voltage is the contact potential difference voltage.
Schematic 1.4 illustrates the V_cpd detection process in more detail. In panel 1.4**a** two metal

electrodes in close proximity but with no contact between them are depicted. They have different work functions, $\Phi_{A,B}$, and their vacuum energy levels, E_{vac}, are aligned. The work function of the tip is usually smaller than the work function of the sample, see assignment of the electrodes in panel 1.4**a**.
In panel 1.4**b** the two metal electrodes are electrically connected. Hence, their Fermi levels align. In the alignment process a charge flow occurs and an electrical field builds up. The two separated electrodes exhibit a net charge of opposite sign and an attractive force between the two electrodes arises.
In panel 1.4**c** the attractive electrostatic force between the two metal electrodes gets minimized by applying a bias voltage to compensate the electrical field. In the compensated situation the vacuum levels align and the electrical field is nullified. The compensation voltage applied equals the contact potential difference voltage, V_{cpd}. This voltage corresponds to the difference of the work functions, $e \cdot V_{cpd} = \Delta\Phi$, of the two conducting electrodes brought into contact.
There are two common detection principles with the FM-AFM, the frequency modulated Kelvin probe force microscopy (FM-KPFM) and the frequency modulated Kelvin probe force spectroscopy (FM-KPFS). With the first method maps of the V_{cpd} are detected over a two-dimensional area of the surface by applying a lock-in scheme [133, 134]. For the second method the tip is held at a fixed position in real space and the bias is swept over a predefined range, so that a Kelvin parabola can be detected [123].
The frequency modulated Kelvin probe method generates LCPD values, which are in good agreement with macroscopic measurements of the CPD [138]. For results of high lateral resolution with few disturbing signal from the surrounding area a sharp tip is obligatory [138, 139].
The lateral resolution can be improved in measurements with close distances between tip and sample [136, 137]. However, the distance should not be too small as problems may arise, such as high tunneling currents or unscreened core charges of single molecules due to Pauli repulsion between tip and molecule [140]. Caution is necessary, as the bias is altered to exclude bias induced localized charges or phantom forces on samples with high resistivity [141, 142].

1.2.4 Charge states and electronic states on thick insulating films

The single-electron sensitivity is an important property of the AFM [136, 144] rendering all the here mentioned experiments possible.
The detection of the Kelvin parabola can be utilized to gain information about the charge state of an adsorbate and a change of its charge state can be detected [53, 55, 136, 143, 145–150]. Moreover, the partial charge distribution within a single molecule can be determined [140, 151–153]. It is even possible to investigate more complex charging processes including charge accumulation and transfer in molecular assemblies [143, 147, 148] or charging induced via mechanical deformation [154].

The Fermi level and the applied bias voltage determine the charge state of an adsorbate

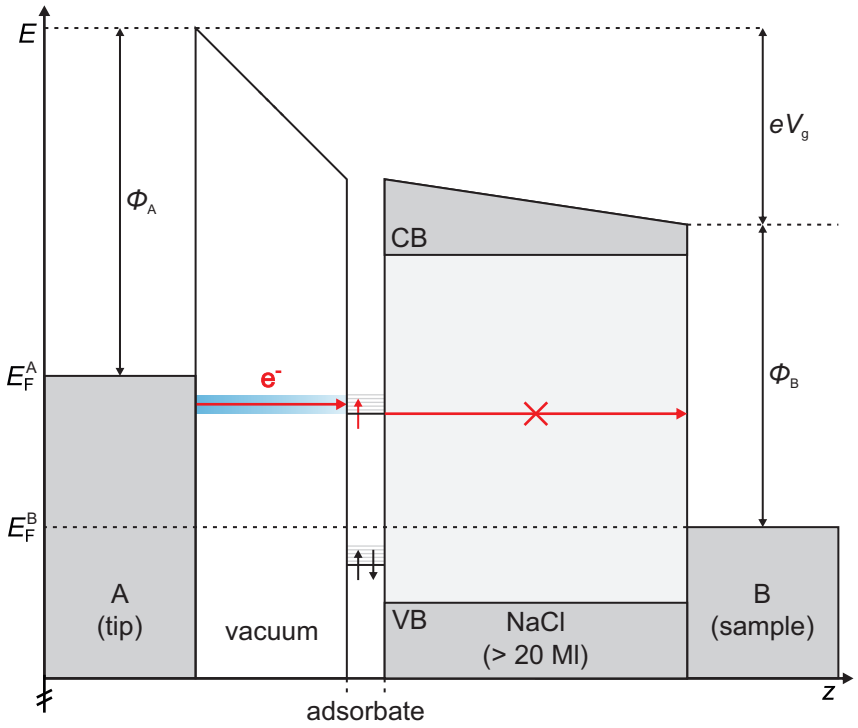

Fig. 1.5. Schematic energy potential perpendicular to the surface plane visualizing experiments on thick insulating NaCl films (> 20 ML). Electrons can resonantly tunnel to electronic levels of the adsorbate or to the vibrational excited higher lying levels indicated by the grey lines. Note that the adsorbate is phononically coupled to the NaCl lattice. The electrons in the adsorbate cannot tunnel through the thick insulating layers into the metallic substrate. The voltage drop occurs to a large extent in the vacuum gap region, while a smaller voltage drop is observable in the NaCl region. Both voltage drops add up to the applied gate voltage V_g. Schematic is not drawn to scale. CB refers to conduction band and VB to valence band.

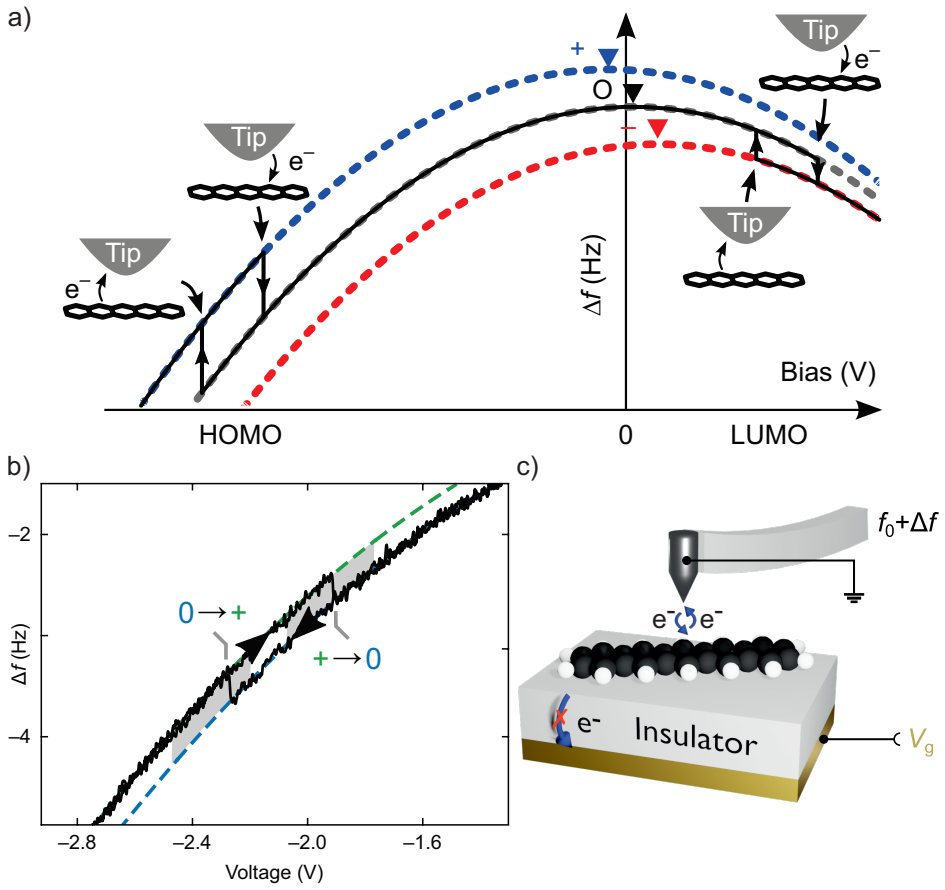

Fig. 1.6. Schematic of charging processes detected by KPFS of adsorbates on thick insulating layers. **a)** Three different Kelvin parabolas of a pentacene molecule adsorbed on a thick NaCl film are displayed corresponding to three different charge states of the adsorbate: The singly positive charged state is represented by the blue curve, the neutral charge state is represented by the black parabola and the red curve corresponds to the singly negative charged state. The image is taken from [143]. **b)** A Zoom-in of a hysteresis loop where a switching of one parabola to another one, corresponding to a different charge state occurs. The grey area represents the voltage window with high charge state switching probability. The switching of the adsorbate from the neutral to the positive charge state has a different bias window compared to the switching from the positive to the neutral charge state. Image is taken from [53] with slight modifications. **c)** Schematic of experiments on thick insulating layers. The pentacene molecule may be charged or discharged, but the electrons cannot tunnel into the metallic substrate. The schematic is similar to the one in [56]. The arrows at the hysteresis loops in **a)** and **b)** indicate the direction of the voltage sweep.

on a metal surface. If an electronic level of an adsorbate lies above the Fermi level of tip and sample, it will stay unoccupied. In contrast, if a formerly unoccupied orbital of an adsorbate on a metal surface lies beneath the Fermi level of the tip, it will be occupied by electrons tunneling from the tip to the orbital level. The electrons will subsequently tunnel from the electronic level of the adsorbate into continuum states of the metal sample if possible. If adsorbates on thin insulating layers are charged with an additional electron occupying an electronic state above the Fermi level of the sample, the electron can tunnel through these thin layers into continuum states of the metal sample.

Switching a charge state of an adsorbate on conducting surfaces can be realized and detected by means of STM [155–158]. Even submolecular resolution of the electronic and geometric changes upon charging single molecules can be resolved [159]. Sufficient decoupling from the surface can be achieved by evaporation of few insulating layers onto the conducting surface [122]. The charging ability of an adsorbate relies on the level alignment with respect to the Fermi level of the tip and the sample and adsorbate orbitals in vicinity to the Fermi level of the sample can be permanently charged [155–157, 159].

On insulators with sufficiently large band gaps, gating of the sample is feasible with no net tunneling current detectable at the substrate. Thick film insulating layers of more than 20 monolayers can be evaporated onto metal substrates [143, 146, 160] to generate this insulating effect where no electrons can tunnel from the tip or from the adsorbate through the thick insulating layers into the metallic substrate on a relevant time scale for the experiment, see figure 1.6**c**.
Figure 1.5 depicts this situation. If the Fermi level of the tip is high enough, so that formerly unoccupied orbital level of adsorbates lie beneath it, the unoccupied level will be populated by electrons tunneling from the tip (red arrow in figure 1.5). As opposed to adatoms or molecules directly adsorbed onto metal samples, the electrons populating the formerly unoccupied orbital cannot tunnel through the thick NaCl film into the metal substrate. During the charging process vibrational and phononic excitations need to be considered. Hence, an electron tunneling from the tip into the adsorbate may occupy vibrational excited states, indicated by the blue region in figure 1.5. The phononic coupling to the NaCl lattice plays an important role and high reorganization energies can be detected upon charging of an adsorbate on thick insulating layers [53].
In figure 1.5 the applied gate voltage drops to a large extent in the vacuum gap region and to a smaller extent in the thick NaCl film. The partial voltage drops sum up to the overall applied gate voltage V_g, see figure 1.5. By choosing an appropriate gate voltage different electronic level of the adsorbate can be addressed.

On insulators or thick insulating layers the switching of charge states of adsorbates can be detected by means of KPFS. If an adsorbate alters its charge state, the corresponding Kelvin parabola will switch to a parabola with a different vertex. The shift of the vertex of the Kelvin parabola can be traced back to the alteration of the local work function and hence the LCPD. The Kelvin parabolas for different charge states are exemplarily

displayed in figure 1.6**a** for a single pentacene molecule adsorbed on thick insulating layers. Additional negative charges in an adsorbate introduce additional electrostatic force contributions sensed by the cantilever in form of a lowered value in the frequency shift, compare figure 1.6**a**. In these type of experiments the charge state of the molecule can be manipulated, but no electrons can tunnel through the thick insulating layers to the metal substrate, as schematically depicted in figure 1.6**c**.
A hysteresis loop can be detected for a charge state switching process, see figure 1.6**b**. This means that the charging and the discharging are occurring at different bias voltages and a bistable voltage window is existing inside the hysteresis loop.
The two switching processes of the charge state in the hysteresis are subject to some stochasticity associated with the involved tunneling processes [53]. The grey areas at the hysteresis loop of figure 1.6**b** indicate the range of different charging or discharging gate voltages observed for a multitude of different bias sweeps.
The two involved charge states are almost degenerate at a voltage corresponding to the center point of the hysteresis loop. However, the respective charging and discharging do not occur spontaneously and the two states are metastable and do not interconvert on time scales of the here commonly performed experiments. The reason why the two states may not interconvert in the center of the hysteresis loop at sufficiently large tip-sample separation distances is due to the fact that an additional term in energy is needed to overcome the Franck-Condon blockade [56, 161]. The most probable transition is usually not from one electronic ground state to another, but to an vibrationally excited level. Only after the transition, a relaxation to the electronic ground state of the new charge state occurs. The difference in energy of the primarily occupied vibrationally excited state and the ground state of the new charge state can be associated with the so-called reorganization energy. During the relaxation process the atomic positions rearrange to a new geometry which is the most stable one for the new charge state. Summing up over the energy differences associated with the relaxation processes of both transitions involved in one hysteresis loop (charging and discharging) yields the reorganization energy for this particular charge transfer process [53]. For molecules adsorbed on an ionic lattice, here NaCl, the positions of the lattice atoms, especially in the surrounding of the adsorbate, also need to be considered. The sodium chloride lattice has a large impact on the value of the reorganization energy which is for molecule-thick NaCl film experiments on the order of hundreds of meV [53, 54].

The investigation of a large variety of charge states, charge state transitions and charge transfer processes of different adsorbates [53, 55, 143, 146, 148–150, 154] on insulators or thick insulating layers is rendered possible by this technique.
Fatayer et al. [53, 54] were able to probe electronic states on thick insulating layers. By detecting time traces of charge switching transitions of adsorbates at different gate voltages they could derive single electron differential tunneling rates [53] from which broadened energetic levels of electronic states could be deduced. In addition to equilibrium states also out-of-equilibrium states could be probed. Reorganization energies of a molecule insulator system [53] and excited states [54] could be investigated with this technique.

1.2.5 Alternate-charging scanning tunneling microscopy

Single electron alternate-charging STM (AC-STM) introduced by Patera et al. [55] is a novel technique, which allows to map orbital structures of individual molecules as a function of their redox state (including out-of-equilibrium states). Even slight changes in the density distribution of a respective orbital upon charging can be investigated [55, 150]. With common scanning tunneling techniques orbital mapping could be realized [122], but this technique is limited to conducting surfaces or thin insulating layers grown on top of conducting surfaces. For the AC-STM technique no net direct current (d.c.) flow needs to be detectable at the substrate and insulators or thick NaCl films on top of metal samples can be employed [55]. The thesis of Dr. Fabian Queck-Scharrer [163] and the publication of Patera et al. [55] contain a detailed description of the AC-STM technique.

In FM-AFM conservative and non-conservative force contributions can be distinguished. Conservative force contributions manifest themselves in a resonance frequency shift of the cantilever, while non-conservative forces may lead to energy loss (or gain) in the motion of the cantilever [78]. This dissipation can be detected in the damping channel recording the additional energy, which is required in order to maintain the cantilever at a constant amplitude.

Charging phenomena occurring on the time scale of the cantilever oscillation have been realized for quantum dots [164–166]. The oscillation of the tip leads to the formation of an alternating electrical field in the junction. Gating of the tip in proximity to a quantum dot may lead to switching of its charge state depending on the cantilevers excitation amplitude. As the process is driven by the oscillating tip at its resonance frequency, the switching of the charge state occurs with comparable frequency and can be recorded in the damping channel [167].

In AC-STM a voltage-pulse scheme is designed to steer single electron tunneling processes with short voltage pulses ($\approx 100\,\mathrm{ns}$) of alternating current (a.c.) polarity and a pulse height of V_{ac} added to a direct current (d.c.) component (V_{dc}). This pulse train is fed to the back-gate electrode at the substrate [55]. The voltage offset of the pulse, V_{dc}, is chosen to be in the center of a charging hysteresis of a selected charge state transition process of an individual molecule impeding the interconversion of the charge states in-between the pulses, compare subsection 1.2.4. The pulse height, V_{ac}, is chosen large enough to induce charging and discharging of the molecule by the pulses of alternating polarity. The form of the a.c. pulses is designed to avoid undesired excitation of the cantilever [55].
The pulse trains and accordingly the charging processes are synchronized with the cantilever oscillation, compare figure 1.7. As indicated in figure 1.7 the phase-relation of the cantilever motion and the occurrence of the charging processes is well defined. Periodic charging and discharging can be observed at the turnaround points of the cantilever with this pulse scheme. One of the two different charge states in an oscillation cycle contains an additional electron and can be distinguished in the measurements through an additional

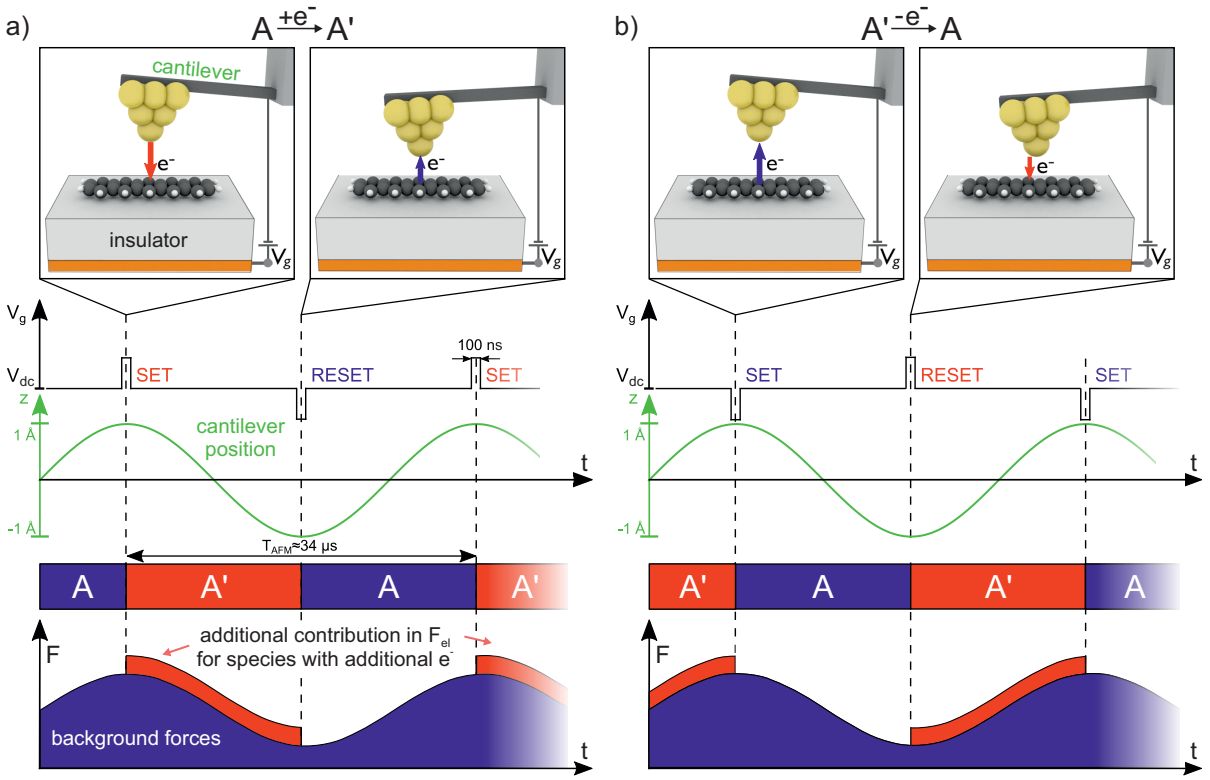

Fig. 1.7. Schematic illustrating the working principle of single electron alternate-charging STM (AC-STM). Voltage pulses of opposite polarity synchronized with the cantilever motion are added to a voltage offset, V_{dc}, inducing periodic charging and discharging of adsorbates beneath the tip (green curve). Pulses occur at the set and at the reset position in time, marked in red and blue, respectively. The processes occurring at the set position are responsible for the submolecular resolution during imaging, whereas at the reset position the adsorbate is reliably set back to its initial state without contributing to the submolecular resolution. The polarity of the pulse is decisive for the type of transition. Charge states with an additional electron compared to the other participating charge state, exhibit an additional electrostatic force contribution, see area highlighted in red in the force versus time diagram. **a)** At the set position in time an electron tunnels from the tip into the adsorbate. Hence, after Koopmans' theorem [162] the electronic state of A is mainly responsible for contrast formation. At the reset point in time an electron tunnels back into the tip and the original charge state is recovered. **b)** At the set position in time electron withdrawal from the adsorbate is induced. Hence, after Koopmans' theorem [162] the highly resolved contrast in the image can be assigned to the electronic state of A'. At the reset point in time an electron tunnels from the tip into the adsorbate. The charging processes happening at the respective set and reset points in time are illustrated in the top row of this figure for the two pulse schemes of **a)** and **b)**. The image was kindly provided by F. Queck-Scharrer [163] and is displayed with slight modifications.

force contribution of electrostatic nature visualized by the red area in the force versus time curve in figure 1.7. This means the force acting on the cantilever differs during its inward and outward movement in one oscillation cycle for this phase-relation leading to a measurable signal in the dissipation channel [55].
The pulse scheme with respect to the cantilever motion is displayed in figure 1.7 for two different charging sequences, **a** and **b**. The pulse occurring when the cantilever has the largest separation to the surface in its oscillation cycle is called set pulse. The pulse occurring when the tip-sample separation distance is smallest in the oscillation cycle of the cantilever is referred to as reset pulse. With the voltage pulse scheme in figure 1.7**a**, charging and subsequent discharging during on oscillation period can be achieved which is indicated by the model images depicted in the upper row of figure 1.7**a**. Equivalently, by changing the polarity of the pulses, see voltage pulse scheme in figure 1.7**b**, discharging and subsequent charging can be accomplished which is indicated by the model images depicted in the upper row of figure 1.7**b**.
Now that the detection mechanism has been explained, in the following the spatial resolution is explained. The signal relies on the tunneling of single electrons between the tip and the addressed orbital of the adsorbed molecule. In AC-STM an amplitude of one Ångström is often chosen, resulting in a separation of the two turnaround points of one oscillation of the cantilever by two Ångström in the z-axis and causing a change in tunneling probability by roughly two orders of magnitude, compare subsection 1.1.1. As a result, for a wide range of tip heights, the reset pulse can effectively discharge (charge) an adsorbate with a success rate close to unity and almost irrespective of the lateral position of the tip [55], while the set pulse can only charge (discharge) less efficient due to the reduced tunneling probability by two orders of magnitude. This reduced tunneling probability leads to a higher spatial resolution in conjunction with resonant tunneling to or from the addressed orbital in the charging process which is further described in the next paragraph for the scenario illustrated in figure 1.7**a**.
An electron has to tunnel from the tip to the LUMO or SUMO (singly unoccupied molecular orbital) of an adsorbate to charge it. The spatial distribution of the electronic density of the orbitals of molecules varies. Assuming a tip with s-character, the differences in orbital overlap in the imaging process can be attributed to the laterally varying orbital density distribution of the adsorbate. Hence, the varying orbital density distribution of the adsorbate can be linked to position dependent enhanced or reduced tunneling probabilities. An electron will tunnel preferentially to areas with high density of the respective orbital and less preferentially to positions with low density of the respective orbital, such as nodal planes. This local variation of the tunneling probability opens up the possibility of mapping the density distribution of different molecular orbitals on insulating layers with submolecular resolution. While the subtle differences of tunneling probability are overall noticeable for the tip furthest retracted from the surface in one oscillation cycle, the tunneling probability at the turnaround point closest to the sample is chosen to be close to unity. With a tunneling rate close to unity, the set pulse does (almost) not contribute to the atomically scaled lateral corrugation of the signal [55]. Hence, the set pulse determines the spatial signature with submolecular resolution, while the reset pulse resets the molecule to

its former redox state without contributing to the submolecular resolution [55]. Therefore, the detection mechanism is only sensitive to the redox-state transition at the set position. The charging process contributing to the submolecular resolution can be chosen by selecting a suitable polarity of the pulse at the set and reset position. In figure 1.7**a** a set pulse with positive polarity is followed by a reset pulse with negative polarity. This will result in an injection of an electron into the orbital of the adsorbate at the set position and subsequent tunneling of an electron to the tip at the reset position. The contrast is then dominated by the transition in conjunction with the injection of the electron ($A + e^- \rightarrow A'$). The arrangement with both pulses being switched in polarity is shown in figure 1.7**b**. In this arrangement the contrast is dominated by the transition in conjunction with an electron tunneling from the molecule to the tip ($A' \rightarrow A + e^-$). According to Koopmans' theorem the electronic transitions responsible for contrast formation can be approximated by the initial state of this transition [162].

Three advantages of this technique can be stated. Orbital structures of single adsorbates can be directly probed on insulators, which could previously only be realized by means of STM on conducting surfaces or on thin insulating layers evaporated onto conducting surfaces. On insulators the coupling of the adsorbate to the substrate is usually minor and often only phononic coupling plays an important role [49]. Therefore, as a second advantage, the adsorbates usually exhibit no or minor change in geometrical and electronic structure upon adsorption on the insulator. A main reason for the low interaction between adsorbate and insulator is inherently given by the electronic structure of the insulator which possesses a large band gap. Due to the large band gap, electrons populating electronic levels of the adsorbate are not able to further tunnel into continuum states of the substrate and are confined in the respective orbital. This bears the possibility of probing different orbitals of the adsorbate with this technique by gating the Fermi level of the tip with respect to the adsorbate insulator system. Hence, as a third advantage, the limitations in conjunction with short time population of the electronic states of molecular or atomic orbitals are revoked as compared to STS measurements on conducting surfaces and various electronic states, including out-of-equilibrium states, can be probed.

Chapter 2

Experimental setup and methods

In this chapter information on the apparatus employed in the measurements is given. Furthermore, the different procedures during sample preparation for various types of samples are described and the modes of data acquisition are explained. The adaptations to improve the sensor built-up with regard to the balance of the time required for built-up and the performance are described and a new dual evaporator for chemical substances is presented.

2.1 Apparatus

Data acquisition was carried out with a home-built combined STM and AFM at low temperatures (LT) and ultra high vacuum (UHV). The temperatures during the measurements range from 5 K to 7 K and the pressure in the UHV environment is in the range of $1{\cdot}10^{-10}$ to $5{\cdot}10^{-11}$ mbar. The sensor used for the measurements is a commercially purchased qPlus sensor [85, 90–92].
The apparatus consists of three separate vacuum chambers. The load-lock (I), the preparation chamber (II) and the measuring chamber (III), compare figure 2.1.
The load-lock can easily be brought to ambient pressure and serves for the insertion of samples and evaporators. A turbo molecular pump (VI, figure 2.1) adjacent to the load lock helps to quickly achieve a low pressure of down to $1{\cdot}10^{-8}$ mbar.
In the preparation chamber the sample can be cleaned with a sputter gun, followed by annealing cycles. Additionally, salt evaporators are permanently installed in this chamber, to e.g. dose thin or thick films of sodium chloride onto a sample. Evaporators for subliming small amounts of chemical substance onto the sample can be inserted via the load lock and can be positioned directly in front of the shield surrounding the STM/AFM-scan head. An ion getter pump and a titanium sublimation pump (V, figure 2.1) connected to the preparation chamber ensures the maintenance of the low pressures.
In the third chamber the measurements are carried out. Directly above the STM/AFM-scan head a liquid helium (lHe) and a liquid nitrogen (lN_2) bath cryostat (IV, figure 2.1) are mounted. By this the sample can be cooled down to temperatures of about 5 K to 7 K. The investigation of single molecules on insulating layers can usually only be performed at

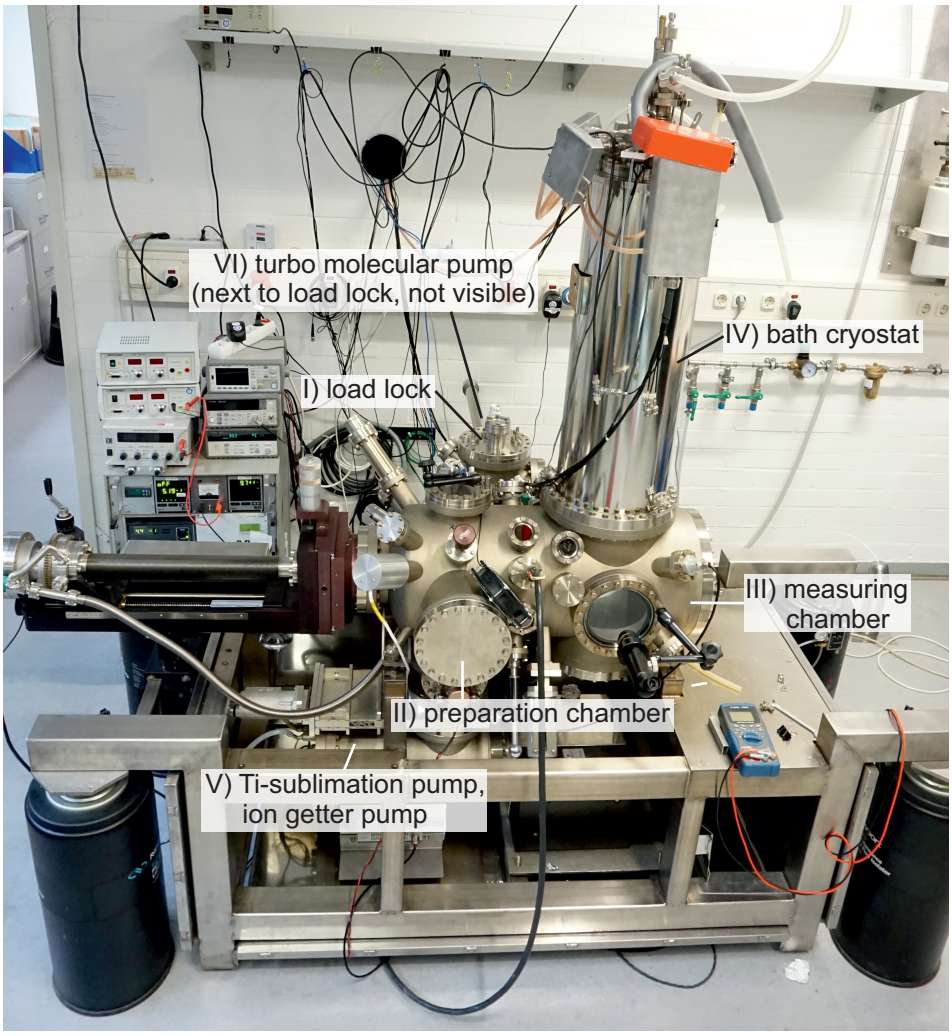

Fig. 2.1. Apparatus consisting of three different chambers (load lock (I), preparation chamber (II), measuring chamber (III)) with a liquid helium and a liquid nitrogen bath cryostat (IV) above the STM/AFM-scan head. Required material can be inserted into the load lock. A turbo molecular pump (VI) at the load lock can quickly build up a vacuum of down to $1{\cdot}10^{-8}$ mbar. In the preparation chamber the pressure is held low with an ion getter pump and a titanium sublimation pump (V). The liquid helium bath cryostat improves the vacuum even more so that the pressure in the preparation chamber and in the measuring chamber are usually about $1{\cdot}10^{-10}$ to $5{\cdot}10^{-11}$ mbar. Photograph courtesy of and kindly provided by Thomas Buchner.

such low temperatures. At elevated temperatures the molecules first become mobile and then desorb. The lHe bath cryostat contributes to ensure the stable low pressure in the UHV chamber.
A more detailed description of the vacuum chambers and the scan head design is provided by Münnich [168] and Neu [169].

2.2 Sample preparation

Single crystal metal substrates with specific surface terminations are employed. Metal surfaces vary in terms of work functions, growth processes, reactivity and catalytic activity. These aspects are taken into account for choosing a suited substrate for a system under investigation.
In this thesis often the copper (111) single crystal surface (Cu(111)) is chosen. Growing sodium chloride of the amount of one monolayer at temperatures between 270 K to 290 K on top of this surface will result in a half-covered sample with double layered defect free (100)-terminated sodium chloride islands [124, 126].
A gold (111) single crystal surface (Au(111)) was employed for measurements, where a weak interaction between the adsorbate and the metal surface was desired. The Au(111) single crystal surface is regarded as relatively inert. Hence, in a lot of publications, where metal surfaces were mandatory for the experiment, the Au(111) surface is employed in the investigation of new reactive compounds, which should maintain a state comparable to the gas-phase condition [10–12, 14–16, 40, 170–174].

As a first step in the preparation process the sample needs to be cleaned. This is realized by several sputtering and annealing cycles. Sputtering is carried out with ionized neon. After each sputtering cycle the sample is annealed to 770 K.

In some preparations thin- or thick-film sodium chloride adlayers are desired. Those are sublimed onto the sample surface, with the sample being held at a certain temperature. The amount of material sublimed onto the sample can be detected with a quartz crystal micro-balance.
For thick-film sodium chloride preparations usually a coverage with more than 20 monolayers is required. For thin-film preparations a coverage of one to two monolayers is aimed. For thin-film preparations of Cu(111) with a coverage of one monolayer of sodium chloride the sample is held at temperatures between 260 K to 300 K during the sublimation process. By choosing the temperature, the size and distribution of the islands on the surface can be steered with a Cu(111) surface but care must be taken as for temperatures below about 175 K the islands crystallize in a random orientation [124]. Thick-film preparations of copper are carried out with sample temperatures between 370 and 390 K. To suppress diffusion of the salt over large areas of the gold surfaces, the temperature in those preparations is held at 280 to 300 K for thin films and to 300 K for thick films.

After these preparational procedures the sample is immediately transferred into to the scan head where it is cooled down to lHe temperatures. In the scan head the sample surface stays clean. If chemical compounds are dosed onto the cooled sample, they will adsorb onto the sample surface and remain there. At these low temperatures diffusion of single adsorbates on the surface is inhibited even on insulating layers, exhibiting much less interaction with adsorbates compared to metal surfaces.

The chemical substance under investigation is sublimed in submonolayer amounts through a pin-hole in the shutter onto the sample. By sublimation through the pin-hole the coadsorption of undesired material can be reduced resulting in a clean sample surface with few isolated adsorbates of the substance of interest. The sublimation of the chemical compounds is carried out with an oxidized Si-wafer which can be resistively heated up to about 770 K. Depending on the properties of the chemical substance, lower temperatures of the Si-wafer are required. Due to the high resistivity of the wafer, the heat-up proceeds comparably fast and the chemical substance is sublimed into the vacuum. Additionally, the geometry of the device is built in a way to prevent readsorption processes onto the Si-wafer and the substance has a small overall residence time on the wafer at elevated temperatures. The small overall residence time of the compound and the passivated surface of the Si-wafer help to sublime the substance of interest without degrading or altering its structure. If the substance possesses a high degree of impurity (compounds with a purity level $< 90\%$) a dual evaporator can be used. The substance is positioned in a heatable crucible. In the crucible the substance can be degased by slowly raising the temperature. In a second step the substance can be sublimed onto a Si-wafer, from where it can be sublimed onto the sample. As opposed to the Si-wafer geometry, the geometry of a crucible favours readsorption processes of the chemical substance in the sublimation process and hence leads to an increased overall residence time on the surface of the crucible which may cause increased degradation.

For high resolution nc-AFM imaging CO-functionalized tips are required. Therefore, CO molecules need to be coadsorbed at the sample surface. CO-gas can be dosed directly into the load-lock. To estimate the right amount of adsorbed CO a product of pressure and time is detected. Usually a decent coverage of CO (approx. one molecule per 100 Å^2 surface area) is obtained for a product of $3.5 \cdot 10^{-7}$ mbar $\cdot$ 3 s measured in the preparation chamber.

2.3 Modes of data acquisation

In the combined LT-UHV STM/AFM apparatus simultaneous measurements of STM and FM-AFM are possible. The bias or gate voltage is applied to the sample with respect to the tip. The different modes of operation are described in the following.

In general, the relevant quantities in STM/S are the topographic signal, the tunneling current and its derivative, $\mathrm{d}I/\mathrm{d}V$.

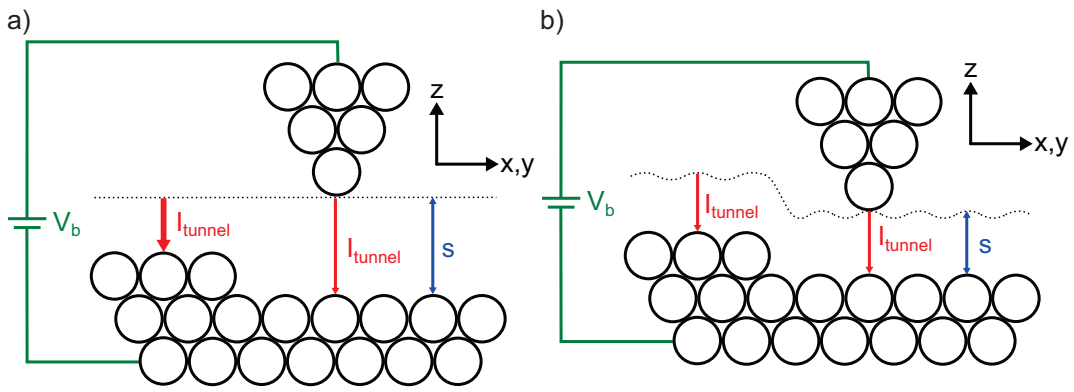

Fig. 2.2. Schematic depicting the working method in constant-height and constant-current mode of the STM. **a)** Constant-height mode: the tip scans with a predefined constant height over the surface and variation of the tunneling current can be detected. **b)** Constant-current mode: By keeping the tunneling current constant and detecting the variations in z the topography of a predefined area can be detected. Large surface areas can be detected with one image in this mode. The combined LT-UHV STM/AFM-apparatus can simultaneously detect STM and AFM data. AFM data can be acquired in similar modes. The constant-Δf mode or the constant-height mode. In the aforementioned mode a feedback loop ensures the maintenance of a constant Δf value, while the variation in z is recorded. In the latter mentioned mode the z-position of the tip is held constant, while recording the variation of Δf. In both modes the voltage is often set to zero. The Image was kindly provided by Dr. Tobias Preis [175].

Topographic images can be taken in a constant-current mode, see figure 2.2**b**. This means that the position of the tip in the z-axis is adjusted with a feedback-loop, so that the tunneling current remains constant. The variation of z provides the topographic information. For a corrugated surface the tip has to be approached (retracted) at a position where the surface is lower (higher) than the height at the former position of the tip, compare figure 2.2**b**. In this mode it is possible to scan large areas of the surface. The information encoded in the tunneling current is a convolution of distance dependence, DOS of the tip and LDOS of the sample, so that the z-maps can often not be interpreted as purely topographic, compare section 1.1.1.

In constant-height mode, see figure 2.2**a**, the tip is held at a constant position in the z-axis, while scanning over the surface. The current can be detected to obtain information about electronic states of the surface, e.g. information about orbitals of single molecules adsorbed on the surface [122].
In constant-height Δf-images submolecular resolution can be achieved and the geometrical structure of single molecules adsorbed on the surface can be detected [2]. The highly resolved Δf-images are often taken with CO-functionalized tips, which are obtained in a standardized procedure [176]. Most commonly the Δf-channel is recorded at zero bias. Thereby, negative effects of the applied voltage on the system with finite resistivity [141] and undesired effects on the adsorbate on conducting surfaces (and on thin insulating layers) due to inelastic excitations [177] can be prevented. Only if the applied voltage differs from zero during the recording of a constant-height Δf-image it will be mentioned hereafter.
In the constant-height modes only small areas of the surface can be scanned at once and there is a risk to crash the tip because of local variations of the height. The chosen height is usually not detected as absolute distance between tip apex and sample surface, s, but as a relative value with respect to the set-point of tunneling current and applied voltage shortly before the z-feedback is switched off, Δz. The value is positive if the tip is approached with respect to the set-point and negative if the tip is retracted with respect to the set-point.

On insulators no tunneling current can be recorded and another mode of operation to scan large surface areas is required. For this the constant-Δf mode can be applied. Here, the z-position of the tip is adjusted in a feedback-loop, such that the Δf signal is constant, while scanning over the surface. This technique may not only be of advantage on insulators, but also if an applied bias voltage on conducting surfaces (or thin insulating layers) inelastically excites adsorbates in the scan area, which then become unstable during the imaging process [177]. In constant-Δf mode with zero voltage these inelastic excitations can be prevented.

Various spectroscopic measurements can be carried out with the combined STM/AFM-apparatus. In the framework of this thesis I-V_b-, $\mathrm{d}I/\mathrm{d}V$-V-, Δf-z- and Δf-V-curves are recorded. Multiple curves can be detected along a line or along a dense grid [178, 179].

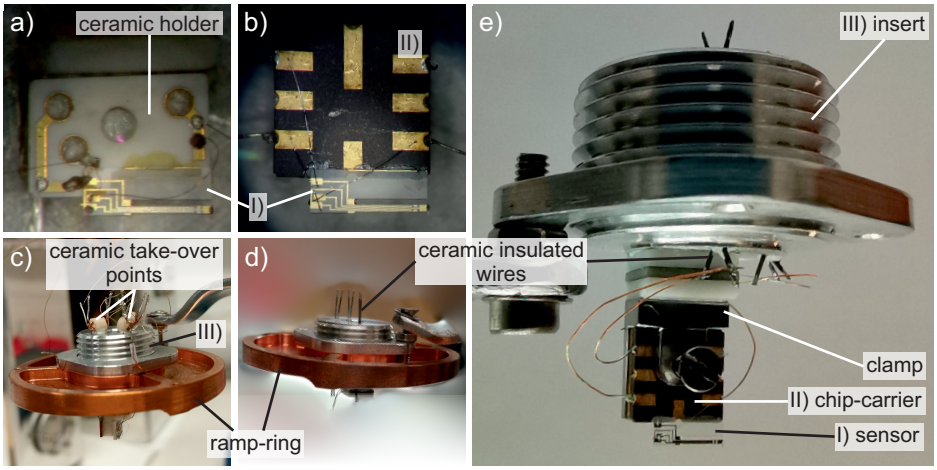

Fig. 2.3. Images of different sensor mounting designs. **a)** qPlus sensor glued to a ceramic holder: Wires connecting the sensor with the holder are glued **b)** qPlus sensor glued to a chip-carrier: Wires connecting the sensor with the chip-carrier are bonded. **c)** Sensor mount on the ramp-ring with ceramic take-over points and teflon wires **d)** Sensor mount on the ramp-ring with ceramic insulated wires as feed-through at the insert **e)** Chip-carrier design mounted onto the insert with a clamp. The stack on the insert consists of a ceramic plate, the excitation piezo, an additional ceramic plate and a clamp out of stainless steel. The wiring from the chip-carrier to the ceramic insulated feed-through are connected by soldering.

On insulators the AC-STM method (section 1.2.5), can be applied. Detailed information on this method is already given in the sections 1.2.4 and 1.2.5. Damping versus bias voltage curves, with applied AC-STM voltage pulses, are recorded to find a suited gate voltage offset. To obtain information about the electronic structure of the adsorbate, the damping channel is recorded while scanning over a surface area with alternating voltage pulses. The important parameters, which need to be chosen for this type of experiment are the tip sample distance, Δz, the d.c. voltage offset, V_{dc}, and the width as well as the height, V_{ac}, of the alternating voltage pulses.

2.4 Sensor

The sensor is a qPlus sensor [85, 90–92]. It is made out of a specially cut quartz tuning fork. The sensor has a stiffness, k, of around $1800\,\mathrm{N}\cdot\mathrm{m}^{-1}$ to ensure stable oscillations at small amplitudes, at which the lateral resolution of FM-AFM images is typically high, compare section 1.2. The sensor is glued onto a ceramic holder and a precut PtIr-tip is attached to the cantilever, compare figure 2.3**a**. This ceramic holder is then mounted onto an insert, which can in turn be screwed into the ramp-ring, see panel 2.3**d,e**. The ramp-ring is positioned onto sapphire spheres, which are mounted on top of piezo-stacks which can move the ramp-ring in x,y and z-direction [168, 169]. The insert can be adjusted to

the right height with respect to the ramp-ring and afterwards secured with a lock nut. The material of the insert is conductive (aluminium). Hence, care must be taken to not built a conducting connection between the insert and the wires, which should run from the sensor over the ceramic holder through holes in the insert to the respective connections in the STM/AFM scan-head. Also take-over points need to be implemented after the run of the cables through the insert holes.
As a first try, ceramic takeover points were built on the site of the insert opposite to the sensor, see figure 2.3**c**. To avoid conducting contact with the insert, thin teflon insulated wires were taken, which are compatible with the LT-UHV conditions of the apparatus. The take-over points turned out to be unhandy and would break off from the insert easily. Handling insulated wires on the sensor site of the insert also turned out to be unhandy and not straightforward to replace if needed.
A new solution included ceramic insulated wires as take-over points. These were stripped at the ends and then glued into the holes of the insert, see figure 2.3**d**. Thus a mechanically stable and LT-UHV compatible solution is found. Additionally, the take over points on the sensor far side are automatically created and the wires from the sensor to the ceramic wire feed-through can be non-insulated.
An additional problem was the long preparation times for the built-up of a new sensor mount. To improve this, the sensor was glued onto a chip-carrier and the formerly glued wires from the sensor to the sensor mount could be bonded in a bonding machine, compare panel 2.3**b**. These steps decreased the preparation time drastically. The connection from the sensor mount to the ceramic feed-through, formerly glued as well, can be soldered in this design. A stainless steel clamp with a screw was implemented to mount the chip-carrier onto the insert. The stack on the insert consists of a ceramic plate, the excitation piezo, an additional ceramic plate and the clamp, see figure 2.3**e**. In ambient conditions the resonance peak appeared of comparable quality as in the old design, but at LT-UHV conditions the quality factor was drastically reduced compared to the old design. By exchanging the clamp design back to a glued design excellent quality factors can be obtained under LT-UHV conditions, while still saving a lot of preparation time, due to the bonding and soldering of the wires at the sensor side of the insert.

2.5 Dual evaporator

To have a clean preparation with single molecules in submonolayer amounts on a respective sample surface, purities of chemical compounds higher than 98 % are needed. Often the chemical substances have lower purity, which is why a dual evaporator was built. It consists of an crucible evaporator (I) and an oxidized Si-wafer (II), see figure 2.4**a,b**. Both can be resistively heated independent from each other. The crucible evaporator has a thermocouple close to its heating filament to detect the temperature. The amount of sublimed substance can be detected with a quartz crystal microbalance.
The crucible can be filled with the chemical substance of interest under ambient conditions. It is important that the chemical compound is rather stable with respect to high temper-

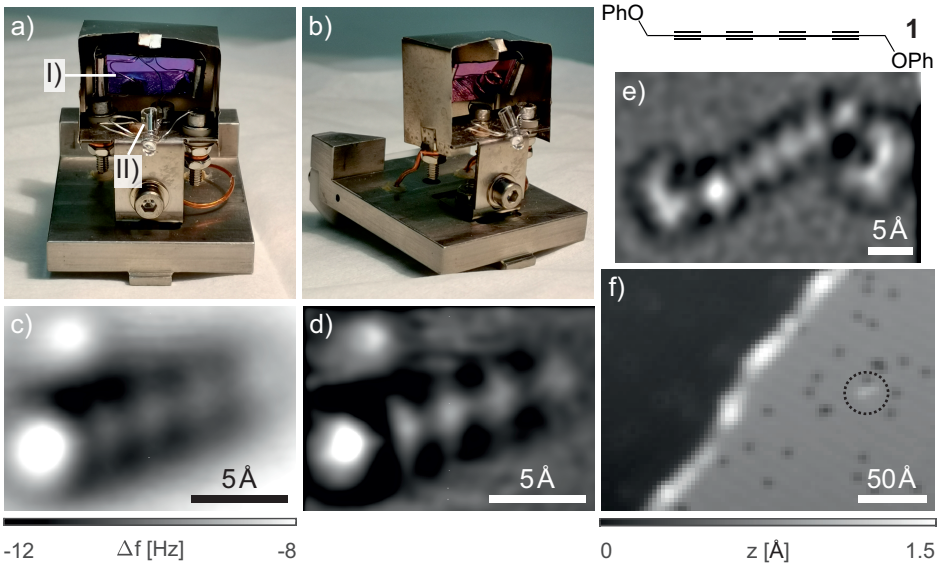

Fig. 2.4. Images of the dual evaporator, a combination of crucible (I) and an oxidized Si-wafer (II) evaporator and 7of the results of the sublimation. The chemical substance is filled into the crucible. In the UHV preparation chamber the crucible is resistively warmed up and held at a certain temperature to degas the chemical compound. This process may destroy the chemical substance, which is why only thermally stable compounds may be chosen. After the purification step, the crucible is heated up even more and the substance is sublimed onto the Si-wafer. Note that the crucible is oriented in a way so that the clean substance can adsorb directly on the Si-Wafer. In the next step the evaporator is brought into position and the substance is sublimed onto the sample. **a)** Front view of the dual evaporator **b)** Side view of the evaporator. **c)** Constant-height Δf-image of a fragment of the molecule **1**, after deposition of the substance with the dual evaporator ($\Delta z = 0.8\,\text{Å}$ at an STM set-point of $I = 0.5\,\text{pA}$ and $V_\text{b} = 1.0\,\text{V}$). **d)** Laplace filtered version of c), features assigned to the triple bonds could be resolved. **e)** Laplace filtered constant-height Δf-image of intact molecule **1**, after deposition with a resistively heated oxidized Si-wafer ($\Delta z = 0.6\,\text{Å}$ at an STM set-point of $I = 0.35\,\text{pA}$ and $V_\text{b} = 1.0\,\text{V}$). **f)** Constant-current topographic image of the surface after deposition of species **1** with the dual evaporator. The surface is clean, only CO molecules (black dots) and one molecule (in the dashed circle) can be found in this area ($I = 0.65\,\text{pA}$ and $V\text{b} = 1.5\,\text{V}$). Images c), d) and e) are taken with a CO-tip, image f) is taken with a Cu terminated tip.

atures and does not have the tendency to thermally decompose or react with impurities. Inside the UHV preparation chamber the crucible can be degased by warming it up. The temperature needs to be raised slightly below the sublimation temperature.
After the degasing process is completed the Si-Wafer needs to be flashed at elevated temperatures of about 820 K to clean it. Afterwards, the substance can be sublimed from the crucible onto the Si-wafer. The crucible is oriented in a way that the substance is directly shot onto the Si-Wafer, see figure 2.4**b**.
In a last step, the evaporator is positioned in front of the shutter of the scan head containing a sample and the chemical substance is sublimed from the Si-wafer onto the sample surface.
First results of dosing species **1** onto the sample with the dual evaporator look promising. The sample surface is very clean, which can be seen in the topographic overview in panel 2.4**f**. The amount of dosed species is below a monolayer coverage of the surface, as desired. A single molecule on a salt layer is marked with a dashed circle in the overview of panel 2.4**f**. High resolution imaging of the species with a CO functionalized tip is shown in panel 2.4**c** and its Laplace filtered version is shown in panel 2.4**d**. Clearly the structure can be related with the structure of the intact precursor dosed with a common oxidized Si-wafer, which is displayed in panel 2.4**e**. By comparing the two images of figure 2.4**d,e**, it can be deduced that the molecule displayed in panel 2.4**d** is a fragment of the precursor **1**, see also section 4.2. The fragmentation may be attributed to thermolysis during the degasing and sublimation process. However, since the substance was stored for quite a time before using and the attempt of dosing the substance directly after this deposition with a simple oxidized Si-wafer failed, it is also conceivable that the substance degradated during the storage time.
Nevertheless, the results reveal that a clean sublimation of a chemical substance can be realized with this dual evaporator design if the respective substance is stable against thermolysis.

Chapter 3

Investigation of stable organic radicals on a gold surface

The work presented in this chapter has been published in Angewandte Chemie.[1] *Parts of the text are identical to the publication. The calculations presented in this chapter were carried out by Dr. Laerte L. Patera in the course of the cooperation which resulted in this paper. The two investigated Blatter radical derivatives were synthesized and kindly provided by Dr. Jonathan Z. Low in the group of Prof. Dr. Luis Campos from the Columbia University. A related publication originated from a fruitful cooperation.*[2]

The Blatter radical was first presented by Blatter and Lukaszewski [180]. It is a stable organic radical with the radical baring moiety being a benzotriazinyl unit.
In this Chapter the results of the investigation of two Blatter radical derivatives, namely 1-phenyl-3-[4-(thiomethyl)phenyl]-7-thiomethyl-1,4-dihydro-1,2,4-benzotriazin-4-yl (**2**) and 1,3-diphenyl-7-thiomethyl-1,4-dihydro-1,2,4-benzotriazin-4-yl (**3**), are presented. In the experiments the species are adsorbed on a Au(111) single crystal surface and combined STM/S and highly resolved nc-AFM measurements at LT-UHV conditions are carried out. Beforehand, the topic is embedded in the literature explaining the important mechanism behind the measurements, the Kondo effect, and elucidating essential stabilizing mechanisms of purely organic radicals.

3.1 The Kondo effect in STM

The Kondo effect is a complicated many-particle phenomenon, which arises when a magnetic impurity interacts with the conduction electrons of a solid state object. The inter-

[1] L. L. Patera, S. Sokolov, J. Z. Low, L. M. Campos, L. Venkataraman, J. Repp. 'Resolving the Unpaired-Electron Orbital Distribution in a Stable Organic Radical by Kondo Resonance Mapping'. In: *Angew. Chem. Int. Ed.* 58 (2019), 11063-11067.

[2] J. Z. Low, G. Kladnik, L. L. Patera, S. Sokolov, G. Lovat, E. Kumarasamy, J. Repp, L. M. Campos, D. Cvetko, A. Morgante, L. Venkataraman. 'The Environment-Dependent Behaviour of the Blatter Radical at the Metal-Molecule Interface'. In: *Nano Lett.* 19 (2019), 2543-2548.

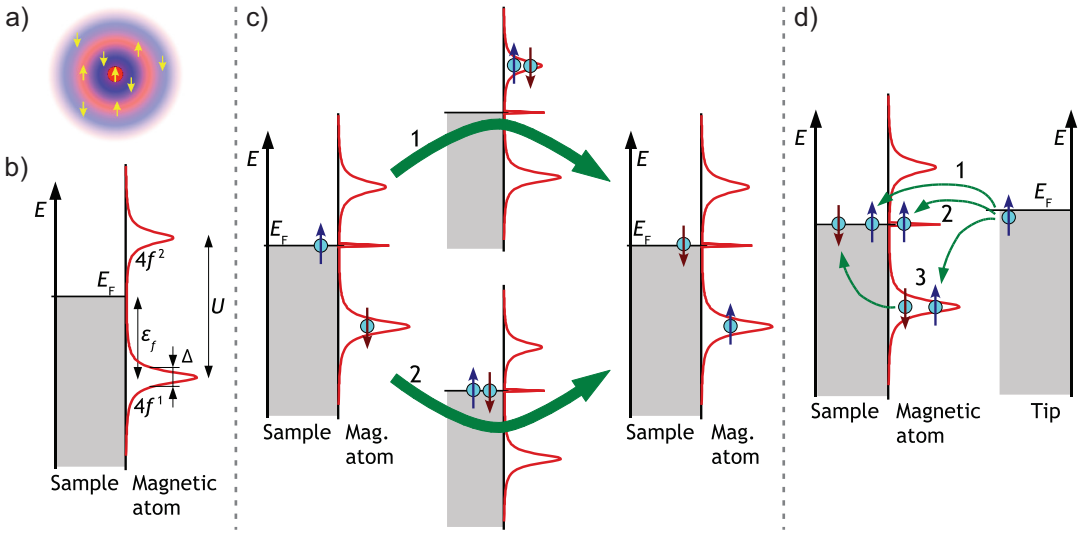

Fig. 3.1. Schematics explaining the Kondo effect in STS experiments. **a)** Kondo screening cloud: The magnetic moment of the impurity is screened by the spin of the bulk electrons. **b)** Singly occupied atomic orbital (AO) of Ce ($4f^1$) electronically coupled to the metal leading to a broadening, Δ. The singly occupied AO is by $|U|$ lower in energy than the doubly occupied AO ($4f^2$), with U being the Coulomb repulsion energy. The $4f^1$ and the $4f^2$ AO's are distributed around the Fermi energy with the $4f^1$ AO being lower in energy than the Fermi level, rendering the single occupation of the 4f state possible. In this scheme no Kondo effect is considered yet. **c)** Emergence of the Kondo resonance at the Fermi level through spin-flip exchange interaction of the localized state with the continuum of the band states. **d)** Three different tunneling pathways in STS experiments in a bias voltage window close to the Fermi level of the sample: 1) tunneling into unoccupied states of the metal, 2) tunneling into the Kondo state and 3) tunneling into the orbital of the adsorbate and subsequent tunneling to a state in the metal close to the Fermi level. Schematic is taken from [181].

Fig. 3.2. Schematic of the Fano function with different values for the form factor q. For large q-values the peak shape approaches a fully symmetric Lorentzian peak (predominantly tunneling into the Kondo resonance), for $q = 0$ the peak represents a Lorentzian dip (predominantly tunneling into metal states at the Fermi energy) and for $q = 1$ the peak has an asymmetric shape (contributions from both tunneling pathways). Figure taken from [182].

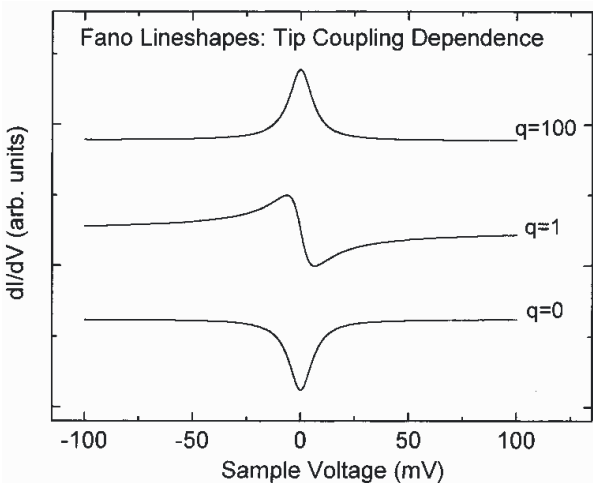

action manifests itself as a discrete energy level pinned to the Fermi level of the metallic solvent. Early on, unexpected behaviour of the resistance was found in an experiment, where a metal was successively cooled down. After passing a minimum in resistance, the resistance of the substance under investigation increased with decreasing temperature [183, 184]. This phenomenon only occurred if magnetic impurities were dissolved in the metal.
Anderson [185] applied a simple self-consistent Hartree-Fock treatment to investigate the interaction between a bulk metal and a single magnetic impurity state. The theory should not be regarded as a quantitative approach to predict properties of a certain system, but important qualitative information was discovered. The competition of the Coulomb interaction and the matrix elements determining the interaction of the local state with the band sates of the metal was accentuated by Anderson [185] as a first step towards the discovery of the Kondo effect.
In contrast to Anderson's method [185], the perturbative ansatz of Kondo [186] naturally fits the many-particle problem, where the electron-electron interaction has an important stabilizing role.
Kondo [186, 187] explained the mechanism based on an s-d interaction model for dilute magnetic alloys [186]. The involvement of the Fermi sphere in the scattering process gives rise to a term in the resistivity which depends logarithmically on the temperature with the concentration of the magnetic impurity, c, as a prefactor, $c \log T$ [186]. This result could reproduce the experimental results for negative values of the s-d exchange integral, J [186], and for temperatures above the so-called Kondo temperature, T_K [188].
The Kondo effect can also be described in terms of Fermi liquid theory for low temperatures provided the fluctuations occur rapidly enough so that only electron renormalization and interaction needs to be considered [189]. At low temperatures ($< T_\mathrm{K}$) the temperature dependence of the resistivity changes its behaviour ($\propto 1 - c(\frac{T}{T_\mathrm{K}})^2$) [181].
In general the effect of negative exchange integral J is a result of a large mixing of the wave functions of the conduction electrons of the metal solvent with the d-electrons of the magnetic solute [185, 186]. The balance between kinetic and potential stabilization effects is decisive on the type of interaction observed in a system.
The antiparallel spin alignment ($J < 0$) is crucial for the dynamic interaction in the localized spin system. The spins of the conduction electrons of the host metal interact with the localized spin of the impurity. An antiparallel alignment of the spin of the impurity and the surrounding spins of the conducting electrons called Kondo screening cloud, as depicted in figure 3.1**a**, screens the spin of the impurity and leads to a stabilizing term in the kinetic energy. This type of interaction is of dynamic nature in form of exchange processes accompanied by a spin-flip in the localized orbital of the magnetic impurity.
To understand this exchange processes in more detail a single cerium (Ce) atom adsorbed on a metal surface is considered and it is only focussed on the interaction of the 4f atomic orbital (AO). Figure 3.1**b** depicts the hybridization process of the singly and doubly occupied Ce 4f AO [181]. In the example depicted in figure 3.1**b** the $4f^1$ and $4f^2$ hybridized AOs of a Ce adatom are distributed around the Fermi level separated by the Coulomb charging energy U and broadened by Δ. Only the $4f^1$ hybridized AO lies below the Fermi

level resulting in a single occupation of this AO on the respective surface. The peaks of the hybridized singly and doubly occupied 4f AOs, depicted in figure 3.1**b**, are often referred to as Coulomb-blockade peaks and can be detected in STS measurements [46, 190].
The single occupation of an AO or a molecular orbital (MO) might result in a Kondo-type of interaction with the charge carriers of the host metal, depicted exemplarily for the Ce adatom in figure 3.1**c** [181]. Two distinct exchange processes can contribute to the dynamic many-body Kondo interaction. An electron of a continuum state close to the Fermi level can tunnel into the 4f state resulting in a double occupation and subsequently an electron of the $4f^2$ state tunnels back into an unoccupied continuum metal state close to the Fermi level. Here, the importance of the antiparallel spin alignment of the electron from the continuum state and the electron populating the $4f^1$ state reveals itself. The process is depicted in figure 3.1**c** pathway 1. In the transition process of an electron in a continuum state in the Fermi sea to the 4f state, the electrons close to the Fermi level in energy have a lower transition barrier resulting in a higher transition probability. The second exchange process participating in the Kondo interaction is emptying the $4f^1$ state by tunneling into an unoccupied metal state close to the Fermi level and subsequent back-tunneling of an electron of the metal close to the Fermi level back into the $4f^1$ state, depicted in figure 3.1**c** pathway 2. Note that the two important transition processes contributing to the Kondo interaction, depicted in figure 3.1**c**, both include a spin flip.
A narrow Kondo resonance emerges at the Fermi level, when considering many of such exchange processes involving electronic levels of the metal close to the Fermi level, see figure 3.1**c**. This many-body phenomenon has a screening effect on the localized spin and results in an overall non-magnetic Kondo singlet state with the spin impurity being paired with many electrons of the metal continuum states [181], compare with figure 3.1**a**. The full width at half maximum (FWHM) of the Kondo peak, $2\Gamma_\mathrm{K}$, bares important information of the properties of the system and can be related to the Kondo temperature, T_K, which is a function of the Coulomb charging energy U, the energy of the singly occupied orbital of the adsorbate, ϵ_f in figure 3.1**b**, and the broadening of the atomic orbitals upon adsorption on the metal, Δ in figure 3.1**b** [181]. For T= 0 K the Kondo temperature can be written as [181],

$$T_\mathrm{K} = \frac{\Gamma_\mathrm{K}}{k_\mathrm{B}}. \tag{3.1}$$

The advances in the field of nanotechnology led to an increased interest in the Kondo effect [188]. The first experiments of the Kondo effect carried out by means of STS were demonstrated by Li et al. [45] and Madhavan and colleagues [44]. A dip-like feature was observed in the $\mathrm{d}I\,/\,\mathrm{d}V$-spectra in vicinity to the Fermi energy of the metal substrate if the spectra were taken on top of a single magnetic adatom.
The temperature dependence of the peak shape is generally a good way to determine the main mechanism responsible for the broadening of the peak. Nagaoka et al. [191] found agreement of the temperature dependent broadening of the Kondo peak in a STS experiment of a single Ti adatom on a Ag(100) surface with theoretical results of the temperature

dependence developed in the framework of Fermi liquid theory with the Anderson impurity model [185]. Through the agreement of experimental and theoretical results the main scattering mechanism can be attributed to electron-electron scattering. The broadening of the Kondo resonance at finite temperatures can be related to the Kondo temperature [191] by,

$$\Gamma_{\mathrm{K}}(T) = \sqrt{(\pi k_{\mathrm{B}} T)^2 + 2(k_{\mathrm{B}} T_{\mathrm{K}})^2}. \tag{3.2}$$

In this equation k_{B} is the Boltzmann constant and T is the temperature during the experiment. The Kondo temperature, T_{K}, is the only free fitting parameter of equation 3.2. Since the equation is derived from the Anderson impurity model based on the Fermi liquid theory it is important to chose a suited temperature range, where the theory can be compared to experiment. The temperature of the experiment should in general not be much higher than the Kondo temperature of the system [189]. For temperatures above the Kondo temperature the dependence of the resistivity was determined to be logarithmically with temperature [186], as aforementioned.
To understand differential conductance measurements of the Kondo signature in more detail, the different tunneling pathways of an electron tunneling from the tip into the system under investigation should be considered at an applied bias voltage close to zero, see figure 3.1**d** [181]. The electron can tunnel into unoccupied states of the metal close to the Fermi level, pathway 1 in figure 3.1**d**. Another pathway is the tunneling of the electron from the tip into the Kondo state, pathway 2 in figure 3.1**d**. A third tunneling channel in the considered system would be a co-tunneling process, pathway 3 in figure 3.1**d**. Concurrently, an electron tunnels form the tip into the singly occupied $4f^1$ orbital and the electron from the occupied $4f^1$ orbital tunnels into a continuos metal state close to the Fermi level. This co-tunneling process is accompanied by a spin-flip event. Note that the final state of this process has an altered spin state compared to the final states of the two other processes.
Fano [192] defined a way to describe the interference of a discrete autoionized state with a continuum of states, giving rise to a characteristic asymmetric peak. The theory can be applied to describe the Kondo signature in STS experiments [44, 45, 191, 193]. Frota [194] developed another formula to determine the shape of the Kondo resonance based on the Fermi liquid theory.
The fit equation describing the Fano line shape, applicable for STS measurements, is given by [57, 192],

$$\begin{aligned} \frac{\mathrm{d}I}{\mathrm{d}V} &= A + B \cdot \frac{(q+\epsilon')^2}{1+\epsilon'^2} \\ \text{with } \epsilon' &= \frac{(eV_{\mathrm{b}} - E_{\mathrm{K}})}{\Gamma_{\mathrm{K}}}. \end{aligned} \tag{3.3}$$

Here, A and B denote fit parameter of the background and the peak amplitude and ϵ' is a normalized energy with E_K being the position in energy of the Kondo resonance with respect to the Fermi energy. The important parameter to understand more about the different contributions of the tunneling processes to the interference peak of the Kondo signature in a differential tunneling conductance spectrum is q, the so-called form parameter.

A contribution to the quantum interference term can only stem from the two tunneling channels ending up in the same quantum state, which are the tunneling pathways 1 and 2 depicted in figure 3.1**d**. The third tunneling pathway (3 in figure 3.1**d**) does not contribute to the interference peak.

The value of the form factor is decisive for the shape of the peak, as displayed in figure 3.2. It carries information on the amount of contribution of the different tunneling channels (1 and 2 in figure 3.1**d**) to the overall peak shape. The form factor, q, is a function of the tunneling matrix elements of the transition to the discrete Kondo state and the transition to a continuum conduction-band state at the Fermi energy [182, 192]. For high q values (for example: figure 3.2, $q = 100$) the peak shape approaches a symmetric Lorentzian peak with, in a simple picture, the dominant tunneling pathway being tunneling into the Kondo resonance [181]. For $q = 1$, shown in figure 3.2, the peak shape is asymmetric and both tunneling channels contribute (1 and 2 in figure 3.1**d**). For $q = 0$ the peak has the form of a Lorentzian dip often indicating tunneling into metal states at the Fermi energy being the dominant contributing tunneling channel [181].

A Lorentzian dip-like feature was found in the differential conductance spectrum of Li et al. [45] (Ce adatoms on Ag(111)) and of Madhavan et al. [44] (Co adsorbates on Au(111)) on top of the adsorbates. The q value of the fit of close to zero was thought to indicate that the dominating tunneling channel in the measurements was tunneling into metal states at the Fermi energy. Madhavan et al. [44] determined the change of the peak shape with laterally moving the tip away from the center of the adatom towards the bare metal surface. The peak changes from a symmetric dip to an asymmetric shape until it vanishes. This highlights the lateral confinement of the Kondo state and the variation of the peak shape might be rationalized by assuming a constant tunneling rate for the tunneling to the continuum metal states and a laterally varying tunneling rate for the tunneling process into the Kondo state [44].

However, closer investigation of Madhavan et al. [182] strongly suggest the tunneling pathway into the Kondo state to be determining, despite the dip-like feature usually being assigned to a dominating tunneling into the metal states. Spectroscopic measurements at different tip heights were carried out and it was found that the Kondo peak remained almost unchanged over a large range of different heights, an unexpected behaviour for tunneling processes into the metal states [182]. In the experiment of Manoharan et al. [195] a single Co atom was positioned at the focal point of an ellipse built of other Co atoms. Since at the second focal point of the ellipse, where no Co atom was positioned, a second Kondo peak could be detected with a reduced intensity, this experiment might hint towards tunneling into the Kondo state playing an important role. Concluding one might

say that developing a qualitative understanding of the contribution of the different tunneling channels to the overall Kondo interference peak is not straightforward. It should also be pointed out that the LDOS of the metal surface might vary and hence the contribution of direct tunneling into continuum states of the metal sample might also change. There are several publications investigating the environment and the effect of the LDOS on the fit parameters q and T_K [182, 196, 197].
The Kondo temperature of a certain system, with respect to other reference values, can reveal information about the strength of the interaction of the magnetic impurity with its surrounding [198, 199]. In general, measurements of the Kondo temperature of magnetic impurities embedded in the bulk metal strongly deviate from measurements determined of adsorbates on a conducting surface [44, 182]. The reason for this is that impurities in the bulk have more neighbouring atoms and the interactions with those sum up to a larger overall interaction than for adsorbates on a surface.
Due to experimental limitations with regard to the STS method it is not straightforward to determine the Kondo temperature with a high accuracy [193]. Different modulation voltages, varying temperature of the tip or different bias voltage windows selected for the fit can lead to pronounced variations of the fit result for the Kondo temperature [193]. While the first issue can be fixed by executing the measurements at low modulation voltages, the exact tip temperature cannot be detected easily in most STS setups.
Nevertheless, the Kondo signature is a good and versatile tool to investigate spin systems on surfaces with the advantage of submolecular resolution. A very engaging field of research deals with magnetism in graphene nanoribbons (GNRs). Interesting behaviour was found for atomically precise armchair edge GNRs (AGNRs) adsorbed on a Au(111) surface with a porphyrin-based magnetic molecule, TBrPP-Co, coadsorbed on the surface [200]. The TBrPP-Co molecule exhibited similar Kondo signature directly adsorbed on the metal surface and adsorbed on top of an AGNR, even though the AGNR lead to a separation of the metal organic molecule and the metal surface of about 7.5 Å.
In another publication of Li et al. [42] a Kondo resonance peak could be found at the junction of fused chiral GNRs directly adsorbed on Au(111) without coadsorbing additional magnetic adsorbates.
There are many different physical concepts to introduce magnetism to purely organic systems. Among them are introducing a sublattice imbalance in a nanographene structure through geometric considerations or by introducing defect sites [14, 51, 170]. Another approach is to introduce topological frustration [170].

3.2 Stable organic radicals

Stable organic radicals are known to be synthesized for 150 years [203]. They regained a lot of interest for spintronic applications [204, 205]. Low energy dissipation in spin information processing and high conductivity at low voltages due to Fermi level pinning of the radical state [206–209] makes open-shell systems interesting for memory, transport and switching devices.

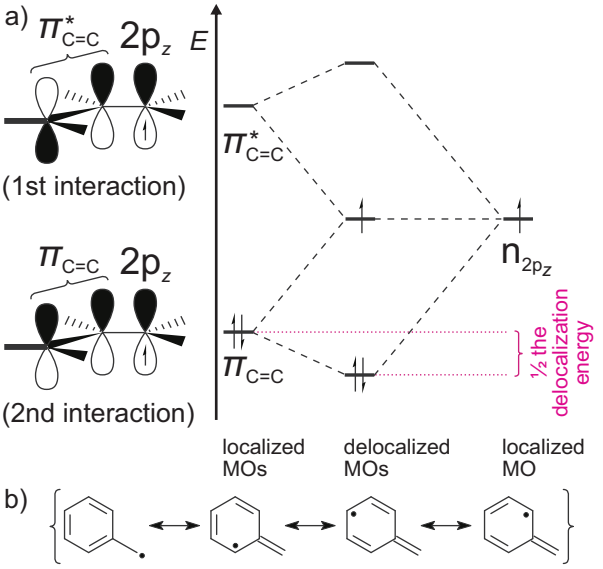

Fig. 3.3. Schematics explaining the conjugative stabilization of a radical center in an organic molecule. **a)** Conjugative stabilization with a π-system adjacent to the radical site. **b)** Conjugative effect explained in terms of the valence-bond (VB) model. Schematics are adapted from [201] with slight adjustments.

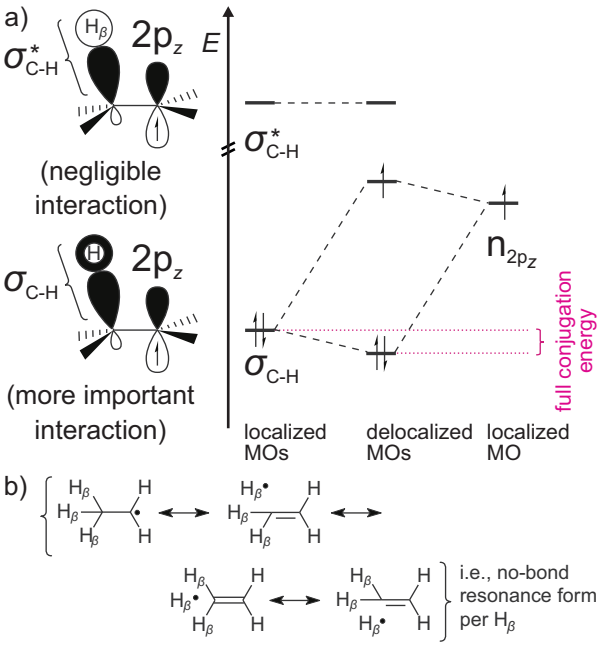

Fig. 3.4. Schematics explaining the hyperconjugative stabilization of a radical center in an organic molecule. **a)** Hyperconjugative interaction with an C-H bond in α-position to the radical center. **b)** Hyperconjugative effect illustrated in the VB-model with no-bond resonance forms. Schematics are adapted from [201] with slight adjustments.

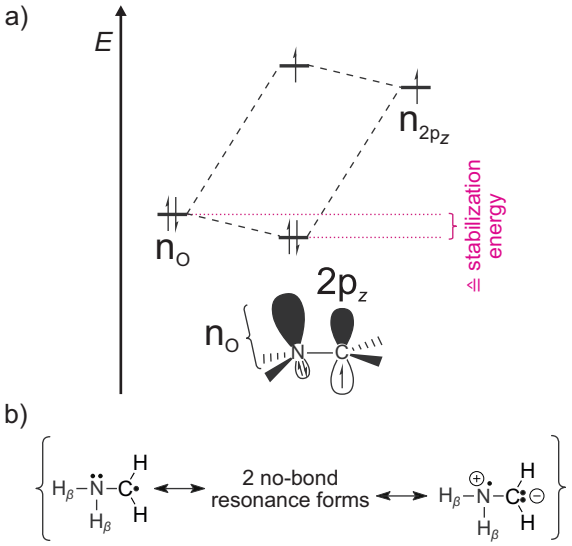

Fig. 3.5. Schematics explaining the stabilization of a radical center in an organic molecule by a heteroatom. Exemplarily an oxygen atom is employed as a heteroatom in this schematic. **a)** Stabilizing interaction with a vicinal heteroatomic free electron pair. **b)** Heteroatomic stabilization visualized in the VB-model with a zwitterionic resonance form. Schematics are adapted from [201] with slight adjustments.

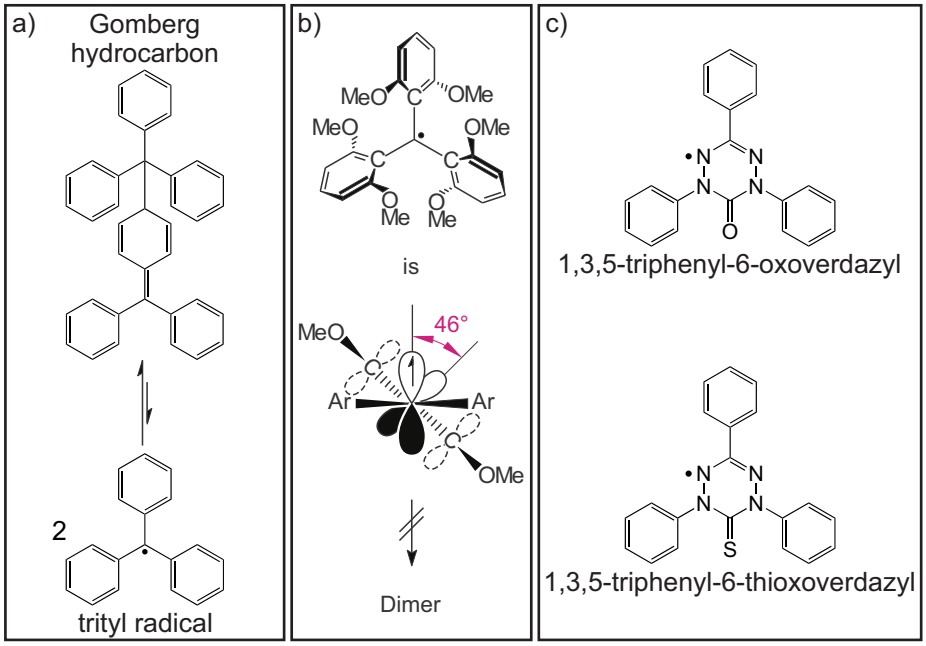

Fig. 3.6. **a)** Reversible formation reaction of a trityl radical out of a Gomberg hydrocarbon, adapted from [201] with slight adjustments. **b)** Trityl radical derivative with no tendency to dimerize due to steric hindrance, adapted from [201] with slight adjustments. **c)** Organic radicals employed in reference [202]

Two important types of relaxation need to be considered when investigating open-shell compounds. These are spin-lattice and spin-spin relaxations and the related relaxation times are the population relaxation time (T1) and the phase memory time (T2), respectively [210–212]. While a long T1 relaxation time is especially important for information storing, the T2 relaxation time for example needs to be considered for spin based information processing [210].
Stable organic radicals are a group of open-shell systems of high importance, because they lack efficient mechanisms for spin-relaxation [210–212]. Usually the main mechanisms of spin-relaxation include spin-orbit coupling and hyperfine interaction, both are weak in organic molecules possessing no heavy atoms and few atoms with net nuclear spin [204, 205]. Studies with organic molecules show applicability in transport [204, 205, 209, 213, 214] as well as switching and memory processes [205, 206, 208]. Even potential application for spin filters is revealed theoretically [215].
Metal organic compounds are often investigated from the view of spintronic applications [210–212], since in a lot of metal organic compounds the spin-relaxation is slow as well. The group of metal organic radicals comprises well characterized stable compounds and the spin can be easily introduced with a metal atom. There are even studies where the spin can be delocalized towards the organic ligands of a metal organic radical [216, 217].
However, substances which are stable at ambient conditions or elevated temperatures with even higher spin relaxation times need to be found. For purely organic radicals a large variety of stabilization mechanisms of the radical sites is already known, which is a good starting point for engineering compounds applicable to spintronic devices. The radical character of a chemical compound must survive even upon contacting with a metal electrode in spintronic applications.
To engineer stable or persistent radicals, it is important to understand the underlying stabilization mechanisms. Persistent means sufficiently long-lived but not isolable [218]. With the stabilization mechanisms for organic radicals interactions with surrounding compounds and the surface can be foreseen and the electronic structure can be anticipated.
The stabilizing mechanisms can be subdivided in conjugative and hyperconjugative effects, stabilization via substituents with free electron pairs and destabilizing of potentially formed bonds at the radical center such as the bond pairing the radicals to dimers.
If a π-conjugated system adjacent to a radical site in an organic molecule has a suited orientation the radical site can be stabilized. This stabilizing effect is termed conjugation and results from an interaction of a π-system with the n_{2p_z} AO of a carbon centred radical. This interaction type is depicted schematically in the MO-model in figure 3.3**a**. If the π-system is oriented in the right way with respect to the radical site a π-type of overlap can occur between the $\pi_{C=C}$ and the n_{2p_z} orbitals (2nd interaction in figure 3.3**a**) as well as between the $\pi^*_{C=C}$ and the n_{2p_z} orbitals (1st interaction in figure 3.3**a**), resulting in an overall lowering of the energy of the system. A conjugated system starting at the C_α position to the radical site, such as in allyl or benzyl radicals, have the right parallel orientation of the π and π^* MO with respect to the n_{2p_z} AO so that this type of interaction may occur. The amount of delocalization and hence the amount of stabilization to the system can be estimated by the number of possible resonance structures and their relative weighting.

Exemplarily, the different resonance structures describing the overall delocalization of the radical site of a benzyl radical are shown in figure 3.3**b**.
A similar stabilizing effect but smaller in magnitude is the hyperconjugation occurring for (poly)alkylated radicals. Here, a vicinal non-orthogonal $\sigma_{\text{C-H}}$ bond can overlap with the singly occupied n_{2p_z} orbital. The alignment of the two interacting orbitals is not parallel due to the sp^3-hybridization of the carbon in α-position to the radical site. This deviation from the parallel alignment leads to a reduced interaction and a reduced stabilization as compared to an adjacent conjugated system. The interaction of the $\sigma_{\text{C-H}}$ orbital is significant, whereas the interaction with the antibonding $\sigma^*_{\text{C-H}}$ orbital is negligible. The reason for the latter interaction being negligible is that the symmetry of the $\sigma^*_{\text{C-H}}$ orbital is not suited for a π-type of overlap with the n_{2p_z} orbital, compare figure 3.4**a**. The stabilizing effect due to delocalization of the MOs can again be expressed in terms of resonance structures. In this case the residues at the radical center are sp^3-hybridized and so-called no-bond resonance forms have to be employed, which add up to an overall smaller stabilizing effect compared to the common resonance structures (e.g. structures in figure 3.3**b**). An example visualizing the stabilizing effect of alkyl residues at the radical center in the VB-model is shown in figure 3.4**b** for the ethylene radical.
Heteroatoms in α-position to the radical site also have a stabilizing effect. The lone pairs of these heteroatoms can overlap with the singly occupied n_{2p_z} orbital of the radical center. The MO-scheme depicted in figure 3.5**a** has similarities to the one of the hyperconjugative effect, depicted in figure 3.4**a**. The two orbitals depicted in figure 3.5**a** are again not perfectly parallel aligned resulting in a reduced overlap. The amount of stabilizing energy strongly depends on the species of the heteroatom. The less electronegative the species, the more available is the lone pair in terms of delocalization towards the n_{2p_z} orbital. Nitrogen atoms are one of the common heteroatoms in organic molecules exhibiting comparable low electronegativity, making them great substituents to the α-position of C-centred radical species. In the VB-model the additional stabilization gain due to interaction with the lone pairs of an adjacent heteroatom can be expressed by zwitterionic resonance structures. The zwitterionic resonance structures are shown for the aminomethyl radical in figure 3.5**b**.

Another important aspect is the stability of a potentially formed bond at the radical center. If the bond is weak and only a little to no lowering in energy comes along with the bond formation, this process is energetically not favourable and the yield of the respective product is usually negligible. For engineering stable organic radicals this is often an important aspect.
One possibility of protecting the radical site and preventing bond formation at this position is introducing bulky side groups, which shield the radical carbon from other potential reaction partners. A well known example for this stabilizing effect based on steric hindrance is the trityl radical (triphenylmethyl radical) which builds out of the Gomberg hydrocarbon by homolysis, see figure 3.6**a**. In thermal equilibrium at ambient conditions the trityl radical is present in quantities of about 2 mol% [201]. The reason is a stabilizing effect of the radical due to a conjugative effect and more importantly due to steric hindrance. The phenyl groups are tilted resulting in a propeller-like geometry, see e.g. figure 3.6**b**, hinder-

ing other compounds to access the radical center and weakening the bond in the dimerized form. In this geometry the overlap of the orbitals participating in the conjugative effect is significantly reduced. Hence, for most trityl radical derivatives the driving force to built the organic radical is the steric hindrance not the conjugative effect.
Protection against dimerization at the radical site can also be achieved by employing heteroatom centred organic radicals. A reason for the higher stability of heteroatom centred radicals is that the dimer bond between the heteroatoms, e.g. a N-N or a O-O bond, is often much weaker compared to a C-C covalent bond due to the lone pair repulsion [203]. Additionally, heteroatom centred organic radicals are usually less reactive to molecular oxygen, due to their relative high electronegativity [203], which is a significant limitation for the stability of carbon centred radicals.
In conclusion, to understand the transient nature of most radicals it is important to consider their possible reaction pathways. The most common are dimerization, hydrogen abstraction and disproportionation [203]. Most importantly, in terms of radical stability the environment of the radical is crucial.
As already mentioned for potential spintronic applications it is important that the organic molecule retains its open-shell configuration upon contact with metal electrodes. A lot of different aspects can influence and alter the electronic configuration after adsorption or bond formation with the metal, which are not always straightforward, e.g. different adsorption geometries [219, 220] or different adsorption sites [197, 221]. The specific interaction at the interface between the organic and the inorganic compound is crucial [204]. This means a thorough investigation of the specific system is mandatory to decide if it is employable to spintronic applications. Numerous reports investigate the electronic configuration of organic radicals upon adsorption onto a specific surface [205, 222] and the radical character is often preserved upon adsorption onto relatively inert gold surfaces [222–224]. However, most experimental techniques to investigate these interfaces are averaging over a large ensemble of molecules and valuable information can be lost. In contrast, STM/S, AFM and STM break junction (STM-BJ) [225, 226] do not average over a large ensemble of molecules and single molecules in specific environments can be studied to form a detailed understanding of the site specific radical-metal interactions.
A preservation of the open-shell character in single molecule break junctions was found for electrostatic interactions of a perchlorinated trityl radical with the gold electrodes [227] and for covalent bond formation of a gold atom of the electrode with the perchlorinated trityl radical [228].
A lot of metal organic compounds have been investigated on different surfaces by means of STM/S [46, 198–200, 229–235]. In most cases these radicals retain their open-shell structure upon adsorption. In some cases the spin delocalizes into a π orbital of a ligand [230–232, 234]. STM/S investigation revealed that depending on the hybridization with the surface and the charge transfer between surface and adsorbed molecule, organic compounds can exhibit an open-shell configuration upon adsorption without having radical character in the gas phase [193, 219–221]. Even highly delocalized unpaired spin states can be found in (charge-transfer) assemblies on surfaces [158, 236, 237].
However, few STM/S studies of purely organic, stable radicals exist, where stable refers

to being able to isolate the chemical compound and demonstrating its stability in a variety of different environments. Some typical representatives of this group were investigated by means of STM/S and the persistence of the open-shell character could be confirmed [47, 202, 238, 239]. Others were investigated by STM but the radical character was confirmed by other methods [240, 241]. A detailed presentation of the important groups of stable organic radicals would go beyond the scope of this work. However a detailed and comprehensive description can be found by Hicks [203].
Liu et al. [202] were able to compare two similar stable organic radicals, one possessing an oxoverdazyl unit and the other one a thioxoverdazyl moiety, see figure 3.6**c**. While the oxoverdazyl radical derivative retained its radical nature on a gold surface, the thioxoverdazyl radical lost its open-shell configuration upon adsorption. Liu et al. [202] argued that the strong interaction of the sulphur atom with the gold surface most probably resulted into changes of the electronic structure of the thioxoverdazyl derivative and the loss of the radical character upon adsorption.
In conclusion, a lot of different influences upon adsorption of radical species on different surfaces may lead to an alteration of the electronic structure of the adsorbate. Hence, with regard to the open-shell structure of a radical in a specific system a thorough investigation of the whole system at best with highly spatially resolved methods is needed.

3.3 Investigation of two Blatter radical derivatives

In this section, the investigation of two Blatter radical derivatives by means of combined STM/S and nc-AFM measurements are presented. The class of stable benzotriazinyl radicals was named after their first synthesizers, Blatter and Lukaszewski [180]. The two herein presented Blatter radical derivatives are 1-phenyl-3-[4-(thiomethyl)phenyl]-7-thiomethyl-1,4-dihydro-1,2,4-benzotriazin-4-yl (**2**, figure 3.8) and 1,3-diphenyl-7-thiomethyl-1,4-dihydro-1,2,4-benzotriazin-4-yl (**3**, figure 3.11). The two highly pure compounds were synthesized by Dr. Jonathan Z. Low in the group of Prof. Dr. Luis Campos from the Columbia University with a description of the synthesis details in the publication of Low and colleagues [43].

Representatives of the Blatter radical family have been found to endure high temperatures with decomposition temperatures of 561 K, which were higher than their melting point of 433 K [242]. The C7 position of the benzotriazinyl unit (compare figure 3.8**a** and figure 3.11**a** for general labelling) exhibits low stability against oxidation. Protecting this carbon site leads to high oxidative stability [242]. Overall, the class of Blatter radicals comprises purely organic radicals displaying high stability against temperature and oxidation and derivatives that are stable in air and in water can be found [243].

The stability can be understood by exemplarily applying the formerly described general stabilization mechanisms to the here investigated species **2**. The Blatter radical **2** is an N-centred radical and the bond, which would form upon dimerization of two molecules of

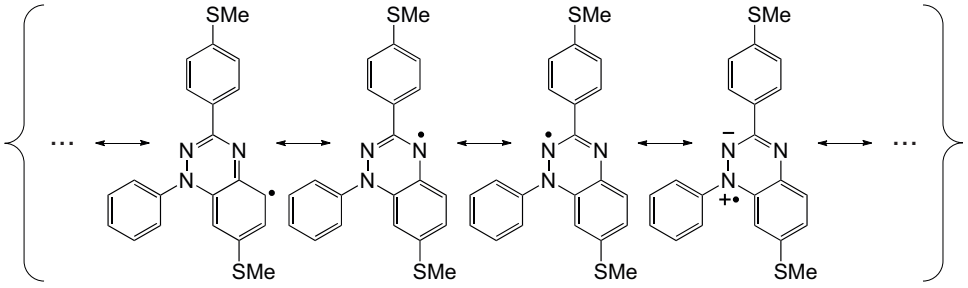

Fig. 3.7. Resonance structures of species **2**. Out of a large number of existent resonance structures, these four were picked to describe the delocalization process on the radical site in detail. The rightmost three resonance structures show the delocalization of the radical over all three nitrogen atoms in the cyclic system. The remaining leftmost resonance structure illustrates exemplarily the delocalization of the radical over the annulated ring. There are additional resonance structures showing the radical delocalization in the annulated ring which are not shown here.

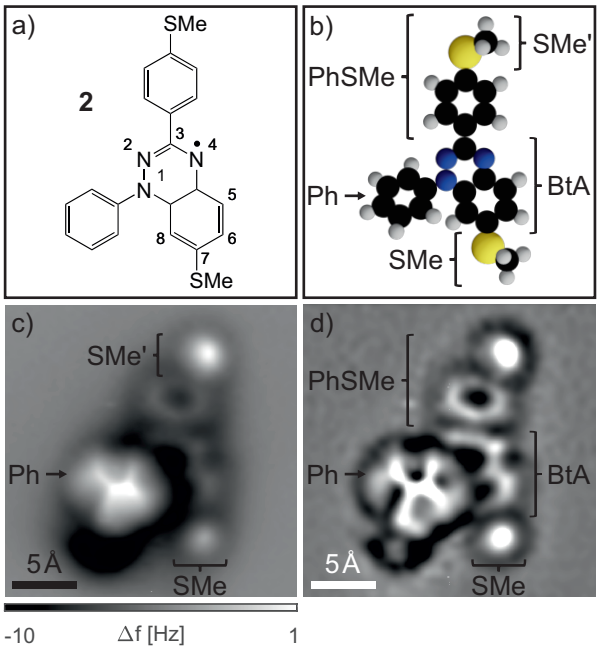

Fig. 3.8. **a)** Structure of the Blatter radical derivative 1-phenyl-3-[4-(thiomethyl)phenyl]-7-thiomethyl-1,4-dihydro-1,2,4-benzotriazin-4-yl (**2**). **b)** Model of structure **2** oriented to fit the nc-AFM image in c) enlarged by 22% with respect to the scaling in c). -SMe and -SMe' refer to thiomethyl groups, Ph refers to the phenyl group, -PhSMe refers to the (thiomethyl)phenyl group and BtA refers to the benzotriazinyl unit. **c)** Δf-image acquired in constant-height mode on a Au(111) surface with a CO-tip ($\Delta z = 2.4\,\text{Å}$ from the STM set-point of $I = 0.7\,\text{pA}$ at $V_\text{b} = 0.5\,\text{V}$). **d)** Corresponding Laplace filtered Δf-image of c). Images and gas-phase geometry calculation (depicted in b) on the basis of [57].

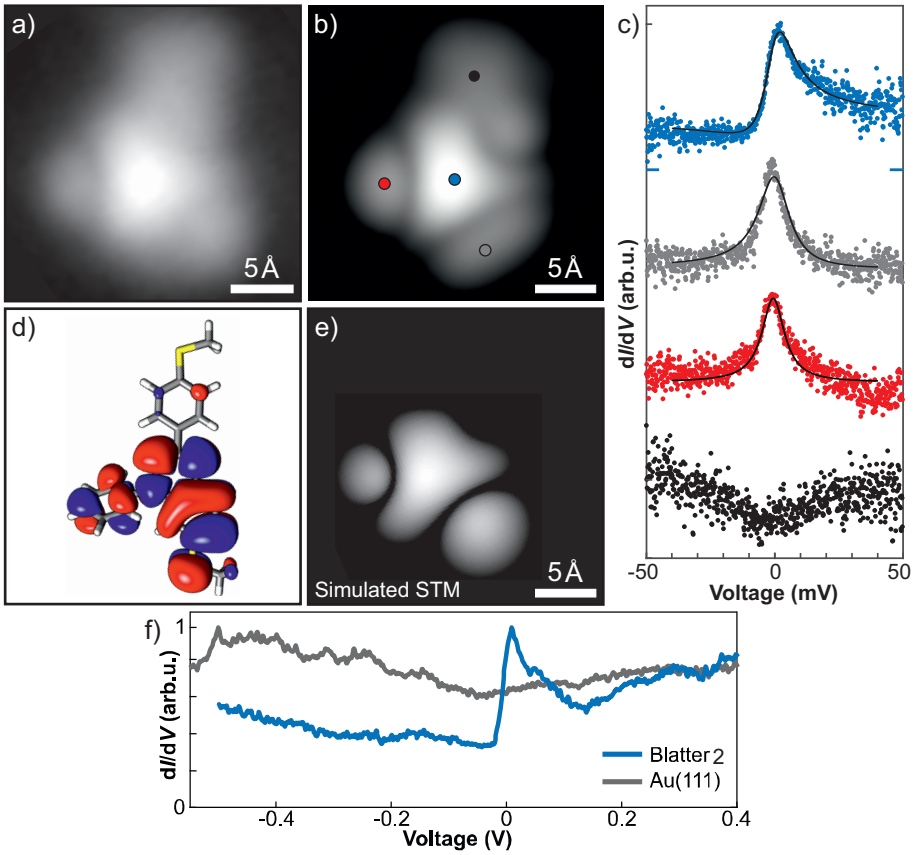

Fig. 3.9. Electronic properties of the Blatter radical **2** adsorbed onto the Au(111) surface. All experimental data displayed in the figure is acquired with a metal tip. **a)** In-gap constant-current STM image of a single molecule of species **2** (STM set-point of $I = 3.8\,\mathrm{pA}$ at $V_\mathrm{b} = 0.1\,\mathrm{V}$). **b)** Constant-current STM image of **2** acquired close to zero bias voltage (STM set-point of $I = 1.9\,\mathrm{pA}$ at $V_\mathrm{b} = 5\,\mathrm{mV}$). **c)** Spatially dependent $\mathrm{d}I\,/\,\mathrm{d}V$-spectra on the Blatter radical **2** with a modulation voltage of $V_\mathrm{mod} = 1.5\,\mathrm{mV_{pp}}$ (STM set-point for opening the feedback loop: $I = 12.0\,\mathrm{pA}$ and $V_\mathrm{b} = 0.1\,\mathrm{V}$). The coloured markers in b) indicate the tip position used for the different spectra. The Fano fits are shown as black solid lines and the spectra are vertically shifted for clarity. Solid blue ticks indicate the zero conductance level of the topmost blue spectrum. **d)** Calculated SOMO (singly occupied molecular orbital) contour of the gas-phase molecule **2**. The model of the molecule is rotated in a way to fit to the STM images of a) and b). **e)** Simulated constant-height STM image probed with an s-like tip wave function at a distance of 6 Å. **f)** $\mathrm{d}I\,/\,\mathrm{d}V$-spectrum taken in the center of a Blatter radical **2**, compared to a reference spectrum taken over the bare Au(111) surface with a modulation voltage of $V_\mathrm{mod} = 30\,\mathrm{mV_{pp}}$ (STM set-point for opening the feedback loop: $I = 5.0\,\mathrm{pA}$ and $V_\mathrm{b} = 0.5\,\mathrm{V}$). The two spectra are normalized by their maximum values. All images and spectra are taken from [57] with changes in the colour coding for consistency.

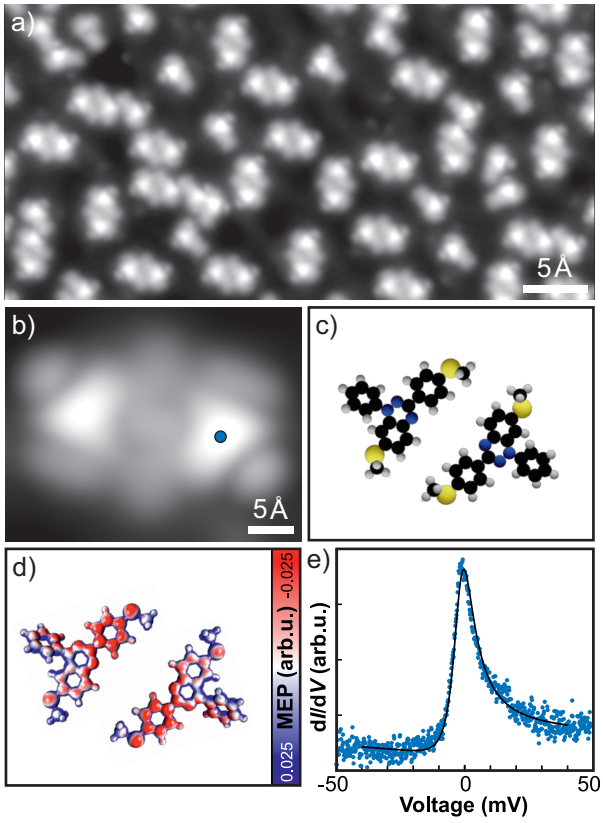

Fig. 3.10. Investigation of the dimerization process after annealing the Au(111) sample to 300 K. All experimental data is acquired with a metal tip. **a)** Constant-current STM overview after the annealing process (STM set-point of $I = 3.0\,\mathrm{pA}$ at $V_\mathrm{b} = 0.1\,\mathrm{V}$). **b)** Highly resolved constant-current STM image of the dimer of **2** acquired close to zero bias voltage (STM set-point of $I = 1.9\,\mathrm{pA}$ at $V_\mathrm{b} = 5\,\mathrm{mV}$). **c)** Model of the Blatter dimer oriented in the same way as the dimer in b). **d)** Molecular electrostatic potential (MEP) map of the gas-phase molecule oriented in the same way as the dimer in b). **e)** Example of one $\mathrm{d}I\,/\,\mathrm{d}V$-spectrum taken on the center of one of the Blatter radicals **2** (indicated by the blue marker in b) exhibiting the same spatial dependent line shape as the isolated molecules in figure 3.9 c). The modulation voltage is $V_\mathrm{mod} = 1.5\ \mathrm{mV_{pp}}$ (STM set-point for opening the feedback loop: $I = 12.0\,\mathrm{pA}$ and $V_\mathrm{b} = 0.1\,\mathrm{V}$). The Fano fit is shown as a black solid line. The figure is taken from [57] with slight changes in the colour coding of the model in c) for consistency reasons.

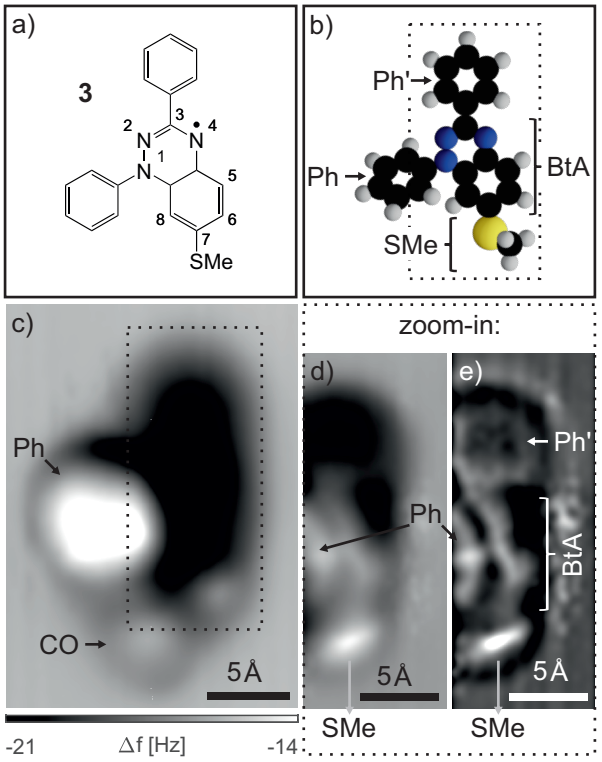

Fig. 3.11. **a)** Structure of the Blatter radical derivative 1,3-diphenyl-7-thiomethyl-1,4-dihydro-1,2,4-benzotriazin-4-yl (**3**). All experimental data presented here is acquired with a CO-tip on a Au(111) surface. **b)** Model of structure **3** oriented to fit the nc-AFM image in c) and d). The adsorption geometry is not calculated and should only serve as a guide to the eye helping to understand the presented nc-AFM images. **c)** Δf-image acquired in constant-height mode ($\Delta z = 2.0\,\text{Å}$ from the STM set-point of $I = 1.1\,\text{pA}$ at $V_\text{b} = 0.15\,\text{V}$). A CO molecule is lying close to the Blatter radical **3** of this image. **d)** Δf-image acquired in constant-height mode ($\Delta z = 2.4\,\text{Å}$ from the STM set-point of $I = 1.1\,\text{pA}$ at $V_\text{b} = 0.1\,\text{V}$). **e)** Corresponding Laplace filtered Δf-image of d).

this species, would be weak due to lone pair repulsion [201, 203]. Additionally, the electron density of the radical is highly delocalized in the cyclic conjugated ring system and hence less available for participating in any type of chemical reaction. The conjugative effect is drastically enhanced in the ring system, since the overlap of the orbitals contributing to the conjugative stabilization of the radical site is maximized in this geometry [203].
A large number of resonance structures contributing to the overall electronic state can be found. Figure 3.7 depicts four of these, which serve as a good basis to discuss the effect of delocalization on the radical site in more detail. The rightmost three resonance structures illustrate the delocalization over all three nitrogen atoms. For the rightmost resonance structure a zwitterionic resonance structure has to be employed in order not to violate the octet rule. The delocalization of the spin density over all three nitrogen atoms in the ring is commonly know in literature, as is the delocalization of the spin density into the annulated ring [203]. The first, leftmost resonance structure in figure 3.7 exemplarily describes the delocalization process of the unpaired electron into the annulated ring. There are additional resonance structures showing the radical delocalization in the annulated ring, which are not shown in this figure.
Understanding the delocalization of the spin density into the two freely rotatable phenyl groups (Ph and -PhSMe in figure 3.8**b**) is not trivial. It is known in literature, that the radical cannot or barely resonate to the C3 position (compare figure 3.8**a** and figure 3.11**a** for general labelling) [243]. As a consequence, the aryl substituent at the C3 position is usually spin isolated [243]. DFT calculations with the B3LYP density functional in com-

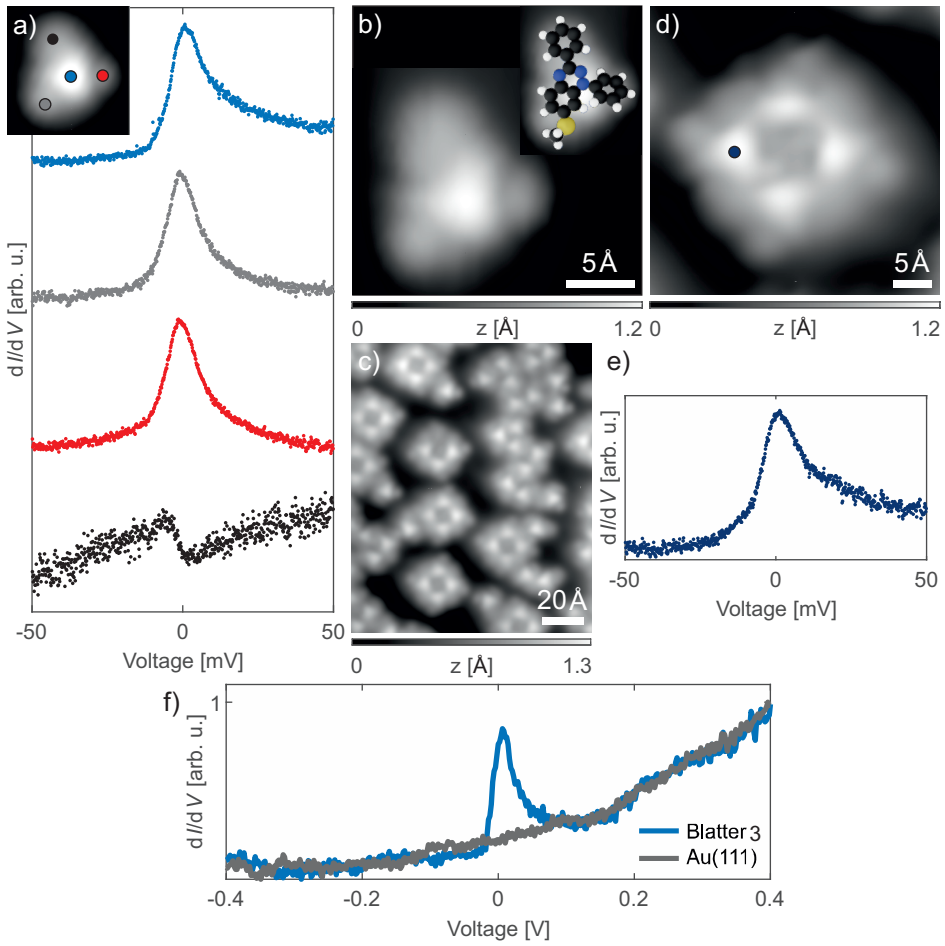

Fig. 3.12. Electronic properties of the organic radical **3** adsorbed onto the Au(111) surface. All the experimental data presented here is acquired with a metal tip. **a)** Spatially dependent $\mathrm{d}I\,/\,\mathrm{d}V$-spectra on the Blatter radical **3** with a modulation voltage of $V_{\mathrm{mod}} = 1.5\,\mathrm{mV_{pp}}$ (STM set-point for opening the feedback loop: $I = 12.0\,\mathrm{pA}$ and $V_{\mathrm{b}} = 0.1\,\mathrm{V}$). The coloured markers in the the inset indicate the tip position used for the different spectra. The spectra are vertically shifted for clarity. **b)** In-gap constant-current STM image of a single molecule of species **3** (STM set-point of $I = 7.0\,\mathrm{pA}$ and $V_{\mathrm{b}} = 0.1\,\mathrm{V}$). The inset shows the STM image overlaid with the model of species **3**. **c)** Constant-current STM overview after annealing the sample to 300 K (STM set-point of $I = 5.0\,\mathrm{pA}$ and $V_{\mathrm{b}} = 0.1\,\mathrm{V}$). **d)** Constant-current STM image of a tetramer built of species **3** (STM set-point of $I = 4.0\,\mathrm{pA}$ and $V_{\mathrm{b}} = 0.1\,\mathrm{V}$). **e)** Example of one $\mathrm{d}I\,/\,\mathrm{d}V$-spectrum taken on the center of one of the Blatter radicals **3** (indicated by the blue marker in d) exhibiting the same spatial dependent line shape as the isolated molecules in a). The modulation voltage is $V_{\mathrm{mod}} = 1.5\,\mathrm{mV_{pp}}$ (STM set-point for opening the feedback loop: $I = 20.0\,\mathrm{pA}$ and $V_{\mathrm{b}} = 0.1\,\mathrm{V}$). **f)** $\mathrm{d}I\,/\,\mathrm{d}V$-spectrum taken in the center of a Blatter radical **3**, compared to a reference spectrum taken over the bare Au(111) surface with a modulation voltage of $V_{\mathrm{mod}} = 30\,\mathrm{mV_{pp}}$ (STM set-point for opening the feedback loop: $I = 1.1\,\mathrm{pA}$ and $V_{\mathrm{b}} = 0.1\,\mathrm{V}$). The two spectra are normalized by their maximum values.

bination with the correlation-consistent double-zeta (cc-pVTZ) basis set for the gas-phase molecule were performed by Dr. Laerte L. Patera in the course of the publication [57] using the ORCA (4.0.1) program package [244]. The gas-phase geometry of these calculations is depicted in figure 3.8**b** and the spatial extend of the SOMO (singly occupied molecular orbital) of these calculations is depicted in figure 3.9**d**.
In the gas-phase geometry one phenyl ring (-PhSMe group in figure 3.8**b**) has a very small tilting angle and nearly lies in the same plane as the benzotriazinyl unit and the other phenyl ring (Ph group in figure 3.8**b**) is slightly tilted with respect to the benzotriazinyl unit. This tilting arises probably due to steric hindrance and usually results in a reduction of the conjugative overlap. However, purely from geometric considerations significant amount of conjugation over the tilted phenyl ring (Ph group in figure 3.8**b**) would be expected. To elucidate the conjugation for tilted phenyl rings, a trityl radical derivative can be considered. A derivative of this class with a dihedral angle of 45° was found to still exhibit half of the resonance stabilization compared to the non-tilted scenario [201]. An example of a trityl radical with a dihedral angle close to 45° is displayed in figure 3.6**b**.
The calculated SOMO contour of the Blatter radical derivative **2** reveals a delocalization of the unpaired spin over the entire benzotriazinyl unit, a delocalization over the Ph unit (in figure 3.8**b**) and almost no density of the unpaired spin can be found at the -PhSMe unit (in figure 3.8**b**) of the molecule.

Certain features arise in the highly resolved Δf-image of the Blatter radical derivative **2** acquired in constant-height mode in figure 3.8**c** which can be attributed to structural units of the molecule. The two bright ellipsoidal features in the upper and lower part of the image in figure 3.8**c** can be assigned to the two thiomethyl groups (-SMe' and -SMe in figure 3.8**b**). More precisely these features most probably can be related to the hydrogens pointing out of the surface plane into the vacuum, while the sulphur atoms serve as anchoring groups exhibiting a strong interaction with the gold metal surface [245].
Another prominent feature is a distorted bright feature in the lower left corner of the image. This feature can be assigned to the phenyl group marked with Ph in figure 3.8**c**. It appears very bright, since the tilting of the ring makes the hydrogen atoms protrude from the surface plane. The feature looks comparable to already observed features for hydrogen atoms on a tilted cyclic organic ring protruding out of the surface plane [246].
The rest of the molecule can be identified in the Laplace filtered form of figure 3.8**c**, shown in figure 3.8**d**. Here, the two ellipsoidal features assigned to the thiomethyl groups are connected to a hexagon and to two connected hexagonal features corresponding to the phenyl ring with the thiomethyl group (-PhSMe in figure 3.8**b,d**) and the benzotriazinyl unit (BtA in figure 3.8**b,d**), respectively. The feature assigned to the benzotriazinyl unit could not fully be resolved, since the signal is partially covered by the signal of the protruding phenyl ring (Ph in figure 3.8**b,d**).
By comparing the features of the constant-height Δf-images to the constant-current STM images (see figure 3.9**a**), chemical structural entities of the Blatter radical **2** can be directly related to features in the constant-current STM images. To illustrate the orientation of species **2** in the STM images of figure 3.9**a,b** the model in figure 3.9**d** is oriented in the

same way.
For employing stable organic radicals to spintronics it is crucial to connect them to conducting metal electrodes without loosing their open-shell character. This is not a condition which can be straightforwardly assured. In most cases the electronic structure of a radical must be investigated in the explicitly desired environment. For the Blatter radical **2**, Low et al. [43] found with X-ray spectroscopic methods that the radical character survives upon adsorption onto a Au(111) single crystal surface under LT-UHV conditions. However, in STM-BJ single-molecule conductance measurements, where gold metal electrodes were employed, it was found that species **2** looses its open-shell configuration in a toluene solution [43]. A significant difference in the two measurements is that the X-ray spectroscopic measurements were performed in vacuum, while the STM-BJ experiments were carried out in a toluene solution [43]. Low et al. [43] related this distinct difference in the environment to the varying electronic configurations of species **2** in the two systems. The reasoning behind this is that small changes in the surrounding may lead to small changes in the energy level alignment of the system [43]. If the SOMO or the SUMO of the radical lies sufficiently close to the Fermi level, already small shifts can affect the electronic configuration of the respective molecule.
A detailed analysis of the electronic structure of the Blatter radical **2** can be carried out by means of STM/S experiments and DFT calculations.
Tunneling conductance spectroscopy with small modulation voltages with the tip positioned above the single molecule **2** reveal a narrow zero bias peak (ZBP), see figure 3.9**c**. The peak shape varies for different areas of the molecule from a rather symmetric peak shape over an asymmetric peak shape to even completely vanish over certain areas of the molecule. The described peak shapes are characteristic for Fano-type quantum interference phenomena, compare section 3.1. Additionally, species **2** was found to maintain its open-shell configuration upon adsorption onto a Au(111) surface under UHV conditions [43]. Due to all these aspects the peak can be attributed to a Kondo-type of interaction, as discussed in section 3.1.
The spectra taken above the two lower lying outer lobes, marked with yellow and orange in figure 3.9**b**, have a rather symmetric peak shape shown in figure 3.9**c** and can be assigned to the tilted phenyl moiety (Ph in figure 3.8**b**) and the thiomethyl group (-SMe in figure 3.8**b**), respectively. The spectrum acquired in the center of the molecule, which can be assigned to the benzotriazinyl unit (BtA in figure 3.8**b**), shows an asymmetric shaped peak (blue spectrum in figure 3.9**c**). The uppermost lobe in the STM image of species **2** in figure 3.9**b** is represented by the violet spectrum in figure 3.9**c**. Here, the Kondo resonance peak completely vanishes.
The FWHM can be determined with a Fano fit, see equation 3.1, and from this the Kondo temperature can be deduced from equation 3.2. For this purpose the temperature of the system needs to be known, which was 6.1 K for the presented experiments [57]. The Fano fits of the different spectra are shown as black solid lines in figure 3.9**c**. The Kondo temperature of the spectrum detected at the center of the Blatter radical **2** (blue spectrum in figure 3.9**c**) could be determined by this procedure to be 26 K [57]. The Kondo temperature was found to vary for different lateral positions from 23 K to 29 K [57], which is in the

range of the overall uncertainty for the detected Kondo temperatures of the here presented experiments of about 20 % [57]. Also a variation in the Kondo temperatures for different fitting procedures was found and is accounted for in the determined overall uncertainty.
The modulation voltage was found to be a crucial parameter in experiments detecting Kondo resonances [193]. The experimental procedure to assure that the modulation voltage is not responsible for a severe broadening of the detected peak is to take spectra of the ZBP at a set position above the single molecule and stepwise decrease the modulation voltage from higher values to small values until the width of the peak is staying constant.
It is rather complicated to gain unequivocal information of this particular system only from the fit parameter T_K and q of the equations 3.1 and 3.2. However, a striking observation is that the Kondo signature completely vanishes over distinct areas of the adsorbed Blatter radical **2**. The area where the Kondo resonance vanishes is at the -PhSMe unit (compare violet dot in figure 3.8**b**). Interestingly, this is exactly the moiety where no delocalized spin density could be found in the gas-phase DFT calculations, compare figure 3.9**d**. Even more conspicuous is the distinct nodal plane structure resolved in the low-bias STM image in figure 3.9**b**.
The highly resolved delicate structure in the low-bias STM image in figure 3.9**b** is in remarkable agreement with the calculated gas-phase SOMO distribution of figure 3.9**d** and the corresponding simulated STM image in figure 3.9**e**.
Comparing the highly resolved low-bias STM image (figure 3.9**b**) with the in-gap STM image (figure 3.9**a**), it becomes clear that the low-bias STM image (figure 3.9**b**) has topographic and electronic contributions.
Adsorbates on metal surfaces usually strongly couple to the metal, leading to a pronounced broadening of the molecular orbitals. This makes orbital imaging complicated on metal surfaces and STM images of adsorbed molecules at their orbital resonance voltages appear blurred and the orbitals nodal plane structure cannot be resolved. Even though orbital imaging of molecules directly adsorbed onto metal surfaces is feasible [247], it can be assumed that in this system the orbital levels of species **2** adsorbed on Au(111) are strongly broadened and no nodal plane structure can be resolved due to common orbital imaging mechanisms [49]. The reasoning behind this hypothesis is that singly occupied orbitals of adsorbates on metal surfaces are known to exhibit Coulomb-blockade peaks [46, 190], which could not be resolved in this experiment. In this measurement no features could be related to the SOMO or SUMO other than the Kondo resonance. The fact that no SOMO or SUMO resonances could be resolved, might indicate that a pronounced broadening of those resonances makes it impossible to resolve them.
With no resonances other than the Kondo resonance close to zero bias voltage, compare figure 3.9**f**, the imaging mechanism behind the highly resolved nodal plane structure in the low-bias STM image must stem from the Kondo interaction in the system. Two clear correlations reinforce this hypothesis. The first one is between the Kondo signal being absent in distinct moieties of the molecule (figure 3.9**c**) with the calculated gas-phase SOMO distribution (figure 3.9**d,e**). The second correlation is between the nodal plan structure of the calculated SOMO distribution (figure 3.9**d,e**) with the resolved structure in the low-bias STM image (figure 3.9**b**). This indicates that the spatial distribution of the SOMO governs

the spatial extend of the spin-metal coupling [57]. At a nodal plane or at a whole moiety of the molecule, where no delocalization of spin density can be found, no coupling of the spin state to the continuum states of the metal may occur and hence, no Kondo signature may be detected. This correlation leading to Ångström resolution enabling to directly detect the delicate nodal plane structure might link to the importance of the tunneling channel into the Kondo state even though an exact determination of the contribution via the form factor q of the fit equation 3.1 was not straightforward, compare with section 3.1 for the theory background.

In the following it should be investigated if the Blatter radical derivative **2** reacts at elevated temperatures and how the radical character is affected under these changed conditions. The substance is dosed with a higher coverage, but still in the submonolayer regime, onto the sample and the sample is annealed to 300 K.
The overview in figure 3.10**a** displays the tendency of the species **2** to dimerize during the annealing process. On the surface predominantly dimers and few single molecules as well as few smaller clusters can be found.
Panel 3.10**b** shows a highly resolved low-bias constant-current STM image of the dimer. The moieties in the respective monomers are nearly identical to the ones in the single molecules (figure 3.9**b**) and hence the orientation of the monomers can be assigned. The two monomers in the dimer in figure 3.10**b** are of the same chirality and are aligned antiparallel with respect to each other. A model in figure 3.10**c** schematically explains this orientation. The nearly identical features of the two monomers hint already to a non-covalent interaction among the two molecules and a preserved radical character.
The two models of the gas-phase geometry of species **2**, displayed in figure 3.10**c**, are fit to the STM image with adapted scaling. By this the separation of the two molecules could be determined to be in the range of roughly 9 Å measured between the two N4 positions (for labelling see figure 3.8**a**). This distance is even when encountering for large errors in the distance determination not in the range of covalent bond lengths, which typically span from 1 to 2 Å [248].
Differential conductance spectra are taken at different tip positions. The line shapes of the different Kondo resonances are closely resembling the spectra of the single molecules for the different moieties in the two monomers. Exemplarily a spectrum at the center of one of the monomers is shown in figure 3.10**e** exhibiting the asymmetric line shape already observed for the single molecules (blue curve in figure 3.9**c**). The position of the tip during the recording of the spectrum in figure 3.10**e** is indicated by the blue dot in figure 3.10**b**. This result underlines the non-covalent character of the interaction, since in the case of covalent bonding between the two N4 radical centres of the respective monomers the formed dimer would most probably form a closed-shell system and no occurrence of a Kondo resonance in the $\mathrm{d}I/\mathrm{d}V$-spectrum would be expected.
To investigate the interaction between the two monomers in more detail a molecular electrostatic potential (MEP) map of the gas-phase molecule was calculated yielding an in-plane electric dipole of $\mu \approx 2.7\,\mathrm{D}$ [57]. Figure 3.10**d** depicts the MEP results, with the two monomers oriented in the same way as the dimer in figure 3.10**b**. The antiparallel orienta-

tion of the two monomers shown in figure 3.10**d** can be explained in terms of dipole-dipole interactions [249].
The Fano fit, displayed as solid black line in figure 3.10**e**, yields a Kondo temperature of 21 K. The value is on the limit of the stated uncertainty of 20 %. A lower value of T_K of a molecule in an assembly compared to the isolated case is known from literature [46, 198]. The reasoning behind this is a reduced interaction of one individual molecule of the assembly with the continuum states of the metal [198]. The effect can be strongly dependent on the amount of nearest neighbours of the molecule under investigation. Iancu et al. [198] and Mugarza et al. [46] found a strong Kondo temperature decrease for a rising number of neighbouring molecules.
For spintronic applications open-shell substances are often immobilized in monolayer amounts or lower onto special substrates [205, 222, 250, 251]. It is desirable that the open-shell character persists in the immobilized form at room temperature. For this reason it can be helpful to understand the interactions among the individual molecules on surfaces and their assembling structures. In order to gain a detailed understanding of the assembly process further investigations are required. However, the fact that the single molecules dimerize at room temperature without the formation of covalent bonds if deposited in submonolayer amounts already gives insight in the persistence of the open-shell character on a single molecular level [205, 222, 250, 251].

The second Blatter radical derivative **3** (figure 3.11**a**) possesses only one thiomethyl group. The thiomethyl group formerly attached to the -PhSMe unit, see figure 3.8**b**, is missing in this derivative and the respective structural unit reduces to an unsubstituted phenyl group (Ph' in figure 3.11**b**). The slight structural change causes a pronounced impact on the highly resolved nc-AFM measurements. As discussed above the -SMe group is a good anchoring group on the Au(111) surface and hence the immobilization of species **3** on the surface is less strong compared to species **2**. This entails problems in the imaging process, since the species appears more mobile on the surface. Figure 3.11**c** shows the complete nc-AFM image of the single Blatter radical **3**. The adsorption geometry differs from the one discussed for the Blatter radical **2**. The derivative **3** is less pinned to the surface and hence the adsorption geometry appears more bulky, specifically one of the phenyl groups (Ph in figure 3.11**b**) appears more tilted. As a result parts of this phenyl group are further away from the surface and hinder the remaining moieties to be fully resolved. To gain more structural information about the entities located closer to the surface a zoom-in of parts of the molecule (marked with dashed lines in figure 3.11**c**) is imaged at closer distances. The zoom-in, displayed in figure 3.11**d**, shows an ellipsoidal feature which can be assigned to the thiomethyl group as explained above. The ring structure can only be identified in the Laplace filtered version of figure 3.11**d**, which is shown in figure 3.11**e**. Here, the Ph' group can be assigned, see figure 3.11**e**. The feature of the benzotriazinyl unit is to a large extend covered by the signal of the tilted phenyl ring, Ph in figure 3.11**e**. However, a feature which can be assigned to a small fraction of the benzotriazinyl moiety can be identified, BtA in figure 3.11**d**.
By comparing STM and nc-AFM images of the same molecule the structural fragments

can be assigned to features in the STM image. Figure 3.12**b** shows a constant-current STM image of species **3**. In the inset of this panel the STM image is overlaid with a model of the structure of **3** to illustrate the orientation of the single molecule in the image. The Kondo signature displayed in figure 3.12**a** is similar to the one of the Blatter radical derivative **2** for equivalent moieties of the molecules.
Interestingly, after annealing the gold sample to 300 K a predominant formation of tetramers can be found, besides unordered larger clusters and single molecules, see constant-current overview in figure 3.12**c**. Figure 3.12**d** displays a constant-current image of the tetramer. The features of the monomers appear unchanged and a non-covalent interaction scheme can be suspected. The Kondo resonance survives upon tetramerization, which is exemplarily shown in the spectrum of figure 3.12**e** with the tip positioned above the center of a monomer, marked in figure 3.12**d**. This observation consolidates the assumption of a non-covalent interaction between the monomers in the tetramer.
Even though the results of species **3** are very similar to the ones of species **2**, they bare important information. Firstly, they consolidate the observations made for species **2**. Secondly, by altering the structure slightly at the spin isolated aryl substituent, it was achieved to not significantly change the electronic properties of the unpaired spin state. At the same time one might relate the changed assembling scheme of species **3** to the altered chemical structure compared to species **2**.
The observation that slight changes in the chemical structure result in different molecular packing has been made for solid state Blatter radical compounds [243]. If the changes occur at the aryl substituent at the C3 position (compare figure 3.8**a** and figure 3.11**a** for general labelling) this often has an impact on physical properties, e.g. the packing-type or packing distances in a solid, and at the same time the radical character of the species is maintained [243, 252–255]. In contrast, the alternation of the aryl substituent at the N1 position (compare figure 3.8**a** and figure 3.11**a** for general labelling) was often reported to alter the magnetic properties [243, 256, 257]. Hence, the observation of the comparable electronic properties of the spin state in species **2** and **3** match with results in literature and can be rationalized by the altered chemical structure fragment being located at the spin isolated moiety. As afore mentioned, it was also found that slight changes in the chemical structure may affect the packing-type or the packing distance in solid-state Blatter radical compound. Accordingly, the different assembling scheme of the two Blatter radical derivatives **2** and **3** can be tentatively related to the slightly altered chemical structure.
However, further investigations are required to connect the altered assembling scheme to the structural changes of the molecule and not to slightly different coverages of the two sample preparations.
Nevertheless, if the assembling scheme could not be attributed to the structural changes but rather to slight differences in the coverage of the sample, a very important aspect remains, namely the survival of the unpaired spin even for higher coverages with closer nearest neighbour distances and hence stronger interaction among neighbouring molecules.

In conclusion, a detailed analysis of species **2** and **3** adsorbed on Au(111) was presented by means of combined highly resolved nc-AFM imaging, STM imaging at low bias voltages

and differential conductance measurements of a zero bias peak (Kondo signature) at low modulation voltages, supported by gas-phase DFT calculations. The two species could be unambiguously identified. Distinct units of the chemical structure could be related to different shaped Kondo signatures. The combined investigation of the low-bias STM image of an individual molecule of species **2** with the spatial distribution of the Kondo signature over the molecule and the gas-phase DFT orbital density calculation of the SOMO and its respective simulated STM image indicated that the spatial distribution of the SOMO governs the spatial extend of the spin-metal coupling [57]. Due to this correlation the delicate nodal plane structure of species **2** adsorbed onto a metal substrate could be directly resolved in the low-bias STM image. The electronic structure, especially the line shape of the Kondo signature, over distinct units of the individual molecules was similar for molecules of species **2** and **3**. The assembling of species **2** and **3** on Au(111) after annealing to 300 K could be investigated and compared. No substantial changes in the electronic structure of species **2** and **3** were found after the annealing step, suggesting the preservation of the radical character without any newly formed covalent bond and solely electrostatic interactions among the molecules. However, different assembling patterns were observed for species **2** and **3** after the annealing process. For the Blatter radical derivative **2** predominantly dimerization was observed, while for the derivative **3** predominantly tetramerization was observed.

Chapter 4

Tip-induced ether-bond fission on insulating bilayers

A manuscript of the work of this chapter is in preparation, with parts of the text being identical to the text of this chapter.[3] *Most of the chemical compounds have been synthesized and were kindly provided by Dr. Steffen Woltering. The calculations with the species adsorbed onto the sodium chloride lattice were carried out and were kindly provided by Dr. Daniel Hernangómez-Pérez.*

In this chapter an ether-bond cleaving reaction is presented for various substances adsorbed on thin sodium chloride bilayers (NaCl(2Ml)) grown on Cu(111). The reaction mechanism and the relevant reaction products are examined by means of nc-AFM, STM and STS measurements. The experimental results are supported by density functional theory calculations (DFT) providing a deeper understanding of the cleaving process of the species adsorbed on sodium chloride.

[3]S. Sokolov, S. Woltering, L. L. Patera, D. Hernangómez-Pérez, L. Gross, F. Evers, H. Anderson, J. Repp. 'Generation of reactive species via tip-induced ether-bond fission on insulating layers'. Manuscript in preparation.

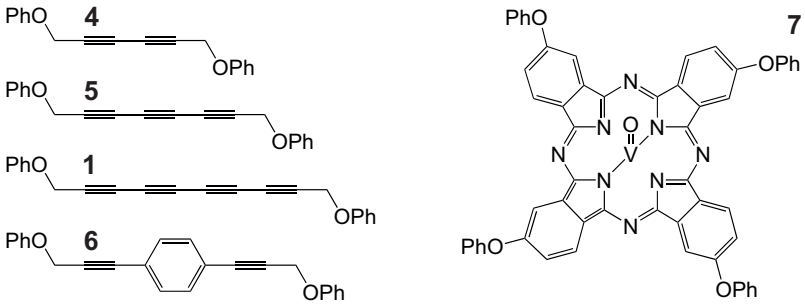

Fig. 4.1. Chemical structures of the investigated species: 1,6-diphenoxy-2,4-hexadiyne (**4**), 1,8-diphenoxy-2,4,6-octatriyne (**5**), 1,10-diphenoxy-2,4,6,8-decatetraiyne (**1**), 1,4-bis(3-phenoxyprop-1-yn-1-yl)benzene (**6**) and vanadyl-2,9,16,23-tetraphenoxy-29H,31H-phthalocyanine (**7**).

Five selected compounds are investigated, namely 1,6-diphenoxy-2,4-hexadiyne (**4**), 1,8-diphenoxy-2,4,6-octatriyne (**5**), 1,10-diphenoxy-2,4,6,8-decatetraiyne (**1**), 1,4-bis(3-phenoxy-prop-1-yn-1-yl)benzene (**6**) and vanadyl-2,9,16,23-tetraphenoxy-29H,31H-phthalocyanine (**7**), compare figure 4.1. The highly pure compounds **1**, **5** and **6** have been synthesized and kindly provided by Dr. Steffen Woltering in the group of Prof. Dr. Harry Anderson from the University of Oxford. The compounds **4** and **7** were purchased from Sigma-Aldrich. For substance **4** no analytical data was available and for the substance **7** a purity of $\geq 98\%$ was listed.

The discussion of the bond dissociation of all species presented in this chapter includes the analysis of precursors and their fragments after bond fission. The charge state of adsorbates on the surface depends on the alignment of their orbitals with the Fermi level of the sample and is not known a priori. In the remainder of this chapter, if reasonable, the species are assumed to be in a neutral charge state and the chemical nomenclature of the species is adapted to the neutral state. However, if the charge state has an impact on the drawn conclusions and a deviation from the neutral charge state is conceivable it will be noted.

The geometrical models of the species and its fragments depicted throughout this chapter visualize, with some exceptions, gas-phase geometry optimizations carried out at the B3LYP-DFT level of theory with a cc-pVTZ basis using the Gaussian 09W program [258]. The depicted orbital isosurfaces (isovalue = $0.02\,\mathrm{e}{\cdot}\mathrm{a}_0^{-3}$) are derived with the optimized gas-phase geometries, with the same B3LYP-DFT theory and cc-pVTZ basis in the Gaussian 09W program [258]. In the process of generating the input files and visualizing the output the program Avogadro was utilized [259].
One exception, where no simple B3LYP-DFT gas-phase calculations were applied, includes the calculations with the species adsorbed onto the sodium chloride lattice. The other exception are the models bearing phenoxy groups. The conformation of molecules adsorbed on sodium chloride sometimes differs from the gas-phase conformation. In this study, especially the phenoxy groups at the precursor molecules or at fragments of the precursor molecules appear rotated with respect to the gas-phase geometry. For this reason the models of the species with phenoxy groups do not show the gas-phase geometry, but the dihedral bond angles in vicinity of the oxygen atoms are rotated to fit the features of the nc-AFM images. As a third exception, calculations of species **7** cannot straightforwardly be executed with standard processing tools, hence the model of this species is not calculated, but displays reasonable dimensions known for similar phthalocyanine species. The scaling of the molecular models is always adapted to the corresponding nc-AFM images.

4.1 On-surface chemical reactions studied by AFM and STM

On-surface synthesis provides the possibility of creating a variety of new substances. In particular, molecular species which cannot be synthesized in solution chemistry can often be synthesized following new approaches on surfaces. With STM, AFM and AC-STM the reaction processes, the reaction products and their orbital structures can be directly resolved on surfaces, while STS and KPFM help to reveal interesting additional properties of the newly synthesized compounds.

On metal surfaces a variety of different reactions could be directly investigated by STM or AFM. In contrast, it is challenging to demonstrate and investigate new on-surface reactions on insulators by STM or AFM. The reason why a lot of publications exist on the topic of on-surface synthesis on metal surfaces as opposed to insulating surfaces is twofold. Firstly, the metal often acts as a catalyst in the on-surface chemical reaction. Notable, intermediate states of Ullmann-type reactions could be resolved and show a stoichiometric occurrence of metal atoms participating in the intermediate state [260, 261], which is also expected for other types of reactions on metal surfaces. The second and very important reason is that the discrete states of the adsorbates strongly couple to the electronic continuum states of the metal. As a consequence of the strong interaction between the metal and the adsorbates, the metal samples can be annealed to high temperatures without desorption of the adsorbates. In most cases, this helps to easily overcome the activation energy barrier of the desired chemical reaction which is often lowered due to the catalytic effect of the metal. Annealing temperatures of up to 700 K [34] are commonly used in on-surface chemical reactions on metal samples. Often this isn't possible on insulators and different strategies to overcome the activation energy barrier need to be considered.

In the following there will be given insight into the impressive variety of on-surface chemical reactions investigated by STM and AFM on metal surfaces. In many examples, the more inert gold surfaces are chosen to facilitate probing of the newly formed species with weaker coupling to the surface than, for example, other noble metal surfaces [10–12, 14–16, 170–174, 262]. Some experiments result in highly resolved images of reactants, intermediate states and products, rendering a detailed analysis possible.
A large proportion of investigated chemical reactions by means of STM or AFM on metal surfaces are of the Ullmann-type [33, 263–265], cyclodehydrogenation reactions [14–16, 170, 172–174, 266], or a combination of both [34, 37, 39, 40, 171, 267–270]. Even multiple step hierarchical Ullmann coupling reactions could be demonstrated [35, 271, 272]. Furthermore, examples of Glaser analogue reactions [36, 273–275] or condensation reactions [276–291] have been shown on metal surfaces. Also dehydrogenation reactions at sp^2- [292] and sp^3-hybridized carbon sites [293, 294] have been revealed in literature. A cyclotrimerization reaction has proven to be successful for building covalently coupled extended 2D-networks on metal surfaces [295, 296]. Some chemical reactions, unique and

new to on-surface chemistry probed by STM and AFM, could be carried out on metal surfaces. Among them are a dehydro-Diels-Alder reaction [297], a Sonogashira-Hagihara cross-coupling analogue reaction [298], a polymerization reaction involving N-heterocyclic carbene intermediates [299], Bergmann analogue reaction types [3, 300, 301], bond dissociation and fragmentation processes including oxygen carrying functionalities [10, 13, 269, 302–304], covalent coupling reactions of isocyanates with amines [305, 306], a polyacetylene formation [307] and azide-alkyne cycloaddition reactions [308, 309], which are classified among the click reaction group. Even a reversible thermally induced dehalogenation reaction was carried out on a Au(111) surface [310]. In summary, a zoo of different chemical reactions are applicable on metal surfaces to generate the desired species and even sequential stepwise reactions including different functionalities and different reaction mechanisms have been demonstrated [275, 288].
With this toolbox a variety of new species can be synthesized on metal surfaces including specially designed graphene nano ribbons (GNR) [34, 37–41, 171, 267–269, 311] or nanographene (NG) structures such as higher acenes [10–12], triangulenes or triangulene based species [14–16, 48], porphyrine based structures [172], Clar's goblet [170], rhombenes [173] or super-nonazethrene [174]. Even extended sp^2-hybridized systems consisting of non-hexagonal cyclic structures have been synthesized on Au(111) [312].
These newly designed structures posses interesting electronic properties which can often be probed on gold surfaces, due to the relatively weak electronic coupling of the inert metal to the adsorbates.
GNRs of varying structures incorporating for example heteroatoms [269], porphyrines [171] , heterojunctions [39, 40, 267, 268] or varying edge structures [38, 39, 41, 311] have been synthesized. By thorough design of the GNR structure, the band structure can be adjusted ranging from relatively large gaps to induced metallicity [37, 38]. Topological protected edge states were directly resolved in $\mathrm{d}I/\mathrm{d}V$-maps [39, 40]. The nature of magnetic coupling (ferromagnetic or antiferromagnetic) was investigated [41] and a concept to change from the presence of magnetic edge states to their absence in GNRs was revealed [311].
In the group of specially designed NGs, singlet-triplet gaps in the range of 14 meV (triangulene dimers [16]) to 102 meV (rhombenes [173]) were found by spin excitation spectroscopy of individual molecules [16, 170, 173]. An interesting example of the topic of NGs is the investigation series of triangulene species on Au(111) surfaces [14–16, 48]. The single triangulene species were found to have an open-shell configuration with the spin-polarized orbital structures resolved in $\mathrm{d}I/\mathrm{d}V$-maps [14, 15]. In a triangulene dimer the open-shell singlet configuration could be probed and singlet-triplet spin excitations were observed [16]. In a follow-up experiment triangulene spin-chains were investigated [48]. In these NG spin-chains the collective coupling could be directly investigated and differences in the metal spin-screening and the spin interactions of the monomers in the chain and at the termini were observed [48]. Congruently, no such differences were found for cyclic triangulene spin chains [48].
This very brief summary of on-surface synthesis of novel compounds on metal surfaces investigated by means of AFM or STM highlights the diversity and the possibilities in this field of research. The here given summary is by far not complete and a lot of reviews exist

on exactly this topic [270, 313–319].

A great advantage, as opposed to metal surfaces, is that on bulk insulators or insulating layers the adsorbates are usually electronically decoupled from the substrate and interactions can be mainly attributed to phononic coupling between surface and adsorbate [49]. Hence, the precautions which need to be taken on bare metal surfaces, due to the non-negligible, albeit in some cases weak, electronic coupling of the adsorbates to the metal, become superfluous on insulators or insulating layers. However, it is challenging to find appropriate approaches for on-surface synthesis on insulators. New strategies for on-surface synthesis need to be found and it is helpful to incorporate the achievements, the knowledge and the experience of on-surface synthesis on metal surfaces.
On non-metallic surfaces a promising strategy is to light-induce chemical reactions. A photo-initiated dimaleimide radical polymerization could be demonstrated on bulk potassium chloride [320]. On graphene surfaces a photo-initiated polymerization reaction including diacetylene functionalities was carried out [321] and a light-induced bond dissociation of bridged diketones lead to the generation of nonacene [322]. Multilayered molecular organic wires could be generated including a photo-initiated coupling step on mica substrates [323].
Another approach is the use of a combination of insulating bulk substrate and reactant with a high degree of interaction among them, so that the system can be thermally annealed to relatively high temperatures without desorption of the precursor molecules. For the calcite bulk insulator so-called anchoring functional groups were found to interact electrostatically with the surface atoms, rendering annealing to high temperatures possible [324]. Several thermally activated reactions similar to the ones described above for metal surfaces could be realized using this approach. Among them are, aryl-halide coupling reactions [325–327], a [2+2]-cycloaddition of C_{60} [328], a diacetylene polymerization reaction [329] and a Glaser analogue homocoupling reaction of terminal alkynes [329]. Notably, a hierarchical aryl-halide coupling reaction has been demonstrated [326]. Detailed information about on-surface synthesis on calcite bulk insulator surfaces can be found in the review by Richter and colleagues [324].
Thermal activation by annealing to high temperatures is found to be possible on hexagonal boron nitride (h-BN) [330, 331]. An aryl-halide coupling was demonstrated on h-BN layers grown ontop of Rh(111) (h-BN/Rh(111)) activated by high annealing temperatures of up to 850 K [330]. Interestingly, the activation energy barrier of an aryl-halide coupling reaction was lowered by catalytically active Cu- and Pd-adatoms evaporated on h-BN/Ni(111), such that moderate annealing temperatures of 340 K (for Cu adatoms) and 300 K (for Pd adatoms) were sufficient to carry out the reaction [331].
Covalent coupling has been observed on iodine passivated metal surfaces [332, 333]. A novel deposition technique with a heated reactive drift tube generates aryl biradicals out of an aryl-halide compound, which then adsorb onto the iodine-terminated surface and couple in a mild annealing step (375 to 425 K) [332].
As already pointed out, thin sodium chloride layers of preferentially two to three monolayers have the advantage of sufficiently decoupling adsorbates from the metal surface, while maintaining good conditions for performing STM and STS experiments. Position-

ing extended π-conjugated species on thin NaCl layers has been carried out by different approaches. For example, saturating the thin layer NaCl/Ag(100) surface with a monolayer of reactant and thermally inducing a coupling reaction, resulted in the formation of an extended covalently bound π-conjugated system proceeding on top of the NaCl layers [334]. Another strategy is the formation of a new species on the catalytically active metal surface and subsequent dragging of the species onto the thin NaCl layers by means of tip-manipulation. With this technique an armchair GNR could be investigated [41].
A successful strategy applicable for synthesis on insulating layers and on bulk insulators is to induce a chemical reaction with the STM-tip. The first Ullmann-type coupling investigated by STM was induced by the tip [263]. Since then this approach has proven to be of high value for the specific purpose of generating and subsequently investigating novel reactive single molecules on surfaces. Several manipulations have been observed on metal surfaces, e.g. for the generation of higher acenes [10–13, 302] or for the manipulation of a GNR edge structure [269].
On insulating sodium chloride bilayers this approach has also been demonstrated successfully and has led to the generation and investigation of, for example, an aryne species [50], triangulene [51], an antiaromatic polycyclic system [8], linear and cyclic polyynes [30–32]. Notably, a reversible Bergman cyclization reaction [5] and a Glaser-analogue intramolecular coupling reaction of terminal alkynes [6] were demonstrated tip-induced on thin insulating layers. A reversible tip-induced aryl-halide bond dissociation could even be demonstrated and investigated on thick insulating layers, fully decoupled from the metal surface [335].
To induce the reactions that lead to the new species listed above a voltage pulse is applied with the STM-tip resulting in the bond dissociation of sp^2-hybridized carbon-halogen bonds (C_{sp^2}-Hal) [30, 32, 50], the bond fission of sp^3-hybridized carbon-hydrogen bonds (C_{sp^3}-H) [8, 51] or bridged diketone split-off [31]. In the process of the reversible Bergmann reaction a C_{sp^2}-Br bond was manipulated [5] and in the intramolecular coupling reaction of the terminal alkynes a C_{sp}-H bond was cleaved [6].
The discovery of novel reaction mechanisms that occur on insulating substrates constitutes an open challenge of surface science. To widen the field of on-surface synthesis on insulators the tip-induced bond dissociation of ether bonds is presented in this chapter. Notably, ether-bond fission has been demonstrated on a Cu(111) and on a Si(111) surface, creating extended sp^3-hybridized alkyl chains in a subsequent coupling step [336, 337]. This is of interest since subsequent covalent coupling might also be possible on insulating layers or bulk insulators. In this chapter the ether-bond fission is applied for the generation of reactive species. The reaction products and the reaction mechanism is discussed in detail with highly resolved nc-AFM images and STM orbital images. By ether-bond dissociation not only single atoms or carbon monoxide (CO) can be cleaved off, but larger molecular fragments. This extends the field of reactants applicable for synthesis.

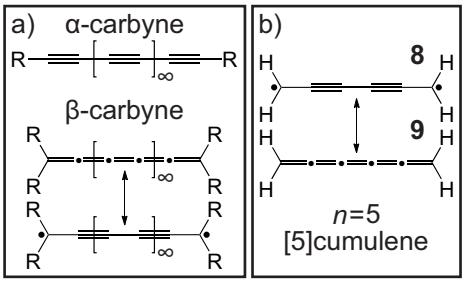

Fig. 4.2. a) Chemical structures of α- and β-carbyne, as well as the biradical structure of β-carbyne. **b)** Possible reaction product of 1,6-diphenoxy-2,4-hexadiyne (**4**) after cleaving off both phenoxy groups homolytically. Two bond orders are conceivable corresponding to the biradical form (1,6-dimethylenediacetylene, **8**) or the [5]cumulene form **9**.

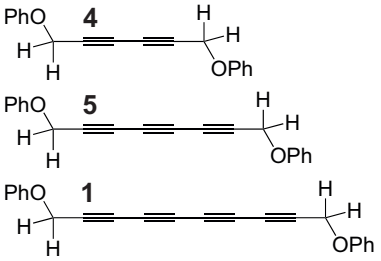

Fig. 4.3. Chemical structures of the investigated dimethylacetylene derivatives: 1,6-diphenoxy-2,4-hexadiyne (**4**), 1,8-diphenoxy-2,4,6-octatriyne (**5**), 1,10-diphenoxy-2,4,6,8-decatetraiyne (**1**)

4.2 Investigation of dimethylacetylene derivatives - Bond fission mechanism and bond-order analysis

Carbyne [17, 18] is a carbon allotrope in an infinite single strand form consisting of sp-hybridized carbon atoms with two forms being proposed, namely α- and β-carbyne [19, 20]. The α-carbyne form is composed of alternating single and triple bonds and the β-carbyne consists of cumulated double bonds [19, 20], compare figure 4.2**a**. Interestingly, the α-carbyne form should exhibit semi-conducting properties, whereas the β-carbyne should rather posses metallic character [21–24].

There is a debate about the existence of carbyne [338, 339] and information about the structure of carbyne is so far not conclusive [18, 19, 340]. Generally, a higher stability is theoretically predicted for the polyyne form (α-form) [18, 19, 339–341], which can be rationalized in terms of Peierls distortion [339, 342, 343].

Interesting properties have been predicted and investigated for small to extended chains of cumulene or polyyne form with proposed applications in the fields of nanoelectronics and spintronics [344–355] (i.a. as nanowires with varying conductance [347, 348, 350, 351, 355–357] or as spin filters [346, 354]), non-linear optics [358–361] and heat conduction [362] among others.

Some publications clearly show that a clear differentiation between polyyne or cumulene character cannot always be drawn and it is important to consider the external conditions. Liu et al. [344], for example, visualized the changes in an sp-hybridized chain under applied tension changing to a higher bond length alteration (BLA) in a theoretical study. Ravagnan et al. [357] theoretically highlighted that axial torsion on sp-hybridized carbon chains has structural impacts with a smooth change in BLA and no clear distinction between cumulene versus polyyne structure. Milani et al. [21] found structural changes in sp-hybridized wires induced by metal nanoparticles in proximity which had an impact on

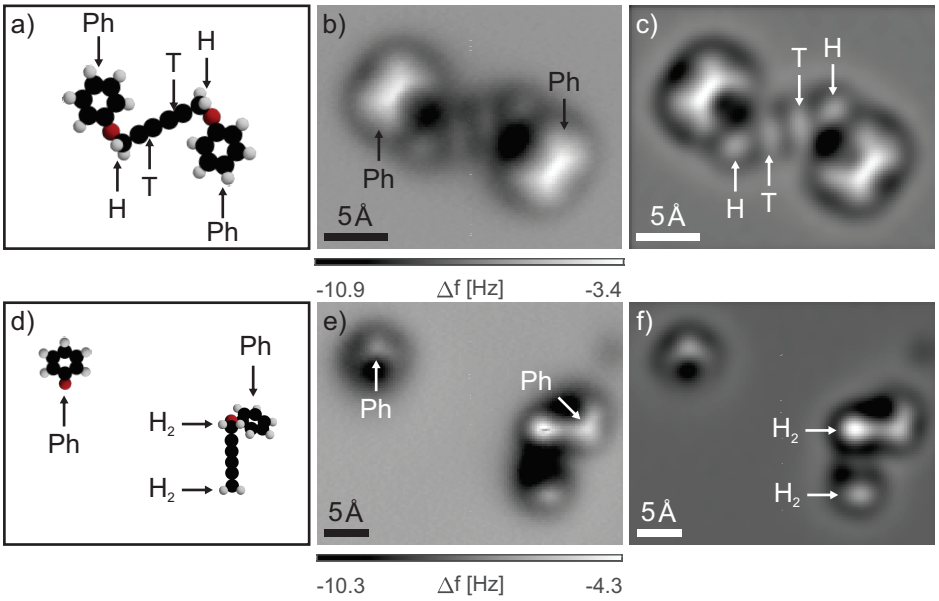

Fig. 4.4. Characterization of the tip-induced cleaving reaction of 1,6-diphenoxy-2,4-hexadiyne (**4**) on NaCl(2Ml)/Cu(111) by means of nc-AFM with a CO-tip. **(a, d)** Model of the precursor **4** and the cleaving reaction product. **(b, e)** Δf-images acquired in constant-height mode of the precursor **4** and the products of the cleaving reaction ($\Delta z = -0.8\,\text{Å}$ and $\Delta z = -0.7\,\text{Å}$, STM set-point: $I = 0.7\,\text{pA}$ and $V_\text{b} = 0.5\,\text{V}$). Bond breaking was induced by scanning the tip over the molecule at $V_\text{b} = 1.6\,\text{V}$ and $I = 1.8\,\text{pA}$. **(c, f)** Laplace filtered versions of b) and e), respectively. Marks indicate the position of the tilted phenyl rings (Ph), the triple bonds (T), the upward pointing H atom (H) and the two upward pointing hydrogen atoms (H_2).

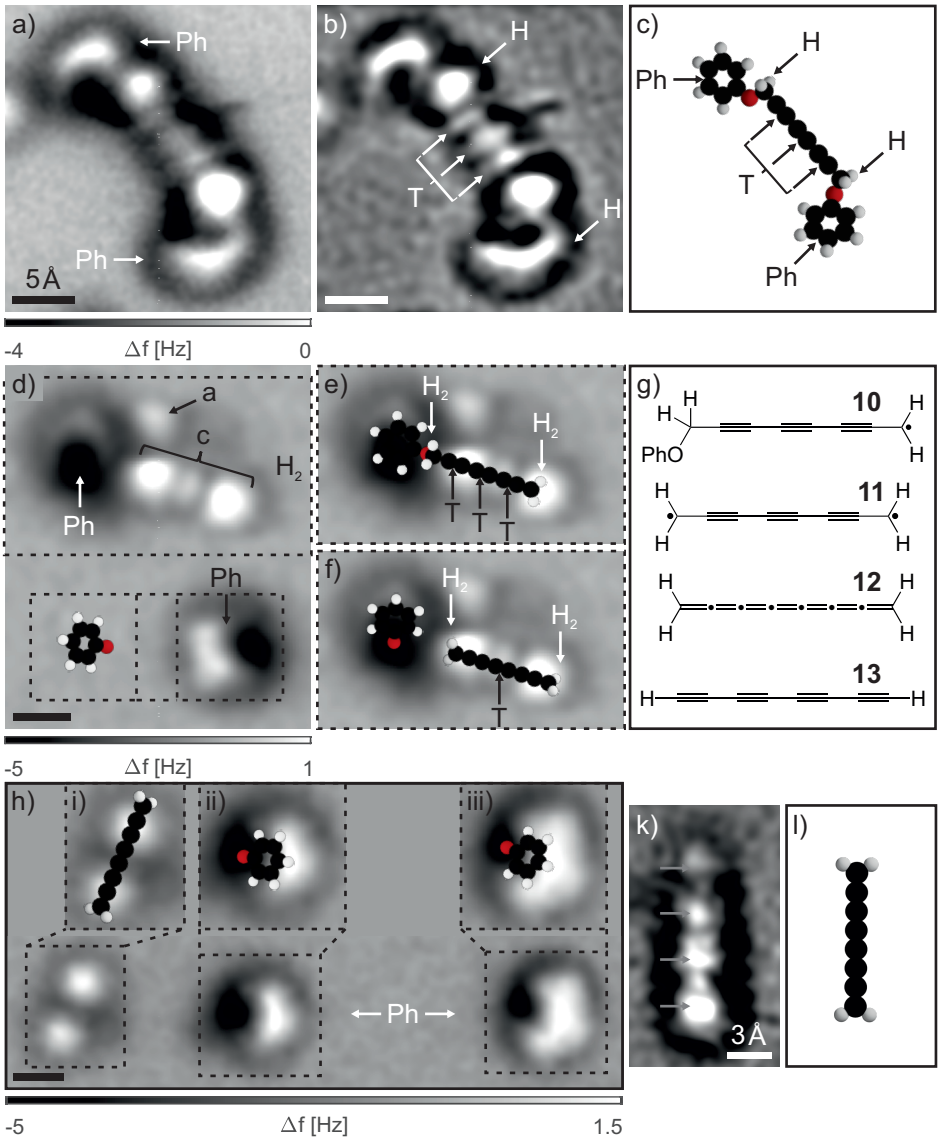

Fig. 4.5. Characterization of the tip-induced cleaving reaction of 1,8-diphenoxy-2,4,6-octatriyne (**5**) on NaCl(2Ml)/Cu(111) by means of nc-AFM with a CO-tip. **a)** Δf-image in constant-height mode of the precursor **5** ($\Delta z = 0\,\text{Å}$, STM set-point: $I = 0.35\,\text{pA}$ at $V_\text{b} = 1.0\,\text{V}$). **b)** Laplace filtered version of a). **c)** Model of the precursor **5**. **d)** Δf-images in constant-height mode after scanning two times with 1.8 V at 0.35 pA over the molecule ($\Delta z = -0.2\,\text{Å}$, STM set-point: $I = 0.35\,\text{pA}$ at $V_\text{b} = 1.0\,\text{V}$). The upper cutout is shown in e) and f), the lower cutout shows the model of the phenoxy fragment. **(e, f)** Cutout of d) overlaid with a model of species **10** and **11**, respectively. **g)** Chemical structures important in the fragmentation process. **h)** Δf-images in constant-height mode after scanning with 2.0 V at 0.35 pA over the molecule ($\Delta z = -0.2\,\text{Å}$, STM set-point: $I = 0.35\,\text{pA}$ at $V_\text{b} = 1.0\,\text{V}$). Insets display cutouts (enlarged by 20 %) of the image overlaid with structural models. **k)** Laplace filtered Δf-image in constant-height mode of a fragment found on the surface ($\Delta z = -0.3\,\text{Å}$, STM set-point: $I = 0.5\,\text{pA}$ at $V_\text{b} = 1.0\,\text{V}$). A mark can be found at the position of the tilted phenyl rings (Ph), the triple bonds (T), the upward pointing hydrogen atoms (H or H_2), the center fragment (c) and at the unknown adsorbate (a). All scale bars correspond to 5 Å, except the one in k), which corresponds to 3 Å.

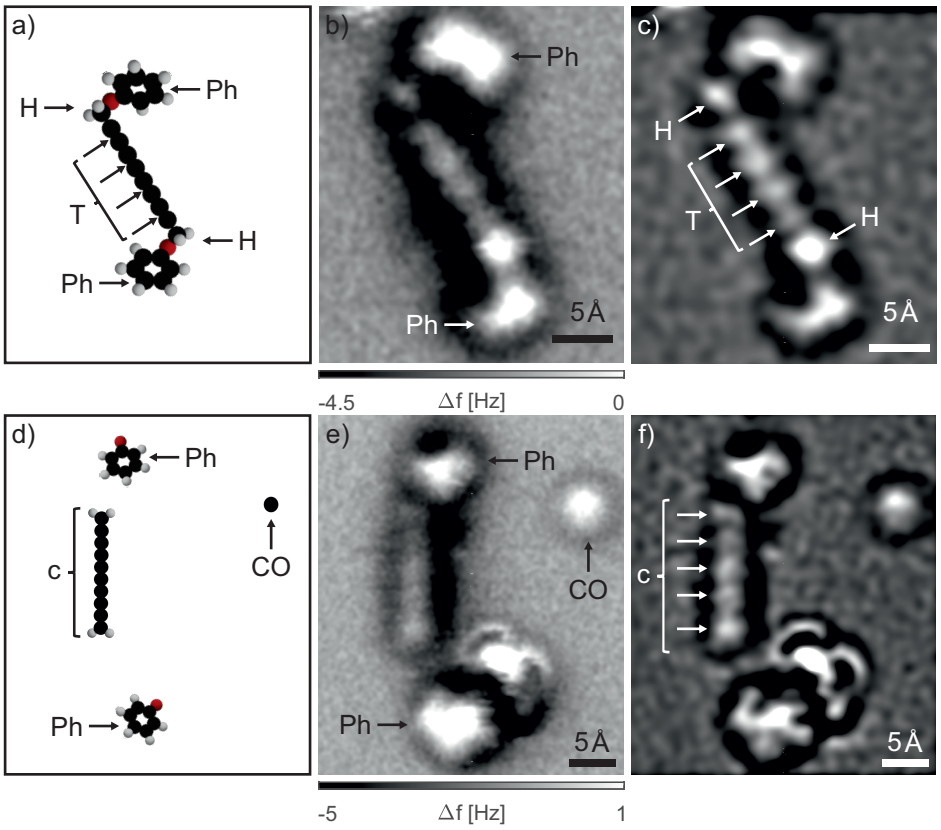

Fig. 4.6. Characterization of the tip-induced cleaving reaction of 1,10-diphenoxy-2,4,6,8-decatetraiyne (**1**) on NaCl(2Ml)/Cu(111) by means of nc-AFM with a CO-tip. **(a)** Model of the precursor **1**. **(b, e)** Δf-images in constant-height mode of the precursor **1** and the products of the cleaving reaction ($\Delta z = 0.6$ Å and $\Delta z = 1.0$ Å, STM set-point: $I = 0.35$ pA at $V_\mathrm{b} = 1.0$ V). The cleaving reaction was induced by scanning with the tip over the molecule at $V_\mathrm{b} = 1.8$ V at a current set point of $I = 0.35$ pA. **(c, f)** Laplace filtered versions of b) and e), respectively. A mark can be found at the position of the tilted phenyl rings (Ph), the triple bonds (T), the upward pointing hydrogen atoms (H), the CO molecule (CO) and at the center fragment (c).

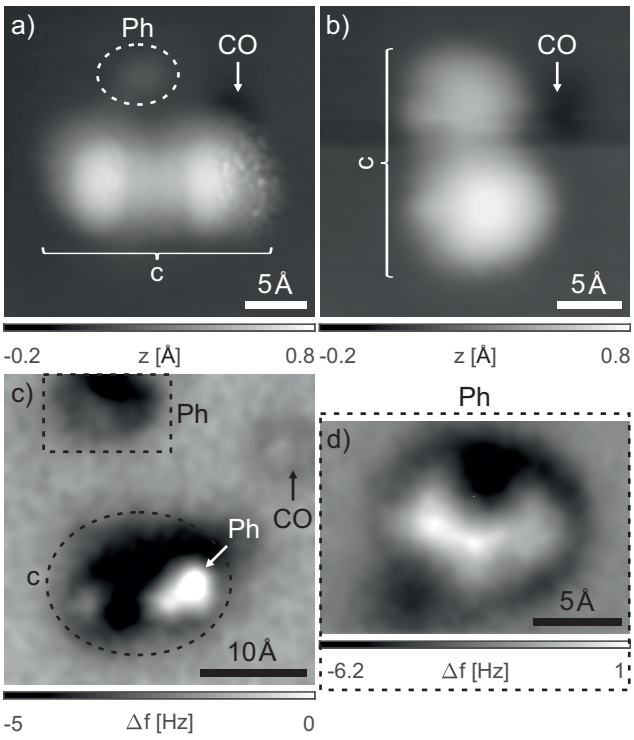

Fig. 4.7. Change of orientation of the reaction products (displayed in figure 4.6 e) and f) on NaCl(2Ml)/Cu(111) imaged with a CO-tip. **a)** Constant-current STM image of the products ($I = 0.35\,\mathrm{pA}$ and $V_\mathrm{b} = 1.0\,\mathrm{V}$). **b)** Constant-current STM image of the products with a changed orientation after scanning the tip over the fragments with $V_\mathrm{b} = 1.5\,\mathrm{V}$ and $I = 0.35\,\mathrm{pA}$ (imaging parameter: $I = 0.35\,\mathrm{pA}$ and $V_\mathrm{b} = 1.0\,\mathrm{V}$). **c)** Δf-image in constant-height mode corresponding to the situation imaged in a) ($\Delta z = 0.2\,\mathrm{Å}$, STM set-point: $I = 0.35\,\mathrm{pA}$ at $V_\mathrm{b} = 1.0\,\mathrm{V}$). **d)** Δf-image in constant-height mode corresponding to a cutout of c) marked as a dashed rectangular in c) ($\Delta z = 0.9\,\mathrm{Å}$, STM set-point: $I = 0.35\,\mathrm{pA}$ at $V_\mathrm{b} = 1.0\,\mathrm{V}$).

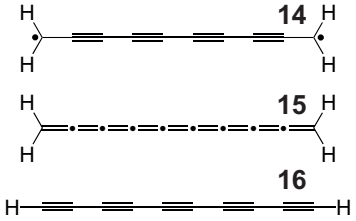

Fig. 4.8. Chemical structures relevant in the fragmentation process of species **1**: 1,10-dimethylenetetraacetylene (**14**), [9]cumulene (**15**), Pentaacetylene (**16**).

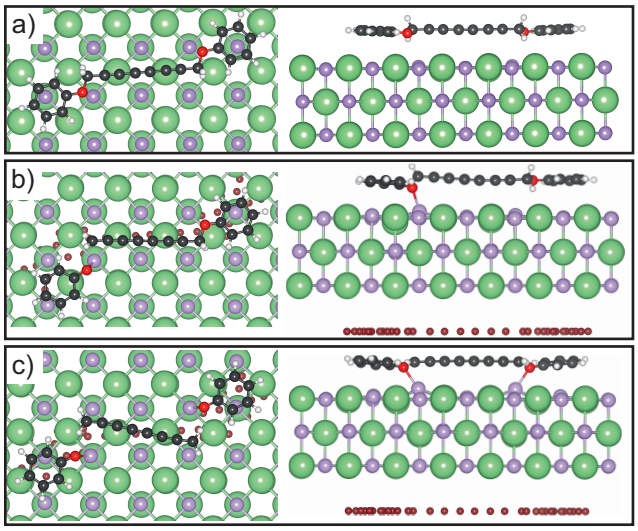

Fig. 4.9. DFT optimized geometries of precursor **5** adsorbed on a NaCl(100) surface. **a)** Top view (left) and side view (right) of the neutral species. **b)** Geometry obtained after charging species **5** with an additional electron. The counter charges in the unit cell are indicated by the red discs at the bottom of the NaCl slab. Bond dissociation occurred at one of the ether bonds. **c)** Same as in b) but after charging the molecule with two additional electrons. Both Phenoxy groups are split off. Figure was kindly provided by Dr. Daniel Hernangómez-Pérez.

the metallicity of the wire. In conclusion, the external conditions and the environment is often determining for the BLA of sp-hybridized carbon chains.

To investigate potential properties of carbyne, smaller-sized model compounds are synthesized. Polyyne representatives could be synthesized with up to 22 acetylene units [363] and for cumulene compounds large representatives consist of nine successive double bonds [19, 20]. Cumulenes are highly reactive compounds which are not straightforward to synthesize [19]. Strategies for stabilization are the introduction of bulky endgroups or rotaxanes [19, 20].
Via UV-Vis spectroscopy and cyclic voltammetry experiments the electronic HOMO-LUMO gap of the model substances can be probed and from X-ray crystallography measurements the BLA of the model substances is often deduced [18–20]. For both, polyyne chains and cumulene chains the trend is a reduction in BLA and electronic gap with increasing chain length [18–20]. With a series of polyyne chains (the longest consisting of 22 acetylene units) it was possible to extrapolate the gap for infinitely long polyyne chains to a finite value of approximately 2.56 eV [363]. In principle, for cumulenes the BLA should approach zero [22, 24, 364] for infinitely long chains with no Peierls distortion present and the gap should close [22–24]. Experimentally, for cumulenes a preliminary estimated asymptotic limit for the BLA is about 0.05 to 0.03 Å [19]. However, the determination of the asymptotic value is limited by the chain length of the synthesized cumulenes in this study and can only be detected with higher accuracy if new, longer cumulenes will be synthesized in the future.
Generally, cumulenes need to be subdivided into even and odd ones, whereas even cumulenes refer to such with an even number of double bonds in the chain and odd cumulenes refer to such with an odd number of double bonds [19, 20]. The distinction is often important, because the two categories differ in conformation of the endgroups and in the two electronic π-systems [19, 20]. Even cumulenes have two degenerated π-conjugated systems [19, 20]. In contrast, the two π-conjugated systems in odd cumulenes are non-degenerate, with one system which spans over the whole cumulene skeleton in length and the other one being considerably shorted [19, 20]. The differences between even and odd cumulenes have detectable impact on e.g. the BLA, and the electronic gap [19, 20, 23].
In general, for sp-hybridized carbyne-like oligo- or polymers not only a polyyne or a cumulene structure is conceivable, but also a diradical structure [19, 365, 366]. Significant singlet biradical character and small singlet-triplet gaps were found theoretically for short-chain [n]cumulenes with terminal carbene groups ($n = 3 - 7$, with n being the number of successive double bonds), whereas neutral even cumulenes exhibit larger singlet-triplet gaps than odd representatives [367]. Experimentally, a singlet biradical character was found for a cumulene with five successive double bonds [368]. Upon lowering the temperature in the system, the emergence of a continuum spin system from formerly localized spin pairs could be observed in spin chains of these [5]cumulene precursors [368].
In the following, a series of molecules is investigated, namely 1,6-diphenoxy-2,4-hexadiyne (**4**), 1,8-diphenoxy-2,4,6-octatriyne (**5**) and 1,10-diphenoxy-2,4,6,8-decatetraiyne (**1**), see figure 4.3. These molecules belong to the same family, with **5** and **1** having one and two

additional triple bonds in the central polyyne-chain compared to **4**. The aim of this study is the generation and investigation of a series of odd [n]cumulenes ($n = 5, 7, 9$). [5]cumulene is depicted exemplarily in figure 4.2**b**. [5]cumulene could be resulting from homolytically cleaving off both phenoxy groups from species **4**. Two bond orders of the envisioned reaction product are conceivable corresponding to a biradical form **8** or the [5]cumulene form **9**, displayed in figure 4.2**b**. The on-surface investigation by nc-AFM has the advantage of the bond order being directly accessible [8, 31, 32, 50, 369]. With information about the bond order of the reaction products, insight about the singlet biradical character can be gained.
Cumulene or acetylene bearing single molecules or nanostructures have been investigated by STM and nc-AFM on metal surfaces and on insulating layers. Cumulene structures [25–29] have a homogenous appearance with no corrugation along the bond axis in nc-AFM images.
Polyynes consist of alternating triple and single bonds. Hence, the BLA must be non-zero which can be directly seen from nc-AFM images of polyynes exhibiting a clear corrugation along the bond axis with characteristic triple bond features [30–32]. Triple bonds appear as bright ellipsoidal features in nc-AFM images [3, 4, 6, 29–32, 110, 301] and are clearly distinguishable from the homogenous non-corrugated appearance of the cumulene structures.

Experiments with single molecules of species **4**, **5** and **1** adsorbed onto a NaCl(2Ml)/Cu(111) surface show that the ether bond can be broken tip-induced under mild conditions. A bond fission attempt is considered successful if images of the precursor and images of the fragments exist. The fragments have to be unambiguously assigned to chemical structures and the spacing between the different fragments must be large enough.
Tip-induced bond fission was tested on ten individual molecules of species **4** on NaCl(2Ml)/Cu(111). Three of these molecules were solely investigated by STM with metal tips. The remaining seven molecules were additionally investigated by atomically resolved nc-AFM with CO-tips. Seven individual molecules could unambiguously be fragmented. In four cases both phenoxy groups were split off. In two cases only one phenoxy group was split off. In one case one phenoxy group was unambiguously split-off, while the other one was close to the remaining fragment and it could not be deduced from the image if it was still covalently bound. In two cases no bond fission could be deduced. Changes were observable, but the features in the images were positioned too close to each other to deduce a dissociation of the ether bonds. One molecule was picked up in the cleaving process and could not be further investigated. To determine the threshold voltage for bond fission, a $I - V_{\mathrm{b}}$-curve was taken and scans above the molecule were taken in 0.5 V steps. These experiments indicate that the fragmentation usually occurs around 1.5 V. The tunneling current set-point was below 1 pA to 2 pA during the experiments. All successful examples were split with a bias voltage of 1.5 V except two examples which were cleaved with a bias voltage of 1.6 V and 2.0 V.
Tip-induced bond dissociation was tested on 14 individual molecules of species **5** on NaCl(2Ml)/Cu(111). Seven individual molecules of species **5** were investigated by STM

with metal tips and seven individual molecules of species **5** were investigated by atomically resolved nc-AFM with CO-tips. The bare metal tip is reactive and molecules or fragments of the molecules were often picked-up hindering the investigation and leading to a bad resolution of the STM images. In three cases investigated by STM a clear fragmentation was observable. From all of the seven molecules investigated by nc-AFM both phenoxy groups could be cleaved off. In four of these cases an intermediate structure consisting of two fragments could be resolved. The two fragments resembled one split-off phenoxy group and one large fragment with the second phenoxy group still bound to the remaining fragment. However, the structure could not fully be resolved and the resolved features often did not fit to structural models. Therefore, it cannot be deduced unambiguously whether the second phenoxy group was still bound to the remaining fragment or split-off. $I - V_\mathrm{b}$-curves indicate a threshold voltage of about 1.7 V to 1.8 V. The experiments indicating this threshold voltage were all executed with a metal tip. As already mentioned, working with a metal tip was not straightforward for this preparation. Most STM images were taken at a bias voltage of 1 V and at this voltage fragmentation was never observed. All of the successful bond fission attempts were induced by bias voltages between 1.7 V to 2.0 V. The intermediate states were observed after bond dissociation was induced by bias voltages of 1.8 V to 1.9 V. During the experiments the tunneling current set-point was always below 1 pA. Negative bias voltages of up to -2.0 V have been applied with no effect on the respective precursor molecule.

Four individual molecules of species **1** have been investigated. Two of these have been examined by STM with metal tips and two of these by atomically resolved nc-AFM with CO-tips. One of the molecules investigated by STM changed its appearance due to voltage pulses of up to 1.8 V but the resulting features were very close to each other and no fragmentation could be deduced. From the second molecule investigated by STM both phenoxy groups were clearly split off induced by one 1.8 V-scan. A cleaving reaction could be induced by one voltage scan at 1.8 V for both molecules investigated by nc-AFM with CO terminated tips. In one case both phenoxy groups were split-off. This example will be discussed in more detail in this section. In the second case clearly only one phenoxy group was cleaved off. The tunneling current set-point was always below 1 pA. Two $I - V_\mathrm{b}$-curves to 1.6 V on two different molecules showed no effect, while three scans at 1.8 V were unambiguously responsible for bond fission of three different molecules. The bias voltage during STM imaging in the course of the experiment was usually about 1 V. At this bias voltage no bond fission event was observed.

In many cases, the mechanism of tip-induced bond fission reactions on insulating layers can be explained via resonant tunneling into the LUMO, which mediates vibronic excitations resulting in energy dissipation and bond dissociation [30, 50, 370, 371]. These processes demonstrate the lowering of activation energy barriers by accessing decoupled ionic states of the molecules [371]. The here investigated bond fission reaction mechanism is tentatively explained in the same way. Since the species display a low diffusion barrier on the insulating layers and are very mobile on the surface, no detailed differential conductance spectroscopy could be performed. However, the low and distinct threshold voltages to induce bond dissociation and the fact that no bond fission could be induced at negative

bias voltages, tested on species **5**, suggest this cleaving reaction mechanism.

Precursor **4** is investigated on NaCl(2Ml)/Cu(111). The chemical structure of species **4** consists of a dimethyldiacetylene center fragment bridging two phenoxy groups, see figure 4.3.
Figure 4.4 displays the intact precursor **4** (top row) and two fragments after tip induced bond dissociation (bottom row). Different characteristic features of the species are identifiable and are discussed in the following.
Panel 4.4**b** displays the nc-AFM image of the intact precursor **4** on an NaCl bilayer. While most of the conformation of species **4** is locked, rotational freedom exists at the ether bonds and the bonds of the adjacent sp^3-hybridized methyl-carbon atom and different conformations can be found on the surface.
In figure 4.4**b** two crescent shaped features appear, similar to features observed for the nc-AFM images of the Blatter radicals, see section 3.3. These features can be assigned to the tilted phenyl rings, marked with Ph. In the Laplace filtered equivalent of figure 4.4**b**, displayed in figure 4.4**c**, the central hexadiyne unit of the precursor **4** is clearly resolved. The bright ellipsoidal features (marked with T in figure 4.4**c**) are characteristic for triple bonds, as reported in literature [3, 4, 6, 29–32, 110, 301]. Circular bright features (marked with H in figure 4.4**c**) can be assigned to one of the hydrogen atoms of the methyl groups pointing out of the molecular plane towards the vacuum. A model of the precursor is displayed in figure 4.4**a**.

In the example of figure 4.4 a bias voltage of 1.6 V is applied at a tunneling current set-point of 1.8 pA and the tip is scanned over a single molecule of species **4** to induce the cleaving reaction, as opposed to holding the tip at a fixed position above the molecule. This has the effect that not only bond dissociation is reliably induced, but additionally, the fragments are dragged apart, due to interactions with the moving tip. The fragments are thus further separated and can be distinguished clearly.

After the tip-induced bond fission, two fragments could be resolved, which are displayed in figure 4.4**e,f** (**f** is the Laplace filtered version of **e**). A model of the two fragments is shown in figure 4.4**d**. The two fragments in figure 4.4**e**,**f** show the previously assigned distinct features including the tilted phenyl rings (Ph in figure 4.4**e**) and hydrogen atoms protruding out of the surface plane towards the vacuum (H_2 in figure 4.4**f**). The conformation of the upper methyl group and the neighbouring phenoxy group displayed in the model of figure 4.4**d** fits best to the nc-AFM image, resulting in two hydrogen atoms protruding out of the surface plane into the vacuum. The conformation of the lower methylene group displayed in the model of figure 4.4**d** is most conceivable, since the reactive carbon site may be stabilized by an interaction with the surface.
The tilting of the split-off phenyl ring in the upper left corner of figure 4.4**e** impedes the fragment from being fully resolved in the image. The tilting arises from the reactive site being created after bond fission, which can be stabilized by the sodium chloride lattice. Due to the tilting of the phenyl ring, the reactive site is closer to the sodium chloride

lattice. Through analysis and assignment of the structural features of the fragments in the nc-AFM image the bond dissociation can be assigned to the area of the ether group.
Most likely the oxygen is staying at the phenyl group, since charges at the oxygen can then be stabilized by the adjacent aromatic π-system. Depending on the orbital alignment of the split-off phenoxy group with the Fermi level of the sample, different charge states of the fragment are conceivable. However, a conjugated π-system in α-position to the oxygen atom may stabilize a radical site, a negative charge at the oxygen atom, as well as a positive charge at the oxygen atom via resonance [372]. Considering the unknown charge state of the fragment it is named phenoxy fragment in the following referring to the functional group rather than to the charge state of the species.

Species **5** consists of a dimethyltriacetylene chain bridging two phenoxy groups, see figure 4.3. The investigation of species **5** on NaCl(2Ml)/Cu(111) was carried out with the aim to split off both phenoxy groups and to fully resolve the center fragment.

Figure 4.5 displays the fragmentation process of a single molecule of species **5** on NaCl(2Ml)/ Cu(111). Figure 4.5**a-c** display the precursor molecule **5**. A model in panel 4.5**c** illustrates the conformation of the single molecule **5** shown in the nc-AFM image of figure 4.5**a** and its Laplace filtered version in figure 4.5**b**. Similar features as in the nc-AFM image of precursor **4** in figure 4.4**b,c** arise, which can be assigned to the tilted phenyl rings (Ph in figure 4.5**a**), the triple bonds (T in figure 4.5**b**) and the hydrogen atom features (H in figure 4.5**b**). Compared to the nc-AFM image of the precursor **4** in figure 4.4**b,c** in the nc-AFM image of the precursor **5** in figure 4.5**a,b** an additional triple bond feature can be identified.

Bond breaking was achieved by scanning over the molecule with a bias voltage of 1.8 V and 0.35 pA. To induce a change in conformation of the built fragments with the aim to be able to resolve the full structure, the tip was scanned over the surface with the same parameter for a second time.

The image taken after these scans is displayed in figure 4.5**d**. The round bright feature marked with a in figure 4.5**d** is an unknown adsorbate. The two phenoxy groups can be resolved (marked Ph in figure 4.5**d**). The fragment marked with c in figure 4.5**d** consists of an ellipsoidal feature, characteristic for triple bonds, in the center surrounded by two bright lobes, similar to the hydrogen features (H) assigned in figure 4.4**e**. The phenoxy fragment in the lower part of figure 4.5**d** is separated from the other fragments and thus was clearly split off during the bond fission process. A cutout overlaid with a structural model of the phenoxy fragment is displayed in figure 4.5**d**. It is not straightforward to assign a chemical structure to the features in the upper region of figure 4.5**d**.
Panels 4.5**e,f** tentatively depict two different model structures overlaying a cutout of the upper fragment of the nc-AFM image of figure 4.5**d**. In figure 4.5**e** a model of 6-phenoxy-2,4,6-octatriyn-1-ylidyne (**10** in figure 4.5**g**) with adjusted scaling and conformation is overlaid with the nc-AFM cutout. In the model the cleaved site is modelled as a carbon

centred radical with two $\sigma_{\text{C-H}}$ and one $\sigma_{\text{C-C}}$ bond. The phenoxy group and the terminal methylene group do coincide with the respective feature in the nc-AFM image. However, the features of the triple bond and the leftmost hydrogen feature do not coincide with the positions of the respective hydrogens of the model (marked with T and H_2) in figure 4.5**e**. In figure 4.5**f** two separate structure models are overlaid with the nc-AFM cutout, a phenoxyl and a 1,8-dimethylenetriacetylene model (**11** in figure 4.5**g**). If both phenoxy groups are split off homogeneously, two different bond orders are conceivable for the remaining fragment, a biradical structure with three triple bonds (**11**) or a [7]cumulene structure (**12**), see figure 4.5**g**. The model of the biradical species **11** coincides with the features in the image. The ellipsoidal triple bond feature coincides with the central triple bond of the model (marked with T) and the protruding hydrogen features coincide with the terminal methylene hydrogen atoms of the model (marked with H_2) in figure 4.5**f**. The fragment appears slightly too long to fit perfectly with the length of the fragment in the image. If a biradical is adsorbed to a surface it will, if possible, bent towards the surface, so that the two radical sites may interact with the lattice atoms of the surface. For this reason it is not surprising that the gas-phase geometry is slightly protruding the actual nc-AFM feature.
In summary, the features in the upper region of the image in figure 4.5**d** cannot unambiguously be assigned to a chemical species. But the model of species **11** in figure 4.5**g** does fit well to the underlying nc-AFM cutout, suggesting that in this image both phenoxy groups are split off.

Only by scanning the tip over the fragments with a bias voltage of 2.0 V at 0.35 pA, the three fragments were dragged further apart. The result is displayed in figure 4.5**h**. Three separated fragments could be imaged. The insets of figure 4.5**h** show cutouts of the nc-AFM image overlaid with structure models, see subfigure 4.5**i-iii**. The two rightmost ring features in figure 4.5**h** can be assigned to the split-off tilted phenoxy fragments, see insets 4.5**h(ii,iii)** for the overlaid models. The leftmost fragment cannot be assigned straightforwardly. In the inset 4.5**h(i)** the model of species **11** is overlaid with the nc-AFM feature of the rightmost fragment of the nc-AFM image. The length of the fragment in the nc-AFM image does not match the length of the model and no internal resolution of the fragment can be resolved by imaging at closer tip-sample separation distances. This might suggest, that the fragment has changed during the additional 2 V-scan.

At another area of the sample a fragment was found that can clearly be identified as the central chain unit of precursor **5**. The Laplace filtered nc-AFM image of this species is displayed in figure 4.5**k** with a structure model displayed in figure 4.5**l**. Four ellipsoidal features can be discerned in figure 4.5**k** reminiscent of triple bond features (marked with arrows). The two conceivable bond orders for the fragment (**11** and **12**), do not explain the four ellipsoidal features resolved for the fragment in figure 4.5**k**. A way to obtain four triple bonds for the fragment, as opposed to the three triple bonds of species **11**, would be by additional C-H bond dissociation. If one hydrogen atom of each methylene group of the biradical **11** would split off, a bond rearrangement would lead to the formation of

four triple bonds resulting in species **13** (tetraacetylene) depicted in figure 4.5**g**. However, the average bond energy of a $\sigma_{\text{C-H}}$ bond is high (416 kJ/mol [373]). Since effects of the electronegativity of the carbon and the hydrogen atom do only contribute in negligible amount to a $\sigma_{\text{C-H}}$ bond, the bond can generally be considered to have predominantly covalent character. As a result, charging of the species will not lead to a severe lowering of the bond fission energy barrier, such that the energy required to cleave a $\sigma_{\text{C-H}}$ bond is normally too high to be split by the voltages applied here. However, only with a structure fragment similar to species **13** the four triple bond features in figure 4.5**k** can be explained. A possible explanatory approach is to include interactions of the fragment with the salt lattice. It is a well known principle in chemistry that different resonance structures contribute with different weighting to one actual electron density distribution. The resolved bond order in figure 4.5**k** with the four ellipsoidal features could be explained by having significant contribution from the cumulene structure fragment **12** and a structure fragment similar to species **13**. A bond order similar to species **13** without splitting off one hydrogen of each methylene group of the fragment can be achieved by weakening one of the $\sigma_{\text{C-H}}$ bonds of the methylene groups. This is conceivable in the system if an interaction of the respective hydrogen atom with a chloride anion of the lattice is considered. A mixture of this bond order with the cumulene bond order would lead to less pronounced triple bond features because they are only partially contributing and the other contribution, from the cumulene structure fragment **12**, would lead to a homogeneous contrast [25–29] of all the seven double bonds of the fragment in a nc-AFM image.

In the following, precursor **1** is investigated on NaCl(2Ml)/Cu(111). Species **1** consists of a decatetraiyne chain bridging two phenoxy groups, see figure 4.3.
Figure 4.6 displays the fragmentation process of a single molecule of species **1** on NaCl(2Ml)/Cu(111). Figure 4.6**a-c** display the precursor molecule **1**. A model in panel 4.6**a** illustrates the conformation of the single molecule **1** shown in the nc-AFM image (figure 4.6**b**) and its Laplace filtered version (figure 4.6**c**). Similar features as in nc-AFM images of precursor **4** and **5** arise, which can be assigned to the tilted phenyl rings (Ph in figure 4.6**b**), the triple bonds (T in figure 4.6**c**) and the hydrogen atom features (H in figure 4.6**c**).

Bond breaking was induced by scanning over the molecule at a bias voltage of 1.8 V with a tunneling current set point of 0.35 pA. The fragments could not clearly be resolved, see figure 4.7**c**. Hence, the tip was scanned for a second time over the molecule but with a lower bias voltage of 1.5 V at 0.35 pA. The lower bias voltage was sufficient to change the conformation and the position of the fragments. The image taken after these scans is shown in figure 4.6**e** with its Laplace filtered version displayed in panel 4.6**f**. A model is displayed in figure 4.6**d**. A CO molecule lies next to the fragments, marked with CO in figure 4.6**e**. The feature in the upper area of panel 4.6**e** marked with Ph can be clearly assigned to a phenoxy group. However, solely from this image it is not possible to deduce, whether this phenoxy group is covalently connected to the fragment beneath.

The orientation of the two fragments lying in the upper area of figure 4.6**e** is investigated

before and after the 1.5 V-scan. Thereby, it can be validated, whether the two fragments are dissociated or still covalently connected. For species **1** generally no bond fission was observed at bias voltages of 1.5 V or below. The two orientations of the fragments before and after the 1.5 V-scan are displayed in figure 4.7.
The STM image in panel 4.7**a** shows the orientation of the fragments before the 1.5 V-scan, whereas the STM image displayed in panel 4.7**b** illustrates the altered orientation of the large bright fragment after the 1.5 V-scan. The orientation in the STM image shown in figure 4.7**b** corresponds to the nc-AFM image displayed in figure 4.6**e,f**. Figure 4.7**c** is the nc-AFM image corresponding to the orientation shown in the STM image of panel 4.7**a**. Figure 4.7**d** shows the upper fragment of figure 4.7**c** (marked with a dashed rectangle) at a smaller tip-sample separation distance. The fragment displayed in panel 4.7**d** has the characteristic features previously assigned to a split-off tilted phenoxy fragment. The position and orientation of this phenoxy fragment is comparable to the position and orientation it has in the nc-AFM image taken after the 1.5 V-scan, see figures 4.6**e,f**. The same holds true for the CO molecule, compare figure 4.7**c** with figure 4.6**e,f**. The only piece that has changed its position and orientation after the 1.5 V-scan is the one marked in figure 4.7**a-c** with c. The fragment c is separated from the upper phenoxy fragment (Ph) in the nc-AFM image in figure 4.7**c** and hence this phenoxy group can be deduced to be split off. The other phenoxy group is probably close to the fragment c in panel 4.7**c** (marked with Ph). However, the resolution is not good enough to unambiguously assign this feature. From the comparison of the STM images of figure 4.7**a,b**, it can be seen that the fragment c has not changed its appearance and hence most probably also not its chemical structure. It may be assumed that the scan has simply induced a rotation of the fragment. In conclusion, the fragment c can be assumed to remain unchanged in figure 4.7**b** and 4.6**e,f** and the upper phenoxy fragment in these figures can be assumed to be disconnected from the fragment c.

In figure 4.6**f** the internal resolution of fragment c is enhanced. Five ellipsoidal features reminiscent of triple bond features, can be identified (marked with arrows in figure 4.6**f**. This matches to the structural features found for species **5** in figure 4.5**k** and implies a mixture of a [9]cumulene bond order as displayed by species **15** in figure 4.8 with an altering single triple bond order similar to the one of species **16** in figure 4.8. Negligible influence is expected from the bond order of species **14** in figure 4.8, possessing only four triple bonds. On a sodium chloride bilayer the latter bond order can be envisioned by considering a bond weakening of the $\sigma_{\text{C-H}}$ bond at the methylene centres of the molecule by an interaction of the respective hydrogen atoms with chloride anions of the lattice, as already described for the fragment displayed in figure 4.5**k**.

After the detailed investigation of the fragmentation process of the series of species **4**, **5** and **1** on a bilayer of sodium chloride some observations should be consolidated by DFT calculations including the influence of the sodium chloride lattice and the mechanism underlying the tip-induced ether-bond fission. The calculations presented in the following were performed and kindly provided by Dr. Daniel Hernangómez-Pérez in the group of Prof. Dr. Ferdinand Evers from the University of Regensburg.

Figure 4.9 represents the important information deducible from these calculations. Figure 4.9**a** displays the optimized geometry of precursor **5** adsorbed on a NaCl(100) surface from a top and a side view. The oxygen atoms are positioned close to sodium cations of the lattice suggesting an electrostatic interaction with an anchoring effect of these oxygen atoms with the sodium cations.
In the following an additional electron is introduced to the precursor in the calculations, which leads to bond dissociation of one ether bond. The optimized geometry of the singly negatively charged species on the sodium chloride is displayed in figure 4.9**b**. The ether bond is cleaved and the oxygen atom stays at the split-off phenyl group as already postulated. The split-off phenoxy fragment is slightly tilted as can be seen in the side view of figure 4.9**b**. This tilting can be explained by an electrostatic interaction between the oxygen atom of the phenoxy fragment with a sodium cation of the lattice indicated in figure 4.9**b**. The tilting of the split-off phenoxy group is also observed experimentally, as discussed above.
A second electron is added to the precursor in the calculations. Figure 4.9**c** displays the optimized geometry of the doubly negative charged species on sodium chloride. As can be seen in figure 4.9**c** the second phenoxy group is cleaved and the oxygen of this fragment also interacts with a sodium chloride atom of the lattice electrostatically resulting in a tilting of the fragment. Notably, in the top view of figure 4.9**c** one of the hydrogen atoms of each methylene group of the center fragment is closely positioned to a chlorine anion of the lattice. This underlines the hypothesis made above to explain the respective four and five triple bond features observed in figure 4.5**k** and figure 4.6**f**.
The calculations particularly give insight into the reaction mechanism of the cleaving reactions investigated so far. Bond fission was induced by charging the precursor molecule by one or two additional electrons, respectively. This matches the experimental observation that small and distinct threshold bias voltages were required to induce the bond dissociation. Importantly, whole phenoxy groups, including the oxygen atoms, were cleaved off in the fragmentation process of the calculations. This can be rationalized by the enhanced resonance stabilization of the reactive oxygen site in this fragment.

In conclusion, the series of chemical compounds **4**, **5** and **1** was fragmented and examined on thin NaCl bilayers. Low bias voltages were required to reliably split off the phenoxy groups, ranging from approximately 1.5 V for species **4** to approximately 1.8 V to 2.0 V for species **5** and **1** at low tunneling-current set-points of up to approximately 2.0 pA. The bond order of the center fragments after cleaving off both phenoxy groups could be investigated for species **5** and species **1**. Interestingly, the center fragment of species **5** was found in two different forms, one relatable to the chemical structure **11** and one with a bond order assigned to a mixture of the [7]cumulene structure type **12** with a bond order similar to the one of species **13**. For the center fragment of species **1** only one form was found, assigned to a mixture of the bond order of the [9]cumulene structure **15** with a bond order similar to the one of species **16**.

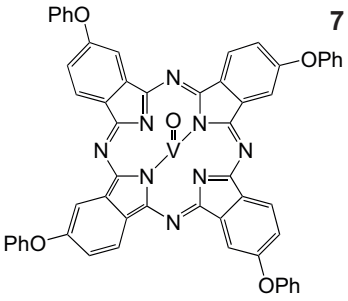

Fig. 4.10. Chemical structure of vanadyl-2,9,16,23-tetraphenoxy-29H,31H-phthalocyanine (**7**)

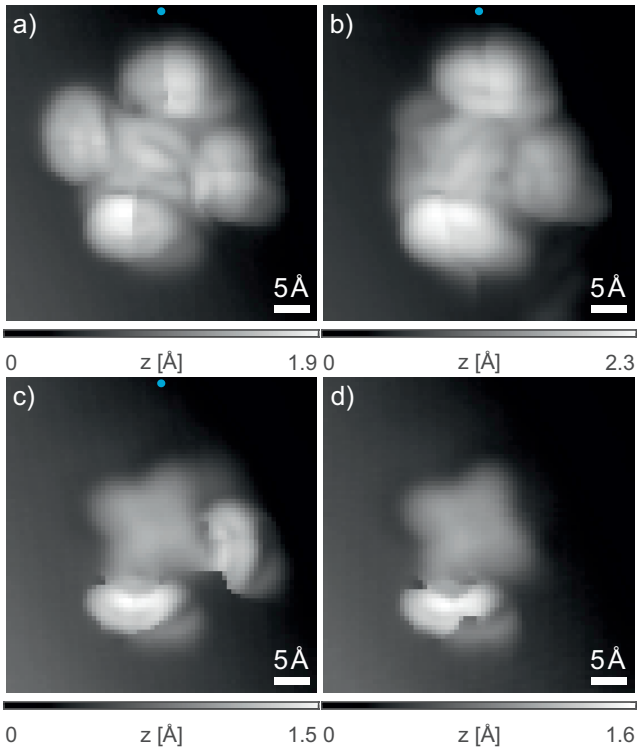

Fig. 4.11. Sequential non-local tip-induced cleaving reaction of vanadyl-2,9,16,23-tetraphenoxy-29H,31H-phthalocyanine (**7**). **(a-d)** Constant-current STM images of a precursor molecule of species **7** and its products of the first, second and third ether-bond dissociation, respectively ($I = 0.8\,\mathrm{pA}$ and $V_\mathrm{b} = 0.8\,\mathrm{V}$). The images were acquired on NaCl(2Ml)/Cu(111) imaged with a metal-tip. The blue dots indicate the position of the tip during the tip-induced cleaving processes. Bond fission was induced by holding the bias voltage for several seconds at 3.0 V (and $I = 10\,\mathrm{pA}$) for the first two splits and at 3.2 V (and $I = 26\,\mathrm{pA}$) for the third bond fission.

4.3 Investigation of a phthalocyanine derivative - A non-locally induced bond fission mechanism

Phthalocyanines (Pc) and the structurally related naphthalocyanines (NPc) are especially well characterized by scanning tunneling and atomic force methods [53–55, 150, 152, 159, 229, 370, 374–379]. Additionally, the structure of these compounds is very different to the series of compounds **4**, **5** and **1**, investigated in section 4.2. For this reason, Pc or NPc derivatives are suitable model compounds to investigate the general applicability of the tip-induced ether-bond dissociation on insulating layers. In the following the chemical compound vanadyl-2,9,16,23-tetraphenoxy-29H,31H-phthalocyanine (**7** in figure 4.10) is investigated on NaCl(2Ml)/Cu(111). The species consists of a vanadyl-phthalocyanine core with four surrounding phenoxy residues. These four phenoxy units can be split off.

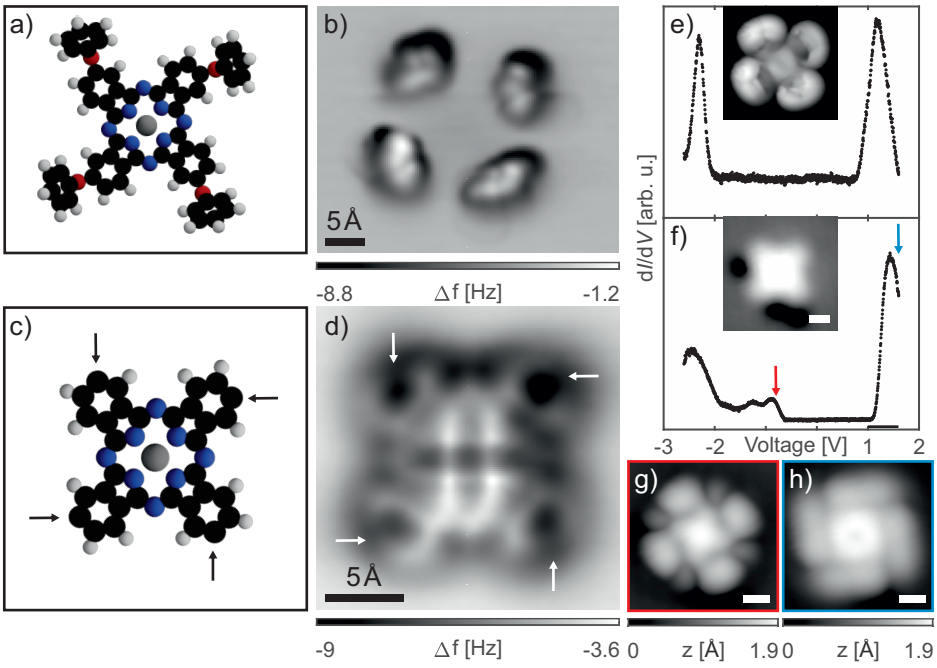

Fig. 4.12. Characterization of the non-locally tip-induced cleaving reaction of the precursor vanadyl-2,9,16,23-tetraphenoxy-29H,31H-phthalocyanine (**7**) and investigation of the reaction product with all four phenyl residues being split off on NaCl(2Ml)/Cu(111). **(a,c)** Model of the precursor **7** (enlarged by 50%) and the cleaving reaction product. **(b,d)** Δf-images in constant-height mode of the precursor **7** and the reaction product with a CO-tip ($\Delta z = -2.4$ Å, STM set-point: $I = 0.6$ pA at $V_\mathrm{b} = 0.8$ V and $\Delta z = 0.2$ Å, STM set-point: $I = 1.0$ pA at $V_\mathrm{b} = 0.8$ V). The cleaving reaction has been achieved by positioning the tip in proximity of the molecule (position not in the area of the images) and applying a bias voltage of 4.5 V at $I = 63$ pA. The arrows in d) point to the darker features of the ring, which might be a result of a lowering of this part of the ring. **(e,f)** $\mathrm{d}I/\mathrm{d}V$-spectrum of the precursor **7** and of the reaction product taken with the metal tip positioned above the center of the molecules with a modulation voltage of $V_\mathrm{mod} = 40\,\mathrm{mV_{pp}}$ and the tip being retracted by Δz = -1.0 Å with respect to the STM set-point (STM set-point for opening the feedback loop: $I = 2.2$ pA and $V_\mathrm{b} = 0.8$ V). The insets display constant-current STM images of a precursor molecule **7** and a reaction product with all four phenoxy units cleaved off. **(g,h)** Orbital imaging of the product with a metal tip ($I = 1.2$ pA at $V_\mathrm{b} = -0.8$ V and 1.6 V, respectively). All scale bars correspond to 5 Å.

Figure 4.11 displays a sequential split series of a single molecule of species **7** on NaCl(2Ml)/ Cu(111) with a metal-tip. Bond-dissociation could be induced non-locally with high bias voltages and tunneling current set-points. Non-locally induced bond dissociation on thin NaCl layers has been observed in literature [30, 31, 371, 380]. The cleaving reaction mechanism is found to be mediated by hot carriers injected from the tip into the NaCl/Cu(111) interface state or for reactions on bare noble metal surfaces by hot carrier injection into the surface state [30, 31, 371, 380–382]. This mechanism is tentatively suggested to be part of the here presented cleaving reaction. The voltages required to induce bond breaking are high, which is why the state responsible for mediating the hot carrier transport is tentatively assigned to an image potential state [383, 384]. Interestingly, tip-induced bond fission was not successful on the bare metal surface. Additionally, no bond dissociation occurred at negative bias voltages of down to -4.5 V at tunneling current set-pints of up to 80 pA. Resonant tunneling into the LUMO orbital of the adsorbates must play a negligible role, as the LUMO energy lies much below the threshold voltage for bond dissociation for species **7**, see figure 4.12**e**.
Figure 4.11**a** displays an STM image of species **7**. The four outer lobes can be assigned to the phenoxy residues. Positioning the tip next to the molecule and holding the bias voltage for several seconds at 3.0 V and 10 pA resulted in the first split with a reduction of four to three outer lobes in the STM image of figure 4.11**b**. Repeating this with the same bias voltage and tunneling current set-point resulted in the second split with two outer lobes visible in the STM image of figure 4.11**c**. For the bond dissociation of the third phenoxy unit a higher bias voltage of 3.2 V (at $I = 26$ pA) was applied for several seconds. In the STM image taken after the third bond fission only one outer lobe is resolved, see figure 4.11**d**. To split off all four phenoxy groups, a bias voltage of 4.5 V at higher tunneling current set-points of around 50 to 100 pA is usually required. An example for a product with all four phenoxy groups cleaved off is displayed in figure 4.12**d,f-h**.

The example of figure 4.11 is illustrative for the non-local bond fission process of species **7**. However, the aim was to cleave-off all phenoxy residues, since these units are bulky and the reaction products with remaining phenoxy groups bound to the phthalocyanine core cannot be resolved fully. To generated the cleaving reaction product with no remaining phenoxy groups in higher yields, higher bias voltages of 4 V to 4.5 V were applied at tunneling current set-point ranging between 50 pA to 100 pA for the other examples. Ten individual molecules were examined before and after a voltage pulse with theses parameters. In all of the ten cases the induced bond fission was successful with one to four phenoxy groups being split off. One molecule had three bound phenoxy groups after the pulse, one molecule had two bound phenoxy groups after the pulse, five molecules had one bound phenoxy group after the pulse and three molecules exhibited no bound phenoxy group after the pulse.

In figure 4.12 the results of the cleaving reaction of an individual precursor of species **7** are summarized. Figure 4.12**b** displays the nc-AFM image of the precursor **7**. A model for the conformation of the molecule **7** of figure 4.12**b** is depicted in panel 4.12**a**. Only fea-

tures assigned to the phenoxy groups protruding out of the surface plane could be resolved in figure 4.12**b**. Compared to the bound phenoxy groups, the central core of the molecule is closer to the surface and cannot be resolved in figure 4.12**b**. The conformation deviates from the gas-phase geometry, but can be rationalized by visualizing an electrostatic interaction between the oxygen atoms of the molecule with sodium cations of the surface. In the conformation fit to the nc-AFM image (model in figure 4.12**a**) all the oxygen atoms are close to the surface, while the phenyl units protrude towards the vacuum.
In figure 4.12**d** the product after cleaving all four phenyl residues is shown. The split-off of all four phenyl groups has been achieved by positioning the tip in proximity of the molecule and applying a bias of 4.5 V at a tunneling current set point of 63 pA. A model for this species is given in figure 4.12**c**. The appearance of this cleaving product displayed in figure 4.12**d** almost completely coincides with the structure of vanadyl-phthalocyanine resolved by nc-AFM in the publication of Kaiser et al. [375] in the adsorption conformation with the oxygen pointing towards the surface. The only difference is a darker contrast at the positions, where formerly the phenoxy units were attached (indicated by arrows in figure 4.12**d**). It is unclear whether the oxygen remained at the center part of the molecule or at the split-off phenyl-rings, but considering the high resonance stabilization by a single phenyl unit it is conceivable that the oxygens are staying at the split-off phenyl groups. Hence, in the following it is assumed that the whole phenoxy group is split off. In this context, the observation that all four outer rings have one site appearing darker than the rest, marked with arrows in figure 4.12**d** can be assigned to reactive unsaturated carbon sites bending down towards the surface to interact stronger with the surface atoms and through this be stabilized.
In this example, the HOMO ($V \approx -2.3\,\mathrm{V}$) and the LUMO ($V \approx 1.2\,\mathrm{V}$) of species **7** could be determined by differential conductance spectroscopic measurements, see figure 4.12**e**. The LUMO clearly lies beneath the threshold voltage for cleaving a phenoxy group (3.0 V to 4.5 V) indicating that the cleaving reaction mechanism is in this case not correlated with electronic and vibronic excitations of the LUMO. However, even though the underlying mechanism changed, the bond fission could be conducted reliably.
A change in the spectrum of the reaction product (figure 4.12**f**) can be observed with orbital resonances closer to the Fermi level than in the spectrum of the precursor (figure 4.12**e**). Orbital imaging reflects the chirality of the product, see figure 4.12**g,h**. The four fold symmetry of the two orbital images, displayed in figure 4.12**g,h**, implies a similar bond order and chemical structure at all four outer phenyl units bearing the reactive unsaturated carbon site.
A reliably tip-induced bond fission of ether bonds on species (**7**), which has no similarities except the phenoxy units to the formerly presented group of compounds **4**, **5** and **1**, is accomplished, demonstrating the general applicability of this bond cleaving process for on-surface synthesis on thin insulating layers.

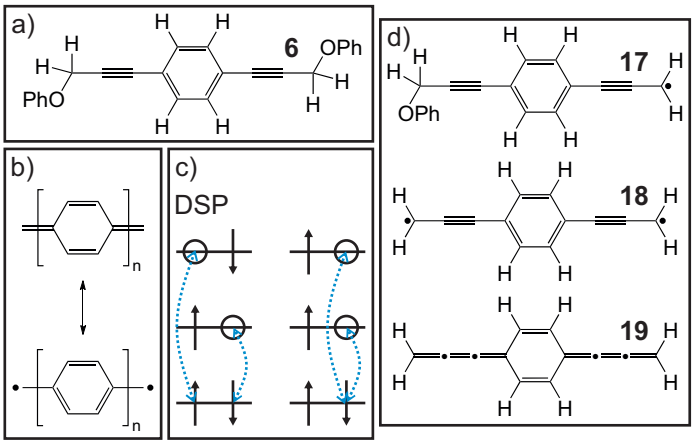

Fig. 4.13. **a)** Chemical structure of the precursor **6**. **b)** model polymer in in its closed-shell quinoidal form (upper structure) or its aromatic open-shell configuration (lower structure). **c)** Scheme of the double spin polarization interaction (DSP) (left) compared to the smaller interaction in a triplet state (right). The level of the states are listed above each other for clarity with no considerations of their energies. **d)** Chemical structures relevant in the fragmentation process of species **6**.

4.4 Investigation of a p-quinodimethane derivative - Non-locally induced bond fission and bond-order analysis

Para-quinodimethane derivatives are interesting compounds with adjustable singlet-triplet gaps [58], which especially find application in materials and compounds for singlet exciton fission [58, 385, 386] or ambipolar charge transfer [58, 387–398].
Tip-induced bond fission is applied to 1,4-bis(3-phenoxyprop-1-yn-1-yl)benzene (**6** in figure 4.13**a**) adsorbed on a bilayer on sodium chloride with the aim to generate the reactive species 3,6-bis(1,2-propadien-1-ylidene)-1,4-cyclohexadiene (**19** in figure 4.13**d**).
Two forms with different bond orders are conceivable for the fragment generated by splitting off two phenoxy groups homogeneously from species **6**. An aromatic biradical form **18** (1,4-bis-(prop-1-yn-1-yl)benzene, figure 4.13**d**) and a closed-shell quinoidal form **19** (3,6-bis(1,2-propadien-1-ylidene)-1,4-cyclohexadiene, figure 4.13**d**). Translating this into the electronic structure of the compound, the question arises whether the generated species will have an open-shell or a closed-shell character, which should be directly detectable with a bond order evaluation by means of nc-AFM [8, 31, 32, 50, 369].
Para-quinodimethane chemical compounds are usually very reactive and can often only be stabilized at low temperatures [58]. Owed to the high reactivity of many of these compounds, they are not fully understood in terms of electronic structure and properties [58]. From this point of view, it is highly interesting to directly resolve a simple model compound of the para-quinodimethane family on a weakly interacting surface to investigate its electronic and related structural properties.
To understand the electronic structure and the resulting properties of para-quinodimethane derivatives a few concepts need to be introduced. In the discussion of the electronic properties of these compounds it is helpful to include the discussion of their BLA and their singlet-triplet gaps. Species **19** has an additional double bond, whereas species **18** has a cyclic aromatic system at the expense of this double bond. This difference in the struc-

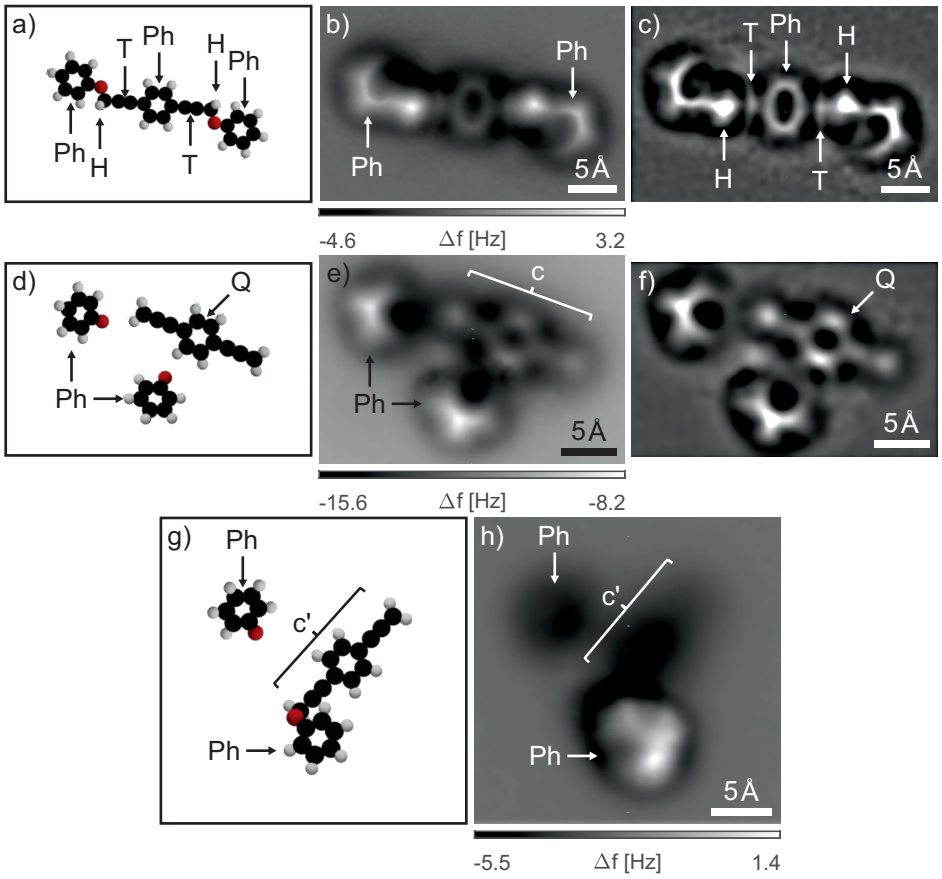

Fig. 4.14. Characterization of the non-locally tip-induced cleaving reaction of 1,4-bis(3-phenoxyprop-1-yn-1-yl)benzene (**6**) on NaCl(2Ml)/Cu(111) by means of nc-AFM with a CO-tip. **(a, d, g)** Model of the precursor **6**, the reaction products after two phenoxy groups were cleaved off and the reaction products after one phenoxy group was cleaved off, respectively. **(b, e, h)** Δf-images in constant-height mode of the precursor **6** and the products of the cleaving reactions ($\Delta z = -0.2\,\text{Å}$, $\Delta z = 0.8\,\text{Å}$ and $\Delta z = -1.0\,\text{Å}$, respectively, STM set-point: $I = 0.5\,\text{pA}$ at $V_\text{b} = 0.9\,\text{V}$). The cleaving reaction was induced by positioning the tip in vicinity of the molecules above the bare NaCl surface and applying a bias voltage of 2.0 V at tunneling current set-points of 50 pA and 10 pA, for splitting off the two phenoxy groups (panel d) to f) and for splitting off one phenoxy group (panel g) and h), respectively. **(c, f)** Laplace filtered versions of b) and e), respectively. A mark can be found at the position of the tilted phenyl rings (Ph), the triple bonds (T), the upward pointing hydrogen atoms (H), the isolated center fragment (c) and the center fragment bound to one phenoxy group (c').

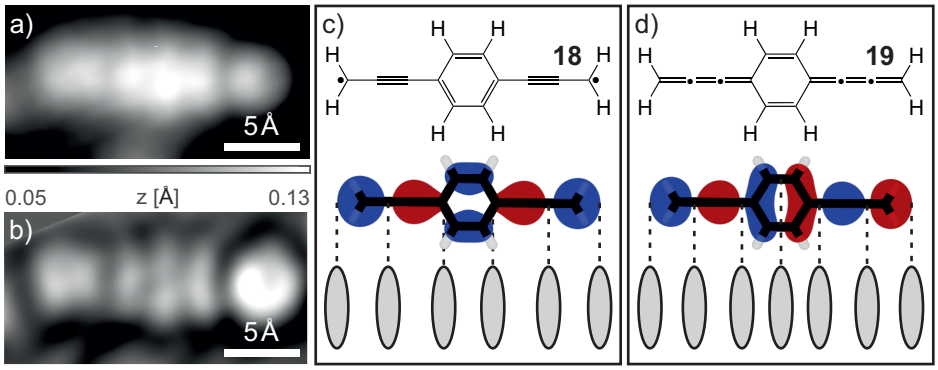

Fig. 4.15. Orbital imaging of the reaction product after cleaving off both phenoxy groups from species **6** on NaCl(2Ml)/Cu(111) with a CO-tip. **a)** Constant-current STM image of the product ($I = 0.5\,\mathrm{pA}$ and $V_\mathrm{b} = 0.9\,\mathrm{V}$). **b)** Laplace filtered version of a). **(c,d)** Calculated gas-phase orbital density visualized as isosurface (isovalue $= 0.02\,\mathrm{e{\cdot}a_0^{-3}}$) of the SUMO of the biradical **18** in a triplet state and the LUMO of the quinoidal form **19**. The grey ellipsoid objects beneath the orbital density isosurfaces indicate positions of features of the lateral gradient of the wave function of the respective orbital.

tures is exemplarily for all compounds of the quinoidal group [58]. There is a competition between net gain of aromaticity and the closed-shell structure of para-quinodimethanes. With the aromatic structure **18** the ambipolar conductance properties can be understood, as aromatic systems may stabilize both, negative and positive charges [58].
For a more detailed understanding a series of model oligo- and polymers consisting of the same structural building block with one quinoidal or aromatic monomer should be envisioned, see figure 4.13**b**. In reality such oligomers or polymers of the same para-quinodimethane group are often heterocyclic and more complex in their structure [58]. A smooth transition from quinoidal to aromatic electronic structure can be observed in terms of the BLA [58] when going from few monomers to a large number of monomers in a polymer similar to the model polymer of figure 4.13**b**. The closing of the singlet-triplet gap is accompanied by a change in BLA [58]. The relation between BLA and singlet-triplet gap can be understood as follows. For oligo- or polymers consisting of an increasing number of repeated quinoidal or aromatic units the spatial separation of the two radicals will grow. This leads to a stepwise reduction in the overlap of the two SOMO orbitals and to a reduced interaction among them. Decisive for the population of a singlet or triplet state is the electron-electron repulsion, which diminishes with growing distance between the two radicals decreasing the singlet-triplet gap [58]. In the borderline case of large seperation distances of the two radicals with no electron-electron repulsion, the single-triplet gap closes [58]. With existing interaction among the two radicals the singlet state will always be lower in energy. However, chemical compounds of the quinoidal group have been synthesized, with small singlet triplet gaps, resulting in a non-negligible population of the triplet state at room temperature [58, 399].
In summary, a smooth transition proceeds with increasing distance among the two radicals,

from two electrons populating one orbital corresponding to the quinoidal structure, to a state best described by two electrons populating two spatially separated SOMO orbitals with antiparallel spin alignment due to non-negligible indirect interaction among them, to a fully separated non-interacting state with both unpaired electrons in two different SOMO orbitals in parallel spin alignment [58].
The interactions in the system with the two unpaired, antiparallel aligned, spatially separated electrons can be described with a double spin polarization interaction, also called dynamic spin polarization (DSP) [58]. In this type of interaction, the two electrons of an occupied state can interact with the two holes of the partially occupied SOMOs [58]. If the alignment of the electrons populating the two SOMOs is antiparallel, both electrons of a fully occupied orbital can interact with one hole of one respective SOMO, each, see figure 4.13**c** on the left-hand side. In the triplet state the two radical electrons are parallel aligned, hence only one electron of a fully occupied orbital may interact with the vacancies of the two SOMOs, see figure 4.13**c** on the right-hand side. The stabilization resulting from the DSP is larger compared to a similar stabilization in the triplet state. To picture this process one might envision a delocalization of the interacting electrons towards the vacancies of the two SOMOs [58].
Another factor influencing the electronic structure of para-quinodimethane derivatives are extended π-systems. If a π-system in vicinity to the radical leads to a delocalizing effect towards the termini of the structure and hence enlarges the separation distance between the two radicals, the singlet-triplet gap will decrease [58].

In the following the experiments of 1,4-bis(3-phenoxyprop-1-yn-1-yl)benzene (**6**) on NaCl (2Ml)/Cu(111) are described and discussed. Species **6** is a simple representative of the quinoidal group consisting of a central hexagonal ring and two C_3H_2-chains connected in para-position to the ring, see figure 4.13**a**.

Bond fission could be induced locally and non-locally. Compared to the previous example described in section 4.3, much lower threshold bias voltages of about 1.8 V to 2.0 V with tunneling current set-points of about 10 pA to 50 pA were required for the non-locally tip-induced bond fission of species **6**. Tip-induced bond fission was tested on 22 individual molecules. Seven molecules were examined by STM with metal tips and 15 molecules were investigated by atomically-resolved nc-AFM with CO-tips. In six cases no ether bond dissociation could be unambiguously deduced. The fragments were either not sufficiently separated in the images or the molecule or parts of the molecules were picked-up by the tip. On ten individual molecules both phenoxy groups could be split off. In four of these cases the bond dissociation was induced locally and for the remaining six molecules the split was induced non-locally. One example was found with only one phenoxy group split off by a non-locally applied voltage pulse. Six molecules were found to remain intact without induced bond fission after one applied non-local voltage pulse. $I - V_b$-curves and a scan induced split over a pristine molecule indicate a voltage threshold for bond fission of about 1.8 V to 2.1 V for tunneling current set-points below 1 pA. No bond fission was observed for negative bias voltages down to -2.5 V.

Figure 4.14 illustrates the results of the tip-induced fragmentation process of 1,4-bis(3-phenoxyprop-1-yn-1-yl)benzene (**6**) on NaCl(2Ml)/Cu(111). The precursor molecule **6** is displayed in panel 4.14**b**, with a model displaying the conformation of the single molecule **6** in panel 4.14**a**. The outer features can, similar to previously, be assigned to tilted phenyl rings (Ph in figure 4.14**b**). The central phenyl ring is lying in a planar orientation on the surface and all the bonds of the phenyl ring appear in a similar contrast in the nc-AFM image of panel 4.14**b**. In the Laplace filtered version of figure 4.14**b**, shown in figure 4.14**c** the central phenyl ring feature (Ph, panel 4.14**c**) is even better resolved appearing planar and homogeneous in the contrast of its bonds. Additionally, similar to previous assignments, the two triple bonds and the protruding hydrogen atoms can be assigned (T and H in figure 4.14**c**).
Figure 4.14**d-f** display the cleaving reaction product after splitting off both phenoxy groups from the precursor **6**. Bond fission was induced non-locally with a bias voltage of 2.0 V and a tunneling current set-point of 50 pA. Figure 4.14**d** shows a model of the generated species shown in the nc-AFM image in panel 4.14**e** and in its Laplace filtered version in panel 4.14**f**. The two separated tilted phenyl features are resolved in figure 4.14**e** (marked with Ph) and can be, as previously, assigned to two split-off phenoxy fragments. The center fragment is resolved in figure 4.14**e** (marked with c).
In general, two different forms with differing bond order can be envisioned for this fragment, the aromatic form **18** or the quinoidal form **19**, see figure 4.13**d**. For a general distinction of the aromatic and the quinoidal form, see figure 4.13**b**. A change in appearance of the two central ring features (Ph and Q in figure 4.14**c,f**) is evident. Whereas the central ring (Ph) in figure 4.14**c** looks homogenous in contrast, the contrast of the central ring (Q) of the fragment displayed in figure 4.14**f** is varying. Two sides of the hexagon, corresponding to two C=C-double bonds of the ring, clearly appear brighter than the other sides of the hexagon. This unambiguously matches the bond order of the quinoidal structure **19**. The two C_3H_2-chains substituted in para-position at the ring are resolved with an overall homogenous contrast and brighter features at their termini in figure 4.14**f**. The bright features at the termini have a more symmetrical, spherical appearance and are positioned directly at the ends of the chains and not at the position of a carbon bond, which is why they cannot be assigned to a triple bond feature, see figure 4.14**f**. A change in the contrast deviating from a homogenous appearance at the termini, would be expected for reactive sites at the termini of the fragment. This indicates that the fragment has similarities to the biradical form **18**, whereas the homogenous appearance of the inner parts of the C_3H_2-chains rather indicates a cumulene structure which would be assigned to the quinoidal form **19**.
Different features in the resolved structure of the fragment displayed in figure 4.14**e,f** hint to different structural forms of the fragment. This is an interesting observation directly linking to the chemical perception that resonant structures can rather be seen as borderline cases which only in sum describe the real structure. This example is intriguing, as the two borderline cases significantly vary in their shell structure and may even vary in their multiplicity, see discussion above. The observation may explain the high reactivity and directly

resolves the early on postulated high free valance on the terminal carbon atoms [58, 400]. Figure 4.14**h** displays an example of a single phenoxy group being cleaved off the precursor **6**. Bond fission was induced non-locally with a bias voltage of 2.0 V and a tunneling current set-point of 10 pA. The larger fragment could not be resolved fully, because one phenyl ring is protruding out of the surface plane towards the vacuum. Nc-AFM imaging at smaller tip-sample separation distances than displayed in figure 4.14**h** was not possible. However, two separated fragments could be resolved, one is assigned to the split-off phenoxy group (upmost Ph in figure 4.14**h**) and one is assigned to the remains of the precursor **6** with a tilted protruding phenyl ring (lower Ph in figure 4.14**h**). Models of the fragments are depicted in figure 4.14**g** with the remaining fragment after splitting off one phenoxy group presumably possessing the chemical structure **17** (1-(prop-1-yn-1-yl)-4-(3-phenoxyprop-1-yn-1-yl)benzene, figure 4.13**d**) in the neutral charge state.

Due to the high reactivity of the fragments, STS spectra could only be carried out at retracted tip positions of about $\Delta z = -4.0$ Å at an STM set-point of 0.9 V and 0.5 pA. These spectra were completely flat with only one onset of an orbital resonance around 1.4 V. The fragment with both phenoxy groups split off could be imaged at closer distances, $\Delta z = 0$ Å, and the same STM set-point with a CO-passivated tip. An orbital density could be probed, see figure 4.15**a** and the Laplace filtered version in figure 4.15**b**. Caution needs to be taken, when imaging orbital densities with CO-tips, which posses a mixing of s- and p-wave character [378]. The obtained orbital image can hence be regarded as a mixture of the original orbital density with the lateral gradient of the wave function of the respective orbital [70, 378, 401, 402]. The calculated gas-phase orbital densities of the SUMO of the biradical **18** in a triplet state and the LUMO of the quinoidal form **19** are visualized in figure 4.15**c,d**, respectively. The grey ellipsoid objects beneath the orbital density isosurfaces indicate positions of features of the lateral gradient of the wave function, referred to as lateral gradient scheme in the following. The symmetry of the features in the images of figure 4.15**a,b** resembles the symmetry of the grey objects in figure 4.15**d**. Additionally, the spacing of the inner three features seems to be narrower, than the spacing of the inner features to the two outermost features in figure 4.15**a,b**. This spacing can be reproduced well by the spacing of the lateral gradient scheme of species **19**, see figure 4.15**d**, as opposed to the more equidistant distribution in the lateral gradient scheme of species **18** in figure 4.15**c**. For these reasons, under the assumption of predominantly p-wave character of the tip, the structure in the images of figure 4.15**a,b** is tentatively assigned to the LUMO of the quinoidal structure **19**. However, the SUMO+1 orbital density of species **18** displays exactly the same structure as the LUMO orbital density of species **19**, which is why the assignment cannot be carried out unequivocally.
In conclusion, by non-locally tip-induced bond fission a para-quinodimethane model compound could be generated from species **6** and investigated on thin NaCl bilayers. Resolving the geometrical structure of this newly generated model compound via atomically resolved nc-AFM imaging with a CO-tip revealed details in the bond-order, which can be directly related to the electronic structure and electronic properties of the species. The inner hexagonal ring contrast and the appearance of the connected C_3H_2-chains of the fragment could

be related to the quinoidal form (**19**), whereas bright circular features at the termini of the C_3H_2-chains indicate a reactive site with a structure deviating from the cumulene form. A structure could be resolved by STM at positive bias voltages with a CO-tip, which was tentatively assigned to the LUMO of species **19**.

Chapter 5

Detection of triplet state lifetimes by AFM

The work presented in this chapter has been published in Science.[4] *Parts of the text are identical to the publication. The important theory background is presented in chapter 1, especially in the sections 1.2.4 and 1.2.5.*

The non-equilibrium triplet state excitation plays an important role e.g. in photocatalytic processes in chemistry or biology or in photovoltaics. Via AFM it is possible to directly measure the triplet lifetime of a single molecule on a weakly interacting insulating surface with atomic resolution by employing an all-electronic pump-probe pulse scheme. With this new method the lifetime of out-of-equilibrium electronic states, including triplet states, can be probed. The triplet lifetime quenching of single excited pentacene molecules is investigated for molecular oxygen adsorbed in close proximity to this molecule. Different adsorption geometries involving a single pentacene molecule and one or several oxygen molecules are generated by atomic manipulation with the tip and their varying triplet lifetimes could be probed. By combining atomically resolved nc-AFM imaging with the newly introduced lifetime determination technique the correlation of molecular arrangements with the lifetime of the quenched triplet can be directly investigated. The controlled electrical addressing of excited electronic states of single molecules combined with atomic-scale resolution and manipulation gives access to various unexplored routes including the control and investigation of local spin-spin interactions. A detailed description of the experimental procedure can be found in reference [56] and the corresponding supplementary information (SI).

[4] J. Peng, S. Sokolov, D. Hernangómez-Pérez, F. Evers, L. Gross, J. M. Lupton, J. Repp. 'Atomically resolved single-molecule triplet quenching'. In: *Science* 373 (2021), 452-456.

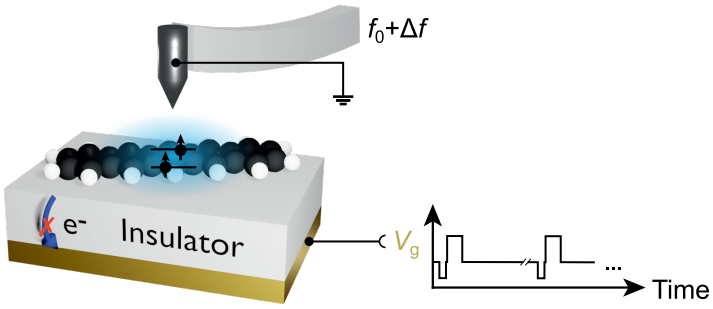

Fig. 5.1. Sketch of the experimental setup for the determination of excited-state lifetimes by AFM. No electrons can tunnel through the thick NaCl layers (insulator) and a tunneling current flow through the metallic substrate is inhibited. A time dependent gate voltage (V_g) is applied inducing a series of single charge exchanges between tip and molecule. Figure is taken from [56].

5.1 Detection principle - The triplet lifetime detection of a pristine individual pentacene molecule

The triplet excited state of individual pentacene molecules is probed on thick insulating layers with the AFM by employing an all-electronic pump-probe pulse scheme. Loth et al. [52] introduced a technique including a pulsing scheme with pump and probe pulse to probe the spin relaxation times of individual atoms by means of STM.
Figures 5.1 and 5.2 visualize the experimental procedure to determine excited-state lifetimes by AFM. Details of this procedure are described in reference [56] and the corresponding SI. The experimental setup is schematically depicted in figure 5.1. A submonolayer amount of pentacene was dosed onto a thick layer (> 20 Ml) NaCl/Au(111) preparation, see sections 2.2 and 1.2.4. The layers were thick enough to prevent the build-up of a tunneling current limiting the tunneling events to single electron exchanges between tip and electronic level of the individual adsorbed pentacene molecules. The charge state of the molecule can be detected with single-electron precision by the AFM, see section 1.2.4. The applied gate voltage, V_g, controls which electronic level of the adsorbate will be addressed, see section 1.2.4 and 1.7. Similar to AC-STM, out-of-equilibrium states of the here investigated individual pentacene molecules adsorbed on NaCl can be populated. Applying a sophisticated pulse scheme and thereby introducing several consecutive single charging events renders access to the triplet excited state population and its lifetime determination.

The time dependent voltage pulse applied to the metal substrate with respect to the conducting tip is displayed in figure 5.2**a**. One measurement cycle can be subdivided in three phases (dashed grey lines of figure 5.2**a-c**. In these three phases the pentacene will adopt two different charge states, the neutral charge state, P^0, and the singly positive charged state, P^+. In the positive charge state the electron configuration corresponds to the doublet ground state, D_0. In the neutral charge state the electron configuration may correspond to the singlet ground state, S_0, or the triplet excited state, T_1. Figure 5.2**b** displays many-body level schemes explaining the processes of the three phases of one measurement cycle. The energetic alignment of the depicted level with respect to each other is

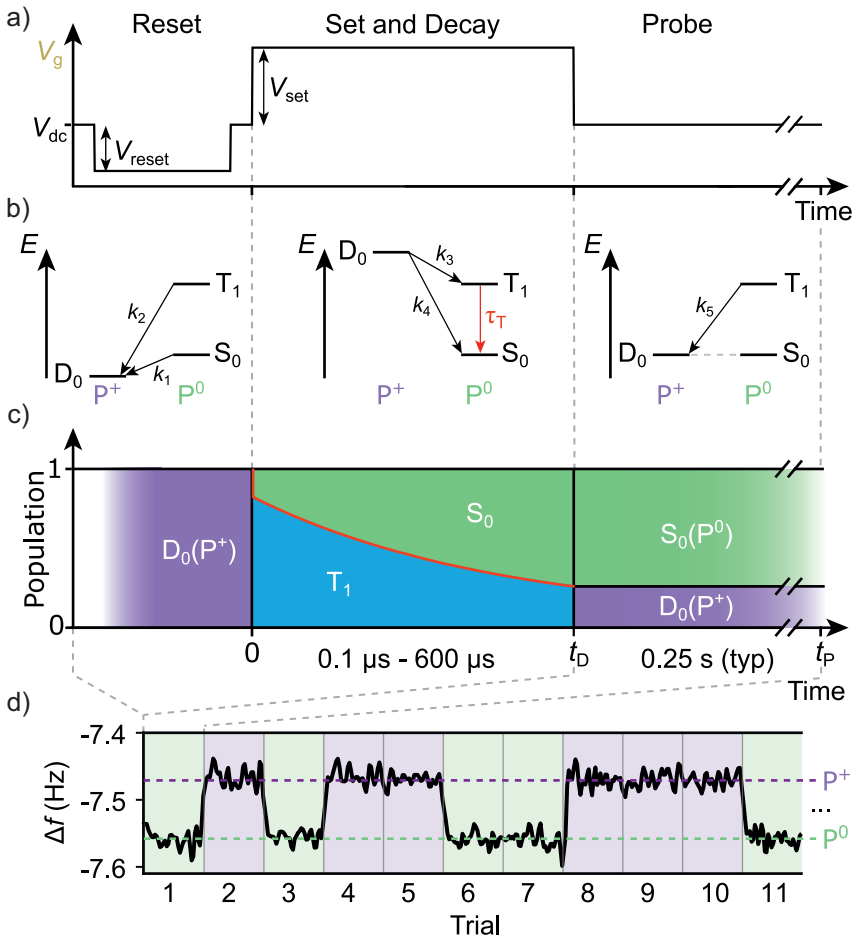

Fig. 5.2. Experimental setup for the determination of excited-state lifetimes by AFM. **a)** Sequence of gate voltages, V_g, which can be categorized in three phases of one measurement cycle (grey dashed lines). $V_{dc} \approx -1.45\,V$ is chosen to render the states S_0 and D_0 degenerate. For this experiment values of $V_{reset} = -1.38\,V$ and $V_{set} = 2.3\,V$ are employed. **b)** Many-body level schemes corresponding to the three phases in the measurement cycle. **c)** Schematic of the time dependent population of the different states in the three measurement phases for several measurement cycles. **d)** An example for an experimental time trace displaying two frequency-shift level corresponding to the two different charge states P^+ and P^0. Each trial segment (1 to 11) can be assigned to one individual measurement trial outcome. Figure is taken from [56].

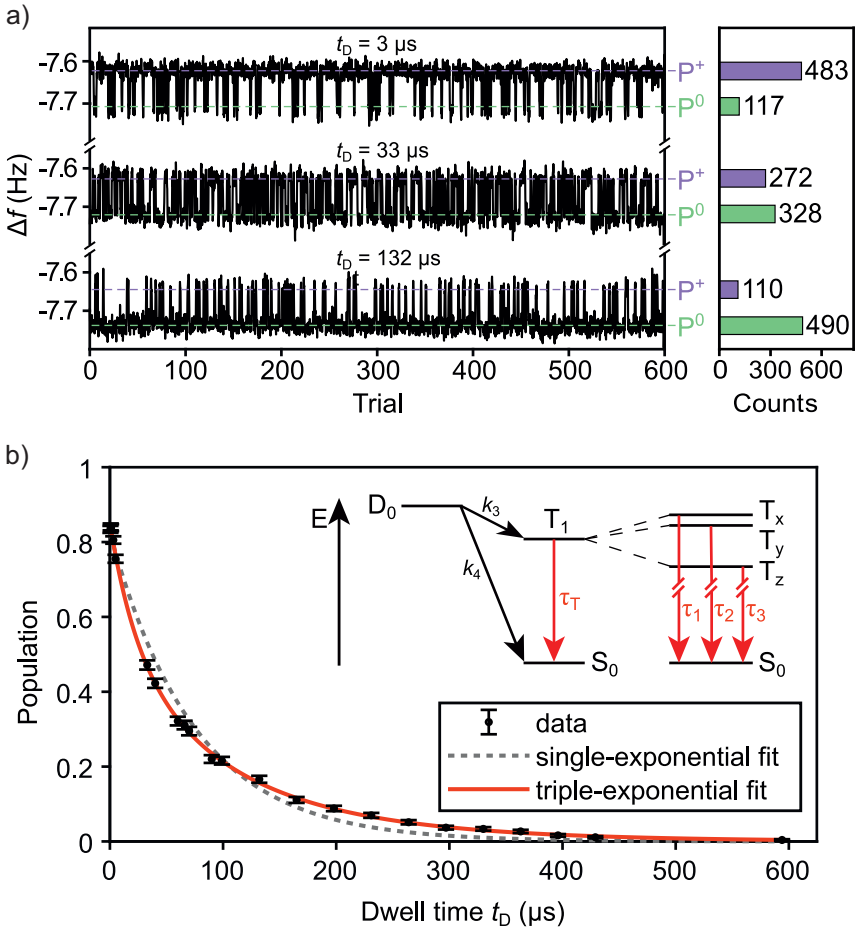

Fig. 5.3. Evaluation of the single molecule triplet lifetime of pentacene. **a)** Δf time traces each consisting of 600 trials with different dwell times t_D. The counts corresponding to the two different charge states P^+ and P^0 are shown on the right-hand side. **b)** Plot of the triplet population $P(t_D)$, obtained from the counts with the binomial distribution function: $N_{P^+}/(N_{P^+} + N_{P^0})$. Extraction of the lifetimes τ_1, τ_2 and τ_3 of the respective three triplet states T_x, T_y and T_z with a triple-exponential decay fit with an equal initial population of all three level, T_x, T_y and T_z (details see SI of reference [56]). Compared to the triple-exponential fit (red), the single-exponential fit (dashed grey) does not coincide well with the experimental data. Each data point corresponds to 1800 individual trials (error bars visualize the standard deviation of the binomial distribution, further information can be found in the SI of reference [56]). The zero-field split of the three states is in the micro-electron volt range and is not drawn to scale in the scheme. Figure is taken from [56].

steered by the gate voltage, see section 1.2.4 and 1.7. For the corresponding single-particle picture see SI of reference [56] and section 1.2.4.
In the first phase, during the reset pulse, V_{reset}, in figure 5.2**a**, D_0 is rapidly occupied by tunneling of one electron from the energetically highest occupied electronic level of the pentacene molecule to electronic states of the tip, ensuring the complete depletion of T_1 and S_0. Schematically this process is depicted in the first many-body level scheme of figure 5.2**b**.
In the second phase, called the set and decay interval, a second voltage pulse, V_{set}, is applied (see figure 5.2**a**). In the very beginning of this pulse the single pentacene molecule accepts a tunneling electron from the tip, resulting in a depletion of the D_0 state and an occupation of the T_1 or the S_0 state, compare with the second many-body level scheme of figure 5.2**b**. A single molecule in the T_1 configuration has time to decay to the S_0 configuration in the dwell time, t_D, following the characteristic triplet lifetime τ_{T}. This dwell time, t_D, is freely adjustable with no relation to the cantilever oscillation frequency and is chosen to span time scales from a small fraction to a large multiple of the excited state lifetime of the investigated molecule. To transfer the pentacene molecule from the D_0 configuration to the T_1 configuration an energetically higher electronic state must be occupied than for the transfer to the S_0 configuration. The energetically higher electronic state experiences a lower remaining tunneling barrier [54] for an electron tunneling from the tip into the molecule. Hence, the charge transfer rate to the T_1 (k_3) state is in general larger than the one to the S_0 state (k_4). The precise ratio of the two transfer rates, k_3 and k_4, can be controlled by adjusting the tip-sample separation distance. The tip-sample separation distance was adjusted to have a tunneling process occurring within the first $\approx 100\,\mathrm{ns}$ of the set and decay interval. For the here employed tip-sample separation distance a population ratio of $P(\mathrm{T}_1)/P(\mathrm{S}_0) = 4/1$ was found. For detailed information see SI of reference [56]. Notably, compared to the duration time t_{D} the charge transfer rates k_3 and k_4 (see figure 5.2**b**) are negligible.
In the last and longest phase the electronic configuration of the single molecule is probed by only transferring the remaining T_1 population to the D_0 state by the tunneling of the electron from the SOMO to the tip, compare with the rightmost many-body level scheme of figure 5.2**b**. The S_0 population is not transferred to the D_0 state. This is accomplished by applying a gate voltage V_{dc} which renders the D_0 and the S_0 state approximately degenerate. Information on the choice of V_{dc} is provided in section 1.2.4 and the SI of reference [56]. Due to the relatively high reorganization energy on NaCl surfaces [53], S_0 and D_0 do not interconvert [53–55, 143]. Summarized this means, the population of S_0 and T_1 are mapped to different charge states ($D_0(P^+)$ and $S_0(P^0)$) during the probe interval and can thus be discriminated with FM-AFM by different values in the frequency-shift [56, 136, 144]. Both ground states ($D_0(P^+)$ and $S_0(P^0)$) are stable on macroscopic time scales and may coexist at the set gate voltage of V_{dc}, which renders a straightforward read-out of the charge state by FM-AFM possible [136, 144]. An example for the experimental read-out of the two discrete Δf-values corresponding to the P^+ and the P^0 charge state is displayed in figure 5.2**d** [56].
In the third phase of one measurement cycle (probe interval in figure 5.2**a**), the probed

single-molecule can only be in one state, more specifically, either in the D_0 or the S_0 state. The described measurement cycle represents one individual Bernoulli trial with two possible outcomes. By repeating the above described measurement cycle multiple times the population $P(t_D)$ of the involved states for one particular dwell time can be obtained. Figure 5.2**c** displays an example of the evolution of the state populations in time summed up over many pulsing cycles. The population of the two states $D_0(P^+)$ and $S_0(P^0)$ is extracted from time traces similar to the one displayed in figure 5.2**d**.

To gain information about the characteristic triplet decay rate the population ratios of $D_0(P^+)$ and $S_0(P^0)$ need to be evaluated for various different dwell times. Three examples for time traces detected with different dwell times are displayed in figure 5.3**a**. The counts of the different charge states (P^+ and P^0) are shown on the right-hand side of figure 5.3**a**. With these counts for different dwell times the population $P(P^+)$, which is reflecting the triplet population, can be plotted as a function of the dwell time, see figure 5.3**b**.
In general, there are three triplet states (T_x, T_y and T_z in figure 5.3**b**, which are non-degenerate considering effects of dipolar or spin-orbit interactions [403, 404]. The zero-field splitting is in the order of micro-electron volts and the lifetimes corresponding to the three different states (τ_1, τ_2 and τ_3 in figure 5.3**b** may differ considerably [403]. Accordingly, the exponential fit of the data shown in the graph of figure 5.3**b** is properly described by a triple-exponential decay function, yielding values of $\tau_1 = 11 \pm 5\,\mu$s, $\tau_2 = 75 \pm 12\,\mu$s and $\tau_3 = 135 \pm 11\,\mu$s. These values were obtained from 23 datasets on several different individual pentacene molecules. Further details are listed in the SI of reference [56]. In optical experiments the initial population of the T_x, T_y and T_z state is not uniform [403]. In contrast, in the here presented experiments the transition rate k_3 (see figure 5.3**b**) is expected to be equal for transitions to T_x, T_y and T_z, since in this process the injected electron has a random spin orientation. The here extracted lifetimes τ_1, τ_2 and τ_3 are comparable to the ones obtained for single pentacene molecules diluted in a host matrix in optical experiments [405, 406] and influences of the AFM tip or the ionic surface can be neglected. Additionally, no appreciable changes in the evaluated triplet decay rates for different tip-sample separation distances ($\Delta z = 1.6\,$Å, $1.2\,$Å and $0.8\,$Å) occur, see SI of reference [56]. Moreover, no variation of the decay rate was found for different lateral tip positions above an individual pentacene molecule, see SI of reference [56].

5.2 Atomically resolved triplet quenching - Individual pentacene molecules in the presence of molecular oxygen

To investigate quenching effects of molecular oxygen on the triplet decay rate of an individual pentacene molecule, O_2 was dosed onto the sample.

Figure 5.4 visualizes the triplet-state quenching for different adsorption geometries (**G1**

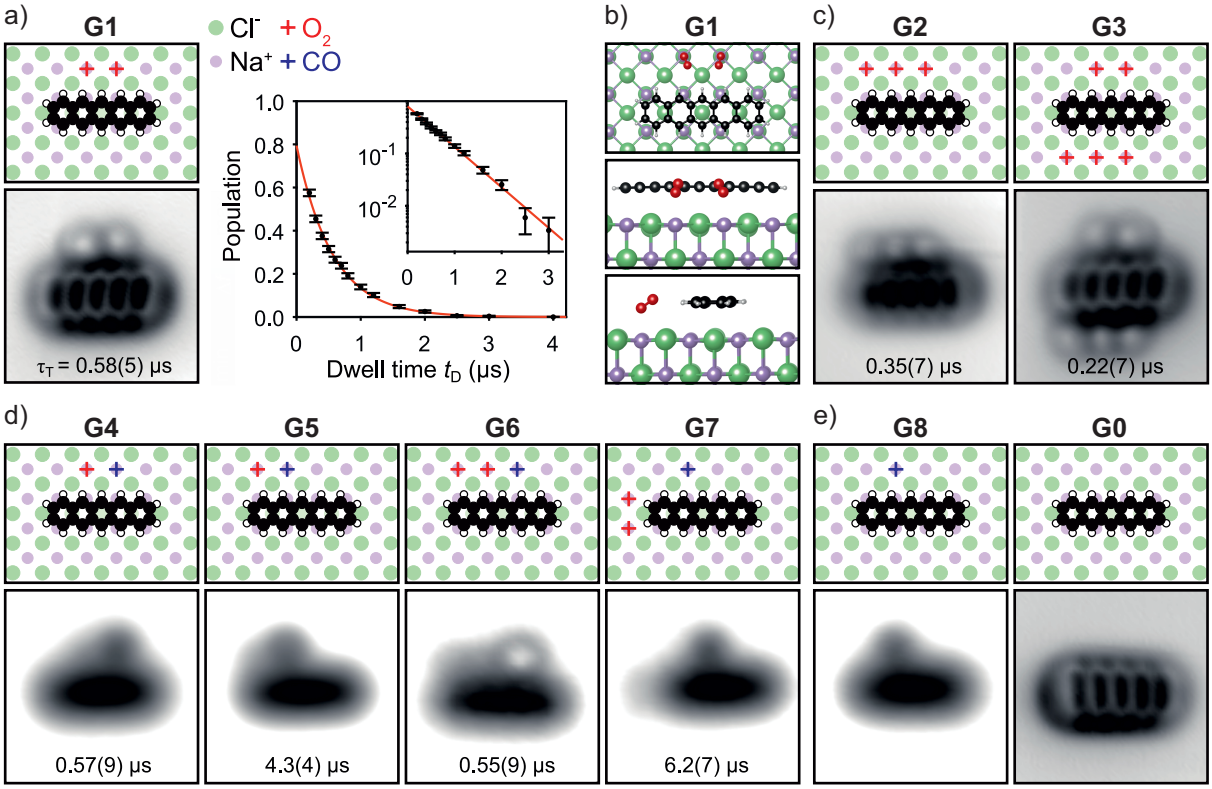

Fig. 5.4. Different atomically resolved adsorption geometries of single pentacene molecules and coadsorbed oxygen molecules and the corresponding lifetimes of the quenched pentacene triplet state. **a)** Δf-image in constant-height mode of geometry **G1** with a model displaying the position of the O_2 molecules and the pentacene molecule with respect to the NaCl lattice. The exponential decay is fitted with a single exponential fit and the error bars display the standard deviation of the binomial distribution, see SI of reference [56]. **b)** Illustration of the adsorption position and conformation of the molecules of **G1** derived by DFT calculations on the basis of the experimental assignment of the adsorption sites of the different species on NaCl. **c)** Decreasing lifetime of the pentacene triplet state with increasing number of surrounding oxygen molecules is exemplarily shown for the case of three (**G2**) or five (**G3**) oxygen molecules close to the pentacene molecule. **d)** Position dependent change of the pentacene triplet lifetime for a given number of surrounding molecular oxygen in different adsorption geometries (compare **G4** and **G5**, or **G6** and **G7**): CO molecules have a stabilizing effect on some adsorption geometries. The tip-sample distance is chosen as close as possible, so that the molecules do not become mobile on the surface. The different tip-sample separation distances result in different attractive and repulsive contributions to the overall resolution of the images. **e)** Experimental results of the triplet lifetimes of a pentacene molecule in geometry **G8** and **G0** in presence and absence of a CO molecule demonstrate that CO molecules do not influence the triplet lifetime of a pentacene molecule. Size of the nc-AFM images: 2.3 nm by 2.3 nm (**G0-G5** and **G8**) and 2.5 nm by 2.5 nm (**G7**). Figure is taken from [56].

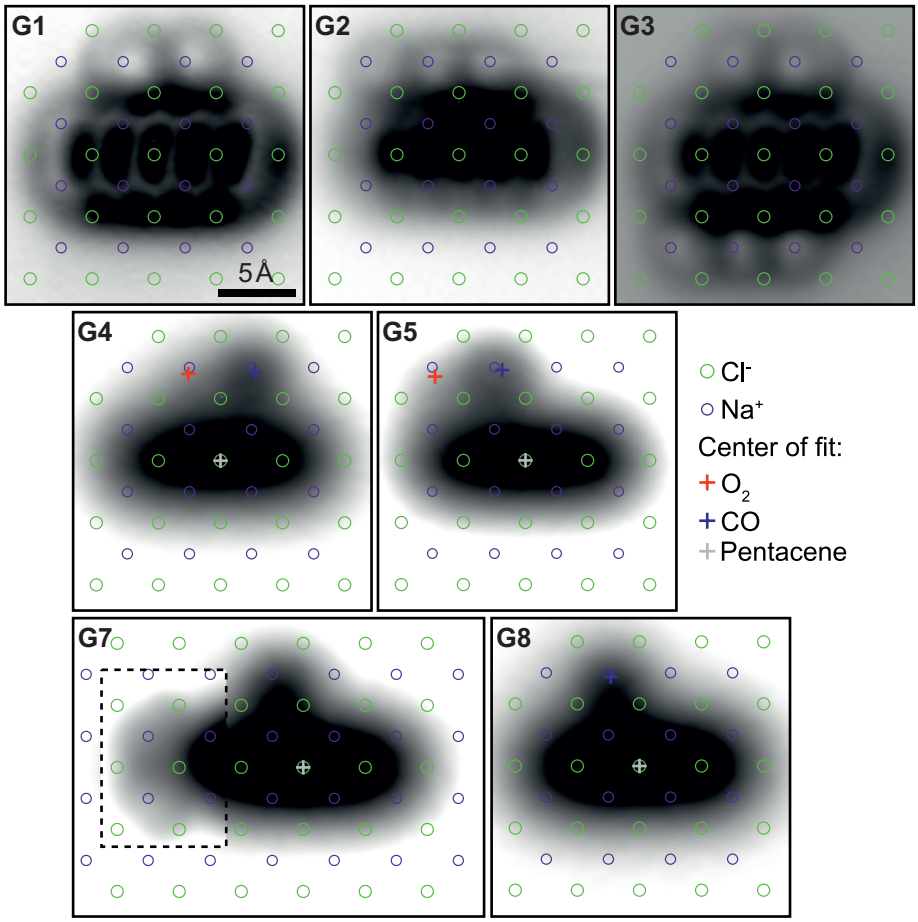

Fig. 5.5. Adsorption site determination of the adsorbed molecular oxygen on NaCl. The adsorption position of an individual pentacene molecule on NaCl is known from literature [122, 407] and was found to be adsorbed with its center on top of a chlorine anion with the long molecular axis aligned with the polar direction of the NaCl surface. The adsorption site and orientation of pentacene on NaCl serves as a reference to include the NaCl lattice (displayed with coloured circles in the images). The crosses indicate center positions of the respective molecules extracted from fits. The inset in the image of **G7** displays an nc-AFM image located at the position indicated in the image with dashed lines at a closer tip-sample separation distance. The O_2 and CO molecules are found to adsorb close to a sodium site of the lattice. The scaling of all images is the same with the corresponding scale bar displayed in the image of the adsorption geometry **G1**. All images are taken from the SI of reference [56].

to **G7**) with atomic resolution in real space. Additional information is given in the SI of reference [56]. Molecular oxygen in its triplet ground state (O_2) is known to quench triplet excited states of other species [408]. After coadsorbing of molecular oxygen onto the sample surface this quenching process could be directly related to the adsorption geometry of the molecular oxygen with respect to a single pentacene molecule.
In panel 5.4**a** an exemplary adsorption geometry **G1** is investigated. In the highly resolved nc-AFM image of figure 5.4**a** taken with a CO terminated tip, a pentacene molecule with two O_2 molecules in close vicinity to its center can be resolved, compare model of the adsorption geometry in figure 5.4**a**. The exponential decay of the triplet population is exemplarily displayed for the adsorption geometry **G1** in figure 5.4**a**. With oxygen in close vicinity to the pentacene molecule the lifetime reduces by approximately two orders of magnitude. Interestingly, in this example the decay of the triplet population is best described with a single exponential fit, see figure 5.4**a**. Suggesting that the triplet decay is dominated by the energy-transfer rate to the molecular oxygen.

Figure 5.5 visualizes the adsorption site determination of molecular oxygen on NaCl based on the experimental results. The adsorption position and orientation of individual pentacene molecules on a NaCl surface is known from literature [122, 407] to adsorb with its center on top of a chlorine anion with the long molecular axis aligned with the polar direction of the NaCl surface. By determination of the center of the resolved pentacene structures in the nc-AFM images, the NaCl lattice could be included in the images (coloured circles in the images of figure 5.5). For the adsorption geometries **G1** to **G3** the position of the NaCl lattice could be adjusted directly by visual determination of the center of the highly resolved pentacene structure. The centres of the pentacene features of the less resolved images was determined by fitting the pentacene feature with a bathtub shape. The center position of this fit is indicated by grey crosses in figure 5.5. In all examples, the O_2 and the CO molecules were found to adsorb close to a sodium site of the lattice. For the examples with larger tip-sample separation distances and lower resolution, where the center of the O_2 and the CO is not easy to identify visually, the corresponding features of the images were fitted with a 2D-Gaussian function. The center determined with these fit functions for the O_2 and the CO molecules are indicated with red and blue crosses, respectively in figure 5.5.

The experimental adsorption site determination was complemented by DFT calculations which confirmed the adsorption of the molecular oxygen on top of sodium sites of the lattice and revealed additional details about the adsorption conformation. Images displaying the results of the simulated adsorption conformation of molecular oxygen on a NaCl surface in vicinity to a pentacene molecule are displayed in figure 5.4**b** for the example of adsorption geometry **G1**. It was found that the O_2 molecule exhibits a pronounced tilting towards the pentacene molecule in the range of 45° to 60°. Additional details to the experimental and theoretical adsorption site and conformation determination can be found in the SI of reference [56].
Notably, the simulations also confirmed that O_2 molecules which are adsorbed on NaCl are

in a triplet ground state, for details see SI of reference [56].
The determination of the triplet population decay is again found to be robust against variations of the tip height, see SI of reference [56].
The lifetime is found to depend on the number of molecular oxygen located directly next to an individual pentacene molecule, as displayed in figure 5.4**c**. Interestingly, a very pronounced difference in the lifetimes of the triplet state population of pentacene was found for the same number of surrounding O_2 molecules located at different adsorption sites, see figure 5.4**d**.
All O_2 molecules in close vicinity of the pentacene molecule could be removed by atomic manipulation, see **G0** in figure 5.4**e**. The average decay time, $\langle k \rangle = \frac{1}{3} \sum_i \tau_i^{-1}$ of the pristine pentacene single molecule measurement without O_2 present on the sample surface was recovered. However, the individual triplet lifetimes τ_1, τ_2 and τ_3, determined from the triple exponential fit, slightly differed. It is very likely that molecular oxygen was adsorbed onto the tip in vicinity of the AFM junction. Notably, the adsorption of O_2 molecules directly at the tip-apex can be excluded, since this would result in a characteristic resolution of the nc-AFM images [115]. Molecular oxygen might for example have adsorbed onto the tip during the dosing procedure or during the tip-manipulation procedures, where O_2 was removed from the vicinity of individual pentacene molecules. Molecular oxygen adsorbed to the tip in vicinity of the AFM junction may create a small dipolar magnetic field [56]. A mixture of the pristine triplet states T_x, T_y and T_z to a new set of three eigenstates can be envisioned in the presence of a magnetic field [56]. This would result in the observed change of lifetimes τ_1, τ_2 and τ_3, whereas the average decay time $\langle k \rangle$ should remain the same. Additional details are discussed in the supplementary text of reference [56].
In a control experiment the presence of a CO molecule adsorbed in the direct vicinity of an individual pentacene molecule was investigated (**G8** in figure 5.4**e**). It was found that CO molecules have no effect on the triplet lifetime of a pentacene molecule and the detected lifetime of **G8** is identical to the one determined for **G0**.

In summary an all-electronic method to detect the lifetime of excited electronic states of single molecules on inert insulating surfaces based on AFM has been presented. The adsorption position dependent strong quenching effects of molecular oxygen in direct vicinity to individual pentacene molecules were detected with atomic-resolution in real-space and could be directly related to single pentacene molecule triplet decay lifetimes.

Chapter 6

Summary and outlook

In this thesis three different topics are treated. All these topics are allocated at the cross-section of physics and chemistry. Questions from the field of chemistry are investigated by physical methods, i.e. by atomic force microscopy (AFM) and scanning tunneling microscopy (STM). The first part of this study addresses a detailed structural and electronic investigation of stable organic Blatter radicals. Due to their atomic composition and the associated low spin-orbit coupling and hyperfine interactions, organic radicals are promising candidates for spintronic applications. The second topic deals with tip-induced ether bond fission of different compounds. In this context, the chemical concept of inducing heterolytic bond fission by charging of species is realized with the STM-tip. With this cleaving mechanism reactive species, such as carbyne model compounds and a p-quinodimethane derivative, could be generated and investigated. In the last section a novel all-electronic AFM-based technique to detect triplet lifetimes is introduced. Using this method, single pentacene triplet lifetimes could be probed and the quenching by closely adsorbed molecular oxygen could be investigated on an atomistic level. All three topics highlight the broad spectrum of AFM/STM applications and its impact on the field of chemistry.

Investigation of the Blatter radical derivatives
Two Blatter radical derivatives were investigated on a Au(111) surface. Distinct features of the substances could be identified by atomically resolved non-contact AFM (nc-AFM) with CO-tips. A narrow zero bias peak could be identified as a Kondo resonance in differential conductance spectra confirming the open-shell character of the adsorbed species. The peak shape correlated with the different units of the molecules. Notably, the Kondo peak vanished over the spin isolated moiety of the single Blatter radicals. Low-bias STM measurements revealed a distinct nodal plane structure corresponding to the SOMO density, via an imaging mechanism which involves the Kondo resonance. The resolution of the probed orbital density was exceptionally high compared to common STM orbital density images on bare metal surfaces. Different assembling schemes of the two compounds were observed for a submonolayer coverage after annealing the sample to room temperature. The differing arrangement of these Blatter radical derivatives on the surface was tentatively explained by the different substitutes at the spin-isolated moiety, suggesting

the possibility of tailoring the assembly while maintaining similar electronic properties, especially the open-shell character.
For spintronic applications it is a prerequisite to immobilize a defined amount of substance on a substrate and contact it with metal electrodes, while, at the same time, maintaining the open-shell character of the compound. Thus, a detailed investigation of the electronic properties and the assembling schemes of the Blatter radical derivatives with respect to the sample coverage, the annealing temperature and the functionalization of the spin-isolated moiety of the radical would be of interest for future spintronic applications.

Tip-induced ether-bond fission
Three carbyne model compounds of different length, a p-quinodimethane derivative and a phthalocyanine derivative were examined on bilayers of NaCl on Cu(111). All of those compounds possess phenoxy groups, which could be split-off reliably by the STM-tip, irrespective of their size and chemical structure. With regard to the structural differences of the different substances under investigation, a general applicability can be suggested. A cleaving reaction mechanism induced by charging the molecules with an electron tunneling from the tip into the lowest occupied molecular orbital (LUMO) was proposed on the basis of the experimental data in combination with DFT calculations. The bond fission mechanism of the phthalocyanine derivative was found to be different. It could be shown that the occupation of the LUMO is not decisive for the bond dissociation. Still, the phenoxy units could be cleaved off reliably.
The bond-order of the products of the carbyne model compounds and the p-quinodimethane derivatives after splitting-off all phenoxy groups from the precursors were investigated by atomically resolved nc-AFM with a CO-tip. For carbyne, a carbon allotrope in an infinite single strand consisting of sp-hybridized carbon atoms, two forms are proposed, linking to two different bond-orders. In one form the carbyne has a cumulene bond-order with metallic properties in the other form it has an alternating single and triple bond-order with semi-conducting properties. Because of these considered differences in the electronic properties, it is intriguing to investigate the bond-order of carbyne model compounds, which possess a similar structure as carbyne but in finite length. P-quinodimethane derivatives may possess small singlet-triplet gaps. This property reflects the competition between two chemical structures with different bond order, an aromatic closed-shell structure and a quinoidal biradical form. Investigation of the bond-order grants direct access to information on these electronic properties. The investigated products exhibited a mixture of the proposed bond-orders, deduced from the chemical resonance structures, illustrating the concept of resonance experimentally for intriguing examples, where the bond-order has considerable impact on important electronic properties of the substance. Interestingly, a long-proposed high free valance on the terminal carbon atoms of the p-quinodimethane product could be directly imaged, underlining the high reactivity of this compound.
Following these results, some starting points for further investigations may be proposed. Experiments on longer representatives of the p-quinodimethane group and the carbyne model compounds would shed light on the trends of the electronic properties with respect to the length of the molecule. Additionally, the mild conditions for bond fission indicate

that by thoroughly engineering the chemical structure of these compounds and by suited selection of the system, the LUMO of the respective compound can be further shifted towards the Fermi level of the sample with the goal to induce spontaneous bond dissociation on the respective surface. Another point might be the formation of longer wires by connecting the reactive center fragments, e.g. via tip-manipulation. Furthermore, it is important to investigate the influence of the electrostatic interaction between the reactive products and the ionic surface. From this perspective, it might be helpful to investigate the substance of interest on different insulating surfaces.

Detection of triplet lifetimes and the effect of oxygen quenching
A new all-electronic method to detect the lifetime of excited electronic states of single molecules on inert insulating surfaces based on AFM has been introduced. The technique has been tested by detecting the triplet decay time of individual pentacene molecules adsorbed onto thick NaCl films ($>$ 20 monolayers) grown on a Au(111) substrate. Single molecule lifetimes are now easily accessible and can be directly related to atomically resolved real-space information enabled through the unique AFM technique.
In this method, a pump-and-probe pulse scheme is applied to a back-gate electrode. By thoroughly gating the sample with this pulse scheme different charging processes can be induced in one measurement cycle. Thereby, an electron can be elevated into an excited electronic state. The outcome of the experiment can be mapped to different charge states. Thus, the population of the different electronic states may be detected by the AFM even if the actual electronic states under investigation have the same charge state. Note that a very critical property of the pump-and-probe pulse scheme is the adjustable dwell time. By adjusting the time between pump and probe pulse different population ratios specific for the respective dwell time can be accessed and the excited state lifetime, here the triplet decay time, can be deduced.
The triplet decay of a pristine single pentacene molecule was best described by a triple exponential fit. A triple exponential fit would be expected, since the three triplet states are generally non-degenerate considering the zero-field splitting evoked by effects of dipolar or spin-orbit interactions. The detected triplet decay times associated with these three triplet states are differing substantially.
The quenching of molecular oxygen adsorbed in close vicinity to the individual pentacene molecules could be investigated. By combining the new technique with atomically resolved nc-AFM imaging with CO-tips, the varying, quenched triplet decay lifetimes could be related to distinct atomically resolved adsorption geometries of the single pentacene and the oxygen molecules. The detected triplet decay lifetimes of individual pentacene molecules in close vicinity to molecular oxygen reduced drastically by almost two orders of magnitude, with the triplet decay being dominated by the energy-transfer rate to the molecular oxygen. The quenching was found to crucially depend on the adsorption geometry of the molecular oxygen with respect to the single pentacene molecule. Different adsorption geometries consisting of one pentacene molecule and one to five oxygen molecules were investigated in the experiments.
In the context of chemical applications, this novel technique has the potential to push

forward into the field of photochemistry and reveal new insights into long-standing fundamental questions of reaction mechanisms involving electronically excited states.

Literature

[1] Hammer, A. *Physikalische Formeln und Tabellen*; Lindauer, 2002.

[2] Gross, L.; Mohn, F.; Moll, N.; Liljeroth, P.; Meyer, G. The Chemical Structure of a Molecule Resolved by Atomic Force Microscopy. *Science* **2009**, *325*, 1110–1114.

[3] de Oteyza, D. G.; Gorman, P.; Chen, Y.-C.; Wickenburg, S.; Riss, A.; Mowbray, D. J.; Etkin, G.; Pedramrazi, Z.; Tsai, H.-Z.; Rubio, A.; Crommie, M. F.; R., F. F. Direct Imaging of Covalent Bond Structure in Single-Molecule Chemical Reactions. *Science* **2013**, *340*, 1434–1437.

[4] Riss, A.; Paz, A. P.; Wickenburg, S.; Tsai, H.-Z.; De Oteyza, D. G.; Bradley, A. J.; Ugeda, M. M.; Gorman, P.; Jung, H. S.; Crommie, M. F.; Rubio, A.; Fischer, F. R. Imaging single-molecule reaction intermediates stabilized by surface dissipation and entropy. *Nat. Chem.* **2016**, *8*, 678–683.

[5] Schuler, B.; Fatayer, S.; Mohn, F.; Moll, N.; Pavliček, N.; Meyer, G.; Peña, D.; Gross, L. Reversible Bergman cyclization by atomic manipulation. *Nat. Chem.* **2016**, *8*, 220–224.

[6] Albrecht, F.; Rey, D.; Fatayer, S.; Schulz, F.; Pérez, D.; Peña, D.; Gross, L. Intramolecular Coupling of Terminal Alkynes by Atom Manipulation. *Angew. Chem. Int. Ed.* **2020**, *59*, 22989–22993.

[7] Mallada, B.; Gallardo, A.; Lamanec, M.; de la Torre, B.; Špirko, V.; Hobza, P.; Jelinek, P. Real-space imaging of anisotropic charge of σ-hole by means of Kelvin probe force microscopy. *Science* **2021**, *374*, 863–867.

[8] Majzik, Z.; Pavliček, N.; Vilas-Varela, M.; Pérez, D.; Moll, N.; Guitián, E.; Meyer, G.; Peña, D.; Gross, L. Studying an antiaromatic polycyclic hydrocarbon adsorbed on different surfaces. *Nat. Commun.* **2018**, *9*, 1198.

[9] Peng, J.; Cao, D.; He, Z.; Guo, J.; Hapala, P.; Ma, R.; Cheng, B.; Chen, J.; Xie, W. J.; Li, X.-Z.; Jelinek, P.; Xu, L.-M.; Gao, Y. Q.; Wang, E.-G.; Jiang, Y. The effect of hydration number on the interfacial transport of sodium ions. *Nature* **2018**, *557*, 701–705.

[10] Krüger, J.; Garcia, F.; Eisenhut, F.; Skidin, D.; Alonso, J. M.; Guitián, E.; Pérez, D.; Cuniberti, G.; Moresco, F.; Peña, D. Decacene: On-Surface Generation. *Angew. Chem. Int. Ed.* **2017**, *56*, 11945–11948.

[11] Zuzak, R.; Dorel, R.; Krawiec, M.; Such, B.; Kolmer, M.; Szymonski, M.; Echavarren, A. M.; Godlewski, S. Nonacene Generated by On-Surface Dehydrogenation. *ACS Nano* **2017**, *11*, 9321–9329.

[12] Urgel, J. I.; Mishra, S.; Hayashi, H.; Wilhelm, J.; Pignedoli, C. A.; Di Giovannantonio, M.; Widmer, R.; Yamashita, M.; Hieda, N.; Ruffieux, P.; Yamada, H.; Fasel, R. On-surface light-induced generation of higher acenes and elucidation of their open-shell character. *Nat. Commun.* **2019**, *10*, 1–9.

[13] Schulz, F.; Garcia, F.; Kaiser, K.; Pérez, D.; Guitián, E.; Gross, L.; Peña, D. Exploring a Route to Cyclic Acenes by On-Surface Synthesis. *Angew. Chem. Int. Ed.* **2019**, *58*, 9038–9042.

[14] Su, J. et al. Atomically precise bottom-up synthesis of π-extended [5]triangulene. *Sci. Adv.* **2019**, *5*, eaav7717.

[15] Mishra, S.; Beyer, D.; Eimre, K.; Liu, J.; Berger, R.; Gröning, O.; Pignedoli, C. A.; Müllen, K.; Fasel, R.; Feng, X.; Ruffieux, P. Synthesis and Characterization of π-Extended Triangulene. *J. Am. Chem. Soc.* **2019**, *141*, 10621–10625.

[16] Mishra, S.; Beyer, D.; Eimre, K.; Ortiz, R.; Fernández-Rossier, J.; Berger, R.; Görning, O.; Pignedoli, C. A.; Fasel, R.; Feng, X.; Ruffieux, P. Collective All-Carbon Magnetism in Triangulene Dimers**. *Angew. Chem. Int. Ed.* **2020**, *59*, 12041–12047.

[17] Shi, L.; Rohringer, P.; Suenaga, K.; Niimi, Y.; Kotakoski, J.; Meyer, J. C.; Peterlik, H.; Wanko, M.; Cahangirov, S.; Rubio, A.; Lapin, Z. J.; Novotny, L.; Ayala, P.; Pichler, T. Confined linear carbon chains as a route to bulk carbyne. *Nat. Mater.* **2016**, *15*, 634–639.

[18] Tykwinski, R. R. Carbyne: The Molecular Approach. *Chem. Rec.* **2015**, *15*, 1060–1074.

[19] A. Januszewski, J.; R. Tykwinski, R. Synthesis and properties of long [n]cumulenes (n $\geq$ 5). *Chem. Soc. Rev.* **2014**, *43*, 3184–3203.

[20] Wendinger, D.; Tykwinski, R. R. Odd [n] cumulenes (n= 3, 5, 7, 9): synthesis, characterization, and reactivity. *Acc. Chem. Res.* **2017**, *50*, 1468–1479.

[21] Milani, A.; Lucotti, A.; Russo, V.; Tommasini, M.; Cataldo, F.; Li Bassi, A.; Casari, C. S. Charge Transfer and Vibrational Structure of sp-Hybridized Carbon Atomic Wires Probed by Surface Enhanced Raman Spectroscopy. *J. Phys. Chem. C* **2011**, *115*, 12836–12843.

[22] Weimer, M.; Hieringer, W.; Sala, F. D.; Görling, A. Electronic and optical properties of functionalized carbon chains with the localized Hartree–Fock and conventional Kohn–Sham methods. *Chem. Phys.* **2005**, *309*, 77–87.

[23] Hoffmann, R. Extended Hückel theory—V: Cumulenes, polyenes, polyacetylenes and Cn. *Tetrahedron* **1966**, *22*, 521–538.

[24] Nori-Shargh, D.; Deyhimi, F.; Boggs, J. E.; Jameh-Bozorghi, S.; Shakibazadeh, R. DFT study and NBO analysis of the mutual interconversion of cumulene compounds. *J. Phys. Org. Chem.* **2007**, *20*, 355–364.

[25] Urgel, J. I. et al. On-Surface Synthesis of Cumulene-Containing Polymers via Two-Step Dehalogenative Homocoupling of Dibromomethylene-Functionalized Tribenzoazulene. *Angew. Chem. Int. Ed.* **2020**, *132*, 13383–13389.

[26] Sun, Q.; Tran, B. V.; Cai, L.; Ma, H.; Yu, X.; Yuan, C.; Stöhr, M.; Xu, W. On-Surface Formation of Cumulene by Dehalogenative Homocoupling of Alkenyl gem-Dibromides. *Angew. Chem. Int. Ed.* **2017**, *129*, 12333–12337.

[27] Cirera, B.; Riss, A.; Mutombo, P.; I. Urgel, J.; Santos, J.; Giovannantonio, M. D.; Widmer, R.; Stolz, S.; Sun, Q.; Bommert, M.; Fasel, R.; Jelinek, P.; Auwärter, W.; Martin, N.; Écija, D. On-surface synthesis of organocopper metallacycles through activation of inner diacetylene moieties. *Chem. Sci.* **2021**, *12*, 12806–12811.

[28] Martin-Fuentes, C.; I. Urgel, J.; Edalatmanesh, S.; Rodriguez-Sánchez, E.; Santos, J.; Mutombo, P.; Biswas, K.; Lauwaet, K.; M. Gallego, J.; Miranda, R.; Jelinek, P.; Martin, N.; Écija, D. Cumulene-like bridged indeno[1,2- b]fluorene π-conjugated polymers synthesized on metal surfaces. *Chem. Commun.* **2021**, *57*, 7545–7548.

[29] Cirera, B.; Sánchez-Grande, A.; de la Torre, B.; Santos, J.; Edalatmanesh, S.; Rodriguez-Sánchez, E.; Lauwaet, K.; Mallada, B.; Zbořil, R.; Miranda, R.; Gröning, O.; Jelinek, P.; Martin, N.; Ecija, D. Tailoring topological order and π-conjugation to engineer quasi-metallic polymers. *Nat. Nanotechnol.* **2020**, *15*, 437–443.

[30] Pavliček, N.; Gawel, P.; Kohn, D. R.; Majzik, Z.; Xiong, Y.; Meyer, G.; Anderson, H. L.; Gross, L. Polyyne formation via skeletal rearrangement induced by atomic manipulation. *Nat. Chem.* **2018**, *10*, 853–858.

[31] Kaiser, K.; Scriven, L. M.; Schulz, F.; Gawel, P.; Gross, L.; Anderson, H. L. An sp-hybridized molecular carbon allotrope, cyclo[18]carbon. *Science* **2019**, *365*, 1299–1301.

[32] Scriven, L. M.; Kaiser, K.; Schulz, F.; Sterling, A. J.; Woltering, S. L.; Gawel, P.; Christensen, K. E.; Anderson, H. L.; Gross, L. Synthesis of Cyclo[18]carbon via Debromination of C18Br6. *J. Am. Chem. Soc.* **2020**, *142*, 12921–12924.

[33] Grill, L.; Dyer, M.; Lafferentz, L.; Persson, M.; Peters, M. V.; Hecht, S. Nano-architectures by covalent assembly of molecular building blocks. *Nat. Nanotechnol.* **2007**, *2*, 687–691.

[34] Cai, J.; Ruffieux, P.; Jaafar, R.; Bieri, M.; Braun, T.; Blankenburg, S.; Muoth, M.; Seitsonen, A. P.; Saleh, M.; Feng, X.; Müllen, K.; Fasel, R. Atomically precise bottom-up fabrication of graphene nanoribbons. *Nature* **2010**, *466*, 470–473.

[35] Lafferentz, L.; Eberhardt, V.; Dri, C.; Africh, C.; Comelli, G.; Esch, F.; Hecht, S.; Grill, L. Controlling on-surface polymerization by hierarchical and substrate-directed growth. *Nat. Chem.* **2012**, *4*, 215–220.

[36] Zhang, Y.-Q.; Kepčija, N.; Kleinschrodt, M.; Diller, K.; Fischer, S.; Papageorgiou, A. C.; Allegretti, F.; Björk, J.; Klyatskaya, S.; Klappenberger, F.; Ruben, M.; Barth, J. V. Homo-coupling of terminal alkynes on a noble metal surface. *Nat. Commun.* **2012**, *3*, 1286.

[37] Ruffieux, P.; Wang, S.; Yang, B.; Sánchez-Sánchez, C.; Liu, J.; Dienel, T.; Talirz, L.; Shinde, P.; Pignedoli, C. A.; Passerone, D.; Dumslaff, T.; Feng, X.; Müllen, K.; Fasel, R. On-surface synthesis of graphene nanoribbons with zigzag edge topology. *Nature* **2016**, *531*, 489–492.

[38] Rizzo, D. J.; Veber, G.; Jiang, J.; McCurdy, R.; Cao, T.; Bronner, C.; Chen, T.; Louie, S. G.; Fischer, F. R.; Crommie, M. F. Inducing metallicity in graphene nanoribbons via zero-mode superlattices. *Science* **2020**, *369*, 1597–1603.

[39] Gröning, O.; Wang, S.; Yao, X.; Pignedoli, C. A.; Barin, G. B.; Daniels, C.; Cupo, A.; Meunier, V.; Feng, X.; Narita, A.; Müllen, K.; Ruffieux, P.; Fasel, R. Engineering of robust topological quantum phases in graphene nanoribbons. *Nature* **2018**, *560*, 209–213.

[40] Rizzo, D. J.; Veber, G.; Cao, T.; Bronner, C.; Chen, T.; Zhao, F.; Rodriguez, H.; Louie, S. G.; Crommie, M. F.; Fischer, F. R. Topological band engineering of graphene nanoribbons. *Nature* **2018**, *560*, 204–208.

[41] Sun, Q.; Yao, X.; Gröning, O.; Eimre, K.; Pignedoli, C. A.; Müllen, K.; Narita, A.; Fasel, R.; Ruffieux, P. Coupled Spin States in Armchair Graphene Nanoribbons with Asymmetric Zigzag Edge Extensions. *Nano Lett.* **2020**, *20*, 6429–6436.

[42] Li, J.; Sanz, S.; Corso, M.; Choi, D. J.; Peña, D.; Frederiksen, T.; Pascual, J. I. Single spin localization and manipulation in graphene open-shell nanostructures. *Nat. Commun.* **2019**, *10*, 200.

[43] Low, J. Z.; Kladnik, G.; Patera, L. L.; Sokolov, S.; Lovat, G.; Kumarasamy, E.; Repp, J.; Campos, L. M.; Cvetko, D.; Morgante, A.; Venkataraman, L. The Environment-Dependent Behavior of the Blatter Radical at the Metal–Molecule Interface. *Nano Lett.* **2019**, *19*, 2543–2548.

[44] Madhavan, V.; Chen, W.; Jamneala, T.; Crommie, M. F.; Wingreen, N. S. Tunneling into a Single Magnetic Atom: Spectroscopic Evidence of the Kondo Resonance. *Science* **1998**, *280*, 567–569.

[45] Li, J.; Schneider, W.-D.; Berndt, R.; Delley, B. Kondo Scattering Observed at a Single Magnetic Impurity. *Phys. Rev. Lett.* **1998**, *80*, 2893–2896.

[46] Mugarza, A.; Krull, C.; Robles, R.; Stepanow, S.; Ceballos, G.; Gambardella, P. Spin coupling and relaxation inside molecule–metal contacts. *Nat. Commun.* **2011**, *2*, 490.

[47] Zhang, Y.-h.; Kahle, S.; Herden, T.; Stroh, C.; Mayor, M.; Schlickum, U.; Ternes, M.; Wahl, P.; Kern, K. Temperature and magnetic field dependence of a Kondo system in the weak coupling regime. *Nat. Commun.* **2013**, *4*, 2110.

[48] Mishra, S.; Catarina, G.; Wu, F.; Ortiz, R.; Jacob, D.; Eimre, K.; Ma, J.; Pignedoli, C. A.; Feng, X.; Ruffieux, P.; Fernandez-Rossier, J.; Fasel, R. Observation of fractional edge excitations in nanographene spin chains. **2021**, arXiv:2105.09102v1 [cond–mat.mes–hall].

[49] Repp, J.; Meyer, G.; Paavilainen, S.; Olsson, F. E.; Persson, M. Scanning Tunneling Spectroscopy of Cl Vacancies in NaCl Films: Strong Electron-Phonon Coupling in Double-Barrier Tunneling Junctions. *Phys. Rev. Lett.* **2005**, *95*, 225503.

[50] Pavliček, N.; Schuler, B.; Collazos, S.; Moll, N.; Pérez, D.; Guitián, E.; Meyer, G.; Peña, D.; Gross, L. On-surface generation and imaging of arynes by atomic force microscopy. *Nat. Chem.* **2015**, *7*, 623–628.

[51] Pavliček, N.; Mistry, A.; Majzik, Z.; Moll, N.; Meyer, G.; Fox, D. J.; Gross, L. Synthesis and characterization of triangulene. *Nat. Nanotechnol.* **2017**, *12*, 308–311.

[52] Loth, S.; Etzkorn, M.; Lutz, C. P.; Eigler, D. M.; Heinrich, A. J. Measurement of Fast Electron Spin Relaxation Times with Atomic Resolution. *Science* **2010**, *329*, 1628–1630.

[53] Fatayer, S.; Schuler, B.; Steurer, W.; Scivetti, I.; Repp, J.; Gross, L.; Persson, M.; Meyer, G. Reorganization energy upon charging a single molecule on an insulator measured by atomic force microscopy. *Nat. Nanotechnol.* **2018**, *13*, 376–380.

[54] Fatayer, S.; Albrecht, F.; Tavernelli, I.; Persson, M.; Moll, N.; Gross, L. Probing Molecular Excited States by Atomic Force Microscopy. *Phys. Rev. Lett.* **2021**, *126*, 176801.

[55] Patera, L. L.; Queck, F.; Scheuerer, P.; Repp, J. Mapping orbital changes upon electron transfer with tunnelling microscopy on insulators. *Nature* **2019**, *566*, 245–248.

[56] Peng, J.; Sokolov, S.; Hernangómez-Pérez, D.; Evers, F.; Gross, L.; Lupton, J. M.; Repp, J. Atomically resolved single-molecule triplet quenching. *Science* **2021**, *373*, 452–456.

[57] Patera, L. L.; Sokolov, S.; Low, J. Z.; Campos, L. M.; Venkataraman, L.; Repp, J. Resolving the Unpaired-Electron Orbital Distribution in a Stable Organic Radical by Kondo Resonance Mapping. *Angew. Chem. Int. Ed.* **2019**, *58*, 11063–11067.

[58] Casado, J. Para-Quinodimethanes: A Unified Review of the Quinoidal-Versus-Aromatic Competition and its Implications. *Top. Curr. Chem.* **2017**, *375*, 73.

[59] Binnig, G.; Rohrer, H.; Gerber, C.; Weibel, E. Tunneling through a controllable vacuum gap. *Appl. Phys. Lett.* **1982**, *40*, 178–180.

[60] Binnig, G.; Rohrer, H.; Gerber, C.; Weibel, E. Surface studies by scanning tunneling microscopy. *Phys. Rev. Lett.* **1982**, *49*, 57–61.

[61] Binnig, G.; Rohrer, H. Scanning tunneling microscopy. *Surf. Sci.* **1983**, *126*, 236–244.

[62] Binnig, G.; Rohrer, H.; Gerber, C.; Weibel, E. 7×7 reconstruction on Si (111) resolved in real space. *Phys. Rev. Lett.* **1983**, *50*, 120–123.

[63] Bardeen, J. Tunnelling from a many-particle point of view. *Phys. Rev. Lett.* **1961**, *6*, 57–59.

[64] Schwabl, F. *Quantenmechanik (QM I): Eine Einführung*, 7th ed.; Springer-Verlag, 2007.

[65] Tersoff, J.; Hamann, D. R. Theory and application for the scanning tunneling microscope. *Phys. Rev. Lett.* **1983**, *50*, 1998–2001.

[66] Tersoff, J.; Hamann, D. R. Theory of the scanning tunneling microscope. *Phys. Rev. B* **1985**, *31*, 805–813.

[67] Bhushan, B., Ed. *Encyclopedia of Nanotechnology*, 2nd ed.; Springer: Dordrecht, 2016.

[68] Lang, N. D. Spectroscopy of single atoms in the scanning tunneling microscope. *Phys. Rev. B* **1986**, *34*, 5947–5950.

[69] Feenstra, R. M. Scanning tunneling spectroscopy. *Surf. Sci.* **1994**, *299*, 965–979.

[70] Chen, C. J. *Introduction to Scanning Tunneling Microscopy*, 2nd ed.; Oxford University Press, 2008.

[71] Repp, J. Rastertunnelmikroskopie und-spektroskopie an Adsorbaten auf Metall-und Isolatoroberflächen. Ph.D. thesis, FU-Berlin, 2002.

[72] Binnig, G.; Quate, C. F.; Gerber, C. Atomic force microscope. *Phys. Rev. Lett.* **1986**, *56*, 930–933.

[73] Binnig, G.; Gerber, C.; Stoll, E.; Albrecht, T. R.; Quate, C. F. Atomic resolution with atomic force microscope. *Europhys. Lett.* **1987**, *3*, 1281–1286.

[74] Albrecht, T. R.; Quate, C. F. Atomic resolution imaging of a nonconductor by atomic force microscopy. *J. Appl. Phys.* **1987**, *62*, 2599–2602.

[75] Meyer, E.; Heinzelmann, H.; Rudin, H.; Güntherodt, H. J. Atomic resolution on LiF (001) by atomic force microscopy. *Z. Phys. B Condens. matter* **1990**, *79*, 3–4.

[76] Meyer, E.; Heinzelmann, H.; Brodbeck, D.; Overney, G.; Overney, R.; Howald, L.; Hug, H.; Jung, T.; Hidber, H. R.; Güntherodt, H. J. Atomic resolution on the surface of LiF (100) by atomic force microscopy. *J. Vac. Sci. Technol. B* **1991**, *9*, 1329–1332.

[77] Meyer, G.; Amer, N. M. Optical-beam-deflection atomic force microscopy: The NaCl (001) surface. *Appl. Phys. Lett.* **1990**, *56*, 2100–2101.

[78] Giessibl, F. J. Advances in atomic force microscopy. *Rev. Mod. Phys.* **2003**, *75*, 949–983.

[79] Giessibl, F. J.; Binnig, G. Investigation of the (001) cleavage plane of potassium bromide with an atomic force microscope at 4.2 K in ultra-high vacuum. *Ultramicroscopy* **1992**, *42*, 281–289.

[80] Ohnesorge, F.; Binnig, G. True atomic resolution by atomic force microscopy through repulsive and attractive forces. *Science* **1993**, *260*, 1451–1456.

[81] Albrecht, T. R.; Grütter, P.; Horne, D.; Rugar, D. Frequency modulation detection using high-Q cantilevers for enhanced force microscope sensitivity. *J. Appl. Phys.* **1991**, *69*, 668–673.

[82] Giessibl, F. J. Atomic resolution of the silicon (111)-(7×7) surface by atomic force microscopy. *Science* **1995**, *267*, 68–71.

[83] Sugawara, Y.; Ohta, M.; Ueyama, H.; Morita, S. Defect motion on an InP (110) surface observed with noncontact atomic force microscopy. *Science* **1995**, *270*, 1646–1648.

[84] Lantz, M. A.; Hug, H. J.; Hoffmann, R.; Schendel, P. J. A. v.; Kappenberger, P.; Martin, S.; Baratoff, A.; Güntherodt, H.-J. Quantitative Measurement of Short-Range Chemical Bonding Forces. *Science* **2001**, *291*, 2580–2583.

[85] Giessibl, F. J. The qPlus sensor, a powerful core for the atomic force microscope. *Rev. Sci. Instrum.* **2019**, *90*, 011101.

[86] Giessibl, F. J. Forces and frequency shifts in atomic-resolution dynamic-force microscopy. *Phys. Rev. B* **1997**, *56*, 16010.

[87] Freund, H.-J.; Wedler, G. *Lehrbuch der Physikalischen Chemie*, 7th ed.; Wiley, 2018.

[88] Tabor, D.; Winterton, R. H. S. The direct measurement of normal and retarded van der Waals forces. *Proc. Math. Phys. Eng. Sci.* **1969**, *312*, 435–450.

[89] Burnham, N. A.; Colton, R. J. Measuring the nanomechanical properties and surface forces of materials using an atomic force microscope. *J. Vac. Sci. Technol. A* **1989**, *7*, 2906–2913.

[90] Giessibl, F. J. High-speed force sensor for force microscopy and profilometry utilizing a quartz tuning fork. *Appl. Phys. Lett.* **1998**, *73*, 3956–3958.

[91] Giessibl, F. J. Atomic resolution on Si(111)-(7×7) by noncontact atomic force microscopy with a force sensor based on a quartz tuning fork. *Appl. Phys. Lett.* **2000**, *76*, 1470–1472.

[92] Giessibl, F. J.; Hembacher, S.; Herz, M.; Schiller, C.; Mannhart, J. Stability considerations and implementation of cantilevers allowing dynamic force microscopy with optimal resolution: the qPlus sensor. *Nanotechnology* **2004**, *15*, 79–86.

[93] Giessibl, F. J.; Bielefeldt, H.; Hembacher, S.; Mannhart, J. Calculation of the optimal imaging parameters for frequency modulation atomic force microscopy. *Appl. Surf. Sci.* **1999**, *140*, 352–357.

[94] Dürig, U. Relations between interaction force and frequency shift in large-amplitude dynamic force microscopy. *Appl. Phys. Lett.* **1999**, *75*, 433–435.

[95] Gotsmann, B.; Anczykowski, B.; Seidel, C.; Fuchs, H. Determination of tip–sample interaction forces from measured dynamic force spectroscopy curves. *Appl. Surf. Sci.* **1999**, *140*, 314–319.

[96] Hölscher, H.; Allers, W.; Schwarz, U. D.; Schwarz, A.; Wiesendanger, R. Determination of Tip-Sample Interaction Potentials by Dynamic Force Spectroscopy. *Phys. Rev. Lett.* **1999**, *83*, 4780–4783.

[97] Dürig, U. Interaction sensing in dynamic force microscopy. *New J. Phys.* **2000**, *2*, 5.

[98] Giessibl, F. J. A direct method to calculate tip–sample forces from frequency shifts in frequency-modulation atomic force microscopy. *Appl. Phys. Lett.* **2000**, *78*, 123–125.

[99] Sader, J. E.; Jarvis, S. P. Accurate formulas for interaction force and energy in frequency modulation force spectroscopy. *Appl. Phys. Lett.* **2004**, *84*, 1801–1803.

[100] Welker, J.; Illek, E.; Giessibl, F. J. Analysis of force-deconvolution methods in frequency-modulation atomic force microscopy. *Beilstein J. Nanotechnol.* **2012**, *3*, 238–248.

[101] Sader, J. E.; Hughes, B. D.; Huber, F.; Giessibl, F. J. Interatomic force laws that corrupt their own measurement. *Nat. Nanotechnol.* **2018**, *13*, 1088–1091.

[102] Lennard-Jones, J. E. Cohesion. *Proc. Phys. Soc. (1926-1948)* **1931**, *43*, 461–482.

[103] Morse, P. M. Diatomic molecules according to the wave mechanics. II. Vibrational levels. *Phys. Rev.* **1929**, *34*, 57–64.

[104] Hamaker, H. C. The London–van der Waals attraction between spherical particles. *physica* **1937**, *4*, 1058–1072.

[105] Haugstad, G. *Atomic Force Microscopy: Understanding Basic Modes and Advanced Applications*; John Wiley & Sons, 2012.

[106] Moll, N.; Gross, L.; Mohn, F.; Curioni, A.; Meyer, G. The mechanisms underlying the enhanced resolution of atomic force microscopy with functionalized tips. *New J. Phys.* **2010**, *12*, 125020.

[107] Bartels, L.; Meyer, G.; Rieder, K.-H.; Velic, D.; Knoesel, E.; Hotzel, A.; Wolf, M.; Ertl, G. Dynamics of Electron-Induced Manipulation of Individual CO Molecules on Cu(111). *Phys. Rev. Lett.* **1998**, *80*, 2004–2007.

[108] Sun, Z.; Boneschanscher, M. P.; Swart, I.; Vanmaekelbergh, D.; Liljeroth, P. Quantitative Atomic Force Microscopy with Carbon Monoxide Terminated Tips. *Phys. Rev. Lett.* **2011**, *106*, 046104.

[109] Hapala, P.; Kichin, G.; Wagner, C.; Tautz, F. S.; Temirov, R.; Jelinek, P. Mechanism of high-resolution STM/AFM imaging with functionalized tips. *Phys. Rev. B* **2014**, *90*, 085421.

[110] Moll, N.; Schuler, B.; Kawai, S.; Xu, F.; Peng, L.; Orita, A.; Otera, J.; Curioni, A.; Neu, M.; Repp, J.; Meyer, G.; Gross, L. Image Distortions of a Partially Fluorinated Hydrocarbon Molecule in Atomic Force Microscopy with Carbon Monoxide Terminated Tips. *Nano Lett.* **2014**, *14*, 6127–6131.

[111] Neu, M.; Moll, N.; Gross, L.; Meyer, G.; Giessibl, F. J.; Repp, J. Image correction for atomic force microscopy images with functionalized tips. *Phys. Rev. B* **2014**, *89*, 205407.

[112] Weymouth, A. J.; Hofmann, T.; Giessibl, F. J. Quantifying Molecular Stiffness and Interaction with Lateral Force Microscopy. *Science* **2014**, *343*, 1120–1122.

[113] Guo, C.-S.; Van Hove, M. A.; Ren, X.; Zhao, Y. High-Resolution Model for Noncontact Atomic Force Microscopy with a Flexible Molecule on the Tip Apex. *J. Phys. Chem. C* **2015**, *119*, 1483–1488.

[114] Mohn, F.; Schuler, B.; Gross, L.; Meyer, G. Different tips for high-resolution atomic force microscopy and scanning tunneling microscopy of single molecules. *Appl. Phys. Lett.* **2013**, *102*, 073109.

[115] Mönig, H.; Hermoso, D. R.; Diaz Arado, O.; Todorović, M.; Timmer, A.; Schüer, S.; Langewisch, G.; Pérez, R.; Fuchs, H. Submolecular Imaging by Noncontact Atomic Force Microscopy with an Oxygen Atom Rigidly Connected to a Metallic Probe. *ACS Nano* **2016**, *10*, 1201–1209.

[116] Kichin, G.; Weiss, C.; Wagner, C.; Tautz, F. S.; Temirov, R. Single Molecule and Single Atom Sensors for Atomic Resolution Imaging of Chemically Complex Surfaces. *J. Am. Chem. Soc.* **2011**, *133*, 16847–16851.

[117] Hapala, P.; Švec, M.; Stetsovych, O.; van der Heijden, N. J.; Ondráček, M.; van der Lit, J.; Mutombo, P.; Swart, I.; Jelinek, P. Mapping the electrostatic force field of single molecules from high-resolution scanning probe images. *Nat. Commun.* **2016**, *7*, 11560.

[118] Zhang, J.; Chen, P.; Yuan, B.; Ji, W.; Cheng, Z.; Qiu, X. Real-Space Identification of Intermolecular Bonding with Atomic Force Microscopy. *Science* **2013**, *342*, 611–614.

[119] Hämäläinen, S. K.; van der Heijden, N.; van der Lit, J.; den Hartog, S.; Liljeroth, P.; Swart, I. Intermolecular Contrast in Atomic Force Microscopy Images without Intermolecular Bonds. *Phys. Rev. Lett.* **2014**, *113*, 186102.

[120] Pavliček, N.; Herranz-Lancho, C.; Fleury, B.; Neu, M.; Niedenführ, J.; Ruben, M.; Repp, J. High-resolution scanning tunneling and atomic force microscopy of stereochemically resolved dibenzo[a,h]thianthrene molecules. *Phys. Status Solidi B* **2013**, *250*, 2424–2430.

[121] Pavliček, N.; Fleury, B.; Neu, M.; Niedenführ, J.; Herranz-Lancho, C.; Ruben, M.; Repp, J. Atomic Force Microscopy Reveals Bistable Configurations of Dibenzo[a,h]thianthrene and their Interconversion Pathway. *Phys. Rev. Lett.* **2012**, *108*, 086101.

[122] Repp, J.; Meyer, G.; Stojković, S. M.; Gourdon, A.; Joachim, C. Molecules on Insulating Films: Scanning-Tunneling Microscopy Imaging of Individual Molecular Orbitals. *Phys. Rev. Lett.* **2005**, *94*, 026803.

[123] Bennewitz, R.; Bammerlin, M.; Guggisberg, M.; Loppacher, C.; Baratoff, A.; Meyer, E.; Güntherodt, H.-J. Aspects of dynamic force microscopy on NaCl/Cu(111): resolution, tip–sample interactions and cantilever oscillation characteristics. *Surf. Interface Anal.* **1999**, *27*, 462–466.

[124] Bennewitz, R.; Barwich, V.; Bammerlin, M.; Loppacher, C.; Guggisberg, M.; Baratoff, A.; Meyer, E.; Güntherodt, H. J. Ultrathin films of NaCl on Cu(111): a LEED and dynamic force microscopy study. *Surf. Sci.* **1999**, *438*, 289–296.

[125] Olsson, F. E.; Persson, M. A density functional study of adsorption of sodium-chloride overlayers on a stepped and a flat copper surface. *Surf. Sci.* **2003**, *540*, 172–184.

[126] Repp, J.; Meyer, G.; Rieder, K.-H. Snell's Law for Surface Electrons: Refraction of an Electron Gas Imaged in Real Space. *Phys. Rev. Lett.* **2004**, *92*, 036803.

[127] Kelvin, L. V. Contact electricity of metals. *Lond. Edinb. Dublin Philos. Mag. J. Sci.* **1898**, *46*, 82–120.

[128] Zisman, W. A. A new method of measuring contact potential differences in metals. *Rev. Sci. Instrum.* **1932**, *3*, 367–370.

[129] Smoluchowski, R. Anisotropy of the electronic work function of metals. *Phys. Rev.* **1941**, *60*, 661–674.

[130] Besocke, K.; Krahl-Urban, B.; Wagner, H. Dipole moments associated with edge atoms; A comparative study on stepped Pt, Au and W surfaces. *Surf. Sci.* **1977**, *68*, 39–46.

[131] Janssens, T.; Castro, G.; Wandelt, K.; Niemantsverdriet, J. Surface potential around potassium promoter atoms on Rh (111) measured with photoemission of adsorbed Xe, Kr, and Ar. *Phys. Rev. B* **1994**, *49*, 14599.

[132] Błaszczyszyn, R.; Błaszczyszyn, M.; Męclewski, R. Work function of the adsorption system of potassium on tungsten. *Surf. Sci.* **1975**, *51*, 396–408.

[133] Weaver, J. M. R.; Abraham, D. W. High resolution atomic force microscopy potentiometry. *J. Vac. Sci. Technol. B* **1991**, *9*, 1559–1561.

[134] Nonnenmacher, M.; O'Boyle, M. P.; Wickramasinghe, H. K. Kelvin probe force microscopy. *Appl. Phys. Lett.* **1991**, *58*, 2921–2923.

[135] Wandelt, K. The local work function: Concept and implications. *Appl. Surf. Sci.* **1997**, *111*, 1–10.

[136] Gross, L.; Mohn, F.; Liljeroth, P.; Repp, J.; Giessibl, F. J.; Meyer, G. Measuring the Charge State of an Adatom with Noncontact Atomic Force Microscopy. *Science* **2009**, *324*, 1428–1431.

[137] Kawai, S.; Glatzel, T.; Hug, H.-J.; Meyer, E. Atomic contact potential variations of Si(111)-7×7 analyzed by Kelvin probe force microscopy. *Nanotechnology* **2010**, *21*, 245704.

[138] Zerweck, U.; Loppacher, C.; Otto, T.; Grafström, S.; Eng, L. M. Accuracy and resolution limits of Kelvin probe force microscopy. *Phys. Rev. B* **2005**, *71*, 125424.

[139] McMurray, H. N.; Williams, G. Probe diameter and probe–specimen distance dependence in the lateral resolution of a scanning Kelvin probe. *J. Appl. Phys.* **2002**, *91*, 1673–1679.

[140] Schuler, B.; Liu, S.-X.; Geng, Y.; Decurtins, S.; Meyer, G.; Gross, L. Contrast Formation in Kelvin Probe Force Microscopy of Single π-Conjugated Molecules. *Nano Lett.* **2014**, *14*, 3342–3346.

[141] Weymouth, A. J.; Wutscher, T.; Welker, J.; Hofmann, T.; Giessibl, F. J. Phantom Force Induced by Tunneling Current: A Characterization on Si(111). *Phys. Rev. Lett.* **2011**, *106*, 226801.

[142] Weymouth, A. J.; Giessibl, F. J. The effect of sample resistivity on Kelvin probe force microscopy. *Appl. Phys. Lett.* **2012**, *101*, 213105.

[143] Steurer, W.; Fatayer, S.; Gross, L.; Meyer, G. Probe-based measurement of lateral single-electron transfer between individual molecules. *Nat. Commun.* **2015**, *6*, 8353.

[144] Schönenberger, C.; Alvarado, S. F. Observation of single charge carriers by force microscopy. *Phys. Rev. Lett.* **1990**, *65*, 3162–3164.

[145] Stomp, R.; Miyahara, Y.; Schaer, S.; Sun, Q.; Guo, H.; Grutter, P.; Studenikin, S.; Poole, P.; Sachrajda, A. Detection of Single-Electron Charging in an Individual InAs Quantum Dot by Noncontact Atomic-Force Microscopy. *Phys. Rev. Lett.* **2005**, *94*, 056802.

[146] Steurer, W.; Repp, J.; Gross, L.; Scivetti, I.; Persson, M.; Meyer, G. Manipulation of the Charge State of Single Au Atoms on Insulating Multilayer Films. *Phys. Rev. Lett.* **2015**, *114*, 036801.

[147] Kocić, N.; Weiderer, P.; Keller, S.; Decurtins, S.; Liu, S.-X.; Repp, J. Periodic Charging of Individual Molecules Coupled to the Motion of an Atomic Force Microscopy Tip. *Nano Lett.* **2015**, *15*, 4406–4411.

[148] Rahe, P.; Steele, R. P.; Williams, C. C. Consecutive Charging of a Molecule-on-Insulator Ensemble Using Single Electron Tunnelling Methods. *Nano Lett.* **2016**, *16*, 911–916.

[149] Fatayer, S.; Albrecht, F.; Zhang, Y.; Urbonas, D.; Peña, D.; Moll, N.; Gross, L. Molecular structure elucidation with charge-state control. *Science* **2019**, *365*, 142–145.

[150] Patera, L. L.; Queck, F.; Scheuerer, P.; Moll, N.; Repp, J. Accessing a Charged Intermediate State Involved in the Excitation of Single Molecules. *Phys. Rev. Lett.* **2019**, *123*, 016001.

[151] Grutter, P. Seeing the charge within. *Nat. Nanotechnol.* **2012**, *7*, 210–211.

[152] Mohn, F.; Gross, L.; Moll, N.; Meyer, G. Imaging the charge distribution within a single molecule. *Nat. Nanotechnol.* **2012**, *7*, 227–231.

[153] Albrecht, F.; Repp, J.; Fleischmann, M.; Scheer, M.; Ondráček, M.; Jelinek, P. Probing Charges on the Atomic Scale by Means of Atomic Force Microscopy. *Phys. Rev. Lett.* **2015**, *115*, 076101.

[154] Rashidi, M.; Vine, W.; Dienel, T.; Livadaru, L.; Retallick, J.; Huff, T.; Walus, K.; Wolkow, R. A. Initiating and Monitoring the Evolution of Single Electrons Within Atom-Defined Structures. *Phys. Rev. Lett.* **2018**, *121*, 166801.

[155] Repp, J.; Meyer, G.; Olsson, F. E.; Persson, M. Controlling the Charge State of Individual Gold Adatoms. *Science* **2004**, *305*, 493–495.

[156] Sterrer, M.; Risse, T.; Martinez Pozzoni, U.; Giordano, L.; Heyde, M.; Rust, H.-P.; Pacchioni, G.; Freund, H.-J. Control of the Charge State of Metal Atoms on Thin MgO Films. *Phys. Rev. Lett.* **2007**, *98*, 096107.

[157] Olsson, F. E.; Paavilainen, S.; Persson, M.; Repp, J.; Meyer, G. Multiple Charge States of Ag Atoms on Ultrathin NaCl Films. *Phys. Rev. Lett.* **2007**, *98*, 176803.

[158] Fernández-Torrente, I.; Franke, K. J.; Pascual, J. I. Vibrational Kondo Effect in Pure Organic Charge-Transfer Assemblies. *Phys. Rev. Lett.* **2008**, *101*, 217203.

[159] Swart, I.; Sonnleitner, T.; Repp, J. Charge State Control of Molecules Reveals Modification of the Tunneling Barrier with Intramolecular Contrast. *Nano Lett.* **2011**, *11*, 1580–1584.

[160] Steurer, W.; Gross, L.; Meyer, G. Local thickness determination of thin insulator films via localized states. *Appl. Phys. Lett.* **2014**, *104*, 231606.

[161] Koch, J.; von Oppen, F. Franck-Condon Blockade and Giant Fano Factors in Transport through Single Molecules. *Phys. Rev. Lett.* **2005**, *94*, 206804.

[162] Helgaker, T.; Jørgensen, P.; Olsen, J. *Molecular Electronic-Structure Theory*; John Wiley & Sons, 2014.

[163] Queck-Scharrer, F. Implementierung der Rastertunnelmikroskopie auf Isolatoren. Ph.D. thesis, Universität Regensburg, 2019.

[164] Cockins, L.; Miyahara, Y.; Bennett, S. D.; Clerk, A. A.; Studenikin, S.; Poole, P.; Sachrajda, A.; Grutter, P. Energy levels of few-electron quantum dots imaged and characterized by atomic force microscopy. *Proc. Natl. Acad. Sci. USA* **2010**, *107*, 9496–9501.

[165] Cockins, L.; Miyahara, Y.; Bennett, S. D.; Clerk, A. A.; Grutter, P. Excited-State Spectroscopy on an Individual Quantum Dot Using Atomic Force Microscopy. *Nano Lett.* **2012**, *12*, 709–713.

[166] Miyahara, Y.; Roy-Gobeil, A.; Grutter, P. Quantum state readout of individual quantum dots by electrostatic force detection. *Nanotechnology* **2017**, *28*, 064001.

[167] Ondráček, M.; Hapala, P.; Jelinek, P. Charge-state dynamics in electrostatic force spectroscopy. *Nanotechnology* **2016**, *27*, 274005.

[168] Münnich, G. Cross-sectional scanning probe microscopy on GaAs: Tip-induced band bending, buried acceptors and adsorbed molecules. Ph.D. thesis, Universität Regensburg, 2014.

[169] Neu, M. Rasterkraftmikroskopie auf atomarer Skala: Van-der-Waals Wechselwirkung in molekularen Systemen. Ph.D. thesis, Universität Regensburg, 2013.

[170] Mishra, S.; Beyer, D.; Eimre, K.; Kezilebieke, S.; Berger, R.; Gröning, O.; Pignedoli, C. A.; Müllen, K.; Liljeroth, P.; Ruffieux, P.; Feng, X.; Fasel, R. Topological frustration induces unconventional magnetism in a nanographene. *Nat. Nanotechnol.* **2020**, *15*, 22–28.

[171] Mateo, L. M.; Sun, Q.; Liu, S.-X.; Bergkamp, J. J.; Eimre, K.; Pignedoli, C. A.; Ruffieux, P.; Decurtins, S.; Bottari, G.; Fasel, R.; Torres, T. On-Surface Synthesis and Characterization of Triply Fused Porphyrin–Graphene Nanoribbon Hybrids. *Angew. Chem. Int. Ed.* **2020**, *59*, 1334–1339.

[172] Sun, Q.; Mateo, L. M.; Robles, R.; Ruffieux, P.; Lorente, N.; Bottari, G.; Torres, T.; Fasel, R. Inducing Open-Shell Character in Porphyrins through Surface-Assisted Phenalenyl π-Extension. *J. Am. Chem. Soc.* **2020**, *142*, 18109–18117.

[173] Mishra, S.; Yao, X.; Chen, Q.; Eimre, K.; Gröning, O.; Ortiz, R.; Di Giovannantonio, M.; Sancho-Garcia, J. C.; Fernández-Rossier, J.; Pignedoli, C. A.; Müllen, K.; Ruffieux, P.; Narita, A.; Fasel, R. Large magnetic exchange coupling in rhombus-shaped nanographenes with zigzag periphery. *Nat. Chem.* **2021**, *13*, 581–586.

[174] Turco, E.; Mishra, S.; Melidonie, J.; Eimre, K.; Obermann, S.; Pignedoli, C. A.; Fasel, R.; Feng, X.; Ruffieux, P. On-Surface Synthesis and Characterization of Supernonazethrene. *J. Phys. Chem. Lett.* **2021**, *12*, 8314–8319.

[175] Preis, T. Electronic characterization of graphene nanoribbons from different perspectives. Ph.D. thesis, Universität Regensburg, 2021.

[176] Bartels, L.; Meyer, G.; Rieder, K.-H. Controlled vertical manipulation of single CO molecules with the scanning tunneling microscope: A route to chemical contrast. *Appl. Phys. Lett.* **1997**, *71*, 213–215.

[177] Swart, I.; Sonnleitner, T.; Niedenführ, J.; Repp, J. Controlled Lateral Manipulation of Molecules on Insulating Films by STM. *Nano Lett.* **2012**, *12*, 1070–1074.

[178] Albrecht, F. Combined STM/AFM with functionalized tips applied to individual molecules: Chemical reactions, geometric structure and charge distribution. Ph.D. thesis, Universität Regensburg, 2017.

[179] Albrecht, F.; Bischoff, F.; Auwärter, W.; Barth, J. V.; Repp, J. Direct Identification and Determination of Conformational Response in Adsorbed Individual Nonplanar Molecular Species Using Noncontact Atomic Force Microscopy. *Nano Lett.* **2016**, *16*, 7703–7709.

[180] Blatter, H. M.; Lukaszewski, H. A new stable free radical. *Tetrahedron Lett.* **1968**, *9*, 2701–2705.

[181] Ternes, M.; Heinrich, A. J.; Schneider, W.-D. Spectroscopic manifestations of the Kondo effect on single adatoms. *J. Phys.: Condens. Matter* **2008**, *21*, 053001.

[182] Madhavan, V.; Chen, W.; Jamneala, T.; Crommie, M. F.; Wingreen, N. S. Local spectroscopy of a Kondo impurity: Co on Au(111). *Phys. Rev. B* **2001**, *64*, 165412.

[183] Meissner, W.; Voigt, B. Messungen mit Hilfe von flüssigem Helium XI Widerstand der reinen Metalle in tiefen Temperaturen. *Ann. Phys.* **1930**, *399*, 892–936.

[184] De Haas, W.; De Boer, J.; Van den Berg, G. The electrical resistance of gold, copper and lead at low temperatures. *Physica* **1934**, *1*, 1115–1124.

[185] Anderson, P. W. Localized magnetic states in metals. *Phys. Rev.* **1961**, *124*, 41–53.

[186] Kondo, J. Resistance minimum in dilute magnetic alloys. *Prog. Theor. Phys.* **1964**, *32*, 37–49.

[187] Kondo, J. Effect of ordinary scattering on exchange scattering from magnetic impurity in metals. *Phys. Rev.* **1968**, *169*, 437–440.

[188] Kouwenhoven, L.; Glazman, L. Revival of the Kondo effect. *Phys. World* **2001**, *14*, 33–38.

[189] Nozières, P. A "Fermi-liquid" description of the Kondo problem at low temperatures. *J. Low Temp. Phys.* **1974**, *17*, 31–42.

[190] Repp, J.; Meyer, G.; Paavilainen, S.; Olsson, F. E.; Persson, M. Imaging Bond Formation Between a Gold Atom and Pentacene on an Insulating Surface. *Science* **2006**, *312*, 1196–1199.

[191] Nagaoka, K.; Jamneala, T.; Grobis, M.; Crommie, M. F. Temperature Dependence of a Single Kondo Impurity. *Phys. Rev. Lett.* **2002**, *88*, 077205.

[192] Fano, U. Effects of configuration interaction on intensities and phase shifts. *Phys. Rev.* **1961**, *124*, 1866–1878.

[193] Gruber, M.; Weismann, A.; Berndt, R. The Kondo resonance line shape in scanning tunnelling spectroscopy: instrumental aspects. *J. Phys.: Condens. Matter* **2018**, *30*, 424001.

[194] Frota, H. O. Shape of the Kondo resonance. *Phys. Rev. B* **1992**, *45*, 1096–1099.

[195] Manoharan, H. C.; Lutz, C. P.; Eigler, D. M. Quantum mirages formed by coherent projection of electronic structure. *Nature* **2000**, *403*, 512–515.

[196] Knorr, N.; Schneider, M. A.; Diekhöner, L.; Wahl, P.; Kern, K. Kondo Effect of Single Co Adatoms on Cu Surfaces. *Phys. Rev. Lett.* **2002**, *88*, 096804.

[197] Ren, J.; Guo, H.; Pan, J.; Zhang, Y. Y.; Wu, X.; Luo, H.-G.; Du, S.; Pantelides, S. T.; Gao, H.-J. Kondo Effect of Cobalt Adatoms on a Graphene Monolayer Controlled by Substrate-Induced Ripples. *Nano Lett.* **2014**, *14*, 4011–4015.

[198] Iancu, V.; Deshpande, A.; Hla, S.-W. Manipulation of the Kondo Effect via Two-Dimensional Molecular Assembly. *Phys. Rev. Lett.* **2006**, *97*, 266603.

[199] Iancu, V.; Deshpande, A.; Hla, S.-W. Manipulating Kondo Temperature via Single Molecule Switching. *Nano Lett.* **2006**, *6*, 820–823.

[200] Li, Y.; Ngo, A. T.; DiLullo, A.; Latt, K. Z.; Kersell, H.; Fisher, B.; Zapol, P.; Ulloa, S. E.; Hla, S.-W. Anomalous Kondo resonance mediated by semiconducting graphene nanoribbons in a molecular heterostructure. *Nat. Commun.* **2017**, *8*, 946.

[201] Brückner, R. *Organic Mechanisms: Reactions, Stereochemistry and Synthesis*; Springer, 2010.

[202] Liu, J.; Isshiki, H.; Katoh, K.; Morita, T.; Breedlove, B., K.; Yamashita, M.; Komeda, T. First Observation of a Kondo Resonance for a Stable Neutral Pure Organic Radical, 1,3,5-Triphenyl-6-oxoverdazyl, Adsorbed on the Au(111) Surface. *J. Am. Chem. Soc.* **2013**, *135*, 651–658.

[203] G. Hicks, R. What's new in stable radical chemistry? *Org. Biomol. Chem.* **2007**, *5*, 1321–1338.

[204] Sanvito, S. Molecular spintronics. *Chem. Soc. Rev.* **2011**, *40*, 3336–3355.

[205] Mas-Torrent, M.; Crivillers, N.; Rovira, C.; Veciana, J. Attaching Persistent Organic Free Radicals to Surfaces: How and Why. *Chem. Rev.* **2012**, *112*, 2506–2527.

[206] Yonekuta, Y.; Susuki, K.; Oyaizu, K.; Honda, K. Battery–Inspired, Nonvolatile, and Rewritable Memory Architecture: a Radical Polymer–Based Organic Device. *J. Am. Chem. Soc.* **2007**, *129*, 14128–14129.

[207] Heimel, G.; Zojer, E.; Romaner, L.; Brédas, J.-L.; Stellacci, F. Doping Molecular Wires. *Nano Lett.* **2009**, *9*, 2559–2564.

[208] Lee, J.; Lee, E.; Kim, S.; Bang, G. S.; Shultz, D. A.; Schmidt, R. D.; Forbes, M. D. E.; Lee, H. Nitronyl Nitroxide Radicals as Organic Memory Elements with Both n- and p-Type Properties. *Angew. Chem. Int. Ed.* **2011**, *50*, 4414–4418.

[209] Yuan, L.; Franco, C.; Crivillers, N.; Mas-Torrent, M.; Cao, L.; Sangeeth, C. S. S.; Rovira, C.; Veciana, J.; Nijhuis, C. A. Chemical control over the energy-level alignment in a two-terminal junction. *Nat. Commun.* **2016**, *7*, 12066.

[210] Warner, M.; Din, S.; Tupitsyn, I. S.; Morley, G. W.; Stoneham, A. M.; Gardener, J. A.; Wu, Z.; Fisher, A. J.; Heutz, S.; Kay, C. W. M.; Aeppli, G. Potential for spin-based information processing in a thin-film molecular semiconductor. *Nature* **2013**, *503*, 504–508.

[211] Bader, K.; Dengler, D.; Lenz, S.; Endeward, B.; Jiang, S.-D.; Neugebauer, P.; van Slageren, J. Room temperature quantum coherence in a potential molecular qubit. *Nat. Commun.* **2014**, *5*, 5304.

[212] Atzori, M.; Tesi, L.; Morra, E.; Chiesa, M.; Sorace, L.; Sessoli, R. Room-Temperature Quantum Coherence and Rabi Oscillations in Vanadyl Phthalocyanine: Toward Multifunctional Molecular Spin Qubits. *J. Am. Chem. Soc.* **2016**, *138*, 2154–2157.

[213] Sugawara, T.; Minamoto, M.; Matsushita, M. M.; Nickels, P.; Komiyama, S. Cotunneling current affected by spin-polarized wire molecules in networked gold nanoparticles. *Phys. Rev. B* **2008**, *77*, 235316.

[214] Hayakawa, R.; Karimi, M. A.; Wolf, J.; Huhn, T.; Zöllner, M. S.; Herrmann, C.; Scheer, E. Large Magnetoresistance in Single-Radical Molecular Junctions. *Nano Lett.* **2016**, *16*, 4960–4967.

[215] Herrmann, C.; Solomon, G. C.; Ratner, M. A. Organic Radicals As Spin Filters. *J. Am. Chem. Soc.* **2010**, *132*, 3682–3684.

[216] McGuire, J.; Miras, H. N.; Donahue, J. P.; Richards, E.; Sproules, S. Ligand Radicals as Modular Organic Electron Spin Qubits. *Chem. Eur. J.* **2018**, *24*, 17598–17605.

[217] McGuire, J.; N. Miras, H.; Richards, E.; Sproules, S. Enabling single qubit addressability in a molecular semiconductor comprising gold-supported organic radicals. *Chem. Sci.* **2019**, *10*, 1483–1491.

[218] Griller, D.; Ingold, K. U. Persistent carbon-centered radicals. *Acc. Chem. Res.* **1976**, *9*, 13–19.

[219] Karan, S. et al. Spin Manipulation by Creation of Single-Molecule Radical Cations. *Phys. Rev. Lett.* **2016**, *116*, 027201.

[220] Choi, T.; Bedwani, S.; Rochefort, A.; Chen, C.-Y.; Epstein, A. J.; Gupta, J. A. A Single Molecule Kondo Switch: Multistability of Tetracyanoethylene on Cu(111). *Nano Lett.* **2010**, *10*, 4175–4180.

[221] Kumar, A.; Banerjee, K.; Dvorak, M.; Schulz, F.; Harju, A.; Rinke, P.; Liljeroth, P. Charge-Transfer-Driven Nonplanar Adsorption of F4TCNQ Molecules on Epitaxial Graphene. *ACS Nano* **2017**, *11*, 4960–4968.

[222] Mas-Torrent, M.; Crivillers, N.; Mugnaini, V.; Ratera, I.; Rovira, C.; Veciana, J. Organic radicals on surfaces: towards molecular spintronics. *J. Mater. Chem.* **2009**, *19*, 1691–1695.

[223] Mugnaini, V.; Calzolari, A.; Ovsyannikov, R.; Vollmer, A.; Gonidec, M.; Alcon, I.; Veciana, J.; Pedio, M. Looking Inside the Perchlorinated Trityl Radical/Metal Spinterface through Spectroscopy. *J. Phys. Chem. Lett.* **2015**, *6*, 2101–2106.

[224] Savu, S.-A.; Biswas, I.; Sorace, L.; Mannini, M.; Rovai, D.; Caneschi, A.; Chassé, T.; Casu, M. B. Nanoscale Assembly of Paramagnetic Organic Radicals on Au(111) Single Crystals. *Chem. Eur. J.* **2013**, *19*, 3445–3450.

[225] Xu, B.; Tao, N. J. Measurement of Single-Molecule Resistance by Repeated Formation of Molecular Junctions. *Science* **2003**, *301*, 1221–1223.

[226] Venkataraman, L.; Klare, J. E.; Tam, I. W.; Nuckolls, C.; Hybertsen, M. S.; Steigerwald, M. L. Single-Molecule Circuits with Well-Defined Molecular Conductance. *Nano Lett.* **2006**, *6*, 458–462.

[227] Frisenda, R.; Gaudenzi, R.; Franco, C.; Mas-Torrent, M.; Rovira, C.; Veciana, J.; Alcon, I.; Bromley, S. T.; Burzuri, E.; van der Zant, H. S. J. Kondo Effect in a Neutral and Stable All Organic Radical Single Molecule Break Junction. *Nano Lett.* **2015**, *15*, 3109–3114.

[228] Bejarano, F.; Olavarria-Contreras, I. J.; Droghetti, A.; Rungger, I.; Rudnev, A.; Gutiérrez, D.; Mas-Torrent, M.; Veciana, J.; van der Zant, H. S. J.; Rovira, C.; Burzuri, E.; Crivillers, N. Robust Organic Radical Molecular Junctions Using Acetylene Terminated Groups for C–Au Bond Formation. *J. Am. Chem. Soc.* **2018**, *140*, 1691–1696.

[229] Zhao, A.; Li, Q.; Chen, L.; Xiang, H.; Wang, W.; Pan, S.; Wang, B.; Xiao, X.; Yang, J.; Hou, J. G.; Zhu, Q. Controlling the Kondo Effect of an Adsorbed Magnetic Ion Through Its Chemical Bonding. *Science* **2005**, *309*, 1542–1544.

[230] Perera, U. G. E.; Kulik, H. J.; Iancu, V.; Dias da Silva, L. G. G. V.; Ulloa, S. E.; Marzari, N.; Hla, S.-W. Spatially Extended Kondo State in Magnetic Molecules Induced by Interfacial Charge Transfer. *Phys. Rev. Lett.* **2010**, *105*, 106601.

[231] Komeda, T.; Isshiki, H.; Liu, J.; Zhang, Y.-F.; Lorente, N.; Katoh, K.; Breedlove, B. K.; Yamashita, M. Observation and electric current control of a local spin in a single-molecule magnet. *Nat. Commun.* **2011**, *2*, 217.

[232] Iancu, V.; Braun, K.-F.; Schouteden, K.; Van Haesendonck, C. Inducing Magnetism in Pure Organic Molecules by Single Magnetic Atom Doping. *Phys. Rev. Lett.* **2014**, *113*, 106102.

[233] Zhou, C.; Shan, H.; Li, B.; Zhao, A.; Wang, B. Engineering hybrid Co-picene structures with variable spin coupling. *Appl. Phys. Lett.* **2016**, *108*, 171601.

[234] Pacchioni, G. E.; Pivetta, M.; Gragnaniello, L.; Donati, F.; Autès, G.; Yazyev, O. V.; Rusponi, S.; Brune, H. Two-Orbital Kondo Screening in a Self-Assembled Metal–Organic Complex. *ACS Nano* **2017**, *11*, 2675–2681.

[235] Knaak, T.; Gruber, M.; Lindström, C.; Bocquet, M.-L.; Heck, J.; Berndt, R. Ligand-Induced Energy Shift and Localization of Kondo Resonances in Cobalt-Based Complexes on Cu(111). *Nano Lett.* **2017**, *17*, 7146–7151.

[236] Fernández-Torrente, I.; Kreikemeyer-Lorenzo, D.; Stróżecka, A.; Franke, K. J.; Pascual, J. I. Gating the Charge State of Single Molecules by Local Electric Fields. *Phys. Rev. Lett.* **2012**, *108*, 036801.

[237] Garnica, M.; Stradi, D.; Barja, S.; Calleja, F.; Diaz, C.; Alcami, M.; Martin, N.; Vázquez de Parga, A. L.; Martin, F.; Miranda, R. Long-range magnetic order in a purely organic 2D layer adsorbed on epitaxial graphene. *Nat. Phys.* **2013**, *9*, 368–374.

[238] Müllegger, S.; Rashidi, M.; Fattinger, M.; Koch, R. Surface-Supported Hydrocarbon π Radicals Show Kondo Behavior. *J. Phys. Chem. C* **2013**, *117*, 5718–5721.

[239] Vranik, R.; Stetsovych, V.; Feigl, S.; Müllegger, S. Stable π-radical 2,2-diphenyl-1-picrylhydrazyl (DPPH) adsorbed at the elbows of 22×3 reconstructed Au(111). *Surf. Sci.* **2020**, *700*, 121676.

[240] Grillo, F.; Mugnaini, V.; Oliveros, M.; Francis, S. M.; Choi, D.-J.; Rastei, M. V.; Limot, L.; Cepek, C.; Pedio, M.; Bromley, S. T.; Richardson, N. V.; Bucher, J.-P.; Veciana, J. Chiral Conformation at a Molecular Level of a Propeller-Like Open-Shell Molecule on Au(111). *J. Phys. Chem. Lett.* **2012**, *3*, 1559–1564.

[241] Grillo, F.; Früchtl, H.; M. Francis, S.; Mugnaini, V.; Oliveros, M.; Veciana, J.; V. Richardson, N. An ordered organic radical adsorbed on a Cu-doped Au(111) surface. *Nanoscale* **2012**, *4*, 6718–6721.

[242] Constantinides, C. P.; Koutentis, P. A.; Krassos, H.; Rawson, J. M.; Tasiopoulos, A. J. Characterization and Magnetic Properties of a "Super Stable" Radical 1,3-Diphenyl-7-trifluoromethyl-1,4-dihydro-1,2,4-benzotriazin-4-yl. *J. Org. Chem.* **2011**, *76*, 2798–2806.

[243] Ji, Y.; Long, L.; Zheng, Y. Recent advances of stable Blatter radicals: synthesis, properties and applications. *Mater. Chem. Front.* **2020**, *4*, 3433–3443.

[244] Neese, F. The ORCA program system. *WIREs Comput. Mol. Sci.* **2012**, *2*, 73–78.

[245] Park, Y. S.; Widawsky, J. R.; Kamenetska, M.; Steigerwald, M. L.; Hybertsen, M. S.; Nuckolls, C.; Venkataraman, L. Frustrated Rotations in Single-Molecule Junctions. *J. Am. Chem. Soc.* **2009**, *131*, 10820–10821.

[246] Kawai, S.; Nishiuchi, T.; Kodama, T.; Spijker, P.; Pawlak, R.; Meier, T.; Tracey, J.; Kubo, T.; Meyer, E.; Foster, A. S. Direct quantitative measurement of the C=O$\cdots$H-C bond by atomic force microscopy. *Sci. Adv.* **2017**, *3*, e1603258.

[247] Soe, W.-H.; Manzano, C.; De Sarkar, A.; Chandrasekhar, N.; Joachim, C. Direct Observation of Molecular Orbitals of Pentacene Physisorbed on Au(111) by Scanning Tunneling Microscope. *Phys. Rev. Lett.* **2009**, *102*, 176102.

[248] Somayajulu, G. On Covalent Bond Length and Bond Order. VIII. *J. Chem. Phys.* **1958**, *28*, 822–824.

[249] de Oteyza, D. G.; Pérez Paz, A.; Chen, Y.-C.; Pedramrazi, Z.; Riss, A.; Wickenburg, S.; Tsai, H.-Z.; Fischer, F. R.; Crommie, M. F.; Rubio, A. Noncovalent Dimerization after Enediyne Cyclization on Au(111). *J. Am. Chem. Soc.* **2016**, *138*, 10963–10967.

[250] Ciccullo, F.; Gallagher, N. M.; Geladari, O.; Chassé, T.; Rajca, A.; Casu, M. B. A Derivative of the Blatter Radical as a Potential Metal-Free Magnet for Stable Thin Films and Interfaces. *ACS Appl. Mater. Interfaces* **2016**, *8*, 1805–1812.

[251] Karecla, G.; Papagiorgis, P.; Panagi, N.; A. Zissimou, G.; P. Constantinides, C.; A. Koutentis, P.; Itskos, G.; C. Hayes, S. Emission from the stable Blatter radical. *New J. Chem.* **2017**, *41*, 8604–8613.

[252] Yan, B.; Cramen, J.; McDonald, R.; L. Frank, N. Ferromagnetic spin-delocalized electron donors for multifunctional materials: π-conjugated benzotriazinyl radicals. *Chem. Commun.* **2011**, *47*, 3201–3203.

[253] Constantinides, C. P.; Berezin, A. A.; Zissimou, G. A.; Manoli, M.; Leitus, G. M.; Bendikov, M.; Probert, M. R.; Rawson, J. M.; Koutentis, P. A. A Magnetostructural Investigation of an Abrupt Spin Transition for 1-Phenyl-3-trifluoromethyl-1,4-dihydrobenzo[e][1,2,4]triazin-4-yl. *J. Am. Chem. Soc.* **2014**, *136*, 11906–11909.

[254] Takahashi, Y.; Miura, Y.; Yoshioka, N. Synthesis and properties of the 3- tert -butyl-7-trifluoromethyl-1,4-dihydro-1-phenyl-1,2,4-benzotriazin-4-yl radical. *New J. Chem.* **2015**, *39*, 4783–4789.

[255] Constantinides, C. P.; Berezin, A. A.; Zissimou, G. A.; Manoli, M.; Leitus, G. M.; Koutentis, P. A. The Suppression of Columnar π-Stacking in 3-Adamantyl-1-phenyl-1,4-dihydrobenzo[e][1,2,4]triazin-4-yl. *Molecules* **2016**, *21*, 636.

[256] Kaszyński, P.; Constantinides, C. P.; Young, V. G. The Planar Blatter Radical: Structural Chemistry of 1,4-Dihydrobenzo[e][1,2,4]triazin-4-yls. *Angew. Chem. Int. Ed.* **2016**, *128*, 11315–11318.

[257] Gardias, A.; Kaszyński, P.; Obijalska, E.; Trzybiński, D.; Domagała, S.; Woźniak, K.; Szczytko, J. Magnetostructural Investigation of Orthogonal 1-Aryl-3-Phenyl-1,4-Dihydrobenzo[e][1,2,4]triazin-4-yl Derivatives. *Chem. Eur. J.* **2018**, *24*, 1317–1329.

[258] Frisch, M. J. et al. Gaussian 09 Revision A.02. 1995; Gaussian Inc. Wallingford CT.

[259] Avogadro Version 1.2.0. `http://avogadro.cc/`, an open-source molecular builder and visualization tool.

[260] Kawai, S.; Sadeghi, A.; Okamoto, T.; Mitsui, C.; Pawlak, R.; Meier, T.; Takeya, J.; Goedecker, S.; Meyer, E. Organometallic Bonding in an Ullmann-Type On-Surface Chemical Reaction Studied by High-Resolution Atomic Force Microscopy. *Small* **2016**, *12*, 5303–5311.

[261] Zint, S.; Ebeling, D.; Schlöder, T.; Ahles, S.; Mollenhauer, D.; Wegner, H. A.; Schirmeisen, A. Imaging Successive Intermediate States of the On-Surface Ullmann Reaction on Cu(111): Role of the Metal Coordination. *ACS Nano* **2017**, *11*, 4183–4190.

[262] Mishra, S.; Beyer, D.; Berger, R.; Liu, J.; Gröning, O.; Urgel, J. I.; Müllen, K.; Ruffieux, P.; Feng, X.; Fasel, R. Topological Defect-Induced Magnetism in a Nanographene. *J. Am. Chem. Soc.* **2020**, *142*, 1147–1152.

[263] Hla, S.-W.; Bartels, L.; Meyer, G.; Rieder, K.-H. Inducing All Steps of a Chemical Reaction with the Scanning Tunneling Microscope Tip: Towards Single Molecule Engineering. *Phys. Rev. Lett.* **2000**, *85*, 2777–2780.

[264] Bieri, M.; Treier, M.; Cai, J.; Ait-Mansour, K.; Ruffieux, P.; Gröning, O.; Görning, P.; Kastler, M.; Rieger, R.; Feng, X.; Müllen, K.; Fasel, R. Porous graphenes : two-dimensional polymer synthesis with atomic precision. *Chem. Commun.* **2009**, 6919–6921.

[265] Gutzler, R.; Walch, H.; Eder, G.; Kloft, S.; M. Heckl, W.; Lackinger, M. Surface mediated synthesis of 2D covalent organic frameworks: 1,3,5-tris(4-bromophenyl)benzene on graphite (001), Cu(111), and Ag(110). *Chem. Commun.* **2009**, 4456–4458.

[266] Mishra, S.; Xu, K.; Eimre, K.; Komber, H.; Ma, J.; Pignedoli, C. A.; Fasel, R.; Feng, X.; Ruffieux, P. Synthesis and characterization of [7]triangulene. *Nanoscale* **2021**, *13*, 1624–1628.

[267] Cai, J.; Pignedoli, C. A.; Talirz, L.; Ruffieux, P.; Söde, H.; Liang, L.; Meunier, V.; Berger, R.; Li, R.; Feng, X.; Müllen, K.; Fasel, R. Graphene nanoribbon heterojunctions. *Nat. Nanotechnol.* **2014**, *9*, 896–900.

[268] Chen, Y.-C.; Cao, T.; Chen, C.; Pedramrazi, Z.; Haberer, D.; Oteyza, D. G. d.; Fischer, F. R.; Louie, S. G.; Crommie, M. F. Molecular bandgap engineering of bottom-up synthesized graphene nanoribbon heterojunctions. *Nat. Nanotechnol.* **2015**, *10*, 156–160.

[269] Nguyen, G. D. et al. Atomically precise graphene nanoribbon heterojunctions from a single molecular precursor. *Nat. Nanotechnol.* **2017**, *12*, 1077–1082.

[270] Zhou, X.; Yu, G. Modified Engineering of Graphene Nanoribbons Prepared via On-Surface Synthesis. *Adv. Mater.* **2020**, *32*, 1905957.

[271] Eichhorn, J.; Nieckarz, D.; Ochs, O.; Samanta, D.; Schmittel, M.; Szabelski, P. J.; Lackinger, M. On-Surface Ullmann Coupling: The Influence of Kinetic Reaction Parameters on the Morphology and Quality of Covalent Networks. *ACS Nano* **2014**, *8*, 7880–7889.

[272] Ji Shi, K.; Zhang, X.; Hui Shu, C.; Yuan Li, D.; Yan Wu, X.; Nian Liu, P. Ullmann coupling reaction of aryl chlorides on Au(111) using dosed Cu as a catalyst and the programmed growth of 2D covalent organic frameworks. *Chem. Commun.* **2016**, *52*, 8726–8729.

[273] Gao, H.-Y.; Wagner, H.; Zhong, D.; Franke, J.-H.; Studer, A.; Fuchs, H. Glaser Coupling at Metal Surfaces. *Angew. Chem. Int. Ed.* **2013**, *52*, 4024–4028.

[274] Cirera, B.; Zhang, Y.-Q.; Björk, J.; Klyatskaya, S.; Chen, Z.; Ruben, M.; Barth, J. V.; Klappenberger, F. Synthesis of Extended Graphdiyne Wires by Vicinal Surface Templating. *Nano Lett.* **2014**, *14*, 1891–1897.

[275] Held, P. A.; Gao, H.-Y.; Liu, L.; Mück-Lichtenfeld, C.; Timmer, A.; Mönig, H.; Barton, D.; Neugebauer, J.; Fuchs, H.; Studer, A. On-Surface Domino Reactions: Glaser Coupling and Dehydrogenative Coupling of a Biscarboxylic Acid To Form Polymeric Bisacylperoxides. *Angew. Chem. Int. Ed.* **2016**, *55*, 9777–9782.

[276] Weigelt, S.; Busse, C.; Bombis, C.; Knudsen, M. M.; Gothelf, K. V.; Strunskus, T.; Wöll, C.; Dahlbom, M.; Hammer, B.; Lægsgaard, E.; Besenbacher, F.; Linderoth, T. R. Covalent Interlinking of an Aldehyde and an Amine on a Au(111) Surface in Ultrahigh Vacuum. *Angew. Chem. Int. Ed.* **2007**, *46*, 9227–9230.

[277] Treier, M.; Richardson, N. V.; Fasel, R. Fabrication of Surface-Supported Low-Dimensional Polyimide Networks. *J. Am. Chem. Soc.* **2008**, *130*, 14054–14055.

[278] Tanoue, R.; Higuchi, R.; Enoki, N.; Miyasato, Y.; Uemura, S.; Kimizuka, N.; Stieg, A. Z.; Gimzewski, J. K.; Kunitake, M. Thermodynamically Controlled Self-Assembly of Covalent Nanoarchitectures in Aqueous Solution. *ACS Nano* **2011**, *5*, 3923–3929.

[279] C. Marele, A.; Mas-Ballesté, R.; Terracciano, L.; Rodriguez-Fernández, J.; Berlanga, I.; S. Alexandre, S.; Otero, R.; M. Gallego, J.; Zamora, F.; M. Gómez-Rodriguez, J. Formation of a surface covalent organic framework based on polyester condensation. *Chem. Commun.* **2012**, *48*, 6779–6781.

[280] Hu, F.-Y.; Zhang, X.-M.; Wang, X.-C.; Wang, S.; Wang, H.-Q.; Duan, W.-B.; Zeng, Q.-D.; Wang, C. In Situ STM Investigation of Two-Dimensional Chiral Assemblies through Schiff-Base Condensation at a Liquid/Solid Interface. *ACS Appl. Mater. Interfaces* **2013**, *5*, 1583–1587.

[281] Ciesielski, A.; El Garah, M.; Haar, S.; Kovařiček, P.; Lehn, J.-M.; Samori, P. Dynamic covalent chemistry of bisimines at the solid/liquid interface monitored by scanning tunnelling microscopy. *Nat. Chem.* **2014**, *6*, 1017–1023.

[282] Yang, B.; Björk, J.; Lin, H.; Zhang, X.; Zhang, H.; Li, Y.; Fan, J.; Li, Q.; Chi, L. Synthesis of Surface Covalent Organic Frameworks via Dimerization and Cyclotrimerization of Acetyls. *J. Am. Chem. Soc.* **2015**, *137*, 4904–4907.

[283] Yu, Y.; Sun, J.; Lei, S. Surface-Confined Synthesis of One-Dimensional Schiff Base Polymers Investigated by Scanning Tunneling Microscopy. *J. Phys. Chem. C* **2015**, *119*, 16777–16784.

[284] Jiang, L.; Papageorgiou, A. C.; Oh, S. C.; Sağlam, O.; Reichert, J.; Duncan, D. A.; Zhang, Y.-Q.; Klappenberger, F.; Guo, Y.; Allegretti, F.; More, S.; Bhosale, R.; Mateo-Alonso, A.; Barth, J. V. Synthesis of Pyrene-Fused Pyrazaacenes on Metal Surfaces: Toward One-Dimensional Conjugated Nanostructures. *ACS Nano* **2016**, *10*, 1033–1041.

[285] Mo, Y.-P.; Liu, X.-H.; Wang, D. Concentration-Directed Polymorphic Surface Covalent Organic Frameworks: Rhombus, Parallelogram, and Kagome. *ACS Nano* **2017**, *11*, 11694–11700.

[286] Zwaneveld, N. A. A.; Pawlak, R.; Abel, M.; Catalin, D.; Gigmes, D.; Bertin, D.; Porte, L. Organized Formation of 2D Extended Covalent Organic Frameworks at Surfaces. *J. Am. Chem. Soc.* **2008**, *130*, 6678–6679.

[287] Dienstmaier, J. F.; Gigler, A. M.; Goetz, A. J.; Knochel, P.; Bein, T.; Lyapin, A.; Reichlmaier, S.; Heckl, W. M.; Lackinger, M. Synthesis of Well-Ordered COF Monolayers: Surface Growth of Nanocrystalline Precursors versus Direct On-Surface Polycondensation. *ACS Nano* **2011**, *5*, 9737–9745.

[288] Schlögl, S.; Sirtl, T.; Eichhorn, J.; M. Heckl, W.; Lackinger, M. Synthesis of two-dimensional phenylene – boroxine networks through in vacuo condensation and on-surface radical addition. *Chem. Commun.* **2011**, *47*, 12355–12357.

[289] Dienstmaier, J. F.; Medina, D. D.; Dogru, M.; Knochel, P.; Bein, T.; Heckl, W. M.; Lackinger, M. Isoreticular Two-Dimensional Covalent Organic Frameworks Synthesized by On-Surface Condensation of Diboronic Acids. *ACS Nano* **2012**, *6*, 7234–7242.

[290] Faury, T.; Clair, S.; Abel, M.; Dumur, F.; Gigmes, D.; Porte, L. Sequential Linking To Control Growth of a Surface Covalent Organic Framework. *J. Phys. Chem. C* **2012**, *116*, 4819–4823.

[291] Guan, C.-Z.; Wang, D.; Wan, L.-J. Construction and repair of highly ordered 2D covalent networks by chemical equilibrium regulation. *Chem. Commun.* **2012**, *48*, 2943–2945.

[292] Fan, Q.; Werner, S.; Tschakert, J.; Ebeling, D.; Schirmeisen, A.; Hilt, G.; Hieringer, W.; Gottfried, J. M. Precise Monoselective Aromatic C–H Bond Activation by Chemisorption of Meta-Aryne on a Metal Surface. *J. Am. Chem. Soc.* **2018**, *140*, 7526–7532.

[293] Zhong, D.; Franke, J.-H.; Podiyanachari, S. K.; Blömker, T.; Zhang, H.; Kehr, G.; Erker, G.; Fuchs, H.; Chi, L. Linear Alkane Polymerization on a Gold Surface. *Science* **2011**, *334*, 213–216.

[294] Veld, M. I.; Iavicoli, P.; Haq, S.; B. Amabilino, D.; Raval, R. Unique intermolecular reaction of simple porphyrins at a metal surface gives covalent nanostructures. *Chem. Commun.* **2008**, 1536–1538.

[295] Liu, J.; Ruffieux, P.; Feng, X.; Müllen, K.; Fasel, R. Cyclotrimerization of arylalkynes on Au(111). *Chem. Commun.* **2014**, *50*, 11200–11203.

[296] Zhou, H.; Liu, J.; Du, S.; Zhang, L.; Li, G.; Zhang, Y.; Tang, B. Z.; Gao, H.-J. Direct Visualization of Surface-Assisted Two-Dimensional Diyne Polycyclotrimerization. *J. Am. Chem. Soc.* **2014**, *136*, 5567–5570.

[297] Di Giovannantonio, M.; Keerthi, A.; Urgel, J. I.; Baumgarten, M.; Feng, X.; Ruffieux, P.; Narita, A.; Fasel, R.; Müllen, K. On-Surface Dehydro-Diels–Alder Reaction of Dibromo-bis(phenylethynyl)benzene. *J. Am. Chem. Soc.* **2020**, *142*, 1721–1725.

[298] Zhang, R.; Lyu, G.; Yuan Li, D.; Nian Liu, P.; Lin, N. Template-controlled Sonogashira cross-coupling reactions on a Au(111) surface. *Chem. Commun.* **2017**, *53*, 1731–1734.

[299] Matena, M.; Riehm, T.; Stöhr, M.; Jung, T. A.; Gade, L. H. Transforming Surface Coordination Polymers into Covalent Surface Polymers: Linked Polycondensed Aromatics through Oligomerization of N-Heterocyclic Carbene Intermediates. *Angew. Chem. Int. Ed.* **2008**, *120*, 2448–2451.

[300] Sun, Q.; Zhang, C.; Li, Z.; Kong, H.; Tan, Q.; Hu, A.; Xu, W. On-Surface Formation of One-Dimensional Polyphenylene through Bergman Cyclization. *J. Am. Chem. Soc.* **2013**, *135*, 8448–8451.

[301] Riss, A.; Wickenburg, S.; Gorman, P.; Tan, L. Z.; Tsai, H.-Z.; de Oteyza, D. G.; Chen, Y.-C.; Bradley, A. J.; Ugeda, M. M.; Etkin, G.; Louie, S. G.; Fischer, F. R.; Crommie, M. F. Local Electronic and Chemical Structure of Oligo-acetylene Derivatives Formed Through Radical Cyclizations at a Surface. *Nano Lett.* **2014**, *14*, 2251–2255.

[302] Krüger, J.; Pavliček, N.; Alonso, J. M.; Pérez, D.; Guitián, E.; Lehmann, T.; Cuniberti, G.; Gourdon, A.; Meyer, G.; Gross, L.; Moresco, F.; Peña, D. Tetracene Formation by On-Surface Reduction. *ACS Nano* **2016**, *10*, 4538–4542.

[303] Urgel, J. I.; Hayashi, H.; Di Giovannantonio, M.; Pignedoli, C. A.; Mishra, S.; Deniz, O.; Yamashita, M.; Dienel, T.; Ruffieux, P.; Yamada, H.; Fasel, R. On-Surface Synthesis of Heptacene Organometallic Complexes. *J. Am. Chem. Soc.* **2017**, *139*, 11658–11661.

[304] Li, Q.; Yang, B.; Lin, H.; Aghdassi, N.; Miao, K.; Zhang, J.; Zhang, H.; Li, Y.; Duhm, S.; Fan, J.; Chi, L. Surface-Controlled Mono/Diselective ortho C–H Bond Activation. *J. Am. Chem. Soc.* **2016**, *138*, 2809–2814.

[305] Boz, S.; Stöhr, M.; Soydaner, U.; Mayor, M. Protecting-Group-Controlled Surface Chemistry–Organization and Heat-Induced Coupling of 4,4'-Di(tert-butoxycarbonylamino)biphenyl on Metal Surfaces. *Angew. Chem. Int. Ed.* **2009**, *48*, 3179–3183.

[306] Jensen, S.; Früchtl, H.; Baddeley, C. J. Coupling of Triamines with Diisocyanates on Au(111) Leads to the Formation of Polyurea Networks. *J. Am. Chem. Soc.* **2009**, *131*, 16706–16713.

[307] Wang, S.; Sun, Q.; Gröning, O.; Widmer, R.; Pignedoli, C. A.; Cai, L.; Yu, X.; Yuan, B.; Li, C.; Ju, H.; Zhu, J.; Ruffieux, P.; Fasel, R.; Xu, W. On-surface synthesis and characterization of individual polyacetylene chains. *Nat. Chem.* **2019**, *11*, 924–930.

[308] Diaz Arado, O.; Mönig, H.; Wagner, H.; Franke, J.-H.; Langewisch, G.; Held, P. A.; Studer, A.; Fuchs, H. On-Surface Azide–Alkyne Cycloaddition on Au(111). *ACS Nano* **2013**, *7*, 8509–8515.

[309] Bebensee, F.; Bombis, C.; Vadapoo, S.-R.; Cramer, J. R.; Besenbacher, F.; Gothelf, K. V.; Linderoth, T. R. On-Surface Azide–Alkyne Cycloaddition on Cu(111): Does It "Click" in Ultrahigh Vacuum? *J. Am. Chem. Soc.* **2013**, *135*, 2136–2139.

[310] Stolz, S.; Di Giovannantonio, M.; Urgel, J. I.; Sun, Q.; Kinikar, A.; Borin Barin, G.; Bommert, M.; Fasel, R.; Widmer, R. Reversible Dehalogenation in On-Surface Aryl–Aryl Coupling. *Angew. Chem. Int. Ed.* **2020**, *132*, 14210–14214.

[311] Shinde, P. P.; Liu, J.; Dienel, T.; Gröning, O.; Dumslaff, T.; Mühlinghaus, M.; Narita, A.; Müllen, K.; Pignedoli, C. A.; Fasel, R.; Ruffieux, P.; Passerone, D. Graphene nanoribbons with mixed cove-cape-zigzag edge structure. *Carbon* **2021**, *175*, 50–59.

[312] Hou, I. C.-Y.; Sun, Q.; Eimre, K.; Di Giovannantonio, M.; Urgel, J. I.; Ruffieux, P.; Narita, A.; Fasel, R.; Müllen, K. On-Surface Synthesis of Unsaturated Carbon Nanostructures with Regularly Fused Pentagon–Heptagon Pairs. *J. Am. Chem. Soc.* **2020**, *142*, 10291–10296.

[313] Franc, G.; Gourdon, A. Covalent networks through on-surface chemistry in ultra-high vacuum: state-of-the-art and recent developments. *Phys. Chem. Chem. Phys.* **2011**, *13*, 14283–14292.

[314] Lackinger, M.; Heckl, W. M. A STM perspective on covalent intermolecular coupling reactions on surfaces. *J. Phys. D: Appl. Phys.* **2011**, *44*, 464011.

[315] Zhang, X.; Zeng, Q.; Wang, C. On-surface single molecule synthesis chemistry: a promising bottom-up approach towards functional surfaces. *Nanoscale* **2013**, *5*, 8269–8287.

[316] Held, P. A.; Fuchs, H.; Studer, A. Covalent-Bond Formation via On-Surface Chemistry. *Chem. Eur. J.* **2017**, *23*, 5874–5892.

[317] Hu, J.; Liang, Z.; Shen, K.; Sun, H.; Jiang, Z.; Song, F. Recent Progress in the Fabrication of Low Dimensional Nanostructures via Surface-Assisted Transforming and Coupling. *J. Nanomater.* **2017**, *2017*, e4796538.

[318] Sun, Q.; Zhang, R.; Qiu, J.; Liu, R.; Xu, W. On-Surface Synthesis of Carbon Nanostructures. *Adv. Mater.* **2018**, *30*, 1705630.

[319] Clair, S.; de Oteyza, D. G. Controlling a Chemical Coupling Reaction on a Surface: Tools and Strategies for On-Surface Synthesis. *Chem. Rev.* **2019**, *119*, 4717–4776.

[320] Para, F.; Bocquet, F.; Nony, L.; Loppacher, C.; Féron, M.; Cherioux, F.; Gao, D. Z.; Federici Canova, F.; Watkins, M. B. Micrometre-long covalent organic fibres by photoinitiated chain-growth radical polymerization on an alkali-halide surface. *Nat. Chem.* **2018**, *10*, 1112–1117.

[321] Deshpande, A.; Sham, C.-H.; Alaboson, J. M. P.; Mullin, J. M.; Schatz, G. C.; Hersam, M. C. Self-Assembly and Photopolymerization of Sub-2 nm One-Dimensional Organic Nanostructures on Graphene. *J. Am. Chem. Soc.* **2012**, *134*, 16759–16764.

[322] G. Ayani, C.; Pisarra, M.; I. Urgel, J.; Jesús Navarro, J.; Diaz, C.; Hayashi, H.; Yamada, H.; Calleja, F.; Miranda, R.; Fasel, R.; Martin, F.; Parga, A. L. V. d. Efficient photogeneration of nonacene on nanostructured graphene. *Nanoscale Horiz.* **2021**, *6*, 744–750.

[323] Palma, C.-A. et al. Photoinduced C–C Reactions on Insulators toward Photolithography of Graphene Nanoarchitectures. *J. Am. Chem. Soc.* **2014**, *136*, 4651–4658.

[324] Richter, A.; Floris, A.; Bechstein, R.; Kantorovich, L.; Kühnle, A. On-surface synthesis on a bulk insulator surface. *J. Phys.: Condens. Matter* **2018**, *30*, 133001.

[325] Guo, C.; Wang, Y.; Kittelmann, M.; Kantorovitch, L.; Kühnle, A.; Floris, A. Mechanisms of Covalent Dimerization on a Bulk Insulating Surface. *J. Phys. Chem. C* **2017**, *121*, 10053–10062.

[326] Kittelmann, M.; Nimmrich, M.; Lindner, R.; Gourdon, A.; Kühnle, A. Sequential and Site-Specific On-Surface Synthesis on a Bulk Insulator. *ACS Nano* **2013**, *7*, 5614–5620.

[327] Kittelmann, M.; Rahe, P.; Nimmrich, M.; Hauke, C. M.; Gourdon, A.; Kühnle, A. On-Surface Covalent Linking of Organic Building Blocks on a Bulk Insulator. *ACS Nano* **2011**, *5*, 8420–8425.

[328] Lindner, R.; Rahe, P.; Kittelmann, M.; Gourdon, A.; Bechstein, R.; Kühnle, A. Substrate Templating Guides the Photoinduced Reaction of C60 on Calcite. *Angew. Chem. Int. Ed.* **2014**, *53*, 7952–7955.

[329] Richter, A.; Vilas-Varela, M.; Peña, D.; Bechstein, R.; Kühnle, A. Homocoupling of terminal alkynes on calcite (10.4). *Surf. Sci.* **2018**, *678*, 106–111.

[330] Dienel, T.; Gómez-Diaz, J.; Seitsonen, A. P.; Widmer, R.; Iannuzzi, M.; Radican, K.; Sachdev, H.; Müllen, K.; Hutter, J.; Gröning, O. Dehalogenation and Coupling of a Polycyclic Hydrocarbon on an Atomically Thin Insulator. *ACS Nano* **2014**, *8*, 6571–6579.

[331] Zhao, W.; Dong, L.; Huang, C.; Myo Win, Z.; Lin, N. Cu- and Pd-catalyzed Ullmann reaction on a hexagonal boron nitride layer. *Chem. Commun.* **2016**, *52*, 13225–13228.

[332] Galeotti, G.; Fritton, M.; Lackinger, M. Carbon-Carbon Coupling on Inert Surfaces by Deposition of En Route Generated Aryl Radicals. *Angew. Chem. Int. Ed.* **2020**, *59*, 22785–22789.

[333] Lahrood, A. R.; Björk, J.; M. Heckl, W.; Lackinger, M. 1,3-Diiodobenzene on Cu(111) – an exceptional case of on-surface Ullmann coupling. *Chem. Commun.* **2015**, *51*, 13301–13304.

[334] Abel, M.; Clair, S.; Ourdjini, O.; Mossoyan, M.; Porte, L. Single Layer of Polymeric Fe-Phthalocyanine: An Organometallic Sheet on Metal and Thin Insulating Film. *J. Am. Chem. Soc.* **2011**, *133*, 1203–1205.

[335] Fatayer, S.; Moll, N.; Collazos, S.; Pérez, D.; Guitián, E.; Peña, D.; Gross, L.; Meyer, G. Controlled Fragmentation of Single Molecules with Atomic Force Microscopy by Employing Doubly Charged States. *Phys. Rev. Lett.* **2018**, *121*, 226101.

[336] Zhan, G.; Makoudi, Y.; Jeannoutot, J.; Lamare, S.; Féron, M.; Palmino, F.; Bocquet, M.-L.; Thomas, C.; Chérioux, F. On-Surface Radical Oligomerisation: A New Approach to STM Tip-Induced Reactions. **2019**, chemrxiv.6860105.v1.

[337] Geagea, E.; Jeannoutot, J.; Féron, M.; Palmino, F.; M. Thomas, C.; Rochefort, A.; Chérioux, F. Collective radical oligomerisation induced by an STM tip on a silicon surface. *Nanoscale* **2021**, *13*, 349–354.

[338] Smith, P. P. K.; Buseck, P. R. Carbyne Forms of Carbon: Do They Exist? *Science* **1982**, *216*, 984–986.

[339] S. Casari, C.; Tommasini, M.; R. Tykwinski, R.; Milani, A. Carbon-atom wires: 1-D systems with tunable properties. *Nanoscale* **2016**, *8*, 4414–4435.

[340] Yang, S.; Kertesz, M. Linear Cn Clusters: Are They Acetylenic or Cumulenic? *J. Phys. Chem. A* **2008**, *112*, 146–151.

[341] Kertesz, M.; Koller, J.; Aman, A. Ab initio Hartree–Fock crystal orbital studies. II. Energy bands of an infinite carbon chain. *J. Chem. Phys.* **1978**, *68*, 2779–2782.

[342] Peierls, R. E. *Quantum Theory of Solids*; Oxford University Press, 1996.

[343] Hoffmann, R. How chemistry and physics meet in the solid state. *Angew. Chem. Int. Ed.* **1987**, *26*, 846–878.

[344] Liu, M.; Artyukhov, V. I.; Lee, H.; Xu, F.; Yakobson, B. I. Carbyne from First Principles: Chain of C Atoms, a Nanorod or a Nanorope. *ACS Nano* **2013**, *7*, 10075–10082.

[345] Zanolli, Z.; Onida, G.; Charlier, J.-C. Quantum Spin Transport in Carbon Chains. *ACS Nano* **2010**, *4*, 5174–5180.

[346] Zeng, M. G.; Shen, L.; Cai, Y. Q.; Sha, Z. D.; Feng, Y. P. Perfect spin-filter and spin-valve in carbon atomic chains. *Appl. Phys. Lett.* **2010**, *96*, 042104.

[347] Akdim, B.; Pachter, R. Switching Behavior of Carbon Chains Bridging Graphene Nanoribbons: Effects of Uniaxial Strain. *ACS Nano* **2011**, *5*, 1769–1774.

[348] Artyukhov, V. I.; Liu, M.; Yakobson, B. I. Mechanically Induced Metal–Insulator Transition in Carbyne. *Nano Lett.* **2014**, *14*, 4224–4229.

[349] Garner, M. H.; Bro-Jørgensen, W.; Pedersen, P. D.; Solomon, G. C. Reverse Bond-Length Alternation in Cumulenes: Candidates for Increasing Electronic Transmission with Length. *J. Phys. Chem. C* **2018**, *122*, 26777–26789.

[350] Prasongkit, J.; Grigoriev, A.; Wendin, G.; Ahuja, R. Cumulene molecular wire conductance from first principles. *Phys. Rev. B* **2010**, *81*, 115404.

[351] Prasongkit, J.; Grigoriev, A.; Ahuja, R. Mechano-switching devices from carbon wire-carbon nanotube junctions. *Phys. Rev. B* **2013**, *87*, 155434.

[352] Sarbadhikary, P.; Shil, S.; Panda, A.; Misra, A. A Perspective on Designing Chiral Organic Magnetic Molecules with Unusual Behavior in Magnetic Exchange Coupling. *J. Org. Chem.* **2016**, *81*, 5623–5630.

[353] Garner, M. H.; Hoffmann, R.; Rettrup, S.; Solomon, G. C. Coarctate and Möbius: The Helical Orbitals of Allene and Other Cumulenes. *ACS Cent. Sci.* **2018**, *4*, 688–700.

[354] Garner, M. H.; Jensen, A.; Hyllested, L. O. H.; Solomon, G. C. Helical orbitals and circular currents in linear carbon wires. *Chem. Sci.* **2019**, *10*, 4598–4608.

[355] Cretu, O.; Botello-Mendez, A. R.; Janowska, I.; Pham-Huu, C.; Charlier, J.-C.; Banhart, F. Electrical Transport Measured in Atomic Carbon Chains. *Nano Lett.* **2013**, *13*, 3487–3493.

[356] Wang, C.; Batsanov, A. S.; Bryce, M. R.; Martin, S.; Nichols, R. J.; Higgins, S. J.; Garcia-Suárez, V. M.; Lambert, C. J. Oligoyne Single Molecule Wires. *J. Am. Chem. Soc.* **2009**, *131*, 15647–15654.

[357] Ravagnan, L.; Manini, N.; Cinquanta, E.; Onida, G.; Sangalli, D.; Motta, C.; Devetta, M.; Bordoni, A.; Piseri, P.; Milani, P. Effect of Axial Torsion on *sp* Carbon Atomic Wires. *Phys. Rev. Lett.* **2009**, *102*, 245502.

[358] Lucotti, A.; Tommasini, M.; Fazzi, D.; Del Zoppo, M.; Chalifoux, W. A.; Tykwinski, R. R.; Zerbi, G. Absolute Raman intensity measurements and determination of the vibrational second hyperpolarizability of adamantyl endcapped polyynes. *J. Raman Spectrosc.* **2012**, *43*, 1293–1298.

[359] Eisler, S.; Slepkov, A. D.; Elliott, E.; Luu, T.; McDonald, R.; Hegmann, F. A.; Tykwinski, R. R. Polyynes as a Model for Carbyne: Synthesis, Physical Properties, and Nonlinear Optical Response. *J. Am. Chem. Soc.* **2005**, *127*, 2666–2676.

[360] Kminek, I.; Klimovic, J.; Prasad, P. N. Third-order nonlinear optical response of some tetrasubstituted cumulenes. *Chem. Mater.* **1993**, *5*, 357–360.

[361] Albert, I. D. L.; Pugh, D.; Morley, J. O.; Ramasesha, S. Linear and nonlinear optical properties of cumulenes and polyenynes: a model exact study. *J. Phys. Chem.* **1992**, *96*, 10160–10165.

[362] Melis, C.; Fugallo, G.; Colombo, L. Room temperature second sound in cumulene. *Phys. Chem. Chem. Phys.* **2021**, *23*, 15275–15281.

[363] Chalifoux, W. A.; Tykwinski, R. R. Synthesis of polyynes to model the sp-carbon allotrope carbyne. *Nat. Chem.* **2010**, *2*, 967–971.

[364] Innocenti, F.; Milani, A.; Castiglioni, C. Can Raman spectroscopy detect cumulenic structures of linear carbon chains? *J. Raman Spectrosc.* **2010**, *41*, 226–236.

[365] Auffrant, A.; Jaun, B.; Jarowski, P. D.; Houk, K. N.; Diederich, F. Peralkynylated Buta-1,2,3-Trienes: Exceptionally Low Rotational Barriers of Cumulenic C=C Bonds in the Range of Those of Peptide C–N Bonds. *Chem. Eur.* **2004**, *10*, 2906–2911.

[366] Hartzler, H. D. Di-tert-butylvinylidenecarbene, tetra-tert-butylbutatriene, tetra-tert-butylhexapentaene, and tetrakis(di-tert-butylvinylidene)cyclobutane. *J. Am. Chem. Soc.* **1971**, *93*, 4527–4531.

[367] Pinter, P.; Munz, D. Controlling Möbius-Type Helicity and the Excited-State Properties of Cumulenes with Carbenes. *J. Phys. Chem. A* **2020**, *124*, 10100–10110.

[368] Hirao, Y.; Daifuku, Y.; Ihara, K.; Kubo, T. Spin–Spin Interactions in One-Dimensional Assemblies of a Cumulene-Based Singlet Biradical. *Angew. Chem. Int. Ed.* **2021**, *60*, 21319–21326.

[369] Gross, L.; Mohn, F.; Moll, N.; Schuler, B.; Criado, A.; Guitián, E.; Peña, D.; Gourdon, A.; Meyer, G. Bond-Order Discrimination by Atomic Force Microscopy. *Science* **2012**, *337*, 1326–1329.

[370] Qiu, X. H.; Nazin, G. V.; Ho, W. Vibronic States in Single Molecule Electron Transport. *Phys. Rev. Lett.* **2004**, *92*, 206102.

[371] Pavliček, N.; Gross, L. Generation, manipulation and characterization of molecules by atomic force microscopy. *Nat. Rev. Chem.* **2017**, *1*, 0005.

[372] Bruice, P. Y. *Organic Chemistry*, 7th ed.; Pearson, 2014.

[373] Riedel, E. *Allgemeine und Anorganische Chemie*, 10th ed.; Walter de Gruyter, 2010.

[374] Scheuerer, P.; Patera, L. L.; Simbürger, F.; Queck, F.; Swart, I.; Schuler, B.; Gross, L.; Moll, N.; Repp, J. Charge-Induced Structural Changes in a Single Molecule Investigated by Atomic Force Microscopy. *Phys. Rev. Lett.* **2019**, *123*, 066001.

[375] Kaiser, K.; Gross, L.; Schulz, F. A Single-Molecule Chemical Reaction Studied by High-Resolution Atomic Force Microscopy and Scanning Tunneling Microscopy Induced Light Emission. *ACS Nano* **2019**, *13*, 6947–6954.

[376] Uhlmann, C.; Swart, I.; Repp, J. Controlling the Orbital Sequence in Individual Cu-Phthalocyanine Molecules. *Nano Lett.* **2013**, *13*, 777–780.

[377] Münnich, G.; Albrecht, F.; Nacci, C.; Utz, M.; Schuh, D.; Kanisawa, K.; Fölsch, S.; Repp, J. Probing individual weakly-coupled π-conjugated molecules on semiconductor surfaces. *J. Appl. Phys.* **2012**, *112*, 034312.

[378] Gross, L.; Moll, N.; Mohn, F.; Curioni, A.; Meyer, G.; Hanke, F.; Persson, M. High-Resolution Molecular Orbital Imaging Using a *p*-Wave STM Tip. *Phys. Rev. Lett.* **2011**, *107*, 086101.

[379] Liljeroth, P.; Repp, J.; Meyer, G. Current-Induced Hydrogen Tautomerization and Conductance Switching of Naphthalocyanine Molecules. *Science* **2007**, *317*, 1203–1206.

[380] Pavliček, N.; Majzik, Z.; Collazos, S.; Meyer, G.; Pérez, D.; Guitián, E.; Peña, D.; Gross, L. Generation and Characterization of a meta-Aryne on Cu and NaCl Surfaces. *ACS Nano* **2017**, *11*, 10768–10773.

[381] Ladenthin, J. N.; Grill, L.; Gawinkowski, S.; Liu, S.; Waluk, J.; Kumagai, T. Hot Carrier-Induced Tautomerization within a Single Porphycene Molecule on Cu(111). *ACS Nano* **2015**, *9*, 7287–7295.

[382] Schendel, V.; Borca, B.; Pentegov, I.; Michnowicz, T.; Kraft, U.; Klauk, H.; Wahl, P.; Schlickum, U.; Kern, K. Remotely Controlled Isomer Selective Molecular Switching. *Nano Lett.* **2016**, *16*, 93–97.

[383] Pivetta, M.; Patthey, F.; Stengel, M.; Baldereschi, A.; Schneider, W.-D. Local work function Moiré pattern on ultrathin ionic films: NaCl on Ag(100). *Phys. Rev. B* **2005**, *72*, 115404.

[384] Ploigt, H.-C.; Brun, C.; Pivetta, M.; Patthey, F.; Schneider, W.-D. Local work function changes determined by field emission resonances: NaCl/Ag(100). *Phys. Rev. B* **2007**, *76*, 195404.

[385] Kawata, S.; Pu, Y.-J.; Saito, A.; Kurashige, Y.; Beppu, T.; Katagiri, H.; Hada, M.; Kido, J. Singlet Fission of Non-polycyclic Aromatic Molecules in Organic Photovoltaics. *Adv. Mater.* **2016**, *28*, 1585–1590.

[386] Varnavski, O.; Abeyasinghe, N.; Aragó, J.; Serrano-Pérez, J. J.; Orti, E.; López Navarrete, J. T.; Takimiya, K.; Casanova, D.; Casado, J.; Goodson, T. High Yield Ultrafast Intramolecular Singlet Exciton Fission in a Quinoidal Bithiophene. *J. Phys. Chem. Lett.* **2015**, *6*, 1375–1384.

[387] Rudebusch, G. E.; Zafra, J. L.; Jorner, K.; Fukuda, K.; Marshall, J. L.; Arrechea-Marcos, I.; Espejo, G. L.; Ponce Ortiz, R.; Gómez-Garcia, C. J.; Zakharov, L. N.; Nakano, M.; Ottosson, H.; Casado, J.; Haley, M. M. Diindeno-fusion of an anthracene as a design strategy for stable organic biradicals. *Nat. Chem.* **2016**, *8*, 753–759.

[388] Koike, H.; Chikamatsu, M.; Azumi, R.; Tsutsumi, J.; Ogawa, K.; Yamane, W.; Nishiuchi, T.; Kubo, T.; Hasegawa, T.; Kanai, K. Stable Delocalized Singlet Biradical Hydrocarbon for Organic Field-Effect Transistors. *Adv. Funct. Mater.* **2016**, *26*, 277–283.

[389] C. Ribierre, J.; Zhao, L.; Furukawa, S.; Kikitsu, T.; Inoue, D.; Muranaka, A.; Takaishi, K.; Muto, T.; Matsumoto, S.; Hashizume, D.; Uchiyama, M.; André, P.; Adachi, C.; Aoyama, T. Ambipolar organic field-effect transistors based on solution-processed single crystal microwires of a quinoidal oligothiophene derivative. *Chem. Commun.* **2015**, *51*, 5836–5839.

[390] Zhang, C.; Zang, Y.; Gann, E.; McNeill, C. R.; Zhu, X.; Di, C.-a.; Zhu, D. Two-Dimensional π-Expanded Quinoidal Terthiophenes Terminated with Dicyanomethylenes as n-Type Semiconductors for High-Performance Organic Thin-Film Transistors. *J. Am. Chem. Soc.* **2014**, *136*, 16176–16184.

[391] Li, J.; Qiao, X.; Xiong, Y.; Li, H.; Zhu, D. Five-Ring Fused Tetracyanothienoquinoids as High-Performance and Solution-Processable n-Channel Organic Semiconductors: Effect of the Branching Position of Alkyl Chains. *Chem. Mater.* **2014**, *26*, 5782–5788.

[392] Wu, Q.; Li, R.; Hong, W.; Li, H.; Gao, X.; Zhu, D. Dicyanomethylene-Substituted Fused Tetrathienoquinoid for High-Performance, Ambient-Stable, Solution-Processable n-Channel Organic Thin-Film Transistors. *Chem. Mater.* **2011**, *23*, 3138–3140.

[393] Suzuki, Y.; Shimawaki, M.; Miyazaki, E.; Osaka, I.; Takimiya, K. Quinoidal Oligothiophenes with (Acyl)cyanomethylene Termini: Synthesis, Characterization, Properties, and Solution Processed n-Channel Organic Field-Effect Transistors. *Chem. Mater.* **2011**, *23*, 795–804.

[394] Suzuki, Y.; Miyazaki, E.; Takimiya, K. ((Alkyloxy)carbonyl)cyanomethylene-Substituted Thienoquinoidal Compounds: a New Class of Soluble n-Channel Organic

Semiconductors for Air-Stable Organic Field-Effect Transistors. *J. Am. Chem. Soc.* **2010**, *132*, 10453–10466.

[395] Ribierre, J.-C.; Watanabe, S.; Matsumoto, M.; Muto, T.; Nakao, A.; Aoyama, T. Reversible Conversion of the Majority Carrier Type in Solution-Processed Ambipolar Quinoidal Oligothiophene Thin Films. *Adv. Mater.* **2010**, *22*, 4044–4048.

[396] Ribierre, J. C.; Fujihara, T.; Watanabe, S.; Matsumoto, M.; Muto, T.; Nakao, A.; Aoyama, T. Direct Laser Writing of Complementary Logic Gates and Lateral p–n Diodes in a Solution-Processible Monolithic Organic Semiconductor. *Adv. Mater.* **2010**, *22*, 1722–1726.

[397] Handa, S.; Miyazaki, E.; Takimiya, K.; Kunugi, Y. Solution-Processible n-Channel Organic Field-Effect Transistors Based on Dicyanomethylene-Substituted Terthienoquinoid Derivative. *J. Am. Chem. Soc.* **2007**, *129*, 11684–11685.

[398] Chesterfield, R.; Newman, C.; Pappenfus, T.; Ewbank, P.; Haukaas, M.; Mann, K.; Miller, L.; Frisbie, C. High Electron Mobility and Ambipolar Transport in Organic Thin-Film Transistors Based on a π-Stacking Quinoidal Terthiophene. *Adv. Mater.* **2003**, *15*, 1278–1282.

[399] Takahashi, T.; Matsuoka, K.-I.; Takimiya, K.; Otsubo, T.; Aso, Y. Extensive Quinoidal Oligothiophenes with Dicyanomethylene Groups at Terminal Positions as Highly Amphoteric Redox Molecules. *J. Am. Chem. Soc.* **2005**, *127*, 8928–8929.

[400] Coulson, C. A.; Craig, D.; Maccoll, A.; Pullman, A. P-quinodimethane and its diradical. *Discuss. Faraday Soc.* **1947**, *2*, 36–38.

[401] Chen, C. J. Theory of scanning tunneling spectroscopy. *J. Vac. Sci. Technol. B* **1998**, *6*, 319.

[402] Chen, C. J. Tunneling matrix elements in three-dimensional space: The derivative rule and the sum rule. *Phys. Rev. B* **1990**, *42*, 8841–8857.

[403] Köhler, J. Magnetic resonance of a single molecular spin. *Phys. Rep.* **1999**, *310*, 261–339.

[404] Sinnecker, S.; Neese, F. Spin-Spin Contributions to the Zero-Field Splitting Tensor in Organic Triplets, Carbenes and Biradicals A Density Functional and Ab Initio Study. *J. Phys. Chem. A* **2006**, *110*, 12267–12275.

[405] Köhler, J.; Disselhorst, J. A.; Donckers, M.; Groenen, E. J.; Schmidt, J.; Moerner, W. E. Magnetic resonance of a single molecular spin. *Nature* **1993**, *363*, 242–244.

[406] Van Strien, A. J.; Schmidt, J. An EPR study of the triplet state of pentacene by electron spin-echo techniques and laser flash excitation. *Chem. Phys. Lett.* **1980**, *70*, 513–517.

[407] Hernangómez-Pérez, D.; Schlör, J.; Egger, D. A.; Patera, L. L.; Repp, J.; Evers, F. Reorganization energy and polaronic effects of pentacene on NaCl films. *Phys. Rev. B* **2020**, *102*, 115419.

[408] Schweitzer, C.; Schmidt, R. Physical Mechanisms of Generation and Deactivation of Singlet Oxygen. *Chem. Rev.* **2003**, *103*, 1685–1758.